Transient dynamics of beam trusses under impulse loads

Yves Le Guennec

École Centrale Paris

Laboratoire de Mécanique des Sols, Structures et Matériaux
CNRS UMR 8579

Thèse

présentée par

Yves LE GUENNEC

pour l'obtention du grade de

Docteur de l'École Centrale Paris

Specialité	Mécanique, dynamique des structures
Laboratoire d'Accueil	Laboratoire de Mécanique des Sols, Structures et Matériaux

Transient dynamics of beam trusses under impulse loads

Soutenue le 4 février 2013, devant la commission d'examen composée de :

M.Olivier ALLIX	Président
M.Brian MACE	Rapporteur
M.Mohamed ICHCHOU	Rapporteur
M.Basile AUDOLY	Examinateur
M.Anthony GRAVOUIL	Examinateur
M.Etienne BALMÈS	Invité
M.Didier CLOUTEAU	Directeur de Thèse
M.Éric SAVIN	Co-Directeur de Thèse

Thèse numéro : 2013ECAP0016.
Châtenay Malabry

École Centrale Paris

PhD thesis
Specialty: Computational mechanics
Host laboratories: ONERA & MSSMat laboratory

by

Yves LE GUENNEC

Transient dynamics of beam trusses under impulse loads.

ONERA – Dpt. Aéroélasticité et Dynamique des Structures
BP 72 – 29, avenue de la Division Leclerc
F-92322 Châtillon cedex
Tél. +33(1) 46 73 40 40 (standard) — Fax +33(1) 46 73 41 41 — www.onera.fr

Résumé

Ce travail de recherche est dédié à la simulation de la réponse transitoire des assemblages de poutres soumis à des chocs. De tels chargements entraînent la propagation d'ondes haute fréquence dans l'ensemble de la structure. L'énergie qu'elles transportent peut être dommageable pour son fonctionnement ou celui des équipements embarqués. Dans des études précédentes, il a été observé sur des structures expérimentales qu'un régime vibratoire diffusif tend à s'installer pour des temps longs. Le but de cette étude est donc de développer un modèle robuste de la réponse transitoire des assemblages de poutres soumis à des chocs permettant de simuler, entre autres, cet état diffusif.

Les champs de déplacement étant très oscillants et la densité modale élevée, la simulation numérique de la réponse transitoire à des chocs peut difficilement être menée par une méthode d'éléments finis classique. Une approche utilisant un estimateur de la densité d'énergie de chaque mode de propagation a donc été mise en œuvre. Elle permet d'accéder à des informations locales sur les états vibratoires, et de contourner certaines limitations intrinsèques aux longueurs d'onde courtes. Après avoir comparé plusieurs modèles de réduction cinématique de poutre à un modèle de Lamb de propagation dans un guide d'ondes circulaire, la cinématique de Timoshenko a été retenue afin de modéliser le comportement mécanique haute fréquence des poutres. En utilisant ce modèle dans le cadre de l'approche énergétique évoquée plus haut, deux groupes de modes de propagation de la densité d'énergie vibratoire dans une poutre ont été isolés: des modes longitudinaux regroupant un mode de compression et des modes de flexion, et des modes transversaux regroupant des modes de cisaillement et un mode de torsion. Il peut être également montré que l'évolution en temps des densités d'energie associées obeit à des lois de transport.

Pour des assemblages de poutres, les phénomènes de réflexion/transmission aux jonctions ont du être pris en compte. Les opérateurs permettant de les décrire en termes de flux d'énergie ont été obtenus grâce aux équations de continuité des déplacements et des efforts aux jonctions. Quelques caractéristiques typiques d'un régime haute fréquence ont été mises en évidence, tel que le découplage entre les modes de rotation et les modes de translation.

En revanche, les champs de densité d'énergie sont quant à eux discontinus aux jonctions. Une méthode d'éléments finis discontinus a donc été développée afin de les simuler numériquement comme solutions d'équations de transport. Si l'on souhaite atteindre le régime diffusif aux temps longs, le shéma numérique doit être peu dissipatif et peu dispersif. La discrétisation spatiale a été faite avec des fonctions d'approximation de type spectrales, et l'intégration temporelle avec des schémas de Runge-Kutta d'ordre élevé du type "strong-stability preserving". Les simulations numériques ont donné des résultats concluants car elles permettent d'exhiber le régime de diffusion. Il a été remarqué qu'il existait en fait deux limites diffusives différentes: (i) la diffusion spatiale de l'énergie sur l'ensemble de la structure, et (ii) l'équirépartition des densités d'énergie entre les différents modes de propagation. Enfin, une technique de renversement temporel a été développée. Elle pourra être utile dans de futurs travaux sur le contrôle non destructif des assemblages complexes et de grandes tailles.

Mots-clés : *Propagation d'ondes haute fréquence, modèle de Lamb, poutre de Timoshenko, réflexion/transmission, éléments finis discontinus, schéma de Runge-Kutta, renversement temporel.*

Abstract

This research is dedicated to the simulation of the transient response of beam trusses under impulse loads. The latter lead to the propagation of high-frequency waves in such built-up structures. In the aerospace industry, that phenomenon may penalize the functioning of the structures or the equipments attached to them on account of the vibrational energy carried by the waves. It is also observed experimentally that high-frequency wave propagation evolves into a diffusive vibrational state at late times. The goal of this study is then to develop a robust model of high-frequency wave propagation within three-dimensional beam trusses in order to be able to recover, for example, this diffusion regime.

On account of the small wavelengths and the high modal density, the modeling of high-frequency wave propagation is hardly feasible by classical finite elements or other methods describing the displacement fields directly. Thus, an approach dealing with the evolution of an estimator of the energy density of each propagating mode in a Timoshenko beam has been used. It provides information on the local behavior of the structures while avoiding some limitations related to the small wavelengths of high-frequency waves. After a comparison between some reduced-order beam kinematics and the Lamb model of wave propagation in a circular waveguide, the Timoshenko kinematics has been selected for the mechanical modeling of the beams. It may be shown that the energy densities of the propagating modes in a Timoshenko beam obey transport equations. Two groups of energy modes have been isolated: the longitudinal group that gathers the compressional and the bending energetic modes, and the transverse group that gathers the shear and torsional energetic modes.

The reflection/transmission phenomena taking place at the junctions between beams have also been investigated. For this purpose, the power flow reflection/transmission operators have been derived from the continuity of the displacements and efforts at the junctions. Some characteristic features of a high-frequency behavior at beam junctions have been highlighted such as the decoupling between the rotational and translational motions.

It is also observed that the energy densities are discontinuous at the junctions on account of the power flow reflection/transmission phenomena. Thus a discontinuous finite element method has been implemented, in order to solve the transport equations they satisfy. The numerical scheme has to be weakly dissipative and dispersive in order to exhibit the aforementioned diffusive regime arising at late times. That is the reason why spectral-like approximation functions for spatial discretization, and strong-stability preserving Runge-Kutta schemes for time integration have been used. Numerical simulations give satisfactory results because they indeed highlight the outbreak of such a diffusion state. The latter is characterized by the following: (i) the spatial spread of the energy over the truss, and (ii) the equipartition of the energy between the different modes. The last part of the thesis has been devoted to the development of a time reversal processing, that could be useful for future works on structural health monitoring of complex, multi-bay trusses.

Keywords: *High-frequency wave propagation, Timoshenko beam, Lamb model, reflection/transmission, discontinuous finite elements, Runge-Kutta scheme, time reversal.*

Remerciements

En premier lieu, je souhaite remercier très chaleureusement mes deux Directeurs de thèse. Didier Clouteau pour sa disponibilité, son aide précieuse, ses idées toujours pertinentes qui m'ont permises de faire évoluer mon sujet, et bien sûr Éric Savin pour la qualité de son encadrement, ses conseils, le temps qu'il m'a accordé, en particulier pendant la période de rédaction de ce mémoire, et pour m'avoir donné l'occasion d'effectuer cette thèse à l'ONERA sur ce sujet passionnant.

Mes remerciements vont ensuite vers Olivier Allix qui a accepté de présider ma soutenance et aux deux rapporteurs, Mohammed Ichchou et Brian Mace, pour la pertinence de leur relecture du manuscrit et de leurs questions. Je remercie également Anthony Gravouil, Basile Audoly et Étienne Balmès, qui ont accepté de participer au jury de la soutenance, pour leur disponibilité et l'intérêt qu'ils ont montré au sujet.

Grâce à l'ONERA et au département DADS j'ai pu effectuer ce travail de recherche dans de bonnes conditions. Je remercie Jean-Pierre Grisval et Nicolas Piet pour m'avoir accueilli dans leur département et pour m'avoir donné les moyens matériels et financiers de réaliser ces trois ans de recherche. Mais je tiens aussi à témoigner ma reconnaissance à tous les membres du département DADS pour leur sympathie et leurs conseils avisés. Je remercie aussi toutes l'équipe de l'école doctorale pour la gestion administrative sans faille et la qualité des formations proposées. Merci également à mes collègues de Centrale que j'ai appris à mieux connaitre en cette fin de thèse. Bref un grand merci à tous. Merci également à Denis Aubry pour m'avoir donné l'opportunité d'encadrer les TDs de mécanique générale, ce qui fut une expérience très enrichissante pour moi.

Mais je tiens aussi à remercier tous mes proches pour leur soutien pendant ces trois ans. Merci aux membres de la soirée guitare pour les moments de détentes salutaires, à tous ceux qui ont été présent dans les moments durs. Mes pensées vont vers ma famille et plus particulièrement à mon père à qui je dédie cette thèse.

Introduction

Aerospace structures under impulse loads

Aerospace structures are often subjected to mechanical or acoustical impulse loads. These shocks generate strongly oscillating waves in the structures. Typical examples are the unfolding of solar panels of satellites or the pyrotechnic cut (the step of separation between the launcher and the payload, see Fig. 1), that are set off by pyrotechnic shocks. In aeronautics, the landing of a jet on the deck of an aircraft carrier produces a mechanical shock when the tailhook catches the arresting gear (see Fig. 2). These waves could

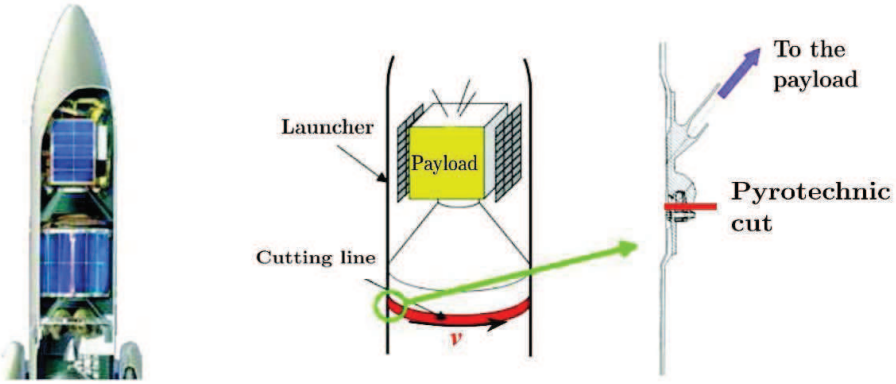

Figure 1: The pyrotechnic cut step.

be highly penalizing because the energy they carry can reach the equipments attached to the structures and disturb their operations. Actually several spatial missions aborted on account of such problems [67]. Thus, it is much desirable to improve the understanding and the prediction of the propagation of the waves in structures at long times. Moreover aerospace structures are mainly composed of beams and plates, and the present study is focused on the case of beam assemblies.

An ideal shock would excite the entire frequency spectrum. In the low frequency range, the structural response is very well characterized by a modal approach. In the high-frequency (HF) range this description is however not relevant any more on account of the small wavelengths and the high modal density of built-up structures. Thus several strategies have been conducted in order to predict more precisely the transient dynamics of such structures under impulse loads. The methods widely used in the industry are global

Figure 2: A landing of an F/A-18 Hornet on an aircraft carrier.

approaches like the Statistical Energy Analysis (SEA). It describes the levels of energy in the substructures of a built-up system and the energetic exchanges between them [61]. However, SEA gives no local information and relies on the determination of some core parameters (like the so-called coupling loss factors characterizing the exchanges of energy) by hybrid methods. An other class of methods gathers local approaches like the Vibrational Conductivity Analogy (VCA) [68]. Although they give a local evolution of the transient response, they are not suitable for complex structures and are not valid in some cases [22, 88]. Wave approaches have been developed like the WKBJ (for Wentzel, Kramers, Brillouin, and Jeffreys) methods [91] which are appropriate for the HF range. But they require the resolution of an eikonal equation, which raises several theoretical and numerical difficulties, in particular for wave superposition or the analysis of caustics. The use of WKBJ-type approximate solutions with complex phase functions like Gaussian beams [13], or the segment projection method [26], allows to alleviate these difficulties. In this type of methods the conversions of wave polarizations are not easily accounted for, though these phenomena typically arise in built-up structures. A last class of methods focuses on the evolution of some energy density estimators into elastic structures using a so-called microlocal analysis [75]. This method is applicable for complex structures and gives local informations on the transient response while relying on weaker hypotheses as compared to the WKBJ approaches. It is thus expected to be adapted to the present survey that consists in developing a reliable method of analysis of the transient response of beam trusses under impulse loads.

Characterization of the HF range dynamics

In the transient domain, impulse loads are ideally represented by a Dirac pulse. The frequency content of such a distribution is the entire real domain. Thus this work potentially concerns the whole frequency range. Nevertheless, it is important to notice that a shock is not really a pulse but a very short excitation containing not all the frequencies but only a part of it. The sharper the shock is, the wider is the frequency content.

The dynamic response of built-up structures to such broadband loads is illustrated by the experiments exposed in [39, 85]. The first one has been conducted at ONERA. The experimental structure is represented in Fig. 3. The employed material is dural, a weakly dissipative aluminum alloy often used for aeronautical applications. Fig. 4 shows the estimated mechanical energy for different sections of the structure displayed in Fig. 3 when a unit point force is applied to one of its vertical edges at one extremity. In the low frequency

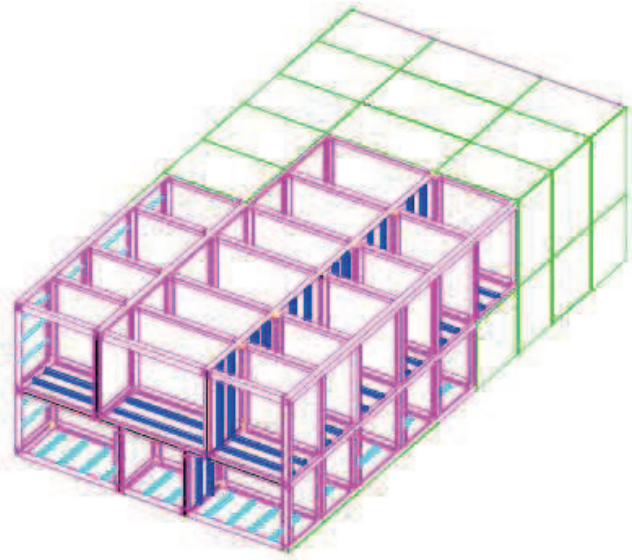

Figure 3: CAD view of the ONERA experimental structure. The structure is entirely closed for experiments, but some outer plates have been removed on the sketch to make its main frame visible. After Savin [85].

range (up to 250 Hz for this structure), the plot exhibits resonance frequencies corresponding to global eigenmodes. These modes are global stationary waves which concentrate the mechanical energy at the eigenfrequencies. They have been intensively investigated in the past decades, see *e.g* [8, 17, 78]. But as the frequency increases, the modal density increases too, such that at about 1200 Hz modes can no longer be distinguished from each other on account of this high modal density and of the damping effects that overlap them. Between these two ranges lies the mid-frequency domain, where the structural response is the transition between the global, low-frequency behavior and the high-frequency behavior. The latter is characterized by vibrational energy levels decreasing significantly when observed at increased distances from the excitation. They are also steadily decreasing with the fre-

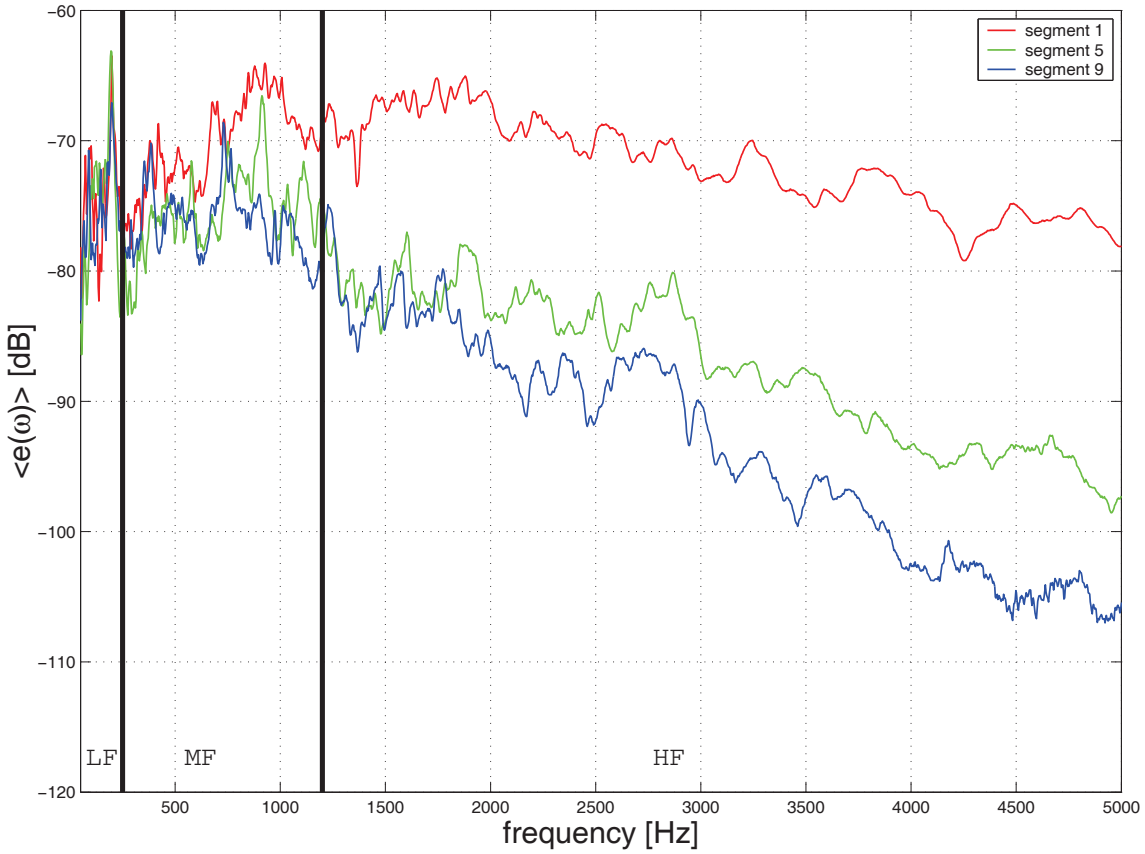

Figure 4: Estimated mechanical energy densities at different segments in the structure of Fig. 3 (red: segment near the excitation, green: middle segment, blue: segment at the other extremity of the structure).

quency. Thus for such higher frequencies the overall mechanical energy remains localized close to the excitation and diffuses only weakly to the other parts of the structure.

An other experiment has been conducted by the Naval Research Laboratory of Washington, DC [39]. The structure is a fuselage section of a CESSNA Citation II, as seen in Fig. 5. The excitation consists in a point force applied at a rib/stringer intersection at one end of the fuselage. Observation of the velocity magnitude in Fig. 6 yields to the same conclusions as for the ONERA experiment, *i.e.* global modes at low frequencies and localization of the mechanical energy near the excitation point in the HF range. This localization can be explained by the effects of the heterogeneities having size of the order or higher than the wavelength that induce multiple scattering of the vibrational waves, and consequently their geometrical diffusion. These scattering phenomena tend to localize the associated energy near the excitation. The plot of the velocity phase of Fig. 7 gives further information. At low frequency, the phase is piecewise constant with jumps of $\pm\pi$, a typical feature of global stationary modes. As the power flow is, in a first approximation, proportional to the (spatial) gradient of the phase, the vibrational energy is spread over the entire structure and concentrated at the resonance frequencies. In the medium frequency range, the phase is rapidly varying thus the energy transfers become important from one substructure to

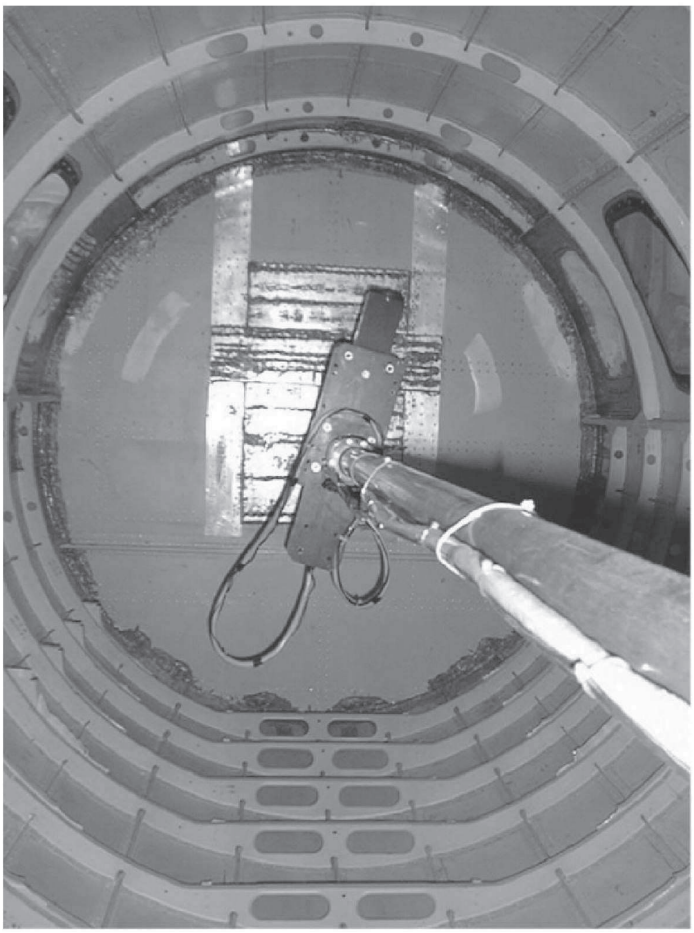

Figure 5: View of the interior of the experimental structure and of the laser measurement device. After Herdic *et al.* [39].

another. The vibrational energy is also primarily carried by clusters of local modes and the higher-order global modes. In the HF range, the phase becomes noisy and accordingly the energy transfers are smoothed out, exhibiting a diffusive behavior. In this latter situation, the mechanical energy tends to remain rather localized in the vicinity of the excitation point on account of the low diffusion constants corresponding to the geometrical spreading of multiply-scattered waves.

Near the excitations, accelerations due to HF waves can reach very high values (of orders of 10^6g, see for example [47]). Equipments attached to a structure subjected to such impulse loads would need to be far from this area in order to avoid any functioning problems. But for aerospace structures such as satellites, the lack of room prevents the engineers from choosing the location of the attachments. It is thus very important to be able to predict the level of energy potentially experienced by the equipments. One of the goal of this thesis is to develop a mathematical and numerical model able to reconstruct the transient response from an initial pulse to a possible diffusive regime.

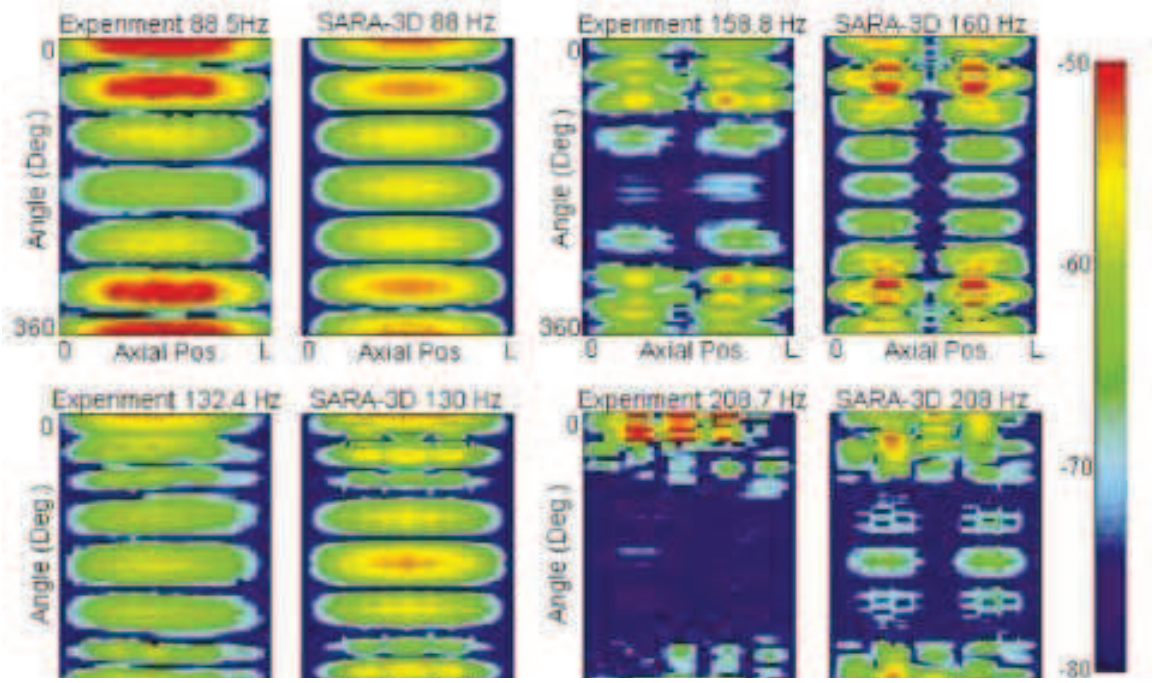

Figure 6: Comparisons of the computed and experimental magnitude distributions of the radial velocity induced by a point force excitation applied to a stiffener intersection of the structure in Fig. 5. After Herdic *et al.* [39].

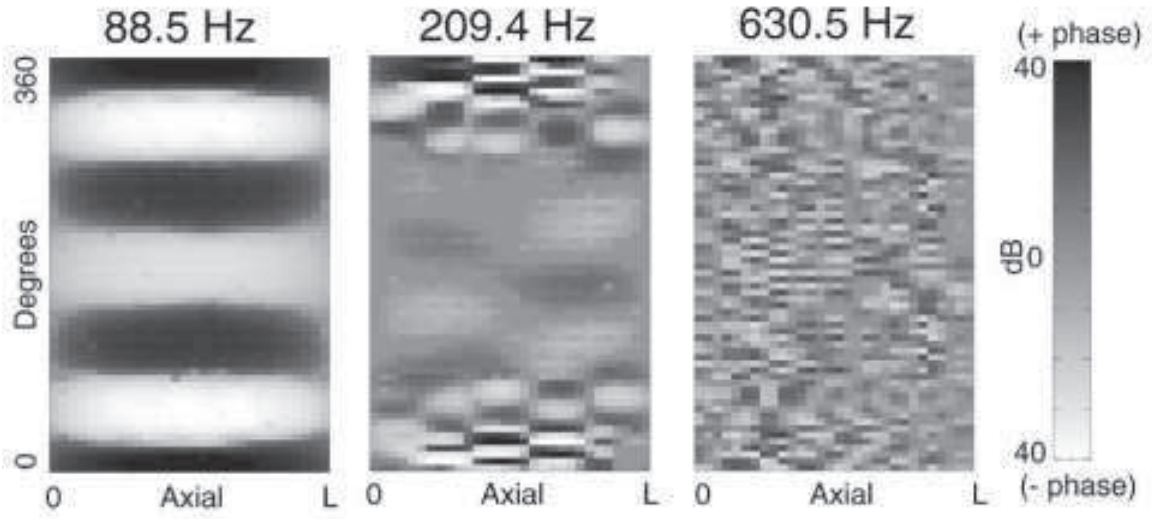

Figure 7: Measurement of the phase distribution of the radial velocity induced by a point force excitation applied to a stiffener intersection of the structure in Fig. 5 in the low-, mid-, and high-frequency ranges. After Herdic *et al.* [39].

Outline of the thesis

The work presented here is dedicated to built-up structures constituted by multi-bay beam trusses since the latter are widely used in the aerospace industry. A typical example is given by the International Space Station (ISS), see Fig. 8. The assembly with two-dimensional slender structures such as plates or shells is left to future researches. In this respect, the dissertation is divided into six chapters. It begins with a review of some numerical and asymptotic methods dealing with HF wave propagation and structural dynamics. Arguments are here developed in favor of a kinetic approach of elastic wave propagation. In the second chapter, the accuracy of several beam models when considered in the HF range are analyzed in regard to the Pochhammer-Chree waveguide model. The third chapter consists in the formulation of a kinetic model for HF waves in three-dimensional beams. The equations describing the evolution of the HF energy density in such structures are outlined. The case of random parameters and the effect of prestressing loads are also considered. In order to study an entire beam truss, the behavior of HF waves at the junctions between beams has to be analyzed. In this respect, the reflection/transmission phenomena are investigated in the this chapter as well. Once the full model is obtained, it is necessary to develop adapted methods of numerical simulation; this is the purpose of the fourth chapter. The implemented method is the discontinuous Galerkin finite element method [41] for spatial discretization, and the Runge-Kutta method [33] for time discretization. In this chapter, the dispersion and the stability of the implemented scheme are also studied. In the fifth chapter, several numerical examples are presented and a test of time reversal processing is detailed. This dissertation is closed with some conclusions and perspectives.

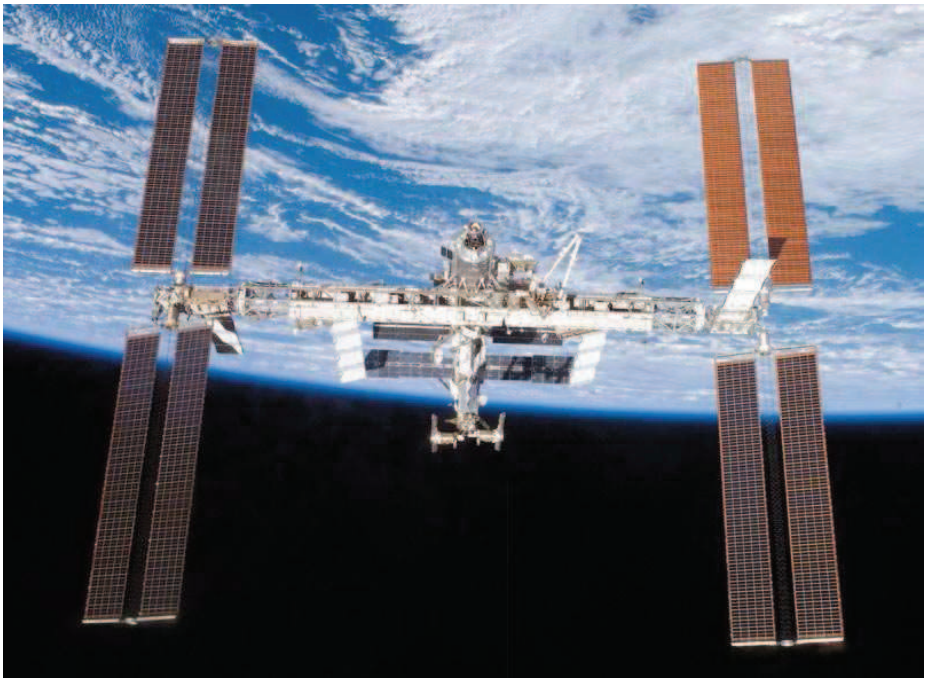

Figure 8: The ISS in July 2011.

Contents

Chapter 1

Modeling high-frequency vibrations in structural dynamics

In this chapter, different approaches of the HF dynamics of bounded elastic media are presented and discussed. The basic equations describing elastic waves are recalled in order to introduce the notations used subsequently in the thesis. We then focus on ways of obtaining approximate numerical or asymptotic solutions of the elastodynamics system, paying a particular attention to the high-frequency range where strongly oscillating solutions are sought for. The characterization of HF vibrations has been classically done in terms of energetic approaches by engineers. These methods are summarized in a subsequent part, in view of motivating our strategy to use kinetic models to describe the evolution of the vibrational energy in built-up structures. This theory is briefly discussed in a concluding section.

1.1 Elastic waves

First it is useful to introduce the basic framework of this study in terms of wave propagation in a three-dimensional elastic medium. The purpose of this section is not to give a detailed overview of elastic waves, but only to introduce the main notations that shall be used subsequently. First, it is assumed that the structures we will consider in this work are constituted by isotropic materials. The equations of motion are derived from equilibrium considerations and the constitutive equation of an elastic body occupying a bounded domain Ω of $\mathbb{R}^3$ at its static equilibrium considered as the reference configuration. The balance of momentum in a fixed reference frame under the action of body forces $\rho\boldsymbol{f}$, reads:

$$\boldsymbol{\nabla}_{\boldsymbol{x}} \cdot \boldsymbol{\sigma} + \rho\boldsymbol{f} = \rho\partial_t^2\boldsymbol{u} \quad \text{in } \Omega\,, \tag{1.1}$$

where $\boldsymbol{\nabla}_{\boldsymbol{x}}$ is the usual gradient vector given in that reference frame $(\hat{\boldsymbol{e}}_1, \hat{\boldsymbol{e}}_2, \hat{\boldsymbol{e}}_3)$ with the corresponding Cartesian coordinates (x, y, z) of a point $\boldsymbol{x}$ in Ω by $\boldsymbol{\nabla}_{\boldsymbol{x}} = \hat{\boldsymbol{e}}_1\partial_x + \hat{\boldsymbol{e}}_2\partial_y + \hat{\boldsymbol{e}}_3\partial_z$. Also $\boldsymbol{\sigma}$ is the second order Cauchy stress tensor, ρ is the density of the medium, and $\boldsymbol{u}$ is the small displacement field at the spatial point $\boldsymbol{x} \in \Omega$ assimilated to a material point $\boldsymbol{p} \sim \boldsymbol{x}$ in the small perturbation context. This hypothesis holds for $\mathrm{Sup}_{\boldsymbol{p},t}\,|\boldsymbol{u}| \ll L$ and $\mathrm{Sup}_{\boldsymbol{p},t}\,|\boldsymbol{\nabla}_{\boldsymbol{p}}\boldsymbol{u}| \ll 1$, where L is a characteristic dimension of the structure, and:

$$|\boldsymbol{\nabla}_{\boldsymbol{p}}\boldsymbol{u}| = \mathrm{Tr}(\boldsymbol{\nabla}_{\boldsymbol{p}}\boldsymbol{u} \cdot \boldsymbol{\nabla}_{\boldsymbol{p}}\boldsymbol{u}^T)^{1/2}\,.$$

$\boldsymbol{A}^T$ denotes the transpose of the second order tensor $\boldsymbol{A}$, and $\mathrm{Tr}\,\boldsymbol{A}$ its trace. The small perturbation hypothesis implies that the difference between the material and spatial gradients is negligible, $\boldsymbol{\nabla_p} \simeq \boldsymbol{\nabla_x}$. Therefore the gradient vector will be simply denoted by $\boldsymbol{\nabla}$ when no ambiguity holds. In this context, ∂_a^i will also stand for i^{th} derivative with respect to a, except for the time derivatives ($a \equiv t$) which will be denoted by $\dot{\boldsymbol{u}} = \partial_t \boldsymbol{u}$ and $\ddot{\boldsymbol{u}} = \partial_t^2 \boldsymbol{u}$.

The balance of momentum (1.1) is supplemented by boundary and initial conditions, whereas the constitutive law gives the relationship between the stress tensor and the gradient of the displacement. Let $\partial\Omega = \Gamma_0 \cup \Gamma$ be the boundary of the structure, such that $\Gamma_0 \cap \Gamma = \oslash$. Let $\hat{\boldsymbol{n}}$ be the outward unit normal of that boundary. The structure is fixed on the part Γ_0 of $\partial\Omega$:

$$\boldsymbol{u} = \boldsymbol{0} \quad \text{on } \Gamma_0\,,$$

and it is free on the other part Γ :

$$\boldsymbol{\sigma}\hat{\boldsymbol{n}} = \boldsymbol{0} \quad \text{on } \Gamma\,.$$

The initial conditions are:

$$\boldsymbol{u}(\boldsymbol{x},0) = \boldsymbol{u}^I(\boldsymbol{x})\,, \quad \dot{\boldsymbol{u}}(\boldsymbol{x},0) = \boldsymbol{v}^I(\boldsymbol{x})\,. \tag{1.2}$$

As the medium is isotropic, the constitutive law is the classical Hooke's law:

$$\boldsymbol{\sigma} = \lambda(\mathrm{Tr}\,\boldsymbol{\epsilon})\boldsymbol{I} + 2\mu\boldsymbol{\epsilon}\,, \tag{1.3}$$

where $\boldsymbol{\epsilon} = \frac{1}{2}(\boldsymbol{\nabla u} + \boldsymbol{\nabla u}^T)$ is the linearized strain tensor, and $\boldsymbol{I}$ is the identity matrix. λ and μ are the first and second Lamé coefficients, the second one being also the shear modulus. Introducing the definition of the linearized strain tensor into Eq. (1.3) and inserting the latter into the equilibrium equation (1.1) under the assumption of a homogeneous medium and $\boldsymbol{f} \equiv \boldsymbol{0}$, leads to the classical Navier equation:

$$\mu\boldsymbol{\Delta u} + (\lambda+\mu)\boldsymbol{\nabla\nabla}\cdot\boldsymbol{u} = \rho\ddot{\boldsymbol{u}}\,. \tag{1.4}$$

Here $\boldsymbol{\Delta}$ is defined as the vector Laplace operator given by $\boldsymbol{\Delta} = \boldsymbol{\nabla}\cdot(\boldsymbol{\nabla u})$.

Solutions of the Navier equation can be sought for in the form of an harmonic plane wave:

$$\boldsymbol{u}(\boldsymbol{x},t) = \boldsymbol{A}\mathrm{e}^{i(\omega t - \boldsymbol{k}\cdot\boldsymbol{x})}\,, \tag{1.5}$$

with $\boldsymbol{A}$ the amplitude vector of the wave, ω is the circular frequency, $\boldsymbol{k}$ is the wave vector, and $k = |\boldsymbol{k}|$ is the wavenumber. Accordingly $\boldsymbol{k}/k$ is the unit vector which indicates the direction of propagation of the wave. Inserting this ansatz into Eq. (1.4) gives the relation between the circular frequency and the wavenumber, the so-called dispersion relation. Let us introduce:

$$\boldsymbol{\Gamma}(\boldsymbol{k}) = (c_l^2 - c_s^2)\boldsymbol{k}\otimes\boldsymbol{k} + c_s^2|\boldsymbol{k}|^2\boldsymbol{I}\,, \tag{1.6}$$

the so-called acoustic or Christoffel tensor of an isotropic medium, where:

$$c_l = \sqrt{\frac{\lambda+2\mu}{\rho}} \tag{1.7}$$

is the phase velocity of the longitudinal waves, and:

$$c_s = \sqrt{\frac{\mu}{\rho}} \tag{1.8}$$

is the phase velocity of the transverse waves. Then the Navier equation reads:

$$\rho \left(\boldsymbol{\Gamma}(\mathrm{i}\, \boldsymbol{\nabla}_{\boldsymbol{x}}) - (\mathrm{i}\, \partial_t)^2 \right) \boldsymbol{u} = \boldsymbol{0}\,, \tag{1.9}$$

such that $\boldsymbol{A}$ and ω arise as the eigenvector and eigenvalue of $\boldsymbol{\Gamma}$, which is positive definite whenever $\boldsymbol{k} \neq \boldsymbol{0}$:

$$\boldsymbol{\Gamma}(\boldsymbol{k})\boldsymbol{A} = \omega^2 \boldsymbol{A}\,. \tag{1.10}$$

The solvability condition $\det \boldsymbol{\Gamma}(\boldsymbol{k}) = 0$ for this eigensystem provides with the dispersion relation, which solutions are the admissible phase speeds:

$$c_\phi = \frac{\omega}{k} = c_l \text{ or } c_s\,.$$

The phase velocity is the speed of material perturbations within the isotropic medium. The dispersion relation allows to define the group velocity as well:

$$\boldsymbol{c}_g = \boldsymbol{\nabla}_{\boldsymbol{k}} \omega\,,$$

such that $|\boldsymbol{c}_g|$ represents the velocity of the energy. Here the phase velocity and the group velocity are the same because the medium is non dispersive. However in a dispersive medium, where the relation between the wavevector and the circular frequency is not necessarily linear, the phase and the group velocity are different. Then the shape of the initial wave is modified as it propagates.

The analysis of the solutions of (1.4) in the case of an unbounded medium can be found in the classical book of Achenbach [2], for example. There a Helmholtz decomposition is invoked, which consists in dividing the wave field into a longitudinal component (also called irrotational, dilatational or pressure wave) having a direction of propagation parallel to the wave vector, and a transverse component (also called shear, equivoluminal, or rotational wave) having a direction of propagation normal to the wave vector. The first is the gradient of a scalar field and the second is the curl of a vectorial field. The transverse component is divided into horizontally and vertically transverse waves which have perpendicular wavevectors. The waves may also be commonly divided into two categories [2, p. 32], namely the propagating and the standing ones. The propagating waves have the form of Eq. (1.5). This type is considered in an unbounded medium or when the wavelength is small compared to a characteristic dimension of the medium. The standing waves are basically the superposition of two propagating waves with the same circular frequency ω and wavelength $\frac{2\pi}{k}$ travelling in opposite directions. They may be given in the form:

$$\boldsymbol{u}(\boldsymbol{x}, t) = \boldsymbol{A} \sin(\boldsymbol{k} \cdot \boldsymbol{x}) \cos(\omega t)\,.$$

If some boundary conditions are considered, then the range of acceptable harmonic motions is subjected to restrictions. The existing waves are standing waves having wavenumbers such that the induced displacement fulfills the boundary conditions. They correspond to

the eigenmodes of the bounded medium.

For heterogeneous media, the acoustic tensor varies pointwise and the foregoing analysis is no longer relevant. The equation of motion (1.1) shall be solved resorting to numerical or asymptotic methods of approximation, of which a short survey is outlined below. The aim of this presentation is however not to give an exhaustive review of all existing approaches. It is rather focused on some of them in view of obtaining approximate solutions to the elastodynamic problem (1.1) for waves propagating in structures (bounded media), with wavelengths possibly small with respect to their characteristic lengths. Regarding numerical methods, both issues related to spatial discretization, on account of the inhomogeneity of the acoustic tensor, and time discretization are addressed in the following.

1.2 Some numerical methods

The construction of approximate solutions to partial differential equations such as the balance of momentum (1.1) is classically done within the framework of the method of weighted residuals, see *e.g.* [115]. Consider Eq. (1.1) in Ω in terms of the displacement field $\boldsymbol{u}(\boldsymbol{x},t)$ solely together with boundary conditions on $\partial\Omega$:

$$\begin{aligned} \left(\boldsymbol{\Gamma}(\boldsymbol{x},\mathrm{i}\,\boldsymbol{\nabla}_{\boldsymbol{x}}) - (\mathrm{i}\,\partial_t)^2\right)\boldsymbol{u} &= \boldsymbol{f} \quad \text{in}\,\Omega\,, \\ \boldsymbol{\mathcal{B}}\boldsymbol{u} &= \boldsymbol{0} \quad \text{on}\,\partial\Omega\,, \end{aligned} \tag{1.11}$$

where $\boldsymbol{\mathcal{B}}$ is a linear partial differential operator. The initial conditions of the above system are (1.2). An approximate solution $\boldsymbol{u}_h$ of (1.11) is a function satisfying, say, $\boldsymbol{\mathcal{B}}\boldsymbol{u}_h = \boldsymbol{0}$ and making the residual:

$$\boldsymbol{\mathcal{R}} := \boldsymbol{H}(\boldsymbol{x},\mathrm{i}\,\boldsymbol{\nabla}_{\boldsymbol{x}},\mathrm{i}\,\partial_t)\boldsymbol{u}_h - \boldsymbol{f}$$

small in some sense, where $\boldsymbol{H}(\boldsymbol{x},\boldsymbol{k},\omega) := \boldsymbol{\Gamma}(\boldsymbol{x},\boldsymbol{k}) - \omega^2\boldsymbol{I}$. That approximation is sought for in a finite-dimensional subspace W_h of some functional Hilbert space W (such as a L^2 space) where the true solutions of (1.11) or its variational form lie. Therefore $\boldsymbol{u}_h$ is expanded on a set of trial functions $(\boldsymbol{\phi}_m)_{0\leq m\leq P}$ spanning W_h as:

$$\boldsymbol{u}_h(\boldsymbol{x},t) = \sum_{m=0}^{P} U_m(t)\boldsymbol{\phi}_m(\boldsymbol{x})\,, \tag{1.12}$$

while a family of test functions $(\boldsymbol{\psi}_m)_{0\leq m\leq P}$ is used to define the smallness of the residual by means of the Hilbert space scalar product and an average boundary integral up to a time $T>0$:

$$(\boldsymbol{\mathcal{R}},\boldsymbol{\psi}_m)_{\mathsf{W}} + \langle\boldsymbol{\mathcal{B}}\boldsymbol{u}_h,\boldsymbol{\psi}_m\rangle_{\partial\Omega} = 0\,, \quad 0\leq m\leq P\,, \quad t\in[0,T]\,. \tag{1.13}$$

Now the finite difference method, the finite element method, or the spectral method among others may be arbitrarily seen as different particularization of the foregoing strategy [74]. Using finite differences, the trial functions are overlapping, locally defined polynomials of generally low order. Using finite elements, the trial functions are locally defined smooth functions, for example polynomials of fixed degrees which are non-zero only on subdomains of Ω. Finite volumes are basically obtained using zeroth-order polynomials in this framework. In spectral methods the trial functions are globally defined smooth functions, such as Fourier series if the approximate solution is periodic.

1.2.1 Finite difference method

In the finite difference method, an approximate solution of (1.11) is given by a local interpolant polynomial, and the partial derivatives in (1.11) are then obtained by differentiating this local polynomial. Here local refers to the use of nearby interpolation points to approximate the solution or its derivatives at given points (both in space and time). This method has been applied to elastic waves by, among others, Virieux [109]. In order to increase the consistency and the stability of the implemented finite difference scheme, the balance of momentum (1.1) and the constitutive equation (1.3) are used to form a first-order system given in terms of the stress tensor and velocity field, rather than the above second-order system given in terms of the displacement field. Consistency is related to the difference between the approximate and the real solutions of a given partial differential equation, and stability is related to the ability of the numerical scheme to evade the occurrence of artificial amplifications during the iterations. In order to have a consistent and stable approximation of the derivatives, the time step needs to be small in regard to the periods considered in the computation (given by the frequency content of the initial condition), and it is also constrained by the mesh size retained for spatial discretization. Thus in the case of the propagation of HF wave, computations can be expensive. Above all, a finite difference discretization is impractical for complex geometries and boundary conditions.

1.2.2 Finite element method

While the finite difference method tries to have an exact solution of an approximate problem, the finite element method seeks the approximate solution of an exact problem. In this method the structure is meshed into finite elements, and the approximate displacement field $\boldsymbol{u}_h^r$ of an element r is expanded in polynomial functions as:

$$\boldsymbol{u}_h^r(\boldsymbol{x}, t) = \boldsymbol{N}(\boldsymbol{x})\boldsymbol{q}_r(t)\,.$$

The low-degree polynomials $\boldsymbol{N}(\boldsymbol{x})$ are typically locally defined Lagrange polynomials, and $\boldsymbol{q}_r(t)$ is the vector of degrees of freedom. Using these trial functions as test functions as well in (1.13) and integrating by parts, a Galerkin formulation is derived leading to the usual differential equation:

$$\mathbb{M}\ddot{\boldsymbol{Q}} + \mathbb{K}\boldsymbol{Q} = \boldsymbol{F}\,, \tag{1.14}$$

where $\mathbb{M}$ is the $(P+1)\times(P+1)$ mass matrix, $\mathbb{K}$ is the $(P+1)\times(P+1)$ stiffness matrix, $\boldsymbol{F}$ is the forcing vector, and $\boldsymbol{Q}$ is the nodal displacement vector. The boundary conditions are directly applied to the trial and test functions on the boundary elements where the displacement field vanishes.

Applying finite element methods to beam networks, the Semi-Analytical Finite Element (SAFE) and Wave Finite Element (WFE) approaches take care of the particular geometry of each beam by expanding their motion in terms of plane waves (sinusoidal functions) along their axis, and finite element basis functions (low-order polynomials) in the transverse directions [7, 47]. The approximate displacement field $\boldsymbol{u}_h^r$ of an element r of a beam cross-section for a particular wavenumber k is then approximated by:

$$\boldsymbol{u}_h^r(\boldsymbol{x}, t) = e^{\mathrm{i}(\omega t - kx)}\boldsymbol{N}(\boldsymbol{x}_\perp)\boldsymbol{q}_r(t)\,,$$

where $\boldsymbol{N}$ are finite element basis functions defined on the cross-section, $\boldsymbol{x}_\perp = (\boldsymbol{I} - \hat{\boldsymbol{e}}_1 \otimes \hat{\boldsymbol{e}}_1)\boldsymbol{x}$ being the transverse coordinates of the spatial position $\boldsymbol{x}$ within that cross-section, and $x = \boldsymbol{x} \cdot \hat{\boldsymbol{e}}_1$ is the position of the cross-section along the axis of the beam oriented by, say, the unit vector $\hat{\boldsymbol{e}}_1$. The vector $\boldsymbol{q}_r(t)$ gathers the expansion coefficients (degrees of freedom) of $\boldsymbol{u}_r$ on the basis functions $\boldsymbol{N}$ of the element r on the cross-section. In the context of finite element methods, a weak formulation is derived from Eq. (1.4) reduced to the cross-section, leading to:

$$(\mathbb{K}_1 - \mathrm{i}\, k\mathbb{K}_2 + k^2\mathbb{K}_3 - \omega^2\mathbb{M})\boldsymbol{Q} = \boldsymbol{F}\,,$$

where the $\mathbb{K}_i$'s are stiffness matrices, $\mathbb{M}$ is the mass matrix, and $\boldsymbol{Q}$ is the vector of degrees of freedom of the cross-section. This system is recast as a linear system with respect to the wavenumber k as:

$$(\mathbb{A} - k\mathbb{B})\tilde{\boldsymbol{Q}} = \tilde{\boldsymbol{F}}\,,$$

with $\tilde{\boldsymbol{Q}} = (\boldsymbol{Q}\,, k\boldsymbol{Q})^T$ and:

$$\mathbb{A} = \begin{pmatrix} \boldsymbol{0} & \mathbb{K}_1 - \omega^2\mathbb{M} \\ \mathbb{K}_1 - \omega^2\mathbb{M} & -\mathrm{i}\,\mathbb{K}_2 \end{pmatrix}, \quad \mathbb{B} = \begin{pmatrix} \mathbb{K}_1 - \omega^2\mathbb{M} & \boldsymbol{0} \\ \boldsymbol{0} & -\mathbb{K}_3 \end{pmatrix}.$$

This system is solved for each circular frequency ω and gives the wavenumbers $k(\omega)$ and the mode shapes. Thus each beam is meshed only in its cross-section, so that the mesh size and the computational costs are greatly reduced in comparison to a three-dimensional computation. In the SAFE method, only a cross-section is meshed, while in the WFE method a short slice of the waveguide is discretized, allowing the use of a commercial finite element software. This class of methods considers steady-state beam dynamics in the frequency domain, which impose to perform an inverse Fourier transform to get to the transient response. For simulation at long times, a large number of modes has usually to be considered. It greatly increases the computational costs and numerical errors induced by the truncation effects.

The use of local polynomial interpolants based on a small number of interpolating grid points in finite difference or finite element methods is very reasonable for slowly varying functions. Indeed, it seems to be meaningless to include informations far away from the area of interest in approximating the variations of such functions. However, low-degree local polynomials require in return very fine grids to accurately resolve solutions containing significant spatial and temporal variations, as for HF waves. The use of fine grids increases significantly the needs in computational resources, so alternative schemes using coarser grids are sought for. The basic feature of spectral methods is to use all available values of a function to construct approximations, while relying on looser meshes. Hence they are often referred to as global methods in the dedicated literature.

1.2.3 Spectral methods

Spectral methods basically use global smooth functions as trial functions, such as trigonometric polynomials (Fourier series) for periodic problems, or higher order Lagrange or orthogonal polynomials (typically Jacobi polynomials such as Tchebychev or Legendre polynomials) for non-periodic problems. They may be classified in different sub-categories depending on the choice of the test functions [40]. Galerkin spectral methods use the same trial and test functions, $\boldsymbol{\psi}_m = \boldsymbol{\phi}_m$, each satisfying the boundary conditions $\boldsymbol{\mathcal{B}}\boldsymbol{\phi}_m = \boldsymbol{0}$. Tau

spectral methods consider as test functions most of the trial functions, however the latter do not necessarily satisfy the boundary conditions. These very conditions are enforced by an additional set of equations obtained by first, expanding $\boldsymbol{\mathcal{B}}\boldsymbol{\phi}_m$ on a set of orthonormal functions $(\boldsymbol{g}_j)_{0\leq j\leq M}$ defined on the boundary $\partial\Omega$ with $M < P$, and then using the expansion (1.12):

$$\boldsymbol{\mathcal{B}}\boldsymbol{\phi}_m(\boldsymbol{x}) = \sum_{J=0}^{M} \phi_{jm}\boldsymbol{g}_j(\boldsymbol{x})\,,$$
$$\boldsymbol{\mathcal{B}}\boldsymbol{u}(\boldsymbol{x}) = \sum_{m=0}^{P}\sum_{J=0}^{M} U_m\phi_{jm}\boldsymbol{g}_j(\boldsymbol{x}) = \boldsymbol{0}\,.$$

Hence the $M+1$ additional constraints are $\sum_{m=0}^{P} U_m\phi_{jm} = 0$ for $0 \leq j \leq M$. Finally collocation, or pseudo-spectral methods consider delta functions at special points, or at special sub-domains, as test functions.

The basic ideas behind spectral methods may be extended to finite element meshes by considering each element as a sub-domain where a "global" approximation is constructed, using higher-order polynomials as trial functions. The average boundary conditions in (1.13) can be used to impose the consistency of the "global" approximations between those sub-domains in a weak form, playing the role of penalty constraints. In this spirit, discontinuous Galerkin finite element methods [41] are obtained using the trial functions as test functions as well. The term "discontinuous" stems from the fact the enforcement of a compatibility condition between the "global" approximations of adjacent sub-domains is done in terms of user-defined boundary fluxes. This approach has become the method of choice in unsteady convection-dominated flow problems for its good shock-capturing features, see for example [41].

1.2.4 Time discretization

The most widely employed method for the numerical solution of the system of coupled linear second-order differential equations (1.14) is the class of Newmark schemes [69]. It is based on a time series expansion of $\boldsymbol{Q}$ and $\dot{\boldsymbol{Q}}$ as:

$$\dot{\boldsymbol{Q}}(t+\Delta t) = \dot{\boldsymbol{Q}}(t) + \Delta t\left((1-\gamma)\ddot{\boldsymbol{Q}}(t) + \gamma\ddot{\boldsymbol{Q}}(t+\Delta t)\right)\,,$$
$$\boldsymbol{Q}(t+\Delta t) = \boldsymbol{Q}(t) + \Delta t\dot{\boldsymbol{Q}}(t) + \frac{\Delta t^2}{2}\left((1-2\beta)\ddot{\boldsymbol{Q}}(t) + 2\beta\ddot{\boldsymbol{Q}}(t+\Delta t)\right)\,.$$

where $0 \leq \beta \leq \frac{1}{2}$ and $0 < \gamma \leq 1$. Implicit methods correspond to $\beta > 0$, and explicit methods correspond to $\beta = 0$. This technique is widely used for industrial applications, but stability and consistency problems may arise. While implicit schemes are unconditionally stable, explicit schemes are not although they are more adapted to wave propagation problems, as argued in [12]. For a one-dimensional scalar equation of the form $\ddot{q}(t)+\omega_0^2 q(t) = 0$, the explicit Newmark schemes read:

$$\begin{pmatrix} q(t+\Delta t) \\ \dot{q}(t+\Delta t) \end{pmatrix} = \begin{bmatrix} 1-\frac{\omega_0^2}{2}\Delta t^2 & \Delta t \\ \frac{1}{2}\gamma\omega_0^4\Delta t - \omega_0^2\Delta t & 1-\gamma\omega_0^2\Delta t^2 \end{bmatrix} \begin{pmatrix} q(t) \\ \dot{q}(t) \end{pmatrix}\,.$$

For the method to be stable the absolute values of the eigenvalues of the amplification matrix on the right-hand side above need to be less than or equal to zero. For the usual choice $\gamma = \frac{1}{2}$ that condition reduces to $\omega_0 \Delta t \leq 2$, so that the critical time-step is $\Delta t_c = \frac{2}{\omega_0}$. In the multi-dimensional setting of Eq. (1.14) the preceding condition reads:

$$\Delta t_c = \frac{2}{\max_\alpha \omega_\alpha}$$

where the $(\omega_\alpha)_{1 \leq alpha \leq P+1}$ are the eigenfrequencies of the structure. So on account of the high modal density of built-up structures in the HF range, that condition may become extremely restrictive. As for the consistency of these schemes, it has been argued in [10] that if there are less than 5 elements for the minimal wavelength, then the wave speeds are modified significantly (dispersion error) and the solution amplitudes decrease with time (dissipation error). The above stability criteria may also be written in terms of a Courant-Friedrichs-Lewy (CFL) number as:

$$\mathrm{CFL} = \frac{\pi}{N} \sum_{j=1}^{3} \frac{c_j \Delta t}{\Delta x_j} \leq 1 \,,$$

where N is the number of elements per wavelength in the spatial discretization, and c_j are the numerical wave speeds for each direction j.

Higher-order time discretization schemes may be required if a high-order spatial discretization is used, as in spectral methods. For the linear differential equations arising from semi-discretized partial differential equations, as in Eq. (1.14) for example, higher-order time discretizations are basically derived by adding terms to the Taylor expansion of the time derivative. This is the approach retained in the derivation of multi-step Runge-Kutta methods [40]. For non linear differential equations or equations involving possibly discontinuous solutions, such as conservation laws, strong stability-preserving (SSP) time discretization methods have been developed in the last decade [33]. These schemes are constructed by convex combinations of forward Euler operators, in such a way that the strong stability-preserving property of the forward Euler operator applied to the differential equation at hand is conserved. If the latter is linear, they are in addition optimal in the sense that they do not worsen the CFL condition of the forward Euler operator. Linear SSP schemes of any order with optimal CFL condition have the form of multi-step Runge-Kutta schemes where the order is the number of stages. They are now widely used for the time integration of linear conservation equations.

1.3 Asymptotic approaches

Solutions of the elastic wave equation can rather be constructed by asymptotic approaches when they depend on a small, high-frequency parameter $\varepsilon \ll 1$. This situation arises when the applied loads depend on ε and are, say, highly oscillating at space-time scales of the order of that small parameter. For example, Eq. (1.11) may be completed with initial conditions:

$$\boldsymbol{u}(\boldsymbol{x}, 0) = \boldsymbol{u}_\varepsilon^I(\boldsymbol{x}) \,, \quad \dot{\boldsymbol{u}}(\boldsymbol{x}, 0) = \boldsymbol{v}_\varepsilon^I(\boldsymbol{x}) \,,$$

which depend on the high-frequency parameter ε, as well as the body forces $\boldsymbol{f}$. The exact form of these data has no relevance to the following study. A typical example could be $\boldsymbol{u}_\varepsilon^I(\boldsymbol{x}) = \varepsilon \boldsymbol{A}(\boldsymbol{x}) \mathrm{e}^{\mathrm{i}\, S^I(\boldsymbol{x})/\varepsilon}$ and $\boldsymbol{v}_\varepsilon^I(\boldsymbol{x}) = \boldsymbol{B}(\boldsymbol{x}) \mathrm{e}^{\mathrm{i}\, S^I(\boldsymbol{x})/\varepsilon}$, as in geometric optics. Here $\boldsymbol{A}$ and $\boldsymbol{B}$ are smooth amplitude functions and S^I is the initial phase. An approximate solution $\boldsymbol{u}_\varepsilon$ of (1.11) provided with these data is then constructed after the latter system has been rescaled accordingly as:

$$\begin{aligned} \left(\boldsymbol{\Gamma}(\boldsymbol{x}, \mathrm{i}\,\varepsilon \boldsymbol{\nabla}_{\boldsymbol{x}}) - (\mathrm{i}\,\varepsilon \partial_t)^2\right) \boldsymbol{u}_\varepsilon &= \boldsymbol{f}_\varepsilon \quad \text{in}\, \Omega\,, \\ \boldsymbol{\mathcal{B}} \boldsymbol{u}_\varepsilon &= \boldsymbol{0} \quad \text{on}\, \partial\Omega\,. \end{aligned} \tag{1.15}$$

The above rescaled wave equation describes the propagation of elastic waves with a small wave length with respect to the heterogeneities of the medium and the propagation distances– the high-frequency regime we are interested in in this work. In this setting, the plane-wave form (1.5) arising as a canonical solution of the elastic wave equation in an homogeneous or piecewise homogeneous medium remains valid locally when $\varepsilon \ll 1$, such that the form of the solutions of (1.15) can be intuited *a priori*. This is the approach retained in the well-known WKBJ method described next.

1.3.1 Ray methods

The WKBJ expansion method, named after the physicists G. Wentzel, H. Kramers and L. Brillouin, and the mathematician H. Jeffreys, who independently formalized it in the 1920s, in fact the oldest and best known technique to deal with high-frequency waves. It is also called ray theory in room acoustics [50] or seismology [108], among others. A first evidence of the method can be found in the early works of F. Carlini (1817) or G. Green and J. Liouville (1837), as noticed by Steele [92]. In the WKBJ approach, solutions of the elastic wave equation (1.15) are assumed to have the form [108]:

$$\boldsymbol{u}_\varepsilon(\boldsymbol{x}, t) \simeq \mathrm{e}^{\mathrm{i}\, S(\boldsymbol{x},t)/\varepsilon} \sum_{k=0}^{\infty} \varepsilon^k \boldsymbol{U}_k(\boldsymbol{x}, t)\,, \tag{1.16}$$

where $S(\boldsymbol{x}, t)$ is the (real) phase function, and the $(U_k(\boldsymbol{x}, t))_{k\geq 0}$ are amplitude functions of the wave at various orders with respect to ε. In the HF range, only the first term (U_0) is significant such that the analysis is usually reduced to the computation of the phase and the first amplitude function [82]. Plugging this ansatz into the elastodynamic equation (1.15) and then equating the various terms of same orders in ε, leads to two equations. The first one is a linear transport equation describing the evolution of the density $|U_0|^2$, and the second one is a non linear eikonal equation describing the evolution of the phase. Adopting a Lagrangian point of view, the eikonal equation can be solved locally by the method of characteristics, or ray tracing. It consists in tracking the phase function solving the eikonal equation locally in time on the so-called bicharacteristic curves of the underlying Hamiltonian system corresponding to the elastic wave equation; see for example [88]. The geometric rays themselves are the projections of the bicharacteristic curves on the physical space. However as it is non-linear, the eikonal equation does not allow the direct treatment of crossing rays, or the superposition of different phases. An alternative solution is to introduce the concept of viscosity solution, as done in [28]. The method of characteristics also fail on the caustics, where the rays arising from different initial positions in phase-space may stack (singularities of the amplitude function due to the convergence of the rays on

some envelop curves). This limitation can be addressed by using a Gaussian beam method. In this approach, the real phase function S is replaced by a complex phase function, which is real only on the rays [13] and has a Gaussian shape about them that narrows as the frequency increases. The treatment of caustics becomes possible because only a limited-order Taylor expansion of the eikonal equation has to be satisfied.

The boundary conditions in Eq. (1.15) are taken into account in these approaches by adding auxiliary terms to the above ansatz (1.16). They add additional amplitude and phase functions corresponding to the reflected rays as obtained by Snell-Descartes laws of reflection/transmission. Hence the consideration of multiply-reflected rays on the boundaries of a bounded medium adds much complexity to the analysis of vibrational fields by such asymptotics.

1.3.2 Wave front tracking methods

In the continuation of ray methods, several numerical approaches have been developed in the last decades to deal with the eikonal equation of geometrical optics. The main concern is in tracking the evolution of the wave fronts arising from sharp (possibly oscillatory) initial conditions. Among the recent studies, the segment projection method [100] consists in seeking the motion of a wave front γ by dividing it into different segments depending on independent parameterizations. The latter are chosen such that they can be given as functions of one variable solely. The method will be explained with the example of a circular front evolving in the context of the scalar wave propagation as done by Tornberg [100] or Engquist *et al.* [26].

The physical space is $\mathbb{R}^2$ and a point in that space is $\boldsymbol{x} = (x, y)$. The wave front γ is then described by the functions $f_n(x,t))_{1\leq n\leq N_x}$ (associated to the x-segment) and $g_m(y,t)_{1\leq n\leq N_y}$ (associated to the y-segment) of the independent variables x and y. N_x and N_y are the numbers of x- and y-segments. The coordinates of a point of the front are then given by $(x, y) = (x, f_n(x))$ or $(x, y) = (g_m(y), y)$. The segments representing the front are constructed as follows. An extremum of a function $f_n(x,t)$ defines a separation point for the y-segment given by the function $g_m(y,t)$ as no y-segment can continue past this point. A similar process is applied for the construction of the x-segments. Then, for each point of the curve γ, there is at least one segment describing the curve. To make the description complete, the information about the connectivity of segments must be provided. For the circular wave front, two x-segments and two y-segments are required (see Fig. 1.1). The segments are then moved by equations depending on the physics describing the motion of the interfaces. In the considered situation, the propagation of a wave front in an isotropic but not necessarily homogeneous two-dimensional medium depends on the velocity field describing the medium $c(\boldsymbol{x})$. A point of the wavefront moves then according the velocity vector defined as $c(\boldsymbol{x})\hat{\boldsymbol{n}} = c_x(\boldsymbol{x})\hat{\boldsymbol{e}}_x + c_y(\boldsymbol{x})\hat{\boldsymbol{e}}_y$ where $\hat{\boldsymbol{n}}$ is the normal of the wavefront at $\boldsymbol{x}$. $c(\boldsymbol{x})$ is the velocity field characterizing the medium. The velocity of the wave front is given by $\boldsymbol{c}_f(\boldsymbol{x}) = c_x(\boldsymbol{x})\hat{\boldsymbol{e}}_x + c_y(\boldsymbol{x})\hat{\boldsymbol{e}}_y$. In this context, it can be shown that the segments related to a high-frequency scalar wave evolve according to the partial differential equations [25]:

$$\begin{aligned} \partial_t f_n + c_x \partial_x f_n &= c_y \,, \\ \partial_t g_m + c_y \partial_y g_m &= c_x \,. \end{aligned} \tag{1.17}$$

These equations are then solved by standard numerical methods. After each numerical step, the segment representation must be updated according to the same rules outlined previously. New segments should be created if new extrema have appeared, and segments should be removed when extrema disappear. The connection between segments must be also updated. An example of updating is provided in Fig. 1.1. This technique is very efficient to track the wave front, nevertheless it breaks down at caustics and crossing points because the normal direction $\hat{\boldsymbol{n}}$ is not defined there. This limitation is removed by tracking the wave front in the phase space [26]. It adds then an other variable that is the direction of propagation. Then at caustics or focus points, the front is still described by at least one segment.

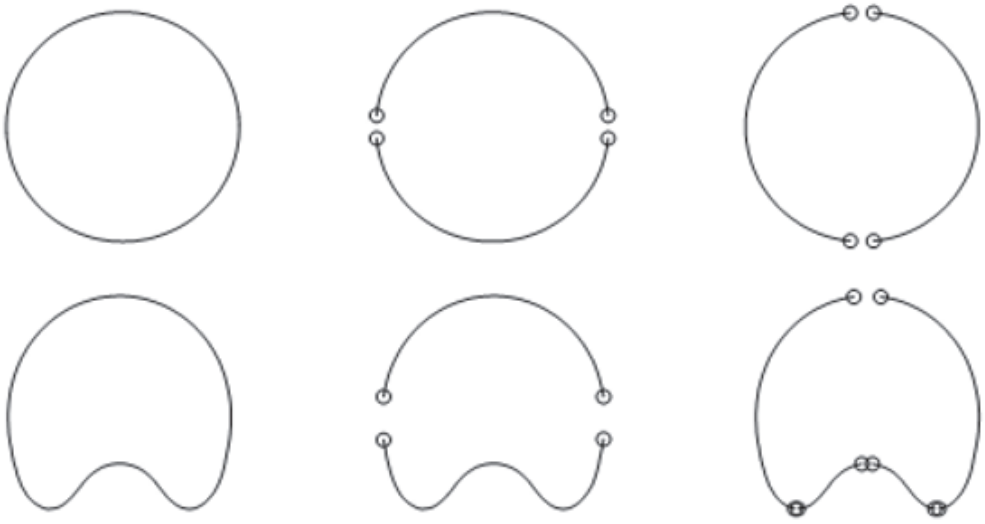

Figure 1.1: Segment structure for the circle (up) and deformed circle (down): curve γ (left), x-segment (middle), and y-segment (right). After Engquist *et al.* [26].

An alternative approach is the method of level-sets [25]. Here the wave fronts are seen as the zeros of a single continuous function $\phi(\boldsymbol{x})$(the level-set function) designed to be positive on one side of the front and negative on the other side. The equation of motion of the fronts is then applied to the whole level-set function as:

$$\partial_t \phi + c(\boldsymbol{x}) \hat{\boldsymbol{n}} \cdot \boldsymbol{\nabla}_{\boldsymbol{x}} \phi = 0 \,,$$

if one considers the same situation as before. This transport equation may be solved by standard numerical methods. The updated wave front is sought as the zero level of the level-set function at the next numerical step.

Asymptotic methods may be numerically efficient, but they are hardly applicable to complex geometries. For instance, the applications with polarized elastic waves are sparse as they become numerically expensive when a lot of wave fronts are present, *i.e.* for diffuse wave fields in bounded elastic media.

1.4 Energy methods

Adopting Eulerian numerical methods, the consideration of high-frequency phenomena in vibrating structures requires a high density of nodes both in the space and time dimensions for the full discretization of the wave equation describing them. If a steady-state regime is rather investigated the sole spatial discretization may be already bulky. Adopting asymptotic ray methods, numerous wave fronts need to be tracked if multiple reflections of the rays on the boundaries and interfaces are considered for the simulation of a diffusive regime. Moreover the effects of the uncertainties of the mechanical parameters are much more sensitive in the HF range on account of the high modal density of built-up structures [88, 90]. These shortcomings may be partially alleviated if the focus is put on the evolution of some global quantities in the system under consideration. That is why engineers have developed alternative approaches using quadratic observables (energetics) in order to smooth out the contributions of highly oscillating, high-frequency wave fields. The most popular methods are the Statistical Energy Analysis (SEA) introduced by Lyon and Maidanik in their seminal paper [62], and the Vibrational Conductivity Analogy introduced by Nefske and Sung [68]. The former adopts a global point of view, while the latter adopts a local point of view.

1.4.1 Global approach: Statistical Energy Analysis

The Statistical Energy Analysis (SEA) exposed in Lyon [60], Lyon and DeJong [61], tracks the evolution of the vibratory energy of subsystems while taking into account the effect of uncertainties. Its principle is to divide a built-up structure into $\mathcal{N}$ substructures, and to quantify the energy levels and the exchanges of mechanical energy between them. Subsystems are constituted by group of modes having the same energetic properties, and SEA predicts the average of the mechanical energy of this group. All the modes in a group are assumed to have the same probability to be excited, leading naturally to the assumption that the modal density is high, the latter holding only in the HF range.

A balance of the energy of the p-th substructure for a frequency band of width $\Delta\omega$ and central frequency ω is:

$$P_p^{\mathrm{in}} = P_p^{\mathrm{d}} + \sum_{q \neq p}^{\mathcal{N}} P_{pq}\,, \quad 1 \leq p \leq \mathcal{N}\,,$$

where P_p^{in} and P_p^d are the input power and the dissipated power in the p-th substructure, respectively, and P_{pq} is the power exchanged between p and an other substructure q. In SEA it is subsequently assumed that the powers that are dissipated and exchanged by the p-th substructure are related to its mechanical energy E_p through [61]:

$$\begin{aligned} P_p^d &= \omega \eta_p E_p\,, \\ P_{pq} &= \omega(\eta_{pq} E_p - \eta_{qp} E_q)\,, \end{aligned} \tag{1.18}$$

where η_p and η_{pq} are the dissipation loss factor and the coupling loss factors, respectively, and E_q is the mechanical energy of the q-th substructure. These parameters are experimentally or analytically established. To be valid, there must be high reflections of the wave field at the boundary between sub-systems, leading to the so-called diffusion approximation of steady-state vibrations. Then the Eq. (1.18) for each subsystem are assembled,

leading to an algebraic system for the complete built-up structure. This procedure exhibits a key advantage of the method in that it leads to a small-sized system. The hypotheses of equipartition of the energy over the modes of a subsystem and of the non-correlation of the response of these modes, leads to $\eta_{pq} = \eta_{qp}$ for conservative couplings. It ensures the symmetry of the SEA algebraic system and thus its ease of resolution.

In its original formulation SEA does not give any information about the transient dynamics of the structure. A time-domain version of SEA has been proposed in [61, 76] as:

$$P_p^{\text{in}} = \frac{dE_p}{dt} + P_p^{\text{d}} + \sum_{q \neq p}^{\mathcal{N}} P_{pq}\,, \quad 1 \leq p \leq \mathcal{N}\,.$$

Many other directions have been followed in the structural-acoustics literature in order to try to release the various assumptions introduced for the derivation of SEA. A complete survey of these works is however clearly out of the scope of this dissertation. One may mention in passing the contribution of Langley [52] for example, who introduced a directional dependence of the energy that relaxes the equipartition approximation. More recently, bringing together a ray tracing method (see Sect. 1.3.2) and SEA, Shorter [89] and Tanner [97] have provided a tool to systematically test the assumptions of SEA and extend its range of validity. SEA has been widely applied in industrial cases for the prediction of the amount of energy of the resonant modes in the HF range at a low numerical cost. Nevertheless, it still relies on the determination of some core parameters such as the input powers or the coupling loss factors, though some recent researches propose to determine them from wave considerations [76, 110–112]. As it stands to date SEA gives only a global information on the steady-sate, not to say transient dynamics of a built-up structure. Approaches based on an analogy with heat conduction are aimed at describing how the mechanical energy is spread locally in a vibrating built-up structure. They are briefly addressed in the next section.

1.4.2 Local approach: Vibrational Conductivity Analogy

The global aspect of the SEA method may not be satisfactory because it requires some stringent assumptions to be applied. Hence some authors have considered local approaches in order to describe more in detail the HF behavior of built-up structures. A first attempt was done by Nefske and Sung [68], starting from earlier works by Rybak [83] or Belov *et al.* [9]. The local variables of interest are then the mechanical energy density $\mathcal{E} := \frac{1}{2}(\rho|\dot{\boldsymbol{u}}|^2 + \boldsymbol{\sigma} : \boldsymbol{\epsilon})$ and power flow density $\boldsymbol{\Pi} := -\boldsymbol{\sigma}\dot{\boldsymbol{u}}$. It is first assumed that this two quantities are connected through a law of heat diffusion type (Fourier's law):

$$\boldsymbol{\Pi} = -D(\omega)\boldsymbol{\nabla}_{\boldsymbol{x}}\mathcal{E}\,, \tag{1.19}$$

where D is a diffusion coefficient depending on the central circular frequency of the applied loads. The local power balance in the structure, or continuity equation, is derived by multiplying Eq. (1.1) with $\dot{\boldsymbol{u}}$:

$$\partial_t \mathcal{E} + \operatorname{div} \boldsymbol{\Pi} + \Pi^{\text{d}} = \Pi^{\text{in}}\,, \tag{1.20}$$

where $\Pi^{in} = \rho \boldsymbol{f} \cdot \dot{\boldsymbol{u}}$ is the input power density and Π^{d} is some dissipated power density. Then, substitution of Eq. (1.19) into Eq. (1.20) leads to a partial differential equation in

terms of the energy density solely. This approach, called the Vibrational Conductivity Analogy (VCA) in the structural-acoustics literature, has been successfully apply to the case of beams [54, 68], and plates [27, 38]. However, it seams to be hardly applicable to more complex structures, because it assumes that the energy density spread over the entire structure by invoking a Fourier's law. This means that the structure should contain numerous scatterers to spread the energy flows in all directions, or that the observation time should be sufficiently large and the structure is sufficiently undamped to reach a state of spatial equipartition of the energy density. Besides, the determination of boundary conditions for coupled structures raises severe theoretical difficulties, because VCA relies on the assumption that the wave field is diffuse in the vicinity of that boundaries as well. Therefore ballistic wave fields can not be captured in principle, and a definition of the power flow reflection/transmission phenomena remains awkward [95].

The main limitation of this method is thus the assumption that the energy density obeys a Fourier's law. The Transient Simplified Energetic Method [95] introduces a modification of this law to account for wave transport phenomena in inhomogeneous media. This law is suitable for short time predictions but it depends on the determination of the same core parameters as an SEA global approach.

1.4.3 Kinetic modeling for the evolution of energy densities

As already mentioned previously, the displacement of HF waves is very oscillating and induces high levels of accelerations. As can been seen from the developments of SEA and VCA, the use of quadratic quantities is more relevant in the HF range [53]. This observation can be explained with the following example. Let $u_\varepsilon(x)$ be a one-dimensional oscillating function of the form, say, $u_\varepsilon(x) = m(x) + \sigma(x)\sin(\frac{x}{\varepsilon})$, where $0 < \varepsilon \ll 1$. Then the weak limit in $L^2(\mathbb{R})$ as $\varepsilon \to 0$ of the series (u_ε) is the mean function $m(x)$, but the series has no strong limit. However consider now the energy limit defined by:

$$\lim_{\varepsilon\to 0} \int_{\mathbb{R}} \phi(x) u_\varepsilon^2(x) dx \,,$$

where ϕ is a smooth function with compact support in $\mathbb{R}$, a so-called observable. Then it can be shown that:

$$\lim_{\varepsilon\to 0} \int_{\mathbb{R}} \phi(x) u_\varepsilon^2(x) dx = \int_{\mathbb{R}} \phi(x) \left(m^2(x) + \frac{1}{2}\sigma^2(x) \right) dx \,.$$

Contrarily to the weak limit $m(x)$, the quadratic quantity associated to the series (u_ε) tends locally at any point x selected by the observable function $\phi(x)$ to $m^2(x) + \frac{1}{2}\sigma^2(x)$. That limit allows to see locally the influence of oscillations at the small scale ε since the deviation $\sigma(x)$ is now apparent. Moreover it no longer has the oscillatory feature of u_ε. The following Fig. 1.2 shows an example of a highly oscillating function $u_\varepsilon(x)$, its mean $m(x)$, and the square root of its energy limit $(m^2(x) + \frac{1}{2}\sigma^2(x))^{\frac{1}{2}}$. It exhibits the interest of the use this very limit in HF propagation phenomena, because it takes into account the influence of the oscillations at a macroscopic scale.

In view of the relevance of quadratic quantities to describe oscillating functions as illustrated above, rigorous estimators of the energy density of HF (strongly oscillating) wave

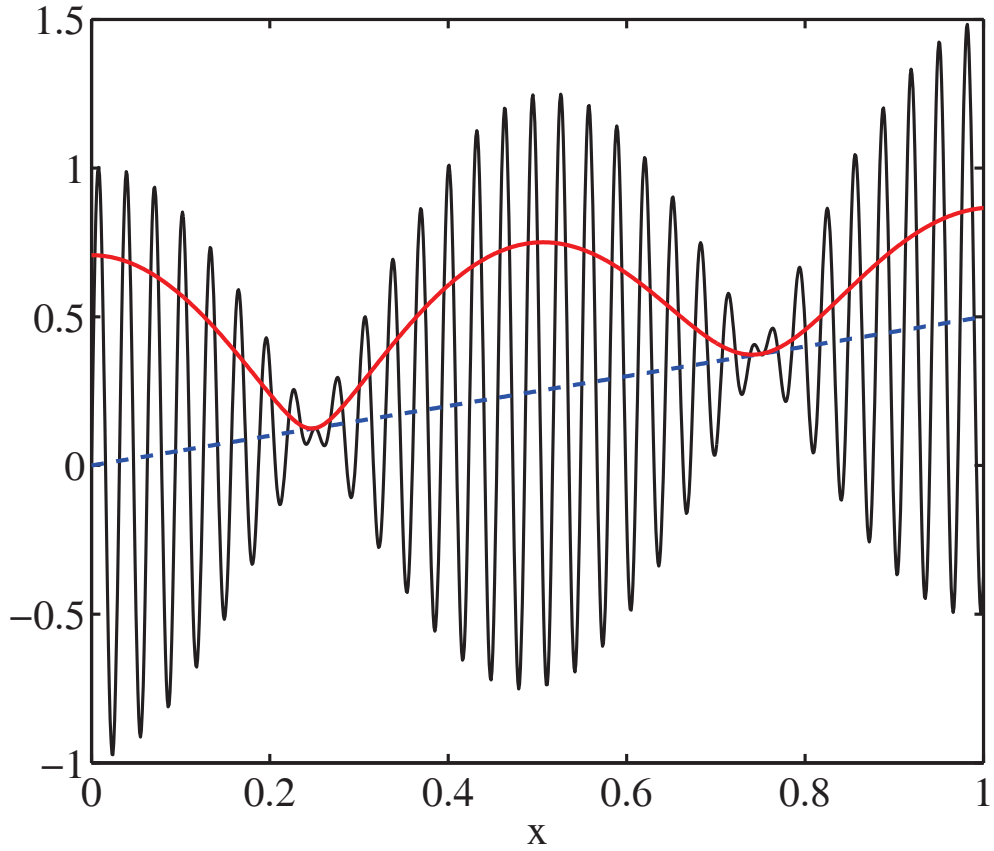

Figure 1.2: The displacement function $u_\varepsilon(x) = 1/2(x) + \cos(2\pi x)\sin(\frac{x}{\varepsilon})$ (thin gray line), its mean function $m(x)$ (thick dashed blue line), and the square root of its energy limit $\sqrt{m^2(x) + \frac{1}{2}\cos^2(2\pi)}$ (thick red line).

fields solutions of Eq. (1.11) can be constructed using semiclassical, or Wigner measures [31, 57]. It may be shown in addition that the latter satisfy Liouville-type transport equations on account of the propagation properties of the underlying wave fields. The developments have strong connections with ray methods, in that they consider the HF limit $\varepsilon \to 0$ of the rescaled system (1.15) in a particular sense bringing out the associated energy density. In Papanicolaou and Ryzhik [75], the authors have extended that theory to several physical systems: quantum waves obeying a Schrödinger equation, acoustic and elastic waves obeying a wave equation, or electromagnetic waves obeying the Maxwell equations. The decisive advantage of this theory is to avoid the resolution of an eikonal equation while allowing the superposition of different wave polarizations and phases. This superposition is possible because Wigner measures depend both on the position and on the wavevector indicating the direction of propagation of the waves. Moreover randomly heterogeneous media can be considered (see Sect. 3.2.4 for more details), the Liouville equation being transformed into a radiative transfer equation in this case [4, 36, 75]. Therefore multiple reflections of the energy rays by the boundaries or the medium heterogeneities are much easier to address in

this setting than by ray methods. The theory has been applied to two dimensional structural elements in [86]. The aforementioned developments are part of a more general approach known in the dedicated literature as kinetic modeling of wave propagation phenomena in heterogeneous media; see for example the recent review [5]. The main point of issue is the consideration of boundary conditions for energy and power flow densities. Classical boundary conditions such Neumann or Dirichlet conditions have indeed to be adapted to the case of quadratic quantities.

1.5 Conclusions

The aim of the thesis is to develop a method able to predict the transient dynamics of beam trusses under impulse loads. Such phenomena are described by high-frequency waves propagating in bounded media. Wave multiple reflections and crossings will arise because of the reflection/transmission processes taking place at the junctions between sub-structures. A kinetic modeling of the evolution of the energy density associated to high-frequency waves allows to consider superposition and such multiple reflections at the boundaries. Moreover it is more pertinent for the modeling of the transient response to shocks than the methods describing directly the displacement fields, on account of the very oscillating disturbances generated by high-frequency waves. At last, compared to an engineering approach as SEA, the model gives local information of the evolution of the energy density.

The numerical schemes to be implemented for the numerical integration of kinetic equations need to be accurate in the sense that they will have to describe rapid phenomena over rather large times (in order to reach the diffusive regime). Moreover the reflection/transmission processes at the junctions generate discontinuities of the energy density fields. Hence, the method retained for the spatial discretization shall be able to account for these singularities. A discontinuous Galerkin method using spectral-like approximation functions seems to be well adapted to this situation. Also the time integration schemes shall have to preserve the accuracy of the spatial discretization schemes achieved using the aforementioned high-order approximations. Therefore, a strong stability-preserving high-order Runge-Kutta scheme shall be implemented.

Before considering the derivation of kinetic equations for beam trusses, several models of beams will be investigated in order to study their accuracy in the high-frequency range. This is done in the next chapter by comparing various kinematical reductions to a three-dimensional Lamb model of a circular waveguide.

Chapter 2

Waves in a beam

As argued in the introduction, the objectives of the thesis are to predict the evolution of the energy density associated to HF wave propagation within beam trusses. In order to introduce this study, different models of beams will be exposed having the higher frequency ranges of vibration in view. Beams are structures with one dimension greater than the two others. The use of such structural components allows to reduce the three-dimensional kinematics of (1.4) into one-dimensional kinematics. In this chapter, the HF behavior of a single beam is first studied considering it as a waveguide through an exact, analytical Lamb model. Then different theories of kinematical reductions are compared to the three-dimensional Lamb model, and their relevance for HF vibrations are discussed.

2.1 Beam as a waveguide

This study of wave propagation in beams begins with the derivation of a Lamb model adapted to beam, also known as the Pochhammer-Chree model. This model gives the characteristics of wave propagation in a one dimensional waveguide, the dispersion relations or the group velocities for example. In his book, Achenbach [2] describes Lamb waves as constructive interactions between the waves in a three-dimensional medium (*i.e.* one longitudinal wave and two transverse waves) coupled by the boundary conditions on the outer surfaces.

The propagation of mechanical waves in a cylinder had been investigated earlier since Pochhammer established the dispersion relation of such waves in 1876 [21]. Its derivation can be found in numerous references, see [2, 65, 66, 80]. But the transcendental equation characterizing dispersion can not be solved analytically and thus it was only in the 1940s that this equation has been solved for low frequencies and real wavenumbers by Bancroft [6] or Hudson [45]. Since these early works, the dispersion curves have been intensively studied. Complete works have been done by Onoe *et al.* [71] for the longitudinal modes (see their definition below) and Pao and Mindlin [73] for flexural motions (see their definition below). Both works rely on a geometrical method, but with the increase of computational power it is now possible to investigate the Pochhammer-Chree spectrum numerically. In this section, the dispersion equations are thus investigated numerically thanks to the method derived by Honarvar *et al.* [42] with a special care of the HF range phenomena. Conclusions of this analysis will allow to evaluate the accuracy of the reduced model used subsequently for the

study of the evolution of the energy density in a beam.

2.1.1 Dispersion relations

Firstly, the derivation of the dispersion relations of wave propagation in a cylindrical waveguide will be recalled. The beam is supposed to be an infinite waveguide with a circular cross-section of radius a constituted by an isotropic and homogeneous material. A point of the waveguide is denoted by $\boldsymbol{x} \in \mathbb{R}^3$ and its coordinates in the Cartesian frame $(\hat{\boldsymbol{e}}_1, \hat{\boldsymbol{e}}_2, \hat{\boldsymbol{e}}_3)$ are (x, y, z). x is the coordinate along $\hat{\boldsymbol{e}}_1$ that is the principal axis of the circular waveguide. The classical wave equation Eq. (1.4) holds in it. Thus it is possible to introduce a Helmholtz decomposition of the displacement field $\boldsymbol{u}$. It consists in expanding it in an irrotational (denoted by $\boldsymbol{\nabla}\Phi$) vector field and a divergence-free (denoted by $\boldsymbol{\nabla} \times \boldsymbol{\Psi}$) vector field. Applying this to the displacement of a point $\boldsymbol{x}$ results in:

$$\boldsymbol{u}(\boldsymbol{x}, t) = \boldsymbol{\nabla}\Phi + \boldsymbol{\nabla} \times \boldsymbol{\Psi}\,. \tag{2.1}$$

In the rest of the thesis $\boldsymbol{a} \times \boldsymbol{b}$ will denote the wedge product between the vectors $\boldsymbol{a}$ and $\boldsymbol{b}$. Inserting Eq. (2.1) into the elastodynamic equation (1.4) leads to two independent wave equations:

$$\begin{aligned} \boldsymbol{\Delta}\boldsymbol{\Psi} &= \frac{1}{c_s^2}\ddot{\boldsymbol{\Psi}}\,, \\ \triangle\Phi &= \frac{1}{c_l^2}\ddot{\Phi}\,, \end{aligned} \tag{2.2}$$

where c_l and c_s are respectively the velocity of the longitudinal and transverse waves given by Eq. (1.7) and Eq. (1.8). On account of the shape of the cross-section, it is more convenient to use a cylindrical frame of reference. So a point of the beam is mapped by $\boldsymbol{x} = r\hat{\boldsymbol{e}}_r(\theta) + x\hat{\boldsymbol{e}}_1$. In this coordinate system, the system (2.2) is given by:

$$\triangle\Phi = \partial_r^2\Phi + \frac{1}{r}\partial_r\Phi + \frac{1}{r^2}\partial_\theta^2\Phi + \partial_x^2\Phi = \frac{1}{c_s^2}\ddot{\Phi}\,, \tag{2.3}$$

$$\triangle\Psi_x = \partial_r^2\Psi_x + \frac{1}{r}\partial_r\Psi_x + \frac{1}{r^2}\partial_\theta^2\Psi_x + \partial_x^2\Psi_x = \frac{1}{c_l^2}\ddot{\Psi}_x\,, \tag{2.4}$$

$$\triangle\Psi_r - \frac{2}{r^2}\partial_\theta\Psi_\theta - \frac{\Psi_r}{r^2} = \partial_r^2\Psi_r + \frac{1}{r}\partial_r\Psi_r + \frac{1}{r^2}\partial_\theta^2\Psi_r + \partial_x^2\Psi_r - \frac{2}{r^2}\partial_\theta\Psi_\theta - \frac{\Psi_r}{r^2} = \frac{1}{c_s^2}\ddot{\Psi}_r\,, \tag{2.5}$$

$$\triangle\Psi_\theta + \frac{2}{r^2}\partial_\theta\Psi_r - \frac{\Psi_\theta}{r^2} = \partial_r^2\Psi_\theta + \frac{1}{r}\partial_r\Psi_\theta + \frac{1}{r^2}\partial_\theta^2\Psi_\theta + \partial_x^2\Psi_\theta + \frac{2}{r^2}\partial_\theta\Psi_r - \frac{\Psi_\theta}{r^2} = \frac{1}{c_s^2}\ddot{\Psi}_\theta\,. \tag{2.6}$$

The equations for Φ and Ψ_z are totally uncoupled but the components Ψ_θ and Ψ_r of $\boldsymbol{\Psi}$ are coupled through Eq. (2.5) and Eq. (2.6). Considering only the waves in the $\hat{\boldsymbol{e}}_1$-direction, the solutions of this set of equations have the form [34]:

$$\Phi = AJ_n(pr)\cos(n\theta)\mathrm{e}^{\mathrm{i}(kx-\omega t)}\,, \tag{2.7}$$

$$\Psi_x = BJ_n(qr)\sin(n\theta)\mathrm{e}^{\mathrm{i}(kx-\omega t)}\,, \tag{2.8}$$

$$\Psi_r = (DJ_{n-1}(qr) + CJ_{n+1}(qr))\sin(n\theta)\mathrm{e}^{\mathrm{i}(kx-\omega t)}\,, \tag{2.9}$$

$$\Psi_\theta = (DJ_{n-1}(qr) - CJ_{n+1}(qr))\cos(n\theta)\mathrm{e}^{i(kx-\omega t)}\,, \tag{2.10}$$

where p and q are defined by:

$$p^2 = \frac{\omega^2}{c_l^2} - k^2 \,, \tag{2.11}$$

and

$$q^2 = \frac{\omega^2}{c_s^2} - k^2 \,, \tag{2.12}$$

and $n \in \mathbb{N}$ the set of the natural integers. The system is under-constrained because there are four constants for three equations. To fix it, the divergence-free condition $\boldsymbol{\nabla} \cdot \boldsymbol{\Psi} = 0$ is added and leads to $D = 0$.

The dispersion relations are derived from the traction-free boundary conditions on the lateral surface of the beam.

$$\boldsymbol{\sigma}(\hat{\boldsymbol{e}}_r)|_{r=a} = \mathbf{0} \,.$$

The stress components are given by Eq. (1.3) together with Eq. (2.1). These equations can be reshaped in a matrix form as:

$$\boldsymbol{\Gamma}(\omega, k, \theta, n)\boldsymbol{A} = \mathbf{0} \,, \tag{2.13}$$

where $\boldsymbol{A} = (A, B, C)^T$ is the amplitude vector. The matrix $\boldsymbol{\Gamma}$ is given in an extended form by:

$$\mathbf{\Gamma} = \begin{pmatrix} (-\lambda(p^2+k^2)J_n(pa) + 2\mu\partial_r^2 J_n(pa))\cos(n\theta) & 2\mu(\frac{n}{a}\partial_r J_n(qa) - \frac{n}{a^2}J_n(qa))\cos(n\theta) & 2\mu\,\mathrm{i}\,k\partial_r J_{n+1}(qa)\cos(n\theta) \\ -\mu\frac{2n}{r}(\partial_r J_n(pa) - \frac{1}{a}J_n(pa))\sin(n\theta) & -\mu(2\partial r^2 J_n(qa) + J_n(qa)q^2)\sin(n\theta) & -\mu\,\mathrm{i}\,k(\frac{n+1}{a}J_{n+1}(qa) - \partial_r J_{n+1}(qa))\sin(n\theta) \\ 2\,\mathrm{i}\,k\partial_r J_n(pa)\cos(n\theta) & \frac{\mu\,\mathrm{i}\,nk}{a}J_n(qa)\cos(n\theta) & \mu(-\frac{n}{a}\partial_x J_{n+1}(qa) + (-q^2+k^2-\frac{n^2+n}{a^2})J_{n+1}(qa))\cos(n\theta) \end{pmatrix} \tag{2.14}$$

Non trivial solutions of the system (2.13) arise for $\det(\mathbf{\Gamma}) = 0$. This dispersion relation gives the couples (ω, k) satisfying $\det(\mathbf{\Gamma}) = 0$ for a given value of n and for all $\theta \in [0, 2\pi[$. Then it is possible to recover the displacement field of Eq. (2.1) by fixing A to 1 and solving the system:

$$\begin{pmatrix} B \\ C \end{pmatrix} = - \begin{pmatrix} \Gamma_{22} & \Gamma_{23} \\ \Gamma_{32} & \Gamma_{33} \end{pmatrix}^{-1} \begin{pmatrix} \Gamma_{21} \\ \Gamma_{31} \end{pmatrix} ,$$

where Γ_{ij} is the element of $\mathbf{\Gamma}$ on the row i and column j.

2.1.2 Modal analysis

The analysis of the dispersion relation and the displacement field of the waveguide is performed for a fixed value of n in $\mathbb{N}$. For $n = 0$, the dispersion relation can be analytically computed:

$$[qaJ_0(qa) - 2J_1(qa)] \left[\frac{2p}{a}(q^2 + k^2)J_1(pa)J_1(qa) - (q^2 - k^2)^2 J_0(pa)J_1(qa) - 4k^2 pqJ_1(pa)J_0(qa)\right] = 0 . \quad (2.15)$$

The first part of the left-hand side concerns the motions along $\hat{\boldsymbol{e}}_\theta$ only, while the second part concerns the motions along $\hat{\boldsymbol{e}}_r$ and $\hat{\boldsymbol{e}}_1$ solely. Thus the first part corresponds to the dispersion relation of the torsional waves while the latter is the Pochhammer equation related to the longitudinal motions. For higher values of n, the dispersion equation can not be factorized. Thus the motion exists along all the axes, leading to the so-called flexural motions. The next subsections deal with the analysis of these dispersion curves.

2.1.2.1 Torsional motions

The dispersion relation for the torsional motion is:

$$qaJ_0(qa) = 2J_1(qa) . \quad (2.16)$$

The solutions of such equation are tabulated in [1]. The first three solutions are

$$\begin{aligned} (aq)_1 &= 0 , \\ (aq)_2 &= 5.1356 , \\ (aq)_3 &= 8.4172 , \end{aligned}$$

but there is an infinite number of roots. Let $\gamma_j = (a)_j$ be a solution of Eq. (2.16). As $q^2 = \frac{\omega^2}{c_s^2} - k^2$, the dispersion relation becomes:

$$k = \pm \frac{1}{ac_s} \sqrt{(a\omega)^2 - (\gamma_j c_s)^2} . \quad (2.17)$$

The HF limit corresponds to $\omega \to \infty$. In this limit, the dispersion relation 2.17 becomes

$$\omega^2 = c_s^2 k^2 , \quad (2.18)$$

and the phase velocity is:

$$\frac{\omega}{k} = \pm \sqrt{\frac{\mu}{\rho}} = \pm c_s . \quad (2.19)$$

That means that, in the HF range, the waveguide is a non-dispersive medium for all the torsional waves. The limit velocity is the same for all torsional modes and corresponds to the velocity of the shear wave c_s in a three-dimensional medium. The dispersion curves of these torsional modes are shown in Fig. 2.1, the phase velocities in Fig. 2.2, and the group velocities in Fig. 2.3. The dispersion curves are obtained finding the roots of the Eq. (2.16) with the algorithm inspired by the one presented in the article of Honarvar *et al.* [42]. In this algorithm, the determinant is evaluated for every couple (ω, k) and sign changes are detected to find the zeros of $\det(\mathbf{\Gamma})$. This method allows to take advantage of the matrix's computation efficiency of Matlab. The velocities are normalized according to the transverse phase velocity c_s.

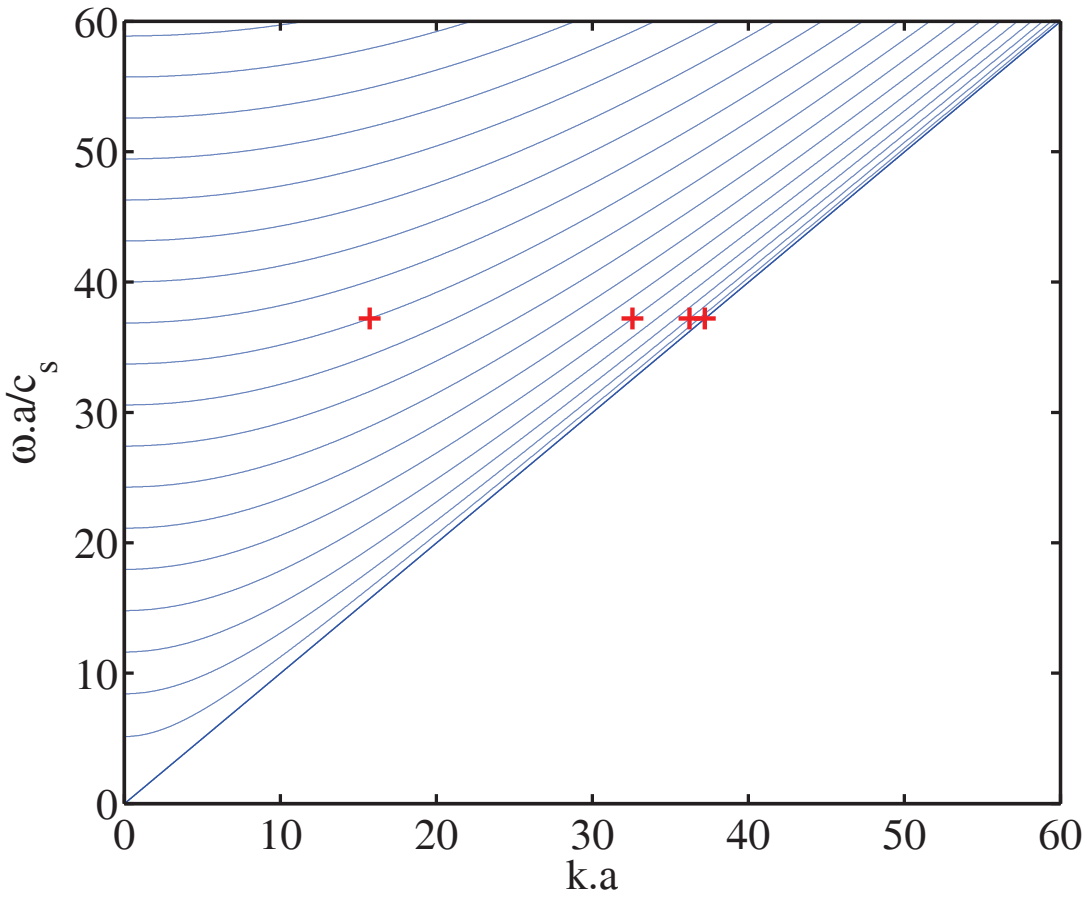

Figure 2.1: Dispersion curves of the torsional modes; the crosses denote the dispersion points for the plot of the modes of Fig. 2.4.

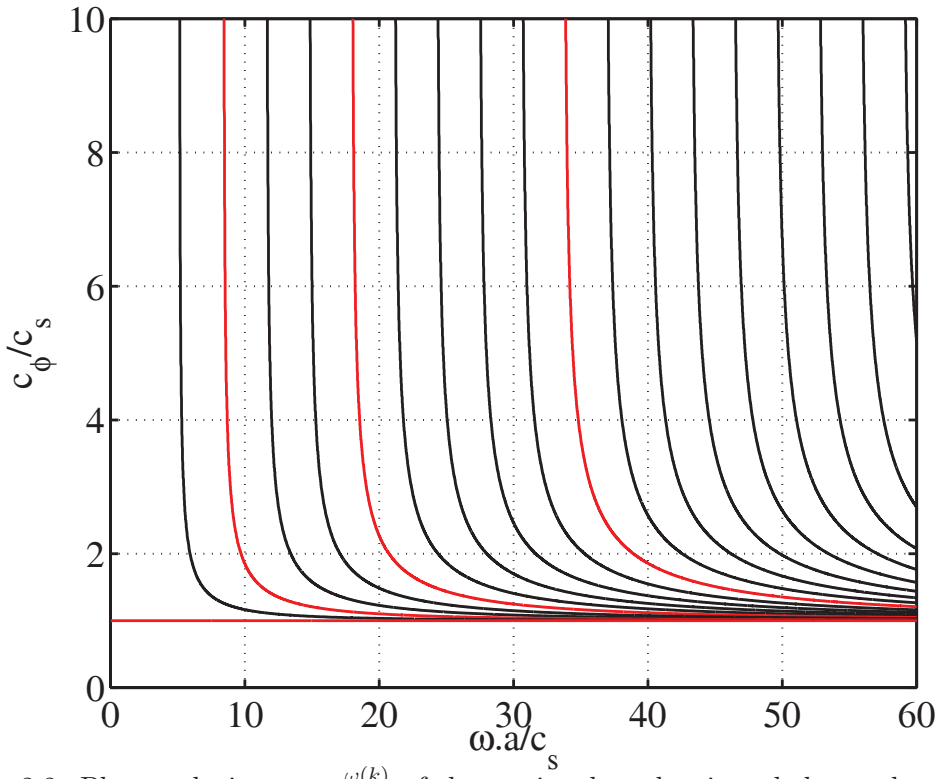

Figure 2.2: Phase velocity $c_\phi = \frac{\omega(k)}{k}$ of the torsional modes; in red the modes selected for the Fig. 2.4.

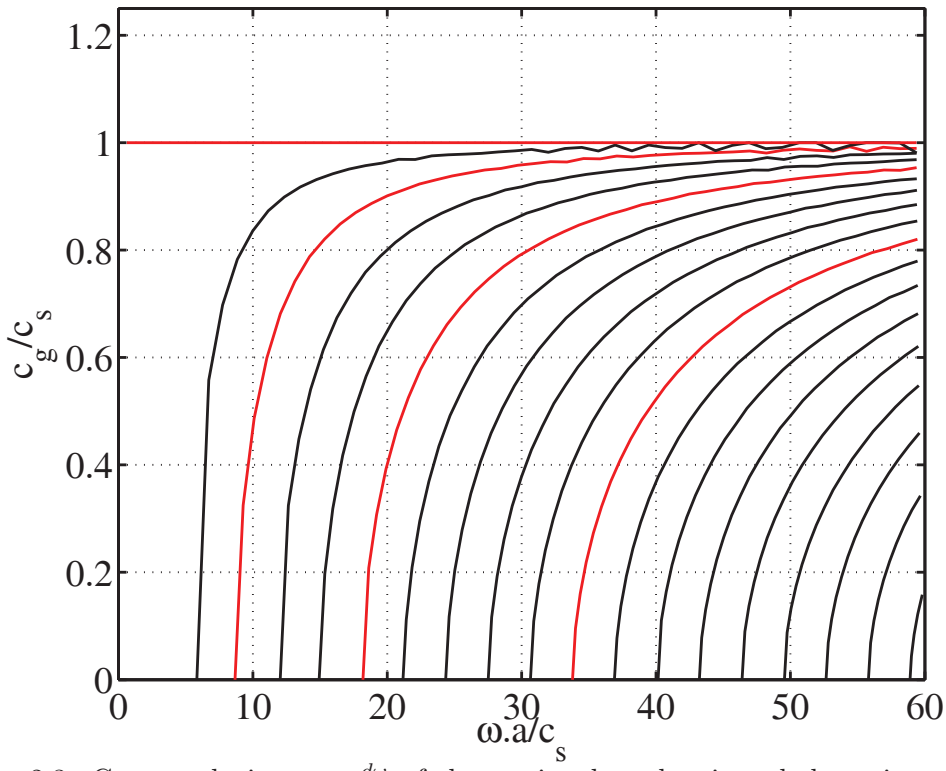

Figure 2.3: Group velocity $c_g = \frac{d\omega}{dk}$ of the torsional modes; in red the points selected for plotting the modes on Fig. 2.4.

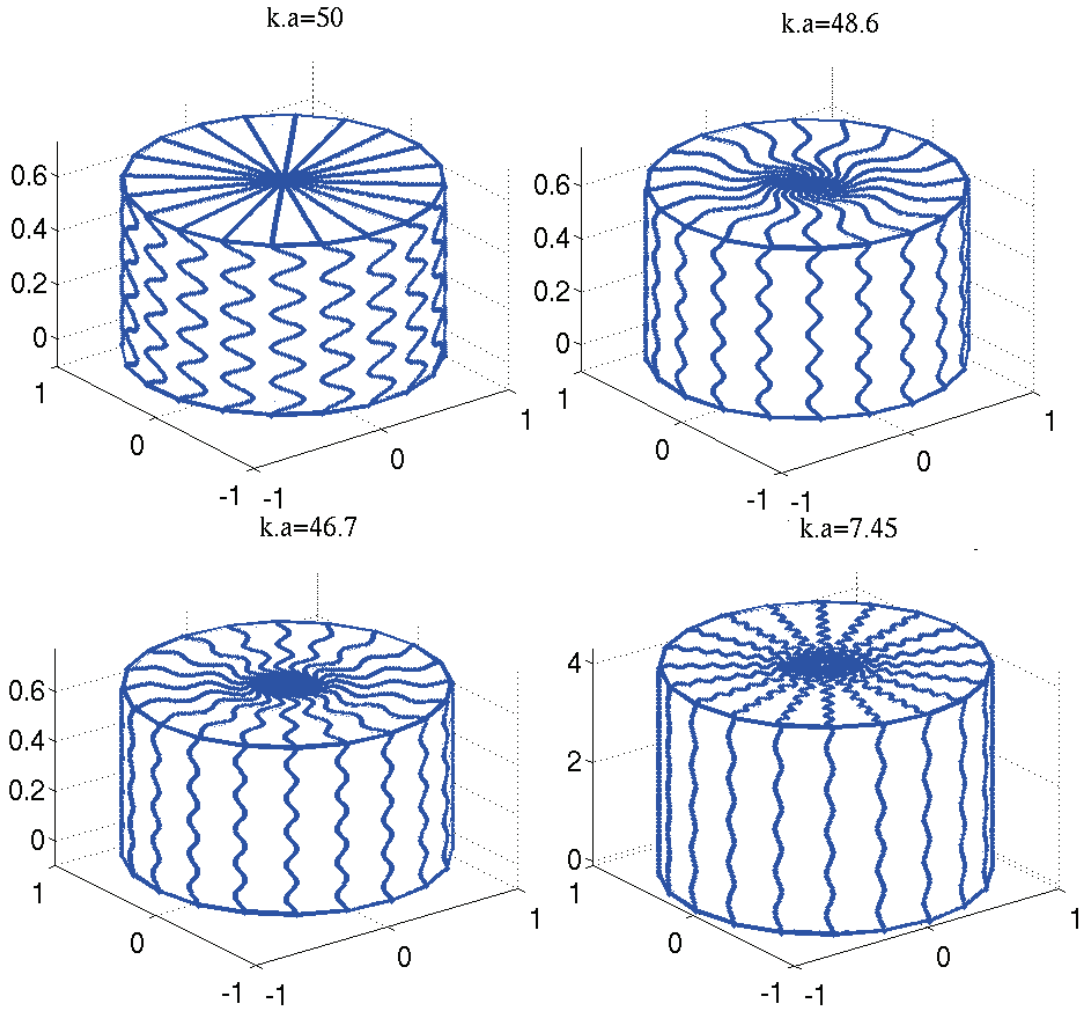

Figure 2.4: Shape of some torsional modes. The top left shape corresponds to the first and non-dispersive mode.

The plots have been confronted and validated by comparison to the ones extracted from the aforementioned references. Moreover the first non-dispersive mode (displayed on the top left on Fig. 2.4) is well retrieved. Some shapes of modes are displayed in Fig. 2.4 below. They are defined as:

$$\boldsymbol{u} = \mathfrak{Re}(\boldsymbol{A}\mathrm{e}^{i(kx-\omega t)})\,, \tag{2.20}$$

where $\mathfrak{Re}(\boldsymbol{A})$ denotes the real part of the components of the vector $\boldsymbol{A}$. Since the components of the amplitude vector $\boldsymbol{A}$ may be complex, the displacement field in the direction $\hat{\boldsymbol{e}}_i, i \in (r, \theta, 1)$ becomes:

$$u_i = |A_i| \cos(k_i - \omega t + \varphi_i)\,, \tag{2.21}$$

where

$$\varphi_i = \tan \frac{\mathfrak{Im}(A_i)}{\mathfrak{Re}(A_i)}\,,$$

is the phase angle of the amplitude along $\hat{\boldsymbol{e}}_i$. For the torsional case, all the modes have a shape that does not depend on the frequency. The higher the number of the mode is, the

more oscillating is its shape. For a sake of clarity of the plots, the rods is displayed such that 5 wavelengths are plotted in the $\hat{e}_1$ direction. This rule of plotting will be kept for all the next mode shape plots.

2.1.2.2 Longitudinal motions

Longitudinal modes correspond to the solutions of the second term of the left hand side of Eq. (2.15). The dispersion equation for such modes is the well known Pochhammer frequency equation:

$$\frac{2p}{a}(q^2+k^2)J_1(pa)J_1(qa) - (q^2-k^2)^2 J_0(pa)J_1(qa) - 4k^2pqJ_1(pa)J_0(qa) = 0\,. \qquad (2.22)$$

Analytical resolution of this equation is not straightforward for the entire frequency range, thus it is resolved thanks to the same numerical method as in the torsional case.

However the low frequency analysis can be done easily performing a first order Taylor expansion for $x \to 0$ of the Bessel functions $J_n(x)\,, n = 0$ or 1: that is $J_0(x) = 1 + O(x^2)\,, J_1(x) = \frac{x}{2} + O(x^2)$. Inserting these expansions into the Pochhammer equation (2.22) leads to the phase velocity of the first longitudinal mode at low frequency:

$$c_\phi = \frac{\omega}{k} = \pm\sqrt{\frac{E}{\rho}} = \pm c_{\mathrm{P}}\,, \qquad (2.23)$$

where E is the Young's modulus defined in terms of Lamé's constants by:

$$E = \frac{\mu(3\lambda+2\mu)}{\lambda+\mu}\,.$$

Unfortunately, in the HF range, an asymptotic expansion of the Bessel functions is not possible because the values of p (Eq. (2.11)) or q (Eq. (2.12)) are not necessarily high. Moreover if $\omega \gg c_s k$ is considered, the asymptotic forms of the Bessel functions are:

$$J_n(x) \approx \sqrt{\frac{\pi}{2x}}\cos(x - \frac{n\pi}{2} - \frac{\pi}{4})\,,$$

leading to an other transcendental equation that must be resolved by a root finding algorithm along the same lines as Eq. (2.22).

The resulting dispersion curves are displayed in Fig. 2.5, followed by the plots of the phase velocities and the group velocities (Fig. 2.6 and Fig. 2.7) and the shapes of some modes in Fig. 2.8.

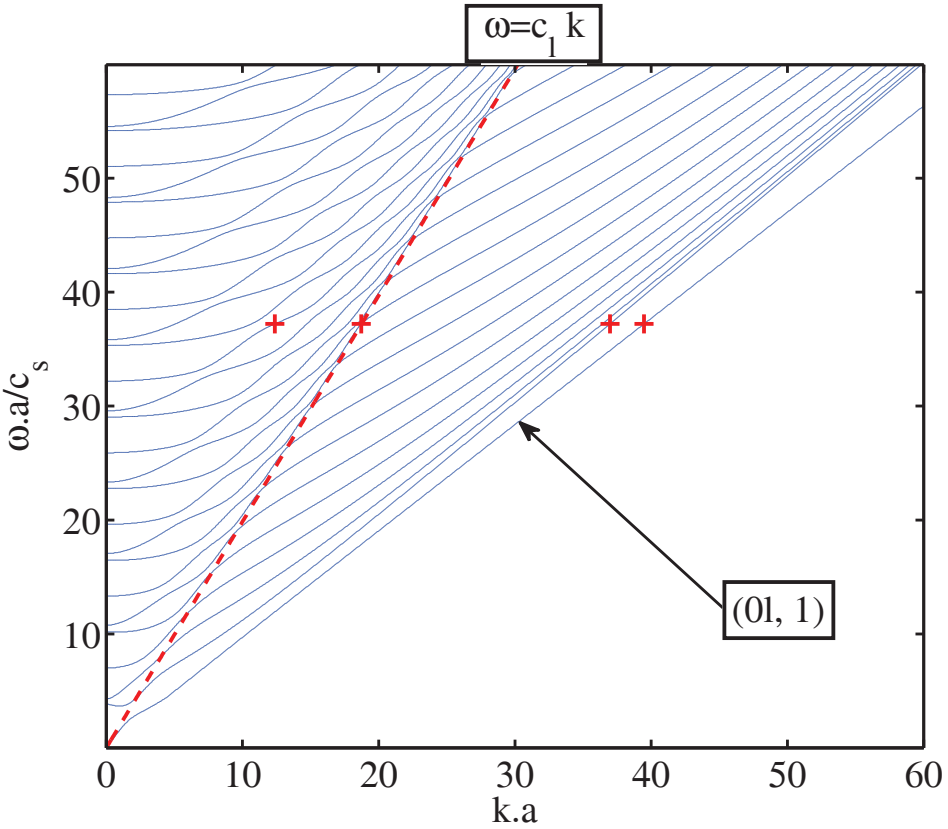

Figure 2.5: Dispersion curves of the longitudinal modes; the crosses denote the dispersion points for the plot of the modes in Fig. 2.8.

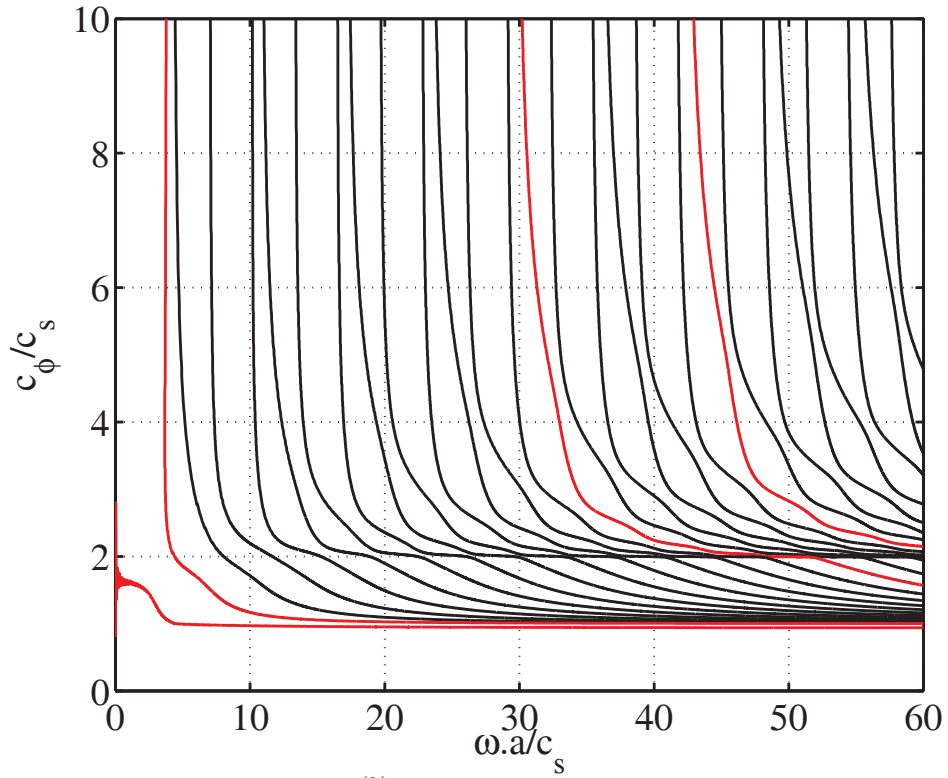

Figure 2.6: Phase velocity $c_\phi = \frac{\omega(k)}{k}$ of the longitudinal modes; in red the modes selected for the Fig. 2.8.

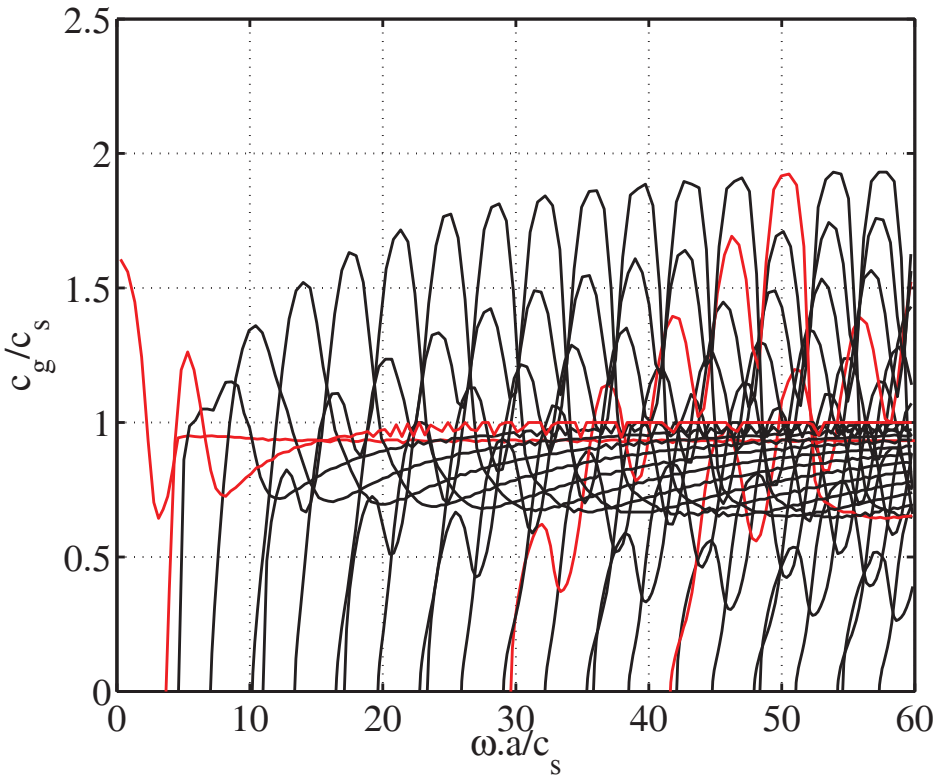

Figure 2.7: Group velocity $c_g = \frac{d\omega}{dk}$ of the longitudinal modes; in red the modes selected for the Fig. 2.8.

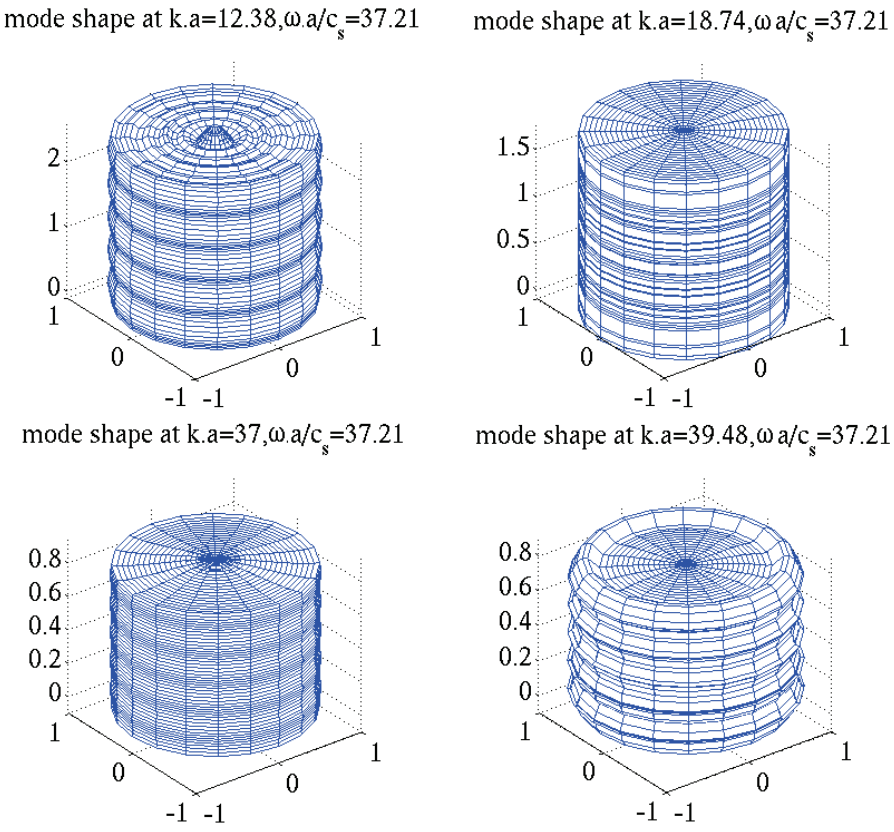

Figure 2.8: Modal shape of some longitudinal modes. The top right modes corresponds to purely longitudinal modes and the bottom right corresponds to the Rayleigh like mode.

These results are confirmed by the comparison with those obtained by several authors, see [2, 65, 71]. A remarkable feature of the spectrum of the longitudinal modes is that their dispersion curves are tangent to the straight line $\omega = c_l k$ (in dashed red line on Fig. 2.5) where c_l is the wave celerity of Eq. (1.7). Inspection of the phase plot Fig. 2.6 shows that, except for the first one, all other modes have a phase velocity that tends to the transverse wave speed of a three-dimensional elastic medium c_s. The phase velocity of the first mode tends to the velocity of the Rayleigh wave. The latter is the root of the equation [64]:

$$\left(\frac{c_r}{c_s}\right)^6 - 8\left(\frac{c_r}{c_s}\right)^4 + 8\left(3 - 2\left(\frac{c_l}{c_s}\right)^2\right)\left(\frac{c_r}{c_s}\right)^2 - 16\left(1 - \left(\frac{c_l}{c_s}\right)^2\right) = 0\,,$$

which may be obtained by substituting $\omega = c_r k$ into the equation

$$(k^2 + q_1^2)^2 = 4k^2 p_1 q_1\,,$$

which is the limit form of the Pochhammer equation (2.22) for large real k and imaginary p and q ($p = \mathrm{i}p_1$ and $q = \mathrm{i}q_1$) [71]. A good approximation of the Rayleigh velocity is [23]:

$$c_r = \frac{0.87 + 1.12\nu}{1 + \nu} c_s\,,$$

where ν is the Poisson ratio, retrieving thus the result of Hudson [45]. It can also be noticed the highest curves have a threshold at $c = c_l$, confirming the asymptote of the dispersion curves. The plot of the group velocities give further informations. All the curves, except for the first mode, have the same behavior: they begin with an increasing trend oscillating to a maximum value, then they drop rapidly to a local minimum value, and finally they increase to a limit which is the shear velocity. The maximum and minimum values tend to a limit as the number of the mode increases. The maximum group velocity is the longitudinal velocity c_l but the minimum value does not seem to correspond to any known wave velocity. It is interesting to note that the longitudinal waves have a non dispersive behavior on the threshold $\omega = c_l k$. They will stay visible at large distance. The dispersion curves seems to be non-dispersion for others dispersion points. They are more numerous for the highest dispersion curves.

The shapes of the propagation modes displayed in Fig. 2.8 give further informations the previous observations. For a wavenumber below the limit $\frac{\omega}{c_l}$ the disturbance oscillates around the position of the cross-section at rest and is mainly longitudinal; in this limit, the motion is purely longitudinal. Beyond this limit, the shape is mainly radial. For the first mode, the disturbance is confined to the vicinity of the lateral surface (denoted by $0l, 1$ on Fig. 2.5), similarly to the behavior of the Rayleigh mode in a semi-infinite medium. The behavior of the dispersion curves around the line $\omega = c_l k$ suggests that some veering phenomena occur between the longitudinal and the radial behavior of the modes [63].

2.1.2.3 Flexural motions

The flexural modes are obtained for $n > 0$. On account of the complexity of the determinant of the matrix $\mathbf{\Gamma}$, the analytical form can not be displayed here and no analytical treatment can be performed. Thus all the developments will be conducted with the help of

the previous algorithm [42].

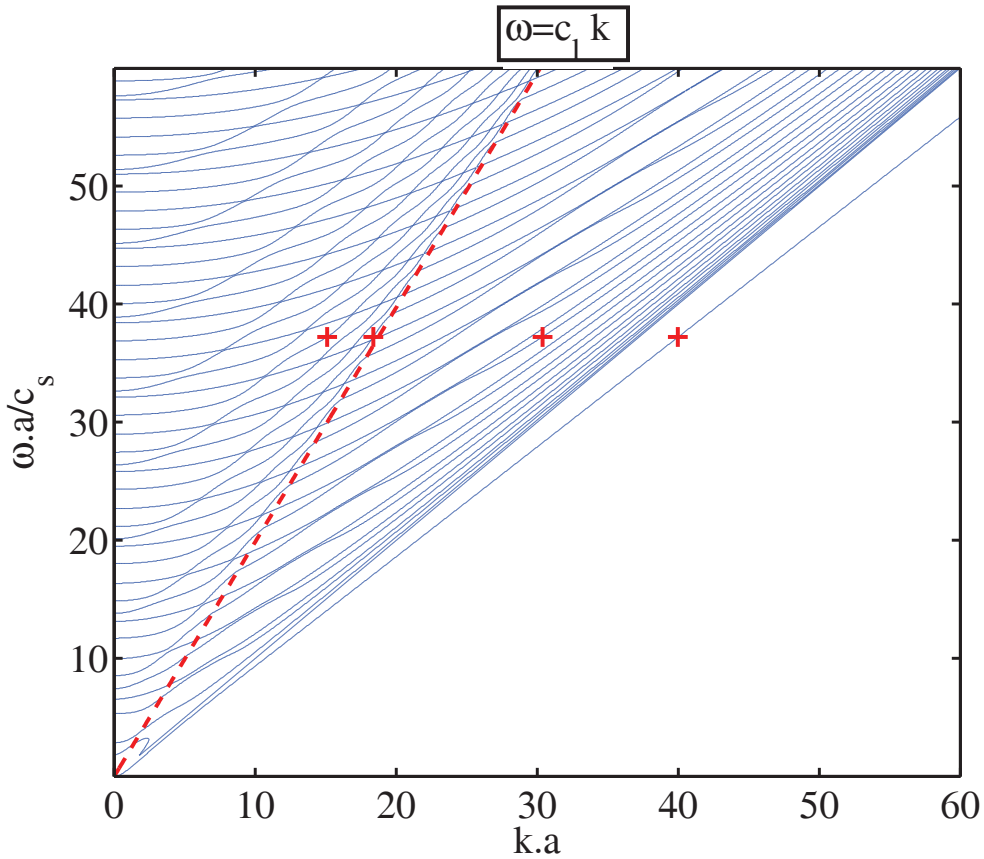

Figure 2.9: Dispersion curves for $n = 1$; the crosses denote the dispersion points for the plot of the modes in Fig. 2.12.

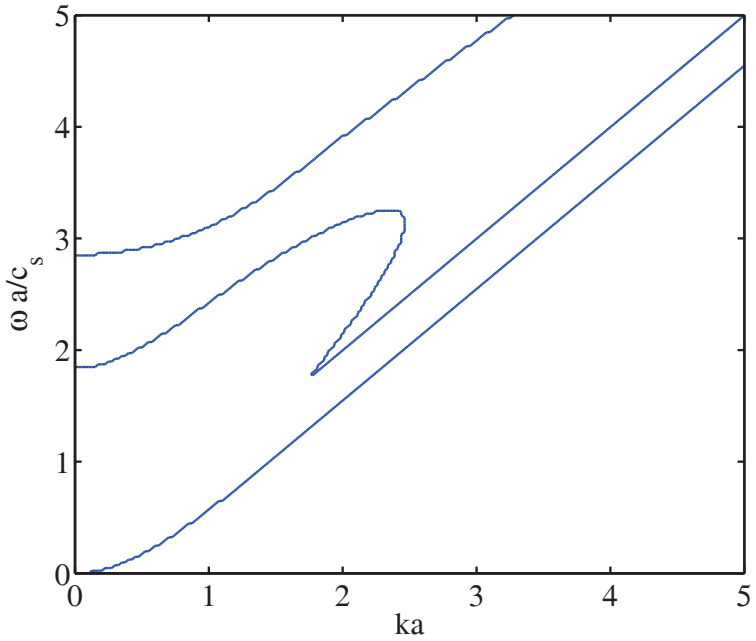

Figure 2.10: Zoom on the low frequency of the dispersion curves for $n = 1$.

The dispersion curves for $n = 1$ are displayed in Fig. 2.9 and the phase velocity in Fig. 2.11. The same results as in Pao and Mindlin [73], Treyssède [101] are found, except for the low frequency behavior of the second branch. This behavior is shown in the Fig. 2.10. It has to be mentioned here that the same feature happens for all odd n. But no reason for the difference between our computation and [73, 101] has been found at this time.

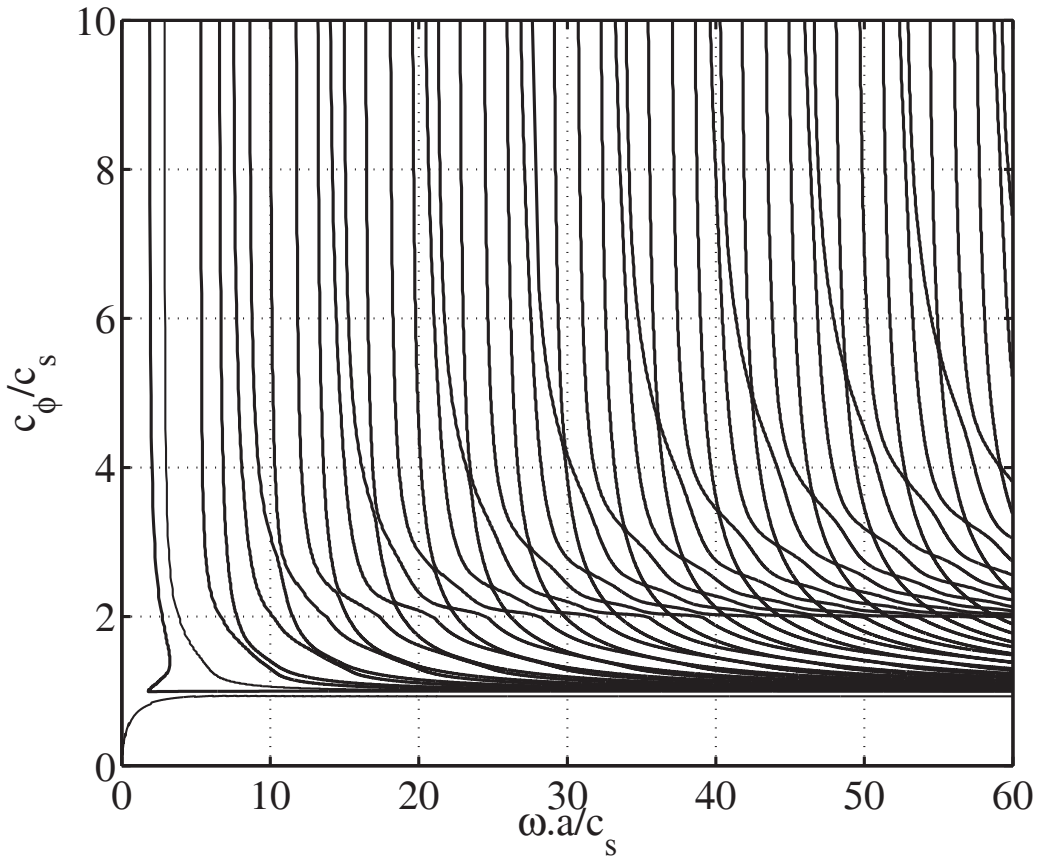

Figure 2.11: Velocity phase $c_\phi = \frac{\omega(k)}{k}$ for $n = 1$.

The dispersion curves have the same asymptotic behavior when $k \to \infty$ as the longitudinal ones. All the modes have a phase velocity which tends to the transverse velocity c_s except the first one which tends to the Rayleigh surface wave velocity. It seems also to exist an asymptote for the highest modes of the same kind as for the longitudinal modes, that is $\omega = c_l k$, on which the modes are non dispersive. The mode shapes (Fig. 2.12) provide further informations. For high values of ω, some modes have a bending behavior (like the mode displayed on the top left of Fig. 2.12). Other are typically shearing modes (like the mode displayed on the top right of Fig. 2.12). It suggests that at high frequencies, the bending and shear modes are separated. Finally the Rayleigh mode exhibits disturbance in the vicinity of the lateral surface. It seems that there is no criteria allowing to predict the class of a mode directly from the dispersion curves. The modes have to be plotted in order to be classified.

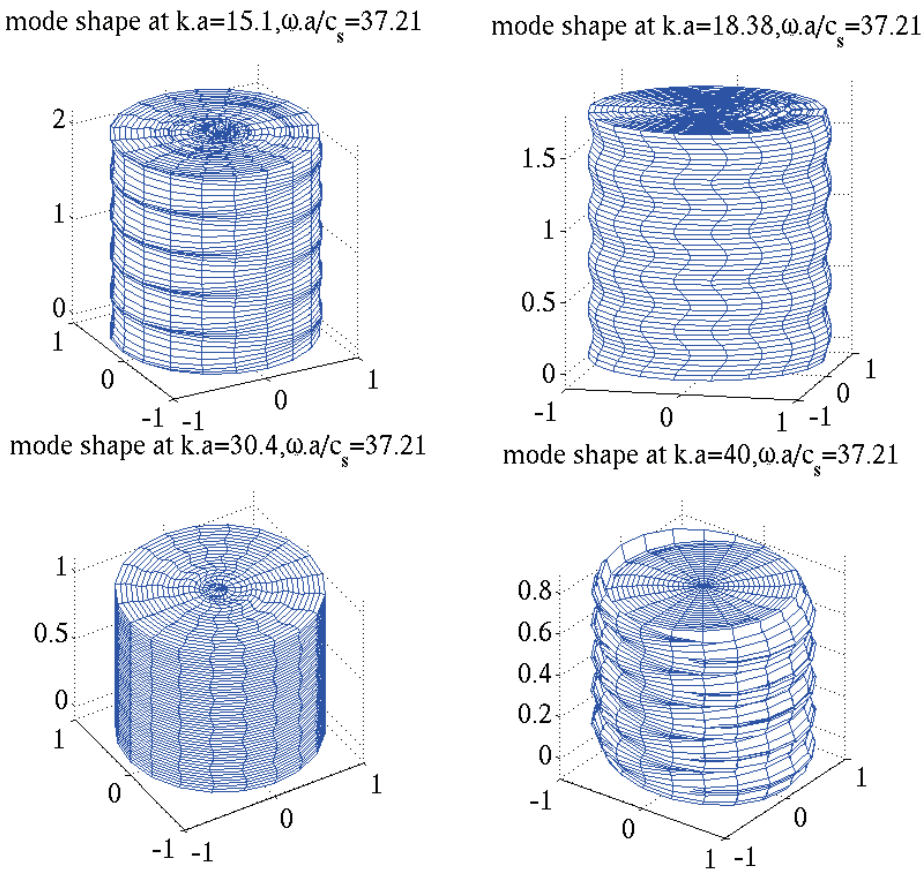

Figure 2.12: Shape of some flexural modes for $n = 1$. The top left corresponds to a purely bending mode, the top right to a purely shear mode, the bottom left to a radial disturbance and the bottom right to a Rayleigh like mode.

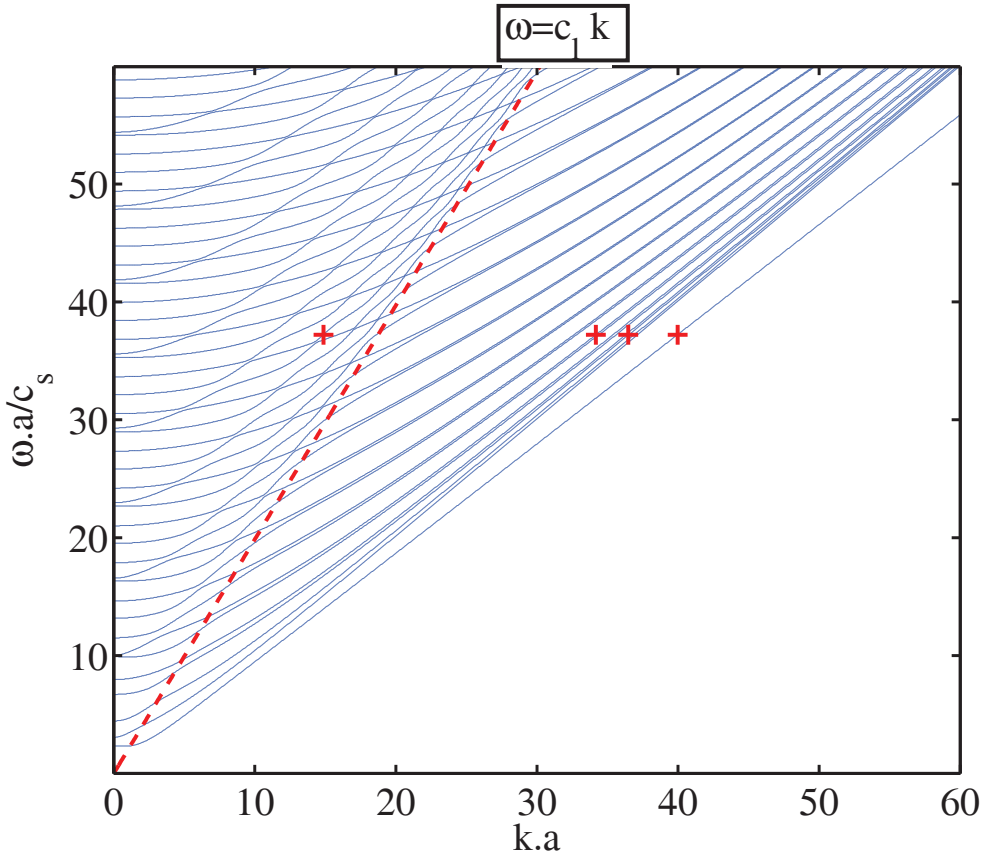

Figure 2.13: Dispersion curves for $n = 2$; the crosses denote the dispersion points for the plot of the modes in Fig. 2.15.

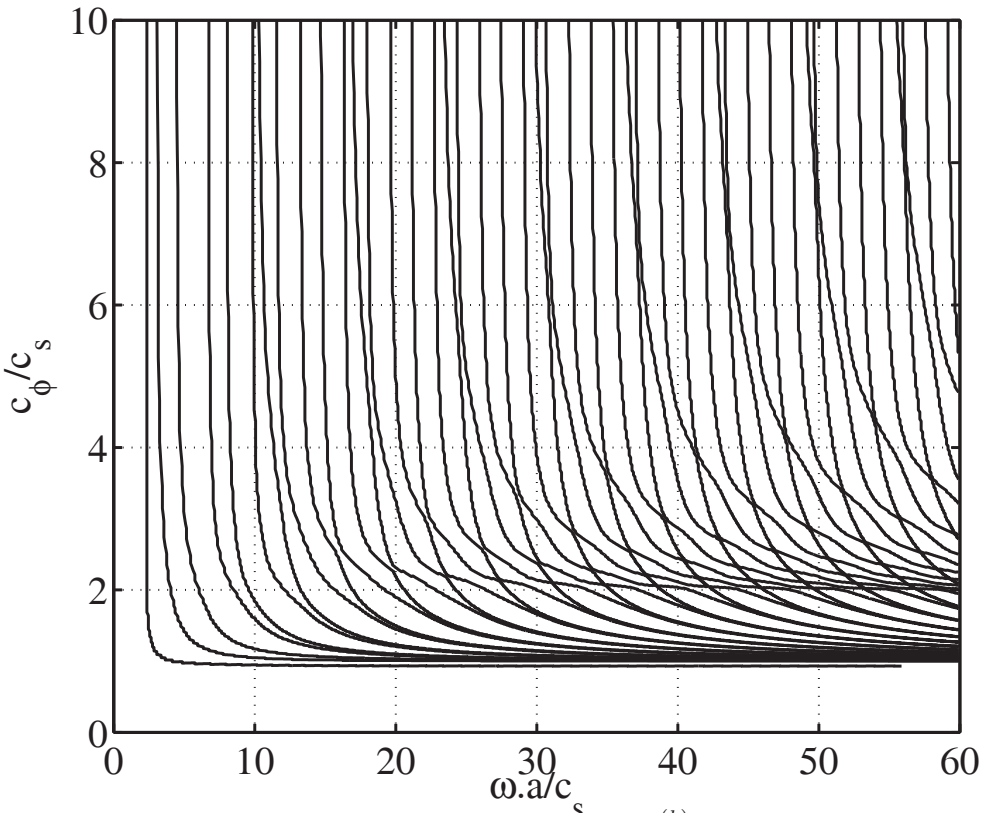

Figure 2.14: Phase velocity $c_\phi = \frac{\omega(k)}{k}$ for $n = 2$.

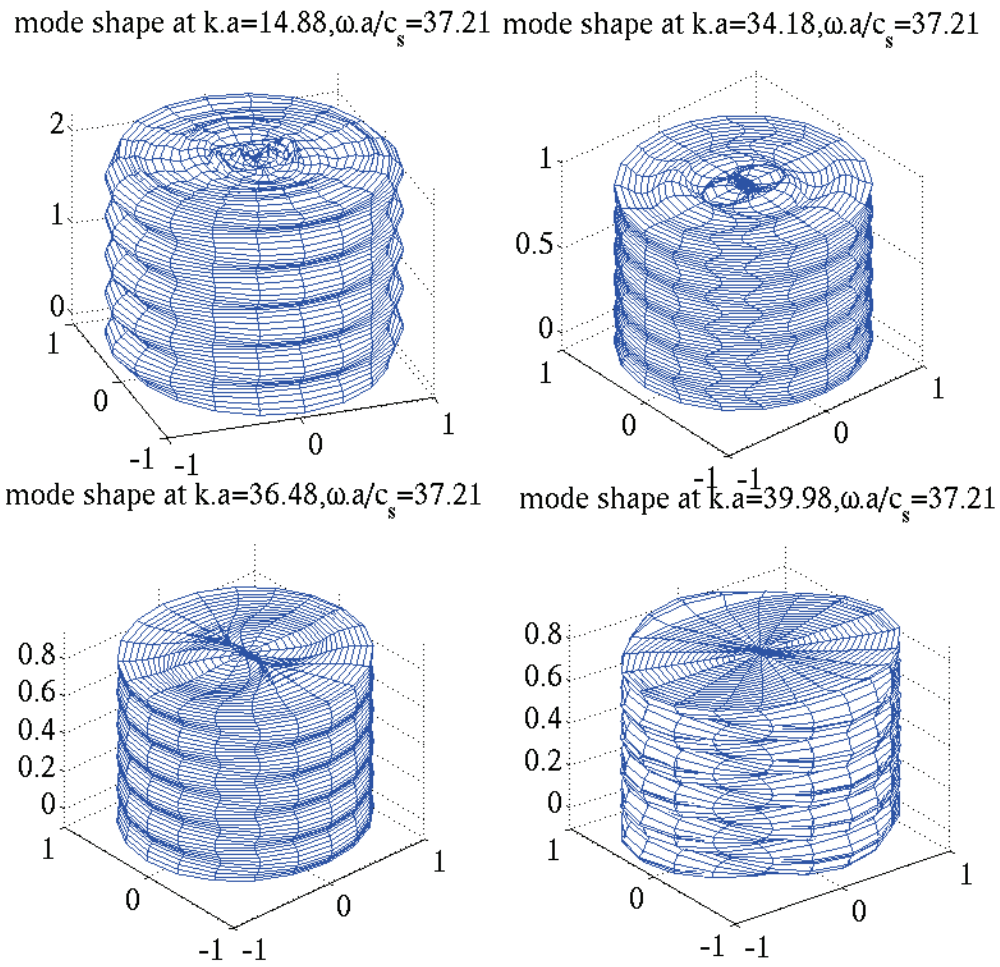

Figure 2.15: Shape of some flexural modes for $n = 2$. The top left shape corresponds to a mainly bending mode, the bottom right corresponds to a Rayleigh mode, and the two others correspond to shear modes with second order radial disturbance.

These dispersion curves for $n = 2$ (Fig. 2.13) are the same as those found in [114]. The dispersion plots for higher values of n present the same features. The mode shapes are separated into four groups: the ones having a second order flexural behavior, the ones having a shearing behavior, the ones with a motion along $\hat{\boldsymbol{e}}_\theta$, and the Rayleigh mode with a displacement in the vicinity of the boundary. Moreover it can be observed that the cut-off frequency (the frequency at which at least one mode becomes propagative) increases with n; it means that for any frequency, even high, only a finite number of modes up to a given order n are likely to propagate. Fig. 2.16 displays the evolution of this cut-off frequency (denoted by ω_o) versus the motion number n. The blue line is the approximation of the cut-off frequency as a first degree polynomial function; its fitted equation is $(0.9725n + 0.5882)$. The group velocity of the flexural modes have not be displayed here because they are very oscillating. They are indeed plotted by derivation of the dispersion curves, and for high value of n, the dispersion curves begin very sensitive to numerical error and are not smooth at a local scale although they give good agreement at large scale.

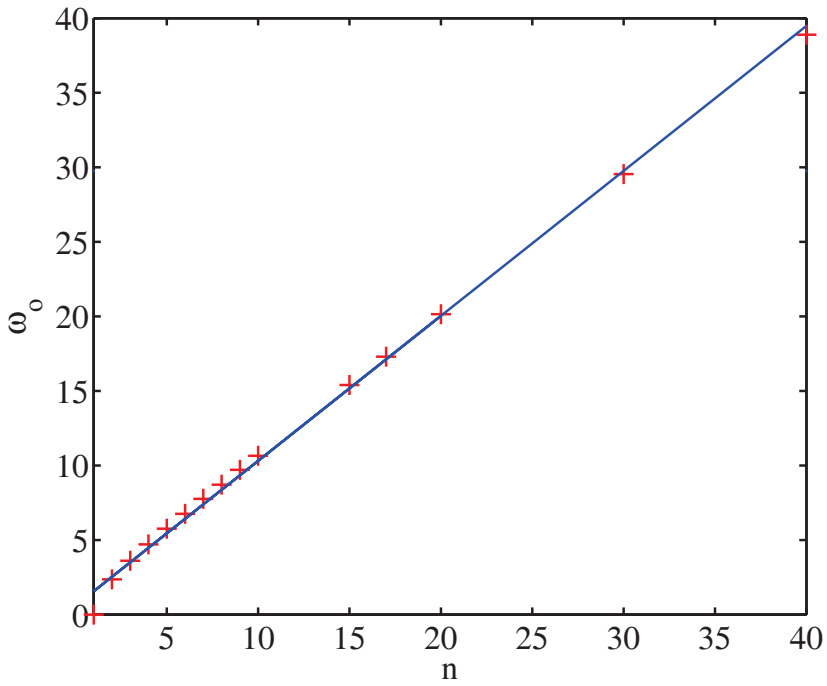

Figure 2.16: Evolution of the cut-off frequency with the number of mode family n.

On Fig. 2.17, the dispersion curves are also plotted for purely imaginary values of k. The same kind of plots as those obtained in the aforementioned references are retrieved. It highlights the transition from evanescent to propagative behavior of the modes. Moreover some propagating modes are in fact coupled in the imaginary part of the figure. The others arise from imaginary branches. Veering effects between evanescent modes are noticeable in this plot. The same kind of figures hold for all values of n. The mode's shapes have been plotted for a single value of ω and it could be interesting to study the evolution of the shape according to ω in a future work.

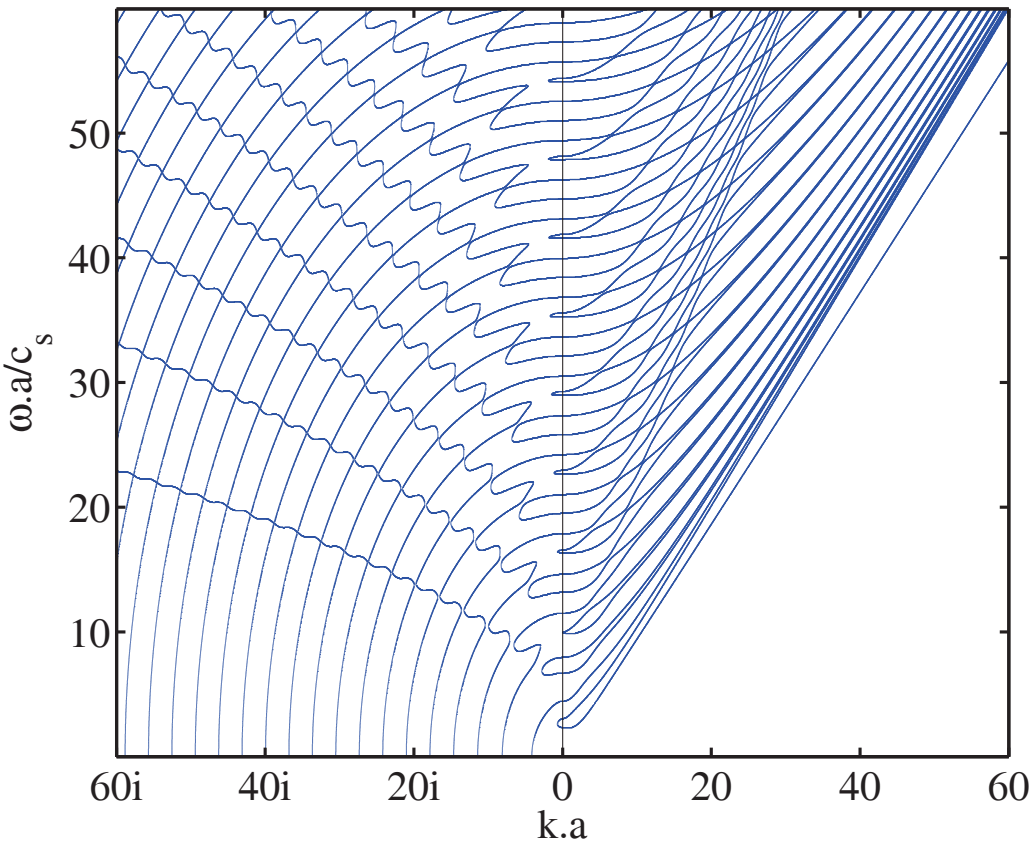

Figure 2.17: Dispersion curves for $n = 2$ for real and purely imaginary value of ka.

2.2 Approximate kinematical theories for waves in a beam

The previous analytical model is impractical for the analysis of beam trusses, because at high frequency a lot of different modes propagate. Hence kinematically reduced beam models are considered for engineering applications. An elementary theory for beams was developed by Euler in 1744 for the static case and by Bernoulli in 1751 for the transient case [102]. At that time, mechanical theories were not directly applied to practical matter, but only for illustration purpose of mathematical concept. The first application of this theory was done by Eiffel in the design of the Eiffel tower (1889). From this elementary theory, a lot of authors developed more refined model. In this part, different reduced beam models will be outlined and confronted to the exact Lamb model of the previous section.

To outlined the reduced kinematics, it is first necessary to define the notion of the neutral fiber of a beam. This line follows the geometrical centers (or centroid) of the beam cross-sections. Mathematically it is taken as the reference point, such that:

$$\int_{\Sigma} \boldsymbol{x}_{\perp} d\Sigma = \mathbf{0}\,, \tag{2.24}$$

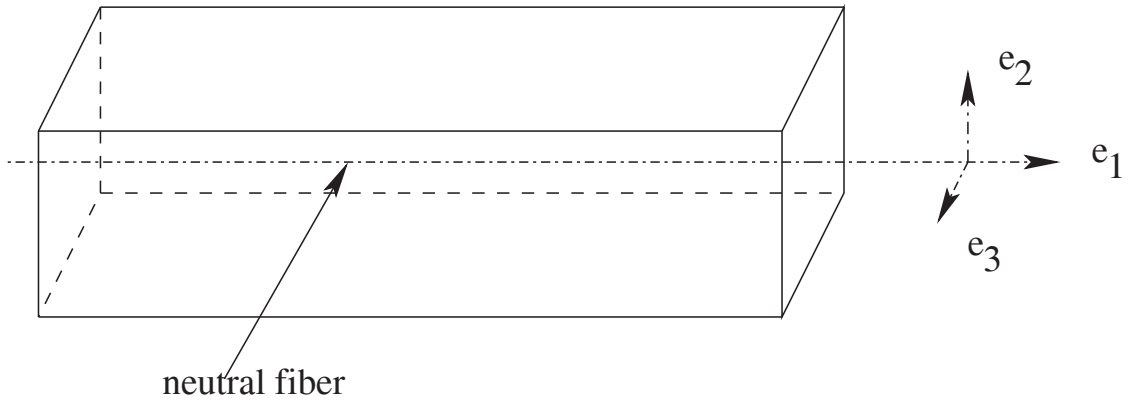

Figure 2.18: An example of straight beam with a rectangular cross-section.

where $\boldsymbol{x}_\perp = \boldsymbol{x} - (\boldsymbol{x}\cdot\hat{\boldsymbol{e}}_1)\hat{\boldsymbol{e}}_1$ is the coordinate of a point in the local cross-section basis, Σ is the cross-section of the beam, and $\hat{\boldsymbol{e}}_1$ is the axis tangent to the neutral fiber. In the following of this chapter, the orthogonal projection of any vector $\boldsymbol{a}$ is defined by $\boldsymbol{a}_\perp = (\boldsymbol{I} - \hat{\boldsymbol{e}}_1 \otimes \hat{\boldsymbol{e}}_1)\boldsymbol{a}$. Under the assumptions of a doubly symmetric distribution of the mass over the cross-section, the geometrical center is coincident with the center of mass $\boldsymbol{x}_m$ defined by:

$$\int_\Sigma \rho(\boldsymbol{x}_\perp - \boldsymbol{x}_m) d\Sigma = \boldsymbol{0}\,.$$

In the same way, it is assumed that all the mechanical parameters have a doubly symmetric distribution over the cross-section. Moreover in the remaining of this chapter, the beam is assumed to be straight and the basis will be denoted by $\hat{\boldsymbol{e}}_i\,, 1 \leq i \leq 3$. The corresponding coordinates are $(x\,, y\,, z)$, thus x locates the center of the cross-section on the neutral fiber. The axes $\hat{\boldsymbol{e}}_2$ and $\hat{\boldsymbol{e}}_3$ are supposed to be the main axes of the beam that is they are axes of symmetry of the cross-section (see Fig. 2.18 for an illustrative example).

2.2.1 Euler-Bernoulli kinematics

In the Euler theory it is assumed that the cross-sections of the beam have only rigid body motions. The displacement field is thus separated into the contributions of:

- the translation of the neutral fiber $\boldsymbol{u}_c(x,t) = u_c(x,t)\hat{\boldsymbol{e}}_1 + \boldsymbol{u}_\perp(x,t)$, where $u_c(x,t)$ is the axial displacement and $\boldsymbol{u}_\perp$ is the transverse displacement,
- and the rotation of the cross-sections about the neutral fiber:

$$\boldsymbol{\theta}(x,t) = \sum_{i=1}^{3} \theta_i(x,t)\hat{\boldsymbol{e}}_i\,.$$

The displacement field is thus expressed as:

$$\boldsymbol{u}(\boldsymbol{x},t) = \boldsymbol{u}_c(x,t) + \boldsymbol{\theta}(x,t) \times \boldsymbol{x}_\perp\,. \tag{2.25}$$

The linearized strain tensor reads:

$$\boldsymbol{\epsilon} = (\boldsymbol{u}_c' - \boldsymbol{\theta} \times \hat{\boldsymbol{e}}_1 + \boldsymbol{\theta}' \times \boldsymbol{x}_\perp) \otimes_s \hat{\boldsymbol{e}}_1\,, \tag{2.26}$$

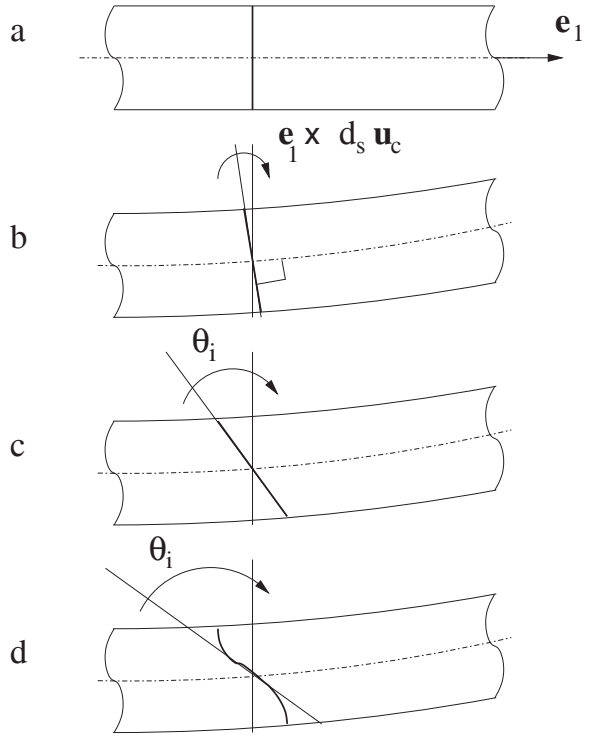

Figure 2.19: Disturbance of the beam for several theories: (a)-beam at rest, (b)-Euler theory, (c)-Timoshenko theory, (d)-Levinson theory (the curved segment is the deformed cross-section).

where $\boldsymbol{a} \otimes_s \boldsymbol{b}$ denotes the symmetrized part of the tensor product $\boldsymbol{a} \otimes \boldsymbol{b}$ and $\boldsymbol{a}'$ is the partial derivative of $\boldsymbol{a}$ with respect to the abscissa x. In the Euler-Bernoulli theory, the cross-sections are assumed to remain normal to the neutral fiber during the motion. Thus the rotation vector of the cross-section becomes:

$$\boldsymbol{\theta} = \hat{\boldsymbol{e}}_1 \times \boldsymbol{u}'_\perp + \theta_1 \hat{\boldsymbol{e}}_1 \,, \tag{2.27}$$

where θ_1 is the angle due to torsion. It is worth noticing that the transverse shear strain defined by $(\boldsymbol{u}'_\perp - \boldsymbol{\theta} \times \hat{\boldsymbol{e}}_1) \otimes_s \hat{\boldsymbol{e}}_1$ vanishes in this case. The displacement of the cross-section in this case is displayed on Fig. 2.19 -(b).

The Hooke's law relating the small strain tensor $\boldsymbol{\epsilon}$ to the stress tensor $\boldsymbol{\sigma}$ is given by:

$$\boldsymbol{\epsilon} = \frac{1+\nu}{E}\boldsymbol{\sigma} - \frac{\nu}{E}\,\mathrm{Tr}(\boldsymbol{\sigma})\boldsymbol{I} \,, \tag{2.28}$$

where ν is the Poisson's ratio. On account of the slenderness of the beam, the hypothesis $\mathrm{Tr}(\boldsymbol{\sigma}) = \sigma_{11}$ is often invoked. Using Eq. (2.28) and Eq. (2.26), the stress vector acting on the cross-section of normal $\hat{\boldsymbol{e}}_1$ is then given by:

$$\boldsymbol{\sigma}\hat{\boldsymbol{e}}_1 = E(u'_c\hat{\boldsymbol{e}}_1 + (\hat{\boldsymbol{e}}_1 \times \boldsymbol{u}''_\perp) \times \boldsymbol{s}_\perp) + \mu\theta'_1\hat{\boldsymbol{e}}_1 \times \boldsymbol{x}_\perp + \boldsymbol{\tau}_\perp \,, \tag{2.29}$$

where $\boldsymbol{\tau}_\perp$ is an additional shear stress vector ($\boldsymbol{\tau}_\perp \cdot \hat{\boldsymbol{e}}_1 = 0$). This stress vector (2.29) can be integrated over the cross-section in order to remove the $\boldsymbol{x}_\perp$ dependency. The axial netforce

and netmoments are then defined as:

$$\begin{aligned} T_1 &= \int_\Sigma \boldsymbol{\sigma} : \hat{\boldsymbol{e}}_1 \otimes \hat{\boldsymbol{e}}_1 dS = ES u_c' \,, \\ \boldsymbol{M} &= \int_\Sigma \boldsymbol{x}_\perp \times \boldsymbol{\sigma} \hat{\boldsymbol{e}}_1 dS = E\boldsymbol{J}(\hat{\boldsymbol{e}}_1 \times \boldsymbol{u}_\perp'') + \mu \theta_1' \boldsymbol{J}(\hat{\boldsymbol{e}}_1) \,, \end{aligned} \tag{2.30}$$

where the geometrical inertia tensor is given by:

$$\boldsymbol{J} = \int_\Sigma (||\boldsymbol{x}_\perp||^2 \boldsymbol{I} - \boldsymbol{x}_\perp \otimes \boldsymbol{x}_\perp) dS \,.$$

The shear forces:

$$\boldsymbol{T}_\perp = \int_\Sigma (\boldsymbol{I} - \hat{\boldsymbol{e}}_1 \otimes \hat{\boldsymbol{e}}_1) \boldsymbol{\sigma}(\hat{\boldsymbol{e}}_1) dS \,,$$

can be found by equilibrium of the netmoments, that is:

$$\boldsymbol{T}_\perp = \hat{\boldsymbol{e}}_1 \times \left(- \int_\Sigma \boldsymbol{x}_\perp \times \rho \ddot{\boldsymbol{u}} dS + \boldsymbol{M}' \right) .$$

From Eq. (2.30), the balance of momentum (1.1) integrated over the cross-section gives:

$$\begin{aligned} \rho \ddot{u}_c &= E u_c'' \,, \\ \rho \ddot{\theta}_1 &= \mu \theta_1'' \,, \\ \rho S \ddot{\boldsymbol{u}}_\perp &= -E\boldsymbol{J}(\boldsymbol{u}_\perp'')'' \,. \end{aligned} \tag{2.31}$$

with ρ the material density of the beams and assuming that $\rho \boldsymbol{J} \ddot{\boldsymbol{u}}_\perp'' \approx 0$. As $\hat{\boldsymbol{e}}_2$ and $\hat{\boldsymbol{e}}_3$ are principle axes of the cross-section, then the inertia tensor $\boldsymbol{J}$ is diagonal and the last two equations of Eq. (2.31) are uncoupled. It is indeed valid for the symmetric cross-section considered here. This set of equations allows to perform a dispersion analysis of this model of kinematics. The solution of the system (2.31) is assumed to be a plane wave of the form $Ae^{i(\omega t - kx)}$. Inserting it into the system (2.31) leads to the dispersion equation of the Euler-Bernoulli beams:

$$\begin{aligned} &\omega = c_{\mathrm{P}} k \,, && \text{for the longitudinal motion, } \textit{i.e.} \text{ the displacement along } \hat{\boldsymbol{e}}_1 \,, \\ &\omega = c_s k \,, && \text{for the torsional motion, } \textit{i.e.} \text{ the rotation along } \hat{\boldsymbol{e}}_1 \,, \\ &\omega = \sqrt{\frac{EJ_i}{\rho S}} k^2 \,, && \text{for the flexural motions, } \textit{i.e.} \text{ the rotations along } \hat{\boldsymbol{e}}_i \,, i = 2, 3 \,, \end{aligned}$$

where the wave velocities c_{P} and c_s are defined by Eq. (1.8) and Eq. (2.23), and $J_i = \boldsymbol{J} : \hat{\boldsymbol{e}}_i \otimes \hat{\boldsymbol{e}}_i$. From this set of equations emerges the main limitation of this theory. As $k \to \infty$, the phase and group velocity go to infinity for the flexural motions, thus allowing the propagation of energy at speeds approaching infinity [78, 98, 99]. This is in contraction with the study of wave in three-dimensional medium made in Sect. 1.1, where the maximum velocity was c_l. Moreover this model overestimates the natural frequencies, and is not accurate for thick beams [106].

2.2.2 Timoshenko kinematics

From this classical beam theory, authors have tried to remove some hypotheses to have more refined and accurate models. Timoshenko proposed modified kinematics which relaxed the hypothesis on the cross-section being normal to the neutral fiber by accounting for the effect of shear strain as well as the effect of rotary inertia [99]. The kinematical assumption is unchanged:

$$\boldsymbol{u} = \boldsymbol{u}_c + \boldsymbol{\theta} \times \boldsymbol{x}_\perp \,, \tag{2.32}$$

but without the restrictive hypothesis on the orthogonality of the cross-section with respect to the neutral fiber given by Eq. (2.27). The rotation of the cross-section of the beam is displayed on Fig. 2.19-(c) in this case. The cross-section is still assumed to be a rigid body. The rigidity assumption is valid in practice for slender, thin beams or rods, and also for moderately thick beams of many structural materials [49]. It leads to the balance equations:

$$\begin{aligned} \rho \ddot{u}_c &= E u_c'' \,, \\ \rho \ddot{\theta}_1 &= \mu \theta_1'' \,, \\ \rho \ddot{\boldsymbol{u}}_\perp &= \kappa\mu(\boldsymbol{u}_\perp'' + \hat{\boldsymbol{e}}_1 \times \boldsymbol{\theta}_\perp') \,, \\ \rho \boldsymbol{J} \ddot{\boldsymbol{\theta}}_\perp &= E\boldsymbol{J}\boldsymbol{\theta}_\perp'' + \kappa\mu S(\hat{\boldsymbol{e}}_1 \times \boldsymbol{u}_\perp' - \boldsymbol{\theta}_\perp) \,. \end{aligned} \tag{2.33}$$

The parameter κ is called the Timoshenko parameter or the shear correction factor in the literature. In the Timoshenko theory, the cross-section is assumed to remain flat, but this is in contradiction with the boundary conditions on the lateral surface of the beam: $\boldsymbol{\sigma}(\boldsymbol{x})\hat{\boldsymbol{n}}|_{\boldsymbol{x}\in\partial\Sigma} = \boldsymbol{0}$. Thus κ is introduced in order to take into account the non-uniform distribution of the shear stress on the cross-section [51]. There are several ways to obtain this coefficient. One of them is to solve:

$$\int_\Sigma \sigma_{1i} dS = \kappa S \mu \theta_i \,, \quad i = 2, 3 \,, \tag{2.34}$$

defining thus κ as the ratio between the average of the three-dimensional distribution of the shear stresses to the shear forces of the dedicated kinematics. Other authors compare the shear forces given by Timoshenko beam theory to the asymptotic solution of the Saint-Venant equations as done by Stephen [93]. Other studies of this parameter can be found in Cowper [20], Pai and Schulz [72], Renton [81], where it is shown that it depends on the Poisson ratio ν and on the shape of the cross-sections. For example, for a rectangular cross-section, it may be approximated by [20]:

$$\kappa = \frac{5(1+\nu)}{6+5\nu} \,, \tag{2.35}$$

and for a circular cross-section by:

$$\kappa = \frac{6(1+\nu)^2}{7+12\nu+4\nu^2} \,. \tag{2.36}$$

Other authors proposed a method based on a finite element solution of the bending problem (see for example [35]). This numerical approach allows to know the shear reduction coefficient for all shapes of cross-sections.

It can be noticed that compared to the Euler-Bernoulli theory, the shear ($\boldsymbol{u}_\perp$) and flexural ($\boldsymbol{\theta}_\perp$) motions get coupled. The frequency spectrum of this equation has been extensively investigated in the aforementioned papers (see for example [94]). From Eq. (2.33), it is possible to derive the equation of motion of the transverse displacement $\boldsymbol{u}_\perp$ given by:

$$\left(E\boldsymbol{J}(\boldsymbol{u}_\perp'')\right)'' + \rho S\boldsymbol{u}_\perp'' - \rho\boldsymbol{J}\left(1+\frac{E}{\kappa\mu}\right)\ddot{\boldsymbol{u}}_\perp'' + \frac{\rho^2\boldsymbol{J}}{\kappa\mu}\ddot{\ddot{\boldsymbol{u}}}_\perp = 0\,. \tag{2.37}$$

As the cross-section is symmetric, these equations are uncoupled and the corresponding dispersion relation is thus:

$$EJ_ik^4 - \rho S\omega^2 - \rho J_i\left(1+\frac{E}{\kappa\mu}\right)k^2\omega^2 + \frac{\rho^2 J_i}{\kappa\mu}\omega^4 = 0\,, \quad \text{for } i=2,3\,. \tag{2.38}$$

Its roots are:

$$k_{i\pm}^2 = \frac{\omega^2}{2}\left(\frac{1}{c_{\mathrm{T}}^2}+\frac{1}{c_{\mathrm{P}}^2}\right) \pm \sqrt{\frac{\omega^4}{4}\left(\frac{1}{c_{\mathrm{P}}^2}-\frac{1}{c_{\mathrm{T}}^2}\right)^2 + \frac{S}{J_ic_{\mathrm{P}}^2}\omega^2}\,, \quad \text{for } i=2,3\,, \tag{2.39}$$

where

$$c_{\mathrm{T}} = \sqrt{\frac{\kappa\mu}{\rho}}\,, \tag{2.40}$$

is the Timoshenko transverse velocity. The wave corresponding to k_{i+} is propagative for every frequency while the wave having the wavenumber k_{i-} has a cut-off frequency ω_{ci}, at which the wavenumber becomes real and thus a wave can propagate. It is given by:

$$\omega_{ci} = c_{\mathrm{T}}\sqrt{\frac{S}{J_i}}\,. \tag{2.41}$$

Moreover when $\omega \to \infty$, $k_{i+} \to \frac{\omega}{c_{\mathrm{T}}}$ and $k_{i-} \to \frac{\omega}{c_{\mathrm{P}}}$. It means that the modes become non-dispersive in the HF range and that the bending and shear motion are separated in this range according to the observation made on the Lamb spectrum (see Sect. 2.1.2.3). A comparison between the Timoshenko theory and the Euler-Bernoulli theory has been conducted by Han *et al.* [37] that shows the improvements brought by the Timoshenko theory. Comparisons between the dispersion curves of the Timoshenko theory and those coming from the analysis of the Lamb spectrum are shown on Fig. 2.20 for the longitudinal mode and on Fig. 2.22 for the bending/shear modes. Fig. 2.21 and Fig. 2.23 shows a zoom of these curves in the frequency range where the Timoshenko dispersion curves match well the Lamb ones.

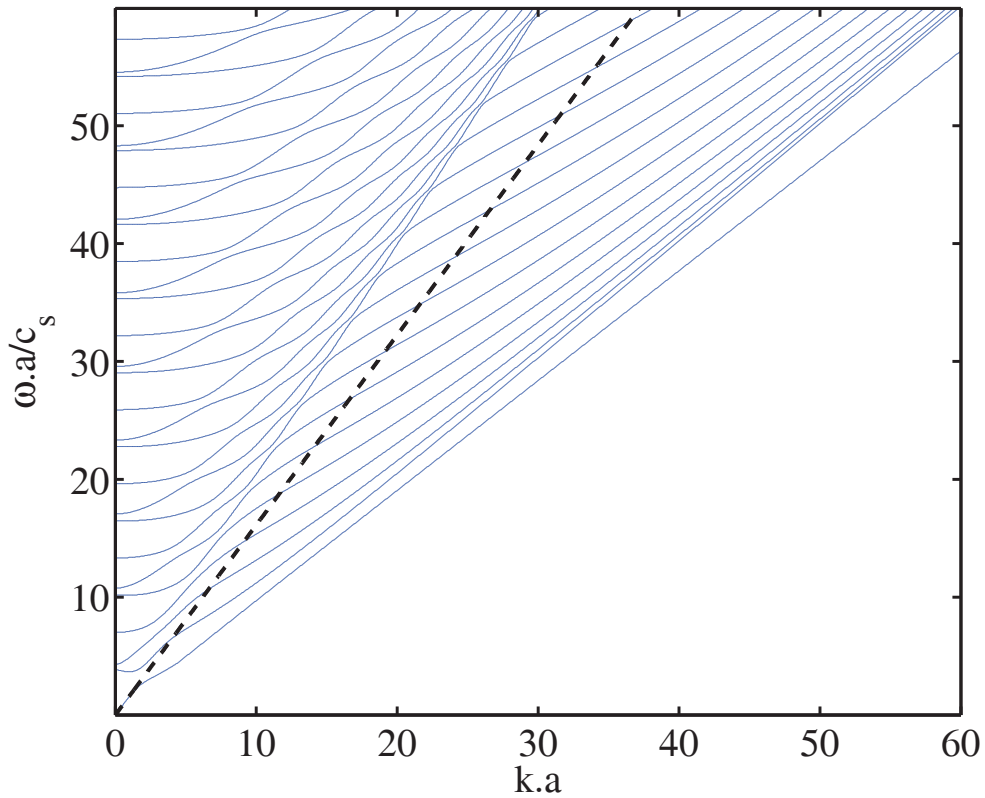

Figure 2.20: Comparison of the longitudinal spectrum of a cylindrical waveguide (solid blue lines) and the longitudinal dispersion curve for a Timoshenko beam (dashed black line).

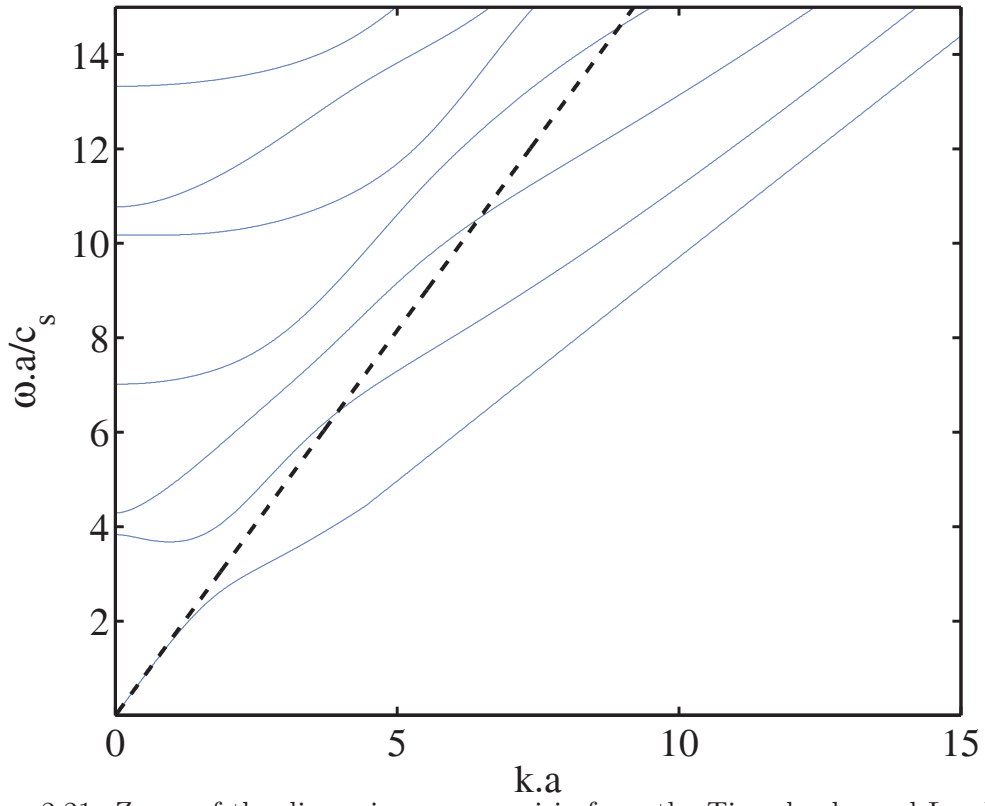

Figure 2.21: Zoom of the dispersion curves arisig from the Timoshenko and Lamb models for the longitudinal mode.

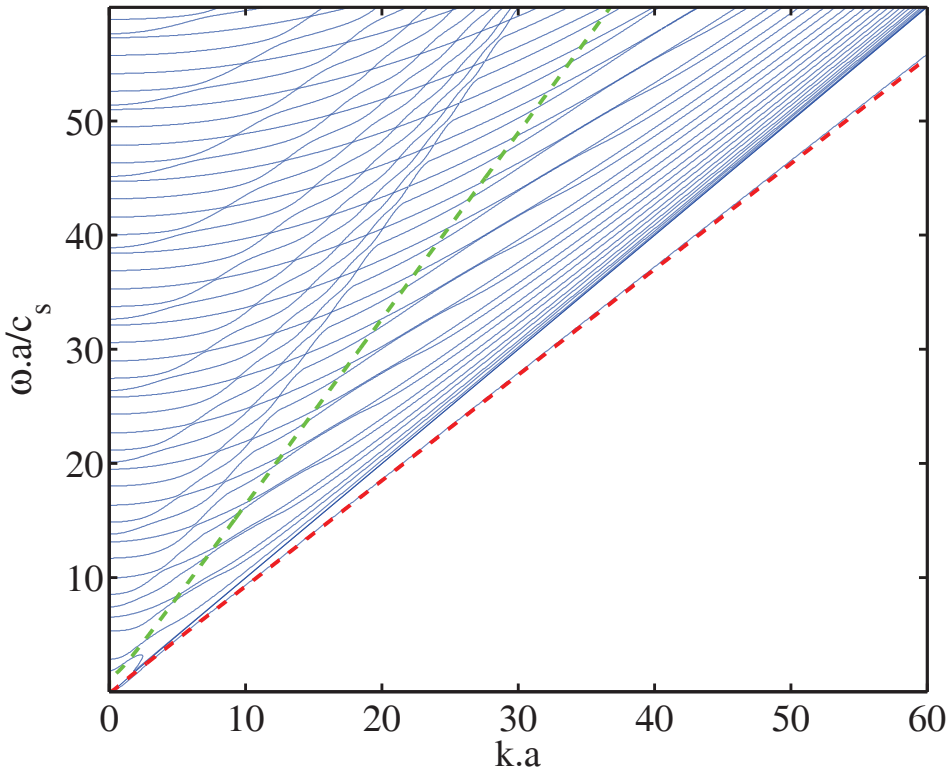

Figure 2.22: Comparison of the flexural spectrum of a cylindrical waveguide for $n = 1$ (solid blue lines), the dispersion curve of the bending mode (dashed green line), and the dispersion curve of the shear modes (dashed red line) for a Timoshenko beam.

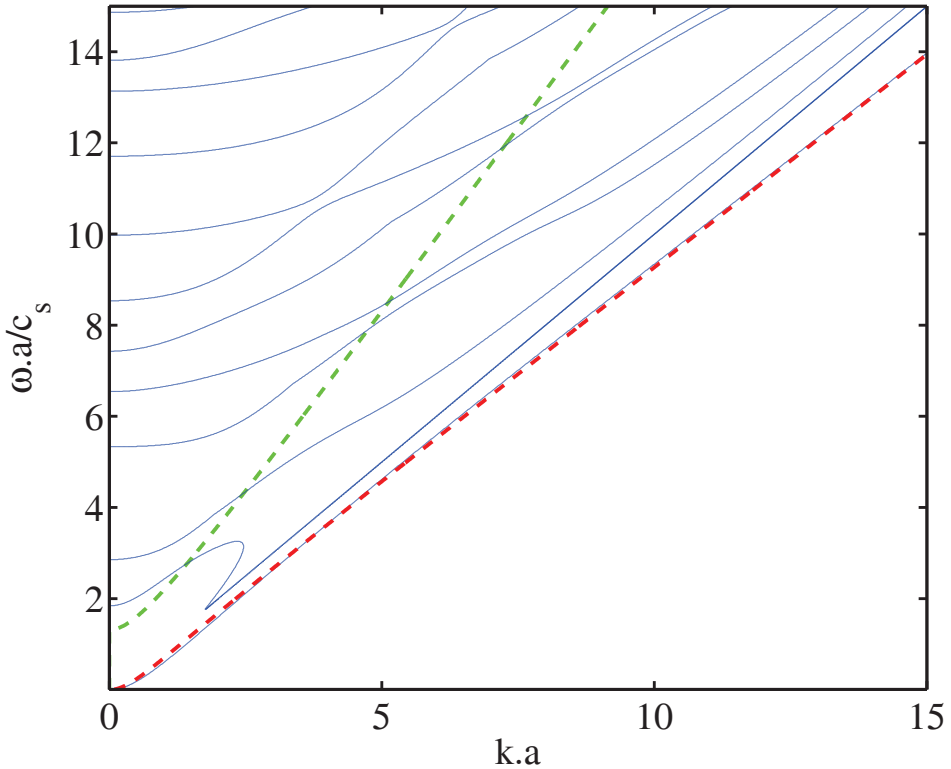

Figure 2.23: Zoom of the dispersion curves arising from the Timoshenko and Lamb models for the bending and shear modes.

The observation of Fig. 2.21 confirms that, in the low frequency range, the behavior of the first longitudinal mode is well retrieved by the Timoshenko theory. However beyond $\omega a/c_s \simeq 4$ it becomes different. It is explained by the emergence of high order longitudinal modes on which the energy spreads. Nevertheless it can be noticed that the group velocity of the longitudinal mode predicted by the Timoshenko theory is between the minimal and maximal value of the group velocity predicted by the Pochhammer spectrum (see Fig. 2.7), indeed $0 \leq c_{\mathrm{P}} \leq c_l$. For the flexural modes, the difference between the lowest flexural mode and the Timoshenko mode associated with k_{i+} is indistinguishable. The shear velocity modified by the shear reduction factor is indeed very close to the Rayleigh wave speed. The second branch of the Timoshenko theory does not match well the cut-off frequency of the Pochhammer-Chree spectrum. In order to correct this slight discrepancy, Doyle [23] suggests to introduce a new correction coefficient κ_2 in order to separate the effect of the rotary inertia from the effect of shear. Hence the equation of 2.33 for the transverse displacement is modified to:

$$\rho \boldsymbol{J} \kappa_2 \ddot{\boldsymbol{\theta}}_\perp = E \boldsymbol{J} \boldsymbol{\theta}''_\perp + \kappa \mu S (\hat{\boldsymbol{e}}_1 \times \boldsymbol{u}'_\perp - \boldsymbol{\theta}_\perp) \,, \tag{2.42}$$

all the other equations remaining the same. The dispersion equation for the shear-bending motion is modified accordingly:

$$E J_i k^4 - \rho S \omega^2 - \rho J_i \left(\kappa_2 + \frac{E}{\kappa \mu} \right) k^2 \omega^2 + \frac{\kappa_2 \rho^2 J_i}{\kappa \mu} \omega^4 = 0 \,, \quad \text{for } i = 1, 2 \,. \tag{2.43}$$

Hence it is is possible to derived the modified cut-off frequency, given by:

$$\omega_{ci} = \sqrt{\frac{\kappa \mu S}{\rho J_i \kappa_2}} \,.$$

Matching this result with the cut-off frequency of the second first order flexural mode, allows to compute κ_2. The HF velocity of the bending waves becomes:

$$c_b = \sqrt{\frac{E}{\kappa_2 \rho}} \,.$$

In the case of a circular cross-section of ray a, $\frac{\omega_{ci} a}{c_s} \simeq 1.83$ leads to:

$$\kappa_2 = \frac{\kappa \mu S a^2}{\rho \boldsymbol{J} \cdot \hat{\boldsymbol{e}}_r (1.83 c_s)^2} \,.$$

Moreover, as in the case of the longitudinal waves, the velocity of the bending, shear waves stays in the limit of the maximal and minimal value of the ones predicted by the Pochhammer-Chree model. It could be interesting in a future work to study how the Timoshenko modes are projected on the Lamb modes in order to quantify the contribution of each Lamb modes in the Timoshenko theory.

2.2.3 Higher order kinematics

Many authors have discussed the accuracy of the Timoshenko theory in the HF range (see for example the paper [106] and references therein). Its main limitation lies in the

kinematical assumption. Indeed it does not allow any warping of the cross-section that would correspond to other propagative modes and thus velocities can be misestimated. Moreover, this kinematics does not fulfil the boundary condition on the lateral surface of the beam. Some authors proposed to enhance the kinematics in order to be able to study such motions. High order beam kinematics just refine the Timoshenko beam kinematics by adding degrees of freedom in a polynomial form. For example Carrera *et al.* [15] assumed that a N degrees of freedom displacement reads:

$$\boldsymbol{u} = \sum_{i=1}^{N} F_i \boldsymbol{u}_i \,, \tag{2.44}$$

where F_i is a polynomial function of $\boldsymbol{x}_\perp$ in the cross-section, and $\boldsymbol{u}_i$ are vectors of degrees of freedom. It is possible to recover the kinematics of the Timoshenko beam setting:

$$\begin{aligned}
&F_1 = 1\,, && \boldsymbol{u}_1 = u_c\hat{\boldsymbol{e}}_1 + v_c\hat{\boldsymbol{e}}_2 + w_c\hat{\boldsymbol{e}}_3\,,\\
&F_2 = y\,, && \boldsymbol{u}_2 = \theta_1\hat{\boldsymbol{e}}_3\,,\\
&F_3 = -y\,, && \boldsymbol{u}_3 = \theta_3\hat{\boldsymbol{e}}_1\,,\\
&F_4 = z\,, && \boldsymbol{u}_4 = \theta_2\hat{\boldsymbol{e}}_1\,,\\
&F_5 = -z\,, && \boldsymbol{u}_5 = \theta_1\hat{\boldsymbol{e}}_2\,.
\end{aligned}$$

The main drawback of this method is that the lateral boundary conditions are not respected. Thus, as in the case of the Timoshenko kinematics, it is necessary to consider shear reduction factors for each degree of freedom. Some authors alleviate this shortcoming by choosing the kinematics according to the boundary conditions. Ghugal and Shimpi [32] performed a review of such second and third order theories. A two-dimensional kinematics has been developed by Levinson [56] or Reddy *et al.* [79]:

$$u(x,y,t) = u_c(x,t) + yv_c'(x,t) + y\left[1 - \frac{4}{3}\left(\frac{y}{h}\right)^2\right]\theta_1(x,t)\,, \tag{2.45}$$

where $v_c = \boldsymbol{u}_\perp \cdot \hat{\boldsymbol{e}}_2$. The corresponding displacement of this theory is sketched on Fig. 2.19-d. Eisenberg performed a frequency study of this displacement [24]. His conclusion is that the difference between this model and the Timoshenko theory is not relevant. It thus justifies the introduction and the computation of shear correction factors dedicated to the frequency range of interest. On the other hand, Rychter [84] developed a theory accounting for transverse shear deformation, transverse normal stress, self equilibrating axial stress, and centroid axial-elongation contraction (due to Poisson effect). Even if it fulfils the boundary conditions, the stress field coming from these hypotheses on the kinematics does not match to the reference stress field arising from three-dimensional elasticity. Thus some authors use a warping function accounting for the three-dimensional elasticity stress field in the cross-section. The three-dimensional stress field in the cross-section is given by warping functions in some special cases by Love [59]. These functions are used by several authors to compute the shear reduction factor (see for example [16, 46, 72, 93, 113]), showing that the kinematics using warping function correspond to the Timoshenko theory.

2.3 Conclusions

In this chapter, the propagation of waves in a beam has firstly been studied for a waveguide of circular cross-section through the Lamb model with a special attention to the HF

range. The waves of this model can be gathered into groups having similar disturbances, that is torsional, longitudinal, flexural and higher-order flexural waves. It has been observed that all the waves are non-dispersive in the HF range. Moreover, for all the values of mode orders n, except for the torsional modes, the velocity of the first propagating mode tends to the velocity of the Rayleigh wave while all the other modes have a velocity tending to the shear velocity of transverse waves in a three-dimensional medium. All torsional modes have a velocity tending to the shear velocity as well. Secondly, several reduced kinematics have been studied. The Euler-Bernoulli and Timoshenko kinematics have been considered. The dispersion curves of the Timoshenko theory have been confronted to the ones of the Lamb model. They fit the dispersion curves predicted by the latter model in the low frequency range. As the frequency increases, some Lamb modes become propagative and the vibrational energy is spread on these modes. Then the dispersion curves of the Lamb model move away from the Timoshenko ones. Nevertheless, the group velocity predicted by the Timoshenko theory stays in the bounds of the group velocities predicted by the Lamb theory. This observation is valid for the flexural, the longitudinal and the torsional Lamb modes. It means that the group velocities predicted by the Timoshenko theory are coherent with the Lamb model. At last, some higher order kinematics have been investigated. They add some degrees of freedom to the Timoshenko theory in order to describe the warping of the cross-section. However they rely on the computation of additional shear coefficients to match the Lamb model. Thus, they do not bring more accuracy to the group velocities than the Timoshenko theory. In the remaining of the thesis, the Tiomoshenko theory will be used for its relative accuracy in the HF range, and because it predicts group velocities consistent with the Lamb model.

Chapter 3

Kinetic modeling of high-frequency waves in beam trusses

In this chapter, we first derive the mechanical equations corresponding to the Timoshenko kinematics in a general framework: the beam may be curved and the cross-section does not need to be symmetric. Then the propagation of HF waves in such a structure is analyzed with the kinetic modeling approach outlined in Sect. 1.4.3. The effects of prestressing forces and random materials are also considered. Finally, reflection/transmission operators for the power flows within beam assemblies are derived, for the application of the proposed kinetic approach to beam trusses.

3.1 Three-dimensional Timoshenko beam model

The application of the transport theory first requires to establish the dynamic behavior of a three-dimensional Timoshenko beam, i.e. its equilibrium and constitutive equations. The purpose of this section is to derive these equations prior to the HF setting proposed subsequently in Sect. 3.2.

3.1.1 Geometry and kinematical hypotheses

The vibrational behavior of the beam is modelled by Timoshenko's beam kinematics. This model is more relevant in the HF range than the Euler-Bernoulli one (see Sect. 2.2). In this work, beams materials are assumed to be isotropic but not necessarily homogeneous. In a first step, the material and geometrical parameters (including the cross-section's shape) vary along the beam axes at a length scale much larger than the wavelength of the excitations imposed to the structure. The implication of this assumption will be apparent in the HF setting of Sect. 3.2 (see Eq. (3.25)). The effect of random heterogeneities with characteristic size of the order of the wavelength will be studied in a subsequent part. Assumptions on the cross-section shape are not necessary to model the mechanical behavior of the beam. The model below allows for curvature and torsion of the neutral fiber which will be denoted by $\mathcal{C}$. It is parametrized by the curvilinear abscissa s in a (bounded or not) subset $\mathcal{S}$ of $\mathbb{R}$. The corresponding curvilinear coordinates are $\boldsymbol{s} = (s, s_2, s_3)^T$ such that a point $\boldsymbol{x}$ in the subdomain Ω of $\mathbb{R}^3$ occupied by the beam is parametrized by $\boldsymbol{x} = \Psi(\boldsymbol{s})$ in a fixed reference frame. Ω is also written $\Omega \equiv \mathcal{C} \times \Sigma(s)$, where Σ is the beam's cross-section. Let $\hat{\boldsymbol{t}}(s)$, $\hat{\boldsymbol{n}}(s)$,

$\hat{\boldsymbol{b}}(s)$ be the unit tangent, unit normal and tangent-normal vectors constituting a Darboux frame defined about $\mathcal{C}$. Also let $\boldsymbol{x}_c(s) = \Psi(s, 0, 0)$ be the position of the neutral fiber, then $\hat{\boldsymbol{t}}(s) = \boldsymbol{x}_c'$, where $\boldsymbol{a}'$ denotes the partial derivative with respect to the curvilinear abscissa s. The unit normal vector corresponds to the unit normal vector of the corresponding Frenet-Serret frame $\hat{\boldsymbol{n}}^F = \left|\hat{\boldsymbol{t}}'\right|^{-1} \hat{\boldsymbol{t}}'$ rotated by an angle α about $\hat{\boldsymbol{t}}$, this angle represents the rotation of the main axes of the cross-section with respect to s. The last unit vector $\hat{\boldsymbol{b}}$ is built in order to form an orthonormal basis, thus $\hat{\boldsymbol{b}} = \hat{\boldsymbol{t}} \times \hat{\boldsymbol{n}}$. The geodesic curvature $\kappa_g(s)$ is defined by $\hat{\boldsymbol{t}}' \cos\alpha = \kappa_g \hat{\boldsymbol{n}}$, the normal curvature $\kappa_n(s)$ by $\hat{\boldsymbol{t}}' \sin\alpha = \kappa_n \hat{\boldsymbol{n}}$ and the relative torsion $\tau(s)$ is defined by $\hat{\boldsymbol{b}}' = -\tau \hat{\boldsymbol{n}}$. In order to have a single valued coordinates system $(s, s_2, s_3)^T$, the cross-section dimensions have to be small with regard to both the curvature and the torsion [44, 101]. Fig. 3.1 shows an example of a beam with one curvature along $\hat{\boldsymbol{b}}$ but no torsion. Contrary to the case evoked in Sect. 2.2, the cross-section is not symmetric anymore, such that the center of mass and the shear center may be different. Moreover in the case of a heterogeneous cross-section, the center of mass differs from the centroid (or geometrical center) of the cross-section.

As in Sect. 1.1, the small transformation hypothesis is assumed to be enforced, then the reference configuration Ω_0 coincides with the current configuration Ω and a material particle at $\boldsymbol{p}$ in the reference configuration is confused with its position in the current configuration $\boldsymbol{x}$. There is thus $\boldsymbol{x} \simeq \boldsymbol{p} \equiv \Psi(\boldsymbol{s})$. Then it is recalled that the displacement of a material particle at $\boldsymbol{s}$ of the beam is given by Eq. (2.32), that is:

$$\boldsymbol{u}(\boldsymbol{s}, t) = \boldsymbol{u}_c(s, t) + \boldsymbol{\theta}(s, t) \times \boldsymbol{s}_\perp \,. \tag{3.1}$$

In the above $\boldsymbol{u}_c(s,t) = u_c(s,t)\hat{\boldsymbol{t}}(s) + \boldsymbol{u}_\perp(s,t)$ is the displacement of the neutral fiber, and $\boldsymbol{\theta}(s,t) = \theta_1(s,t)\hat{\boldsymbol{t}}(s) + \boldsymbol{\theta}_\perp$ is the small rotation vector of the cross-section about the neutral fiber defined as the origin of the Darboux frame. The orthogonal projection is now defined in this frame by $\boldsymbol{a}_\perp = (\boldsymbol{I} - \hat{\boldsymbol{t}} \otimes \hat{\boldsymbol{t}})\boldsymbol{a}$.

3.1.2 Resultant constitutive equations

The derivation of the constitutive equations is adapted from the analysis proposed by Huang [44]. It is based on the computation of the internal work, which is independent of the computational frame. The netforce acting on the cross-section is:

$$\boldsymbol{f}(s,t) = T_1(s,t)\hat{\boldsymbol{t}}(s) + T_2(s,t)\hat{\boldsymbol{n}}(s) + T_3(s,t)\hat{\boldsymbol{b}}(s)\,,$$

T_1 is the normal force along $\hat{\boldsymbol{t}}$, T_2 is the tangent force along $\hat{\boldsymbol{n}}$, and T_3 is the tangent force along $\hat{\boldsymbol{b}}$. The net moment acting on the cross-section at centroid of the cross-section is:

$$\boldsymbol{m}(s,t) = M_1(s,t)\hat{\boldsymbol{t}}(s) + M_2(s,t)\hat{\boldsymbol{n}}(s) + M_3(s,t)\hat{\boldsymbol{b}}(s)\,,$$

M_1 is the torsional moment, M_2 is the bending moment along $\hat{\boldsymbol{n}}$, and M_3 is the bending moment along $\hat{\boldsymbol{b}}$. By definition, the net force acting on the cross-section Σ is:

$$\boldsymbol{f} = \int_\Sigma \boldsymbol{\sigma}\hat{\boldsymbol{t}}\, d\Sigma\,, \tag{3.2}$$

where $\boldsymbol{\sigma}(\boldsymbol{s}, t)$ is the second-order stress tensor within the medium Ω. Also the net moment acting on Σ is:

$$\boldsymbol{m} = \int_\Sigma \boldsymbol{s}_\perp \times \boldsymbol{\sigma}\hat{\boldsymbol{t}}\, d\Sigma\,. \tag{3.3}$$

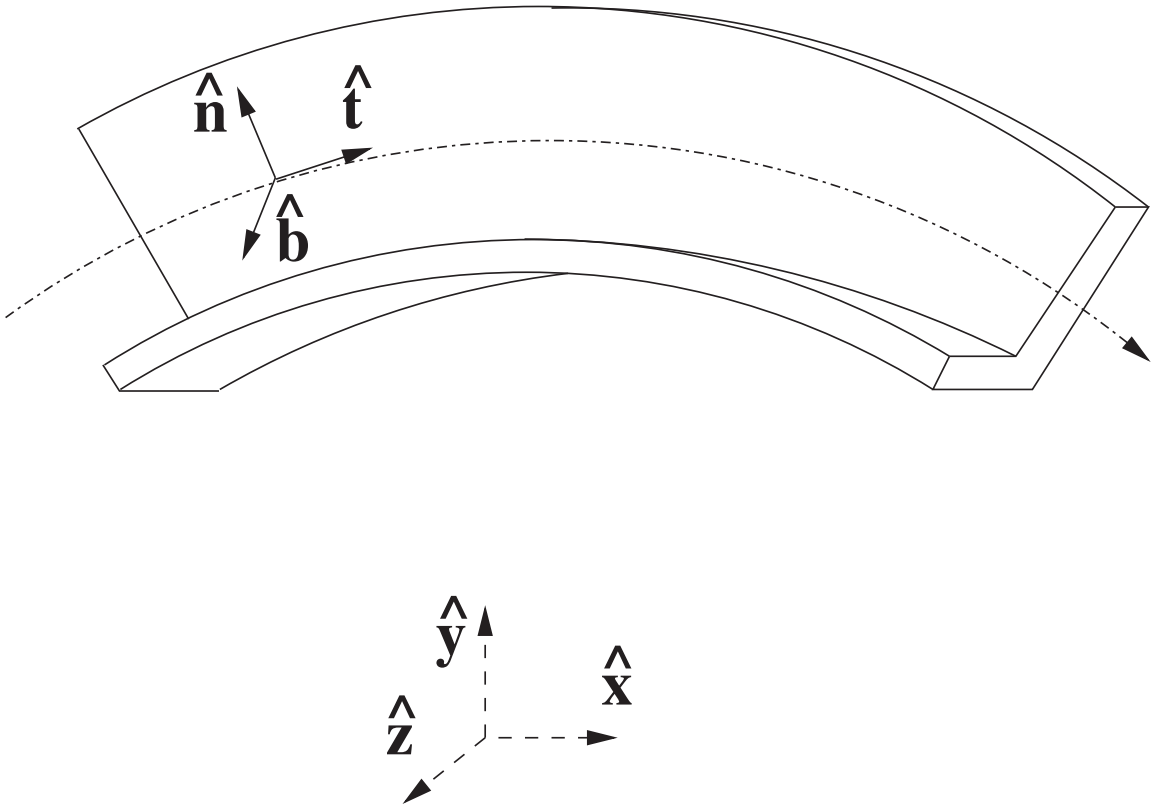

Figure 3.1: Curved L-beam oriented by its local Darboux frame (full arrows), with the tangent ($\hat{\boldsymbol{t}}$), normal ($\hat{\boldsymbol{n}}$), and bi-normal ($\hat{\boldsymbol{b}}$) axes , and the reference frame (dashed arrows). The neutral fiber is the dash-dot black line. The curvature is about the bi-normal axis solely.

As the Darboux frame $(\hat{\boldsymbol{t}}, \hat{\boldsymbol{n}}, \hat{\boldsymbol{b}})$ depends on the curvilinear coordinates s of the neutral fiber, the derivation with respect to s is given by the Darboux formulas:

$$\begin{aligned}
\hat{\boldsymbol{t}}' &= \kappa_g \hat{\boldsymbol{n}} + \kappa_n \hat{\boldsymbol{b}}\,, \\
\hat{\boldsymbol{n}}' &= -\kappa_g \hat{\boldsymbol{t}} + \tau \hat{\boldsymbol{b}}\,, \\
\hat{\boldsymbol{b}}' &= -\kappa_n \hat{\boldsymbol{t}} - \tau \hat{\boldsymbol{n}}\,,
\end{aligned}$$

and so in the case of curvilinear coordinates, $\boldsymbol{a}' = (\boldsymbol{a}\cdot\hat{\boldsymbol{e}}_i)'\hat{\boldsymbol{e}}_i + (\boldsymbol{a}\cdot\hat{\boldsymbol{e}}_i)\hat{\boldsymbol{e}}_i'\,, \hat{\boldsymbol{e}}_i = (\hat{\boldsymbol{t}}, \hat{\boldsymbol{n}}, \hat{\boldsymbol{b}})$. The internal work $V(s,t)$ is:

$$V = -\int_{\mathcal{S}} \left[\boldsymbol{D}\boldsymbol{f}\cdot\boldsymbol{u}_c + (\boldsymbol{D}\boldsymbol{m} + \hat{\boldsymbol{t}}\times\boldsymbol{f})\cdot\boldsymbol{\theta}\right] ds\,, \tag{3.4}$$

where:

$$\boldsymbol{D}(s) = \begin{bmatrix} \partial_s & \kappa_g & \kappa_n \\ -\kappa_g & \partial_s & \tau \\ -\kappa_n & -\tau & \partial_s \end{bmatrix} = \boldsymbol{I}_3\partial_s + \boldsymbol{\Delta}\,, \tag{3.5}$$

is the so-called Frenet-Serret matrix. $\boldsymbol{I}_n$ is the $n \times n$ identity matrix. The skew-symmetric matrix $\boldsymbol{\Delta}$ is given by:

$$\boldsymbol{\Delta} = \begin{pmatrix} 0 & \kappa_g & \kappa_n \\ -\kappa_g & 0 & \tau \\ -\kappa_n & -\tau & 0 \end{pmatrix} .$$

and denotes the curvatures of the neutral fiber. In this thesis, $\boldsymbol{D}$ will denote either that matrix or the corresponding operator. Integrating by parts on $]0, L[\subset \mathcal{S}$ yields:

$$V = \int_0^L \left[\boldsymbol{f} \cdot (\boldsymbol{D}\boldsymbol{u}_c + \hat{\boldsymbol{t}} \times \boldsymbol{\theta}) + \boldsymbol{m} \cdot \boldsymbol{D}\boldsymbol{\theta} \right] ds - \left[\boldsymbol{f} \cdot \boldsymbol{u}_c + \boldsymbol{m} \cdot \boldsymbol{\theta} \right]_{s=0}^{s=L} . \tag{3.6}$$

The boundary conditions prescribe either T_1 or u_c, either T_2 or v_c, either T_3 or w_c, either M_1 or θ_1, either M_2 or θ_2, and either M_3 or θ_3. Substituting Eq. (3.2) and Eq. (3.3) into Eq. (3.6) leads to:

$$V = \int_0^L \int_\Sigma \left[\boldsymbol{\sigma}\hat{\boldsymbol{t}} \cdot (\boldsymbol{D}\boldsymbol{u}_c + \hat{\boldsymbol{t}} \times \boldsymbol{\theta}) + (\boldsymbol{s}_\perp \times \boldsymbol{\sigma}\hat{\boldsymbol{t}}) \cdot \boldsymbol{D}\boldsymbol{\theta} \right] d\Sigma \, ds \tag{3.7}$$

for the internal work in $]0, L[$. The latter may be written as:

$$V = \int_0^L \int_\Sigma \boldsymbol{\sigma} : \boldsymbol{\epsilon} \, d\Sigma \, ds, \tag{3.8}$$

where $\boldsymbol{\epsilon}(\boldsymbol{s}, t)$ is the second-order strain tensor, $\boldsymbol{G} : \boldsymbol{H} := \mathrm{Tr}(\boldsymbol{G}\boldsymbol{H}^T)$ being the tensor scalar product of the second-order tensors $\boldsymbol{G}$ and $\boldsymbol{H}$. Keeping in mind that the tensors $\boldsymbol{\sigma}$ and $\boldsymbol{\epsilon}$ are symmetric and that ϵ_{22}, ϵ_{33}, and ϵ_{23} vanish by computation, Eq. (3.8) gives in an extended form:

$$V = \int_0^L \int_\Sigma \left(\sigma_{11}\epsilon_{11} + 2\sigma_{12}\epsilon_{12} + 2\sigma_{13}\epsilon_{13} \right) d\Sigma \, ds \, . \tag{3.9}$$

Factorizing the terms with respect to σ_{1j} in Eq. (3.7) allows to identify ϵ_{1j} from Eq. (3.8):

$$\boldsymbol{\epsilon}\hat{\boldsymbol{t}} = (\boldsymbol{D}\boldsymbol{u}_c + \boldsymbol{D}\boldsymbol{\theta} \times \boldsymbol{s}_\perp)\hat{\boldsymbol{t}} + \frac{1}{2}(\boldsymbol{D}\boldsymbol{u}_c(\hat{\boldsymbol{n}} + \hat{\boldsymbol{b}}) + \hat{\boldsymbol{t}} \times \boldsymbol{\theta} + \boldsymbol{D}\boldsymbol{\theta}\hat{\boldsymbol{t}} \times \boldsymbol{s}_\perp) \, . \tag{3.10}$$

The expression of the strain tensor given by Eq. (2.26) is retrieved, but without explicit calculation using the kinematics. In an elastic medium and under the assumption of small displacements, the stress-strain relationship is Hooke's law given by:

$$\boldsymbol{\sigma} = \boldsymbol{C} : \boldsymbol{\epsilon} \, . \tag{3.11}$$

$\boldsymbol{C}(\boldsymbol{s})$ is the elasticity tensor depending on the Lamé parameters $\lambda(s)$ and $\mu(s)$ for isotropic material given by Eq. (1.3). In the context of the Timoshenko beam theory, it is recalled that σ_{22} and σ_{33} are small with regard to σ_{11} and thus $\sigma_{11} = E\epsilon_{11}$. Substituting the Hooke's law Eq. (3.11) with the expression of the strain ϵ_{1j} given by Eq. (3.7) and Eq. (3.8) into Eq. (3.2) finally leads to:

$$\boldsymbol{F} = \boldsymbol{J}_0[\boldsymbol{C}_1](\boldsymbol{D}\boldsymbol{U}_c + \hat{\boldsymbol{t}} \times \boldsymbol{\Theta}) - \boldsymbol{J}_1[\boldsymbol{C}_1]\boldsymbol{D}\boldsymbol{\Theta} \, , \tag{3.12}$$

where the capital letters $\boldsymbol{U}_c$, $\boldsymbol{\Theta}$, $\boldsymbol{F}$, $\boldsymbol{M}$ stand equivalently for the vectors in $\mathbb{R}^3$ constituted by the coordinates of the displacement, the rotation, the netforce, and the netmoment,

respectively, in the local frame $(\hat{\boldsymbol{t}}, \hat{\boldsymbol{n}}, \hat{\boldsymbol{b}})$ (for example $\boldsymbol{F}(s,t) = (T_1(s,t), T_2(s,t), T_3(s,t))^T$ or $\boldsymbol{M}(s,t) = (M_1(s,t), M_2(s,t), M_3(s,t))^T$). $\boldsymbol{C}_1(s) := \mathrm{diag}(E, \kappa\mu\boldsymbol{I}_2)$ [1] is the elasticity tensor for the forces, with κ the shear reduction factor accounting for the non-uniformity of the three-dimensional elasticity stress state in the cross-section (see Sect. 2.2.2), and $\boldsymbol{J}_i[\boldsymbol{A}]$ is the matrix associated with the operator $\boldsymbol{\mathcal{J}}^i[\boldsymbol{A}] = \int_\Sigma \boldsymbol{A}(\boldsymbol{s}_\perp \times)^i d\Sigma$. For example, for a diagonal matrix $\boldsymbol{A}$, one have:

$$\boldsymbol{J}_1[\boldsymbol{A}] = \begin{pmatrix} 0 & -J_0^1[A_{11}] & J_1^0[A_{11}] \\ J_0^1[A_{22}] & 0 & 0 \\ -J_1^0[A_{33}] & 0 & 0 \end{pmatrix},$$

$$\boldsymbol{J}_2[\boldsymbol{A}] = \begin{pmatrix} (-J_0^2 - J_2^0)[A_{11}] & 0 & 0 \\ 0 & -J_0^2[A_{22}] & J_1^1[A_{22}] \\ 0 & J_1^1[A_{33}] & -J_2^0[A_{33}] \end{pmatrix},$$

where $J_i^j[a] = \int_\Sigma a s_2^i s_3^j dS$. By definition:

$$\boldsymbol{J}_0[\boldsymbol{A}] = \left(\int_\Sigma \boldsymbol{A} d\Sigma \right).$$

The matrix $\boldsymbol{J}_1[\boldsymbol{C}_1]$ does not a priori vanish because the distributions of the mechanical parameters are not supposed to be doubly symmetric here. Substituting Eq. (3.11) into Eq. (3.3) also leads to:

$$\boldsymbol{M} = \boldsymbol{J}_1[\boldsymbol{C}_2](\boldsymbol{D}\boldsymbol{U}_c + \hat{\boldsymbol{t}} \times \boldsymbol{\Theta}) - \boldsymbol{J}_2[\boldsymbol{C}_2]\boldsymbol{D}\boldsymbol{\Theta}\,, \tag{3.13}$$

where $\boldsymbol{C}_2(s) := \mathrm{diag}(\kappa\mu(s), E(s), E(s))$ is the relaxation tensor for the moments.

3.1.3 Equations of motion

Let us consider a curved beam of material volume density $\rho(\boldsymbol{s})$. Integrating the local dynamic equilibrium equation in Ω on the cross-section Σ and assuming that no external force is applied to the beam, the balance of momentum for the resultant (net) forces is:

$$\boldsymbol{f}' = \int_\Sigma \rho \ddot{\boldsymbol{u}}\, d\Sigma\,. \tag{3.14}$$

Assuming that no external couple is applied to the beam either, the balance of angular momentum for the resultant (net) moments is:

$$\boldsymbol{m}' + \hat{\boldsymbol{t}} \times \boldsymbol{f} = \int_\Sigma \big(\boldsymbol{s}_\perp \times \rho\ddot{\boldsymbol{u}}\big) d\Sigma\,. \tag{3.15}$$

Plugging Eq. (3.1) into Eq. (3.14) yields the first set of equations of motion:

$$\boldsymbol{D}\boldsymbol{F} = \boldsymbol{J}_0[\rho\boldsymbol{I}]\ddot{\boldsymbol{U}}_c - \boldsymbol{J}_1[\rho\boldsymbol{I}]\ddot{\boldsymbol{\Theta}}\,, \tag{3.16}$$

1. Some authors, as Gruttmann and Wagner [35], Tso and Norwood [104], consider two different shear factors for asymmetric cross-sections. The velocities of the shear wave become then distinct. In this study, only one coefficient is adopted in order to have two similar energetic families (the longitudinal and the transverse ones composed of 3 modes each of them having the same velocity). The shear coefficient factor depends on the shape of the cross-section and on the Poisson's ratio. Note that, for symmetric cross-sections, only one coefficient is required [20].

Plugging Eq. (3.1) into Eq. (3.15) yields the second set of equations of motion:

$$\boldsymbol{DM} + \hat{\boldsymbol{t}} \times \boldsymbol{F} = \boldsymbol{J}_1[\rho \boldsymbol{I}]\ddot{\boldsymbol{U}}_c - \boldsymbol{J}_2[\rho \boldsymbol{I}]\ddot{\boldsymbol{\Theta}}\,. \tag{3.17}$$

All these results match those found for beams with symmetric cross-sections by other authors, for example Tsay and Kingsbury [103], or Treyssède [101].

3.1.4 Energetic observables

The dynamics of the beam reduced to its neutral fiber $s \in \mathcal{S}$ by integration over the cross-section $\Sigma(s)$ is described by Eq. (3.16), Eq. (3.17), Eq. (3.12), and Eq. (3.13). Introducing the state vector:

$$\boldsymbol{X} = (\dot{\boldsymbol{U}}_c^T, \dot{\boldsymbol{\Theta}}^T, \boldsymbol{F}^T, \boldsymbol{M}^T)^T \in \mathbb{R}^{12}\,, \tag{3.18}$$

they can be written as a 12×12 first-order system:

$$\begin{cases} \boldsymbol{A}(s)\dot{\boldsymbol{X}} = \left(\boldsymbol{P}^1\partial_s + \boldsymbol{P}^0(s)\right)\boldsymbol{X}\,, \\ \boldsymbol{X}(0,s) = \boldsymbol{X}_0(s)\,, \end{cases} \tag{3.19}$$

where $\boldsymbol{A} = \mathrm{diag}(\boldsymbol{A}_1, \boldsymbol{A}_2)$ with:

$$\boldsymbol{A}_1 = \begin{pmatrix} \boldsymbol{J}_0[\rho\boldsymbol{I}] & -\boldsymbol{J}_1[\rho\boldsymbol{I}] \\ \boldsymbol{J}_1[\rho\boldsymbol{I}] & -\boldsymbol{J}_2[\rho\boldsymbol{I}] \end{pmatrix}, \quad \boldsymbol{A}_2 = \begin{pmatrix} \boldsymbol{J}_0[\boldsymbol{C}_1] & -\boldsymbol{J}_1[\boldsymbol{C}_1] \\ \boldsymbol{J}_1[\boldsymbol{C}_2] & -\boldsymbol{J}_2[\boldsymbol{C}_2] \end{pmatrix}^{-1},$$

$$\boldsymbol{P}^1 = \begin{pmatrix} 0 & \boldsymbol{I}_6 \\ \boldsymbol{I}_6 & 0 \end{pmatrix}, \quad \boldsymbol{P}^0(s) = \begin{pmatrix} 0 & \boldsymbol{P}_1^0 \\ \boldsymbol{A}^2\boldsymbol{P}_2^0 & 0 \end{pmatrix},$$

with

$$\boldsymbol{P}_1^0 = \begin{pmatrix} \boldsymbol{\Delta} & 0 \\ \boldsymbol{\Omega} & \boldsymbol{\Delta} \end{pmatrix}, \quad \boldsymbol{\Omega} = \begin{pmatrix} 0 & 0 & 0 \\ 0 & 0 & -1 \\ 0 & 1 & 0 \end{pmatrix},$$

and

$$\boldsymbol{P}_2^0 = \begin{pmatrix} \boldsymbol{J}_0[\boldsymbol{C}_1]\boldsymbol{\Delta} & -\boldsymbol{J}_1[\boldsymbol{C}_1]\boldsymbol{\Delta} + \boldsymbol{J}_0[\boldsymbol{C}_1]\boldsymbol{\Omega} \\ \boldsymbol{J}_1[\boldsymbol{C}_2]\boldsymbol{\Delta} & -\boldsymbol{J}_2[\boldsymbol{C}_2]\boldsymbol{\Delta} + \boldsymbol{J}_1[\boldsymbol{C}_2]\boldsymbol{\Omega} \end{pmatrix}.$$

Here $\boldsymbol{X}_0(s)$ is a vector of initial conditions. The matrix $\boldsymbol{A}_2$ exists if its Schur complement $-\boldsymbol{J}_2[\boldsymbol{C}_2] + \boldsymbol{J}_1[\boldsymbol{C}_2](\boldsymbol{J}_0[\boldsymbol{C}_1])^{-1}\boldsymbol{J}_1[\boldsymbol{C}_1]$ and $\boldsymbol{J}_0[\boldsymbol{C}_1]$ are invertible. $\boldsymbol{J}_0[\boldsymbol{C}_1]$ is diagonal and thus invertible. The Shur complement is invertible if and only if:

$$(J_0^1[\mu])^2 + (J_1^0[\mu])^2 - (J_0^2[\mu] + J_2^0[\mu])J_0^0[\mu] \neq 0\,,$$

and

$$J_2^0[E](J_0^1[E])^2 - 2J_0^1[E]J_1^0[E]J_1^1[E] + J_0^2[E](J_1^0[E])^2 + J_0^0[E](J_1^1[E])^2 - J_0^0[E]J_0^2[E]J_2^0[E] \neq 0\,.$$

Moreover note that $\boldsymbol{A}$ and $\boldsymbol{P}^1$ are symmetric matrices and it can be shown that $\boldsymbol{P}^0$ is a skew-symmetric matrix. The matrix $\boldsymbol{A}$ is positive definite if $(J_1^1)^2 < J_2^0 J_0^2$. It is assumed that this condition is enforced, then the mechanical energy density $\mathcal{E} \in \mathbb{R}_+$ for the beam motion is:

$$\mathcal{E}(s,t) = \frac{1}{2}(\boldsymbol{X}, \boldsymbol{X})_{\boldsymbol{A}}\,, \tag{3.20}$$

and the power flow density $\Pi \in \mathbb{R}$ within the beam is:

$$\Pi(s,t) = -\frac{1}{2}(\boldsymbol{X},\boldsymbol{X})_{\boldsymbol{P}^1} = -(\boldsymbol{F}\cdot\dot{\boldsymbol{U}}_c + \boldsymbol{M}\cdot\dot{\boldsymbol{\Theta}})\,, \tag{3.21}$$

where the inner product $(\boldsymbol{u},\boldsymbol{v})_{\boldsymbol{G}} := \boldsymbol{v}^T\boldsymbol{G}\boldsymbol{u}$ is introduced for a square matrix $\boldsymbol{G}$. Finally, taking the scalar product of Eq. (3.19) with $\boldsymbol{X}$ leads to the energy conservation law, or continuity equation:

$$\dot{\mathcal{E}} + \Pi' = 0\,. \tag{3.22}$$

3.2 HF wave propagation in a three-dimensional beam

This section focuses on the characterization of the solution of the system (3.19) in the HF regime. HF vibrations of the beam may be generated by initial conditions oscillating at a small length scale ε proportional to the wavelength. The HF regime thus corresponds to $\varepsilon \to 0$. These initial conditions may be chosen for example as plane waves in the form $\boldsymbol{X}^0_\varepsilon(s) = \boldsymbol{\chi}(s)\mathrm{e}^{\mathrm{i}\,ks/\varepsilon}$, where $k \in \mathbb{R}$ and $\boldsymbol{\chi}(s)$ is a slowly varying vector. As easily seen, it is not possible to describe the limit of $\boldsymbol{X}^0_\varepsilon$ as $\varepsilon \to 0$. Since by the hyperbolicity of Eq. (3.19) its solution $\boldsymbol{X}_\varepsilon(s,t)$ has the same oscillatory shape as the initial condition, it is neither possible to describe its HF limit. However the energy input by the initial condition remains finite and will propagate in the beam. One should be able to describe and track it by Eq. (3.22), provided its limit as $\varepsilon \to 0$ is known. As explained in Sect. 1.4.3 energetic quantities associated to $\boldsymbol{X}_\varepsilon$, or observables proportional to $|\boldsymbol{X}_\varepsilon|^2$ in some sense, shall be considered in this very limit. The link between the solution $\boldsymbol{X}_\varepsilon$ of Eq. (3.19) and these observables as $\varepsilon \to 0$ is established using a Wigner transform of $\boldsymbol{X}_\varepsilon$ and its limit as $\varepsilon \to 0$, the so-called Wigner measure. The theory developed by Papanicolaou and Ryzhik [75] or Guo and Wang [36] outlines how the limit is obtained, and how a continuity equation of the form of Eq. (3.22) is derived for the Wigner measure. The main novelty in the proposed analysis is that all energetic quantities shall be resolved in phase space (position × wave vector) in order to correctly built up their HF limits and evolution properties. The general framework is described in Sect. 3.2.1 below, and its application to a curved three-dimensional Timoshenko beam is given in Sect. 3.2.2.

3.2.1 HF energy density and transport properties

In this section, the HF limit of a first-order hyperbolic system of the form Eq. (3.19) is considered in a general setting. First, the Wigner transform and its properties are introduced. This transform is used to estimate the energy density associated to the solutions of system of the from Eq. (3.19). Let $\boldsymbol{X}(s,t)$ be a complex function defined on $\mathbb{R}_s \times \mathbb{R}_t$ with values in $\mathbb{C}^n$. Provided that $\boldsymbol{X}$ is square integrable with respect to s, its spatial Wigner transform is defined by:

$$\boldsymbol{W}_\varepsilon[\boldsymbol{X}](s,k,t) = \frac{1}{2\pi}\int_{\mathbb{R}} \mathrm{e}^{\mathrm{i}\,k\cdot r}\,\boldsymbol{X}\left(s-\varepsilon\frac{r}{2},t\right)\boldsymbol{X}^\star\left(s+\varepsilon\frac{r}{2},t\right)dr\,. \tag{3.23}$$

In the above $\boldsymbol{X}^\star = \overline{\boldsymbol{X}}^T$ stands for the conjugate transpose of $\boldsymbol{X}$. The $n \times n$ matrix $\boldsymbol{W}_\varepsilon[\boldsymbol{X}]$ is Hermitian and not necessarily positive, but it does become so in the HF limit $\varepsilon \to 0$.

Furthermore this (weak) limit always exists for a square integrable function. The Wigner transform also has the property:

$$\int_{\mathbb{R}} \boldsymbol{W}_\varepsilon[\boldsymbol{X}](s,k,t)dk = \boldsymbol{X}(s,t)\boldsymbol{X}^\star(s,t)\,, \tag{3.24}$$

hence its link with the energy if one takes the trace of the above equation. Now let us consider a vector $\boldsymbol{X}_\varepsilon$ in $\mathbb{R}^n$ satisfying the first-order problem:

$$\begin{cases} \varepsilon \boldsymbol{A}(s)\dot{\boldsymbol{X}}_\varepsilon = \left(\boldsymbol{P}^1(\varepsilon\partial_s) + \varepsilon \boldsymbol{P}^0(s)\right)\boldsymbol{X}_\varepsilon\,, \\ \boldsymbol{X}_\varepsilon(0,s) = \boldsymbol{X}^0_\varepsilon(s)\,. \end{cases} \tag{3.25}$$

This system is obtained from Eq. (3.19) by multiplying it with ε, assuming in addition that $\boldsymbol{A}(s)$ and $\boldsymbol{P}^0(s)$ are independent of ε. This assumption was introduced earlier in Sect. 3.1.1. It means that the parameters of the materials constituting the beam and its curvatures vary on a scale much longer than the small wavelength ε imposed by the initial condition $\boldsymbol{X}^0_\varepsilon$. Indeed, the initial data $\boldsymbol{X}^0_\varepsilon$ vary on a scale greater or equal to ε, which is the case of the plane waves $\boldsymbol{X}^0_\varepsilon(s) \propto \mathrm{e}^{\mathrm{i}\,ks/\varepsilon}$ considered above. More generally, these data have to satisfy the so-called ε-oscillatory strong condition stating that $(|\varepsilon\partial_s|\boldsymbol{X}^0_\varepsilon)^2$ remains at least locally integrable on $\mathbb{R}$ [31]. HF plane waves are only a particular case satisfying this condition. Finally, $\boldsymbol{A}$ and $\boldsymbol{P}^1$ are also assumed to be symmetric so that the system (3.25) is said to be symmetric. Then provided that the sequence $(\boldsymbol{X}_\varepsilon)$ remains bounded in the set of square integrable functions with respect to $s \in \mathbb{R}$, its Wigner transform $\boldsymbol{W}_\varepsilon[\boldsymbol{X}_\varepsilon]$ has an Hermitian weak limit (denoted by $\boldsymbol{W}$) as $\varepsilon \to 0$ which is also a non negative measure. This very limit is the so-called Wigner measure of the sequence $(\boldsymbol{X}_\varepsilon)$ [31, 57], obtained as follow. It has the properties that for any pseudo-differential operator $\boldsymbol{a}^W(s,\varepsilon D_s)$ defined for any smooth function $f(s)$ by:

$$a^W(s,\varepsilon D_s)f(s) = \frac{1}{2\pi}\int_{\mathbb{R}\times\mathbb{R}} \mathrm{e}^{ik(s-r)}\boldsymbol{a}\left(\frac{s+r}{2},\varepsilon k\right) f(r)drdk\,,$$

where $\boldsymbol{a}(s,k)$ is a matrix function, one has:

$$\lim_{\varepsilon\to 0}(a^W(s,\varepsilon D_s)\boldsymbol{X}_\varepsilon,\boldsymbol{X}_\varepsilon)_{L^2} = \mathrm{Tr}\int_{\mathbb{R}\times\mathbb{R}} \boldsymbol{a}(s,k)\boldsymbol{W}(ds,dk)\,.$$

Then by an appropriate choice of $\boldsymbol{a}(s,k)$, it can be shown that the HF energy density of Eq. (3.20):

$$\mathcal{E}_\varepsilon(s,t) = \frac{1}{2}(\boldsymbol{X}_\varepsilon,\boldsymbol{X}_\varepsilon)_{\boldsymbol{A}}$$

is given in terms of $\boldsymbol{W}$ by:

$$\lim_{\varepsilon\to 0}\mathcal{E}_\varepsilon(s,t) = \frac{1}{2}\int_{\mathbb{R}} \boldsymbol{A}:\boldsymbol{W}\,dk, \tag{3.26}$$

and the HF power flow density (3.21):

$$\Pi_\varepsilon(s,t) = -\frac{1}{2}(\boldsymbol{X}_\varepsilon,\boldsymbol{X}_\varepsilon)_{\boldsymbol{P}^1} \tag{3.27}$$

is:

$$\lim_{\varepsilon\to 0}\Pi_\varepsilon(s,t) = -\frac{1}{2}\int_{\mathbb{R}} \boldsymbol{P}^1:\boldsymbol{W}\,dk\,. \tag{3.28}$$

Note that $\boldsymbol{P}^0$ does not influence the power flow equation Eq. (3.28) because it is skew-symmetric and thus its contribution vanishes with the inner product 3.27. Since the sequence $(\boldsymbol{X}_\varepsilon)$ satisfies the system (3.25), it can be shown in addition that its Wigner measure reads [36, 75]:

$$\boldsymbol{W}(s,k,t) = \sum_{\alpha=1}^{M} \sum_{i,j=1}^{R_\alpha} w_\alpha^{ij}(s,k,t) \boldsymbol{v}_{\alpha_i}(s,k) \otimes \boldsymbol{v}_{\alpha_j}(s,k)\,. \tag{3.29}$$

In the above $(\boldsymbol{v}_{\alpha_i})_{1\leq i\leq R_\alpha}$ are the eigenvectors of the dispersion matrix:

$$\boldsymbol{\Gamma}(s,k) := k\boldsymbol{A}^{-1}(s)\boldsymbol{P}^1\,, \tag{3.30}$$

associated with the eigenvalues λ_α of which orders of multiplicity are R_α. These orders of multiplicity are assumed to be independent of $(s,k) \in \mathcal{S}\times\mathbb{R}$ and are such that $\sum_{\alpha=1}^{M} R_\alpha = n$. The $R_\alpha \times R_\alpha$ coherence matrices $\boldsymbol{W}_\alpha$, defined as $[\boldsymbol{W}_\alpha]_{ij} = w_\alpha^{ij}$, satisfy the transport equations:

$$\partial_t \boldsymbol{W}_\alpha + \{\lambda_\alpha, \boldsymbol{W}_\alpha\} + [\boldsymbol{W}_\alpha, \boldsymbol{N}_\alpha] = \boldsymbol{0}\,, \tag{3.31}$$

where $\{g,h\} = \partial_k g\cdot\partial_s h - \partial_s g\cdot\partial_k h$ is the usual Poisson's bracket, $[\boldsymbol{G},\boldsymbol{H}] = \boldsymbol{G}\boldsymbol{H} + \boldsymbol{H}^\star\boldsymbol{G}^\star$, and $\boldsymbol{N}_\alpha$ is an $R_\alpha \times R_\alpha$ coupling matrix with elements:

$$[\boldsymbol{N}_\alpha(s)]_{ij} = (\boldsymbol{v}_{\alpha_j}, (\boldsymbol{P}^1\partial_s + \boldsymbol{P}^0(s))\boldsymbol{v}_{\alpha_i}) - \partial_s\lambda_\alpha(\partial_k \boldsymbol{v}_{\alpha_i}, \boldsymbol{v}_{\alpha_j})_{\boldsymbol{A}} - \frac{1}{2}\partial^2_{ks}\lambda_\alpha\delta_{ij}\,. \tag{3.32}$$

This matrix is skew-symmetric on account of its last term $\partial^2_{ks}\lambda_\alpha\delta_{ij}$.

3.2.2 Application to a three-dimensional Timoshenko beam

The transport theory is now applied to a Timoshenko beam. In this case, $n = 12$, the vector $\boldsymbol{X}_\varepsilon$ is the rescalled state vector $\boldsymbol{X}$ given by Eq. (3.18), and the hyperbolic system is the one established in Sect. 3.1 that is Eq. (3.19). Let $\boldsymbol{k} := k\hat{\boldsymbol{t}}$ be the wave vector within a beam oriented by its tangent unit vector $\hat{\boldsymbol{t}}$. As $\boldsymbol{P}^0$ is rescaled as a first-order term in ε, it does not influence the eigenvalues of the dispersion matrix $\boldsymbol{\Gamma}$ of the system (3.19) of Sect. 3.1.4 in the HF limit $\varepsilon \to 0$. Thus the curvatures have no influence on the HF vibrations of the beam. The dispersion matrix $\boldsymbol{\Gamma}$ is self-adjoint with respect to the inner product $(,)_{\boldsymbol{A}}$, thus:

$$(\boldsymbol{\Gamma}\boldsymbol{a},\boldsymbol{b})_{\boldsymbol{A}} = (\boldsymbol{a},\boldsymbol{\Gamma}\boldsymbol{b})_{\boldsymbol{A}}\,, \quad \forall \boldsymbol{a},\boldsymbol{b}\in\mathbb{R}^{12}\,,$$

and thus all the eigenvalues of $\boldsymbol{\Gamma}$ are real and the eigenvectors can be chosen to be orthonormal with respect to $(,)_{\boldsymbol{A}}$.

It is now assumed that the material parameters have a symmetric distribution over the cross-section. It implies that:

$$J_i^j[\boldsymbol{A}] = J_i^j\boldsymbol{A}\,,$$

and thus $\boldsymbol{J}_1 = 0$ on account of the property of the centroid of the cross-section Eq. (2.24). The term J_1^1 does not vanish because the cross-section is not necessarily symmetric and thus $\hat{\boldsymbol{n}}$ and $\hat{\boldsymbol{b}}$ are not the main axes of inertia of the cross-section. Note that it could be possible to remove it by a change of basis to the basis inertia of the beam but it is not required for our calculation. The calculation gives for the eigenvalues of the dispersion matrix $\boldsymbol{\Gamma}$:

$$\begin{aligned} \lambda_{\mathrm{P}}^{\pm}(s,\boldsymbol{k}) &= \pm c_{\mathrm{P}}(s)|\boldsymbol{k}| \quad \text{each of multiplicity } 3\,,\\ \lambda_{\mathrm{T}}^{\pm}(s,\boldsymbol{k}) &= \pm c_{\mathrm{T}}(s)|\boldsymbol{k}| \quad \text{each of multiplicity } 3\,, \end{aligned} \tag{3.33}$$

where c_{P} and c_{T} are the group velocities of longitudinal and transverse waves, respectively given in Eq. (2.23) and Eq. (2.40):

$$c_{\mathrm{P}} = \sqrt{\frac{E}{\rho}}, \quad c_{\mathrm{T}} = \sqrt{\frac{\kappa\mu}{\rho}}. \tag{3.34}$$

Since these waves are non dispersive in the HF range, the group velocities are also the phase velocities. Hence $R_\alpha^\pm = 3$ for $\alpha = \mathrm{P}, \mathrm{T}$ and either the forward $(+)$ or the backward $(-)$ waves. The associated eigenvectors normalized with respect to $(,)_{\boldsymbol{A}}$, are:

$$\begin{aligned}
\boldsymbol{v}^\pm_{\mathrm{P}_1} &= \frac{1}{\sqrt{2}}\left(-\hat{k}\sqrt{\frac{E}{a\rho c}}, 0,0,0,0,0, \pm\sqrt{\frac{aE}{c}}, 0,0,0,0,0\right)^T,\\
\boldsymbol{v}^\pm_{\mathrm{P}_2} &= \frac{1}{\sqrt{2}}\left(0,0,0,0, \frac{\hat{k}}{\sqrt{\rho J_0^2}}, 0,0,0,0,0, \pm\sqrt{EJ_0^2}, \mp J_1^1\sqrt{\frac{E}{J_0^2}}\right)^T,\\
\boldsymbol{v}^\pm_{\mathrm{P}_3} &= \frac{1}{\sqrt{2}}\left(0,0,0,0, \frac{\hat{k}J_1^1}{\sqrt{cJ_0^2\rho}}, \hat{k}\sqrt{\frac{J_0^2}{c\rho}}, 0,0,0,0,0, \pm\sqrt{\frac{cE}{J_0^2}}\right)^T,\\
\boldsymbol{v}^\pm_{\mathrm{T}_1} &= \frac{1}{\sqrt{2}}\left(0, \frac{\hat{k}}{\sqrt{\rho J_0^0}}, 0,0,0,0,0, \pm\sqrt{\kappa\mu J_0^0}, 0,0,0,0\right)^T,\\
\boldsymbol{v}^\pm_{\mathrm{T}_2} &= \frac{1}{\sqrt{2}}\left(0,0, \frac{\hat{k}}{\sqrt{\rho J_0^0}}, 0,0,0,0,0, \pm\sqrt{\kappa\mu J_0^0}, 0,0,0\right)^T,\\
\boldsymbol{v}^\pm_{\mathrm{T}_3} &= \frac{1}{\sqrt{2}}\left(0,0,0, -\frac{\hat{k}J_0^0}{\sqrt{\rho b J_0^0}}, 0,0,0,0,0, \pm\sqrt{\frac{\kappa\mu b}{J_0^0}}, 0,0\right)^T.
\end{aligned} \tag{3.35}$$

where $a = J_0^0(J_2^0J_0^2 - (J_1^1)^2)$, $b = J_0^0(J_0^2 + J_2^0)$, and $c = J_2^0J_0^2 - (J_1^1)^2$. If the cross-section is considered to be symmetric, then the eigenvectors derived in [55] are retrieved, that is:

$$\begin{aligned}
\boldsymbol{v}^\pm_{\mathrm{P}_1} &= \left(\frac{\hat{k}}{\sqrt{2\rho S}}, 0,0,0,0,0, \pm\sqrt{\frac{ES}{2}}, 0,0,0,0,0\right)^T,\\
\boldsymbol{v}^\pm_{\mathrm{P}_2} &= \left(0,0,0,0, \frac{\hat{k}}{\sqrt{2J_0^2\rho}}, 0,0,0,0,0, \pm\sqrt{\frac{J_0^2E}{2}}, 0\right)^T,\\
\boldsymbol{v}^\pm_{\mathrm{P}_3} &= \left(0,0,0,0,0, \frac{\hat{k}}{\sqrt{2J_2^0\rho}}, 0,0,0,0,0, \pm\sqrt{\frac{J_2^0E}{2}}\right)^T,\\
\boldsymbol{v}^\pm_{\mathrm{T}_1} &= \left(0, \frac{\hat{k}}{\sqrt{2\rho S}}, 0,0,0,0,0, \pm\sqrt{\frac{\kappa\mu S}{2}}, 0,0,0,0\right)^T,\\
\boldsymbol{v}^\pm_{\mathrm{T}_2} &= \left(0,0, \frac{\hat{k}}{\sqrt{2\rho S}}, 0,0,0,0,0, \pm\sqrt{\frac{\kappa\mu S}{2}}, 0,0,0\right)^T,\\
\boldsymbol{v}^\pm_{\mathrm{T}_3} &= \left(0,0,0, \frac{\hat{k}}{\sqrt{2(J_2^0 + J_0^2)\rho}}, 0,0,0,0,0, \pm\sqrt{\frac{\kappa(J_2^0 + J_0^2)\mu}{2}}, 0,0\right)^T.
\end{aligned}$$

The eigenvectors associated with the eigenvalues P± are the compressional (1) and bending (2 and 3) energy modes, and the eigenvectors associated with the eigenvalues T± are the shear (1 and 2) and torsional (3) energy modes.

The coupling matrix $\boldsymbol{N}$ is computed using Eq. (3.32). Since $\boldsymbol{P}^0$ is skew-symmetric and the eigenvectors do not depend on k, it is reduced to:

$$\boldsymbol{N}_{\alpha_{ij}} = (\boldsymbol{v}_{\alpha_j}, \boldsymbol{P}^1 \partial_s \boldsymbol{v}_{\alpha_i}) - \frac{1}{2}\partial_k \lambda'_\alpha \delta_{ij}\,,$$

and it may be shown by computation that these terms vanish also. Thus the 3×3 coherence matrices $\boldsymbol{W}_\alpha^\pm$, $\alpha = \mathrm{P}, \mathrm{T}$, satisfy the Liouville-type transport equations:

$$\partial_t \boldsymbol{W}_\alpha^\pm \pm \operatorname{sign}(k) c_\alpha \cdot \partial_s \boldsymbol{W}_\alpha^\pm \mp |\boldsymbol{k}| c'_\alpha \cdot \partial_k \boldsymbol{W}_\alpha^\pm = \boldsymbol{0}\,. \tag{3.36}$$

The sign of the energetic mode has been removed compared to Eq. (3.35) because it denotes the direction of propagation of the mode that is given also by the sign of $\boldsymbol{W}_\alpha^\pm$. Thus $\boldsymbol{W}_{\alpha\mp}^\pm$ vanishes. It may be physically explained because a wave travelling in a direction can not carry energy in the opposite direction in the HF dynamics of the Timoshenko beams. Accordingly, it can be observed that $\boldsymbol{W}_\alpha^-(s,k,t) = \boldsymbol{W}_\alpha^+(s,-k,t)$ for $\alpha = \mathrm{P}, \mathrm{T}$, so that the space time energy density reduces to:

$$\mathcal{E}(s,t) = \lim_{\varepsilon \to 0} \mathcal{E}_\varepsilon(s,t) = \sum_{\alpha = \mathrm{P,T}} \int_{\mathbb{R}} \operatorname{Tr} \boldsymbol{W}_\alpha^+(s,k,t)\, dk\,. \tag{3.37}$$

Similarly, the power flow density vector $\boldsymbol{\Pi}(s,t) := \Pi(s,t)\hat{\boldsymbol{t}}(s)$ in the local frame is:

$$\begin{aligned} \boldsymbol{\Pi}(s,t) = \lim_{\varepsilon \to 0} \boldsymbol{\Pi}_\varepsilon(s,t) &= \sum_{\alpha = \mathrm{P,T}} c_\alpha(s) \int_{\mathbb{R}} \operatorname{Tr} \boldsymbol{W}_\alpha^+(s,k,t)\hat{\boldsymbol{k}}\, dk \\ &= \sum_{\alpha = \mathrm{P,T}} \sum_{j=1}^{R_\alpha} \int_{\mathbb{R}} \boldsymbol{\pi}_\alpha^{jj}(s,\boldsymbol{k},t)\, dk\,. \end{aligned} \tag{3.38}$$

Here $\boldsymbol{\pi}_\alpha^{jj}(s,\boldsymbol{k},t) := c_\alpha(s) w_\alpha^{jj}(s,k,t)\hat{\boldsymbol{k}}$ is the power flow density of a mode $\alpha \in (\mathrm{P}, \mathrm{T})$, $1 \le j \le R_\alpha$, in a beam oriented by its tangent unit vector $\hat{\boldsymbol{t}}$, with $\hat{\boldsymbol{k}} := \frac{\boldsymbol{k}}{|\boldsymbol{k}|} = \operatorname{sign}(k)\hat{\boldsymbol{t}}$. If $k > 0$ the energy flux travels in the same direction as $\hat{\boldsymbol{t}}$, but if $k < 0$ it travels in the opposite direction. For convenience the sign function is denoted by $\operatorname{sign}(k) = \hat{k}$ in the remaining of the thesis. The energy and power flow densities (Eq. (3.37) and Eq. (3.38)) to be computed ultimately depend on the diagonal elements w_α^{jj} of $\boldsymbol{W}_\alpha$ solely. The transport equations 3.36 do not couple them, although the boundary/interface conditions considered in the next section do so. Thus only Eq. (3.36) for the elements $(w_\alpha^{jj})^+$ of $\boldsymbol{W}_\alpha^+$ has to be considered, reminding the symmetry $\boldsymbol{W}_\alpha^+(s,k,t) = \boldsymbol{W}_\alpha^-(s,-k,t)$. Introducing the set of energy modes

$$\mathsf{E} = (\mathrm{P}_1, \mathrm{P}_2, \mathrm{P}_3, \mathrm{T}_1, \mathrm{T}_2, \mathrm{T}_3) \tag{3.39}$$

corresponding to the eigenvectors $\boldsymbol{v}_{\mathrm{P}_j}^+$ and $\boldsymbol{v}_{\mathrm{T}_j}^+$, $1 \le j \le 3$, and the eigenvalues λ_P^+ and λ_T^+ (counted with their orders of multiplicity), the set of transport equations to be considered is finally reduced to:

$$\partial_t w_\alpha + c_\alpha \hat{k}\, \partial_s w_\alpha - |\boldsymbol{k}| c'_\alpha\, \partial_k w_\alpha = 0\,, \quad \alpha \in \mathsf{E}\,. \tag{3.40}$$

Accordingly, the power flow density of a mode $\alpha \in \mathsf{E}$ is denoted by:

$$\boldsymbol{\pi}_\alpha(s, \boldsymbol{k}, t) = c_\alpha(s) w_\alpha(s, k, t) \hat{\boldsymbol{k}} \,. \tag{3.41}$$

These results extend to three dimensional beams the results of Savin [86] for the two-dimensional case.

3.2.3 Effect of the prestressing forces

The effect of a prestressing on a curved beam is now studied. The prestressing introduces a stationary stress denoted by $\boldsymbol{\sigma}_{\text{ref}}$. It is evaluated in practice by static equilibrium consideration. Its introduction requires to modify the balances of momentum (3.14) and (3.15) and the constitutive equations (3.12) and (3.13). The total force becomes:

$$\boldsymbol{f}_t = \int_{\Sigma_0} \boldsymbol{E}\boldsymbol{S}\hat{\boldsymbol{t}}_0 d\Sigma_0 \,, \tag{3.42}$$

where

$$\boldsymbol{f}_t = \boldsymbol{f}_{\text{d}} + \boldsymbol{f}_{\text{ref}}$$

is the total net force acting on the cross-section constituted by the dynamical part $\boldsymbol{f}_{\text{d}}$ and the prestressing part $\boldsymbol{f}_{\text{ref}}$, $\boldsymbol{E} = \boldsymbol{I} + \boldsymbol{\nabla}_{\boldsymbol{s}}(\boldsymbol{u})$, $\boldsymbol{S} \overset{\text{def}}{=} \boldsymbol{\sigma}_{\text{d}} + \boldsymbol{\sigma}_{\text{ref}}$ is the second Piola tensor, and Σ_0 and $\hat{\boldsymbol{t}}_0$ denotes respectively the cross-section and the axis tangent to the neutral fiber for the reference configuration. The net force associated to the prestressed state is:

$$\boldsymbol{f}_{\text{ref}} = \int_{\Sigma_0} \boldsymbol{\sigma}_{\text{ref}} \hat{\boldsymbol{t}}_0 d\Sigma_0 \,.$$

The zero and first order terms of Eq. (3.42) are:

$$\boldsymbol{f}_t = \int_{\Sigma} (\boldsymbol{\sigma}_{\text{d}} + \boldsymbol{\sigma}_{\text{ref}} + \boldsymbol{\nabla}(\boldsymbol{u})\boldsymbol{\sigma}_{\text{ref}}) \hat{\boldsymbol{t}} d\Sigma \,. \tag{3.43}$$

The first term of the right hand side is the dynamic effect while the second and third terms denote the effect of the prestressing. The latter requires to know the gradient of the displacement. It can be shown that:

$$\boldsymbol{\nabla}(\boldsymbol{u}) = (\boldsymbol{u}_c' - \boldsymbol{\theta} \times \hat{\boldsymbol{t}} + \boldsymbol{\theta}' \times \boldsymbol{s}_\perp) \otimes \hat{\boldsymbol{t}} + \boldsymbol{\theta} \times \ . \tag{3.44}$$

With Eq. (3.12), it is possible to express the total forces $\boldsymbol{f}_t$ in a matrix form:

$$\boldsymbol{F}_t = \boldsymbol{J}_0[\boldsymbol{C}_1 + (\boldsymbol{\sigma}_{\text{ref}} : \hat{\boldsymbol{t}} \otimes \hat{\boldsymbol{t}})\boldsymbol{I}_3](\boldsymbol{D}\boldsymbol{U}_c + \hat{\boldsymbol{t}} \times \boldsymbol{\Theta}) - \boldsymbol{J}_1[\boldsymbol{C}_1 + (\boldsymbol{\sigma}_{\text{ref}} : \hat{\boldsymbol{t}} \otimes \hat{\boldsymbol{t}})\boldsymbol{I}_3]\boldsymbol{D}\boldsymbol{\Theta} + \boldsymbol{\Theta} \times \boldsymbol{F}_{\text{ref}} + \boldsymbol{F}_{\text{ref}} \,. \tag{3.45}$$

The total moment is:

$$\boldsymbol{m}_t = \int_{\Sigma_0} (\boldsymbol{s}_\perp - \boldsymbol{\theta} \times \boldsymbol{s}_\perp) \times (\boldsymbol{E}\boldsymbol{S}\hat{\boldsymbol{t}}_0) d\Sigma_0 \,,$$

where $\boldsymbol{m}_t = \boldsymbol{m}_d + \boldsymbol{m}_{\text{ref}}$ with

$$\boldsymbol{m}_{\text{ref}} = \int_{\Sigma_0} s_\perp \times \boldsymbol{\sigma}_{\text{ref}} \hat{\boldsymbol{t}}_0 d\Sigma_0 \,.$$

Developing and keeping the zero and first order terms using Eq. (3.44) and Eq. (3.13) leads to:

$$\boldsymbol{M}_t = \boldsymbol{J}_1[\boldsymbol{C}_2 + (\boldsymbol{\sigma}_{\text{ref}} : \hat{\boldsymbol{t}} \otimes \hat{\boldsymbol{t}})\boldsymbol{I}_3](\boldsymbol{D}\boldsymbol{U}_c + \hat{\boldsymbol{t}} \times \boldsymbol{\Theta}) - \boldsymbol{J}_2[\boldsymbol{C}_2 + (\boldsymbol{\sigma}_{\text{ref}} : \hat{\boldsymbol{t}} \otimes \hat{\boldsymbol{t}})\boldsymbol{I}_3]\boldsymbol{D}\boldsymbol{\Theta} + \boldsymbol{M}_{\text{ref}} \,. \quad (3.46)$$

The balance of momentum for force becomes:

$$\boldsymbol{D}\boldsymbol{F}_t = \boldsymbol{J}_0[\rho \boldsymbol{I}]\ddot{\boldsymbol{U}}_c - \boldsymbol{J}_1[\rho \boldsymbol{I}]\ddot{\boldsymbol{\Theta}} \,, \quad (3.47)$$

and the balance of momentum for the moment is:

$$\boldsymbol{m}' + \hat{\boldsymbol{n}} \times \boldsymbol{f}_t = \int_\Sigma \boldsymbol{s}_\perp \times \ddot{\boldsymbol{u}} \,, \quad (3.48)$$

where $\hat{\boldsymbol{n}}$ is the outward normal to the cross-section. Its first order expansion is $\hat{\boldsymbol{n}} \simeq \hat{\boldsymbol{t}} + \boldsymbol{\theta} \times \boldsymbol{s}_\perp$. First order expansion leads to:

$$\boldsymbol{D}\boldsymbol{M}_t + \hat{\boldsymbol{t}} \times \boldsymbol{F}_t = \boldsymbol{J}_1[\rho \boldsymbol{I}]\ddot{\boldsymbol{U}}_c - \boldsymbol{J}_2[\rho \boldsymbol{I}]\ddot{\boldsymbol{\Theta}} - \boldsymbol{\Theta} \times \hat{\boldsymbol{t}}\boldsymbol{F}\text{ref} \,. \quad (3.49)$$

Finally the dispersion matrix defined in Eq. (3.30) becomes:

$$\boldsymbol{\Gamma} = k \begin{pmatrix} \boldsymbol{0} & \boldsymbol{0} & (\boldsymbol{J}_0[\rho \boldsymbol{I}])^{-1} & \boldsymbol{0} \\ \boldsymbol{0} & \boldsymbol{0} & \boldsymbol{0} & (\boldsymbol{J}_2[\rho \boldsymbol{I}])^{-1} \\ \boldsymbol{J}_0[\boldsymbol{C}_1^*] & \boldsymbol{0} & \boldsymbol{0} & \boldsymbol{0} \\ \boldsymbol{0} & \boldsymbol{J}_2[\boldsymbol{C}_2^*] & \boldsymbol{0} & \boldsymbol{0} \end{pmatrix} , \quad (3.50)$$

where $\boldsymbol{C}_1^* = \boldsymbol{C}_1 + (\boldsymbol{\sigma}_{\text{ref}} : \hat{\boldsymbol{t}} \otimes \hat{\boldsymbol{t}})\boldsymbol{I}_3$, and $\boldsymbol{C}_2^* = \boldsymbol{C}_2 + (\boldsymbol{\sigma}_{\text{ref}} : \hat{\boldsymbol{t}} \otimes \hat{\boldsymbol{t}})\boldsymbol{I}_3$. As a conclusion, the prestressing only affects the values of the wave velocities. The prestressed medium can be thus considered as an equivalent medium of which the material parameters are modified by the prestressing in the HF range.

3.2.4 Effect of material randomness

In the case of material having parameters varying rapidly, at a scale comparable to the scale ε of the wavelength, the transport equation (3.40) can not take into account the scattering phenomena related to these variations. Random perturbations of this parameters of correlation length $l_c \propto \varepsilon$ are considered in order to study the interactions of HF wave propagation with materials varying at the same length scale. However the correlation length has not to be too much high in order to avoid localization phenomena. In this case the evolution of the Wigner measure is given by a radiative transfer equation. For a three-dimensional open medium, the phase space energy density w_α of the energy mode α is the solution of the radiative transfer equation [4, 36, 75]:

$$\dot{w}_\alpha + c_\alpha \hat{\boldsymbol{k}} \cdot \nabla_{\boldsymbol{s}} w_\alpha - |\boldsymbol{k}| \nabla_{\boldsymbol{s}} c \cdot \nabla_{\boldsymbol{k}} w_\alpha + \Sigma_\alpha w_\alpha = \sum_{\beta \in \mathsf{E}} \int_{\mathbb{S}^{d-1}} \sigma_{\alpha\beta}(\boldsymbol{s}, |\boldsymbol{k}|, \hat{\boldsymbol{k}} \cdot \hat{\boldsymbol{p}}) w_\beta(\boldsymbol{s}, \boldsymbol{p}, t) d\Omega(\hat{\boldsymbol{p}}) \,, \quad (3.51)$$

where $\mathbb{S}^{d-1}$ is the unit sphere of $\mathbb{R}^d$ with the uniform probability measure Ω, and E is defined by Eq. (3.39). The scattering cross-section $\sigma_{\alpha\beta}$ gives the rate of energy of a mode β with a wave vector $\boldsymbol{p}$ that is converted to energy of mode α with a wave vector $\boldsymbol{k}$ due to the

scattering on the random inhomogeneities of the medium. The total scattering cross-section $\Sigma_\alpha(\boldsymbol{s}, \boldsymbol{k})$ for the polarization α is defined as:

$$\Sigma_\alpha = \sum_{\beta \in \mathsf{E}} \int_{\mathbb{S}^{d-1}} \sigma_{\alpha\beta}(\boldsymbol{s}, |\boldsymbol{k}|, \hat{\boldsymbol{k}} \cdot \hat{\boldsymbol{p}}) d\Omega(\hat{\boldsymbol{p}}) \,.$$

The scattering cross-section can be computed explicitly from the auto- and cross-correlation spectra of the random perturbations of the mechanical parameters. In this case, the model exhibits the scattering due to random media with continuous fluctuation. If discrete scatterers are considered, then the scattering cross-section of the medium is given by the scattering cross-section of a single scatterer multiplied by the density of scatterers. In any case the Hamiltonian $\omega := c_\alpha |\boldsymbol{k}|$ of Eq. (3.51) is preserved along the energy paths (rays). These results have been adapted to slender structures [88], electromagnetic waves, or the Shrödinger equation in random media [75].

As for a random beam, it is assumed that the material parameters have the form:

$$\begin{aligned} \rho^\varepsilon(s) &= \underline{\rho}(s) \left[1 + \sqrt{\varepsilon} Y_1\left(\frac{s}{\varepsilon}\right)\right] , \\ \frac{1}{E^\varepsilon(s)} &= \frac{1}{\underline{E}(s)} \left[1 + \sqrt{\varepsilon} Y_2\left(\frac{s}{\varepsilon}\right)\right] , \\ \frac{1}{(\kappa\mu)^\varepsilon(s)} &= \frac{1}{\underline{\mu_r}(s)} \left[1 + \sqrt{\varepsilon} Y_3\left(\frac{s}{\varepsilon}\right)\right] , \end{aligned} \tag{3.52}$$

where $(Y_j(s), s \in \mathbb{R}), 1 \leq j \leq 3$ are three real-valued statistically homogeneous and centered second-order stochastic processes with correlation lengths comparable to the wavelength in the medium. $\underline{\rho}(s) = \mathbb{E}\{\rho^\varepsilon(s)\}, \underline{E}(s) = \mathbb{E}\{E^\varepsilon(s)^{-1}\}^{-1}, \underline{\kappa\mu}(s) = \mathbb{E}\{(\kappa\mu)^\varepsilon(s)^{-1}\}^{-1}$ are the average macroscopic density, Young, and reduced shear modulus, $\mathbb{E}\{X\}$ standing for the mathematical expectation of a random variable X. The perturbation amplitude is scaled by $\sqrt{\varepsilon}$ in order to avoid localization while keeping significant effect of the randomness on the propagation of the energy density [75]. Introducing these new parameters in the mechanical equations Eq. (3.12), Eq. (3.13), Eq. (3.14), Eq. (3.15) leads to the new first-order problem:

$$(\boldsymbol{A} + \sqrt{\varepsilon}\boldsymbol{A}_\varepsilon)\partial_t \boldsymbol{X}_\varepsilon = \boldsymbol{P}_1 \partial_s \boldsymbol{X}_\varepsilon + \boldsymbol{P}_0 \boldsymbol{X}_\varepsilon \,, \tag{3.53}$$

where $\boldsymbol{A}_\varepsilon(s)$ is the matrix relative to the randomness of the medium. In the HF limit $\varepsilon \to 0$, the energy density for longitudinal modes w_{P} and transverse modes w_{T} satisfy a radiative transfer equation of the form (3.51) with $d = 1$, $\hat{k} = \pm 1$. It may be show that the latter reduces to [87]:

$$\partial_t w_\alpha + c_\alpha \hat{k} \partial_s w_\alpha - |\boldsymbol{k}| c'_\alpha \partial_k w_\alpha = \Sigma_\alpha(k)(w_\alpha(-k) - w_\alpha(k)) \,, \quad \alpha \in \mathsf{E} \,, \tag{3.54}$$

where E is the set of the energy modes defined by Eq. (3.39) and $\Sigma_\alpha(k)$ is the total scattering cross-section. It gives the amount of energy in the modes α which is scattered to all other modes. Thus in beams no mode conversion occurs on account of the random heterogeneities [87]. The total scattering cross-section is given by:

$$\Sigma_\alpha(k) = \frac{\pi}{2} \zeta_\alpha c_\alpha k^2 S(2k) \,, \tag{3.55}$$

with $S(k) = \frac{1}{2\pi}\int_{\mathbb{R}} R(r)e^{ikr}dr$ the one-dimensional Fourier transform of the normalized correlation function $R(x-y)$ of the random fluctuations of the density and inverse Young and shear modulus, and $\zeta_\alpha = \tilde{\zeta}_\alpha l_c$ is a dimensionless strength factor related to their variation coefficients (or amplitudes) [87]. $R(r)$ is normalized such that $l_c = \int_0^{+\infty} R(r)dr$ is a correlation length of the random fluctuations. Table 3.1 provides some models of correlation. One can define a collision operator by:

$$\mathcal{Q}_\alpha(k) = \Sigma_\alpha(k)(w_\alpha(-k) - w_\alpha(k))\,. \tag{3.56}$$

The wave velocities c_α are given by:

$$\underline{c}_{\mathrm{P}} = \sqrt{\frac{\underline{\underline{E}}}{\underline{\rho}}}\,,$$
$$\underline{c}_{\mathrm{T}} = \sqrt{\frac{\underline{\underline{\kappa\mu}}}{\underline{\rho}}}\,.$$

Table 3.1: Normalized correlation function (NCF) models for beams of correlation length l_c; K_ν is the modified Bessel function of second kind, Γ is the Gamma function, $\nu \in [0,1]$ is the Hurst number in von Karman model (note that the latter reduces to Markov model for $\nu = \frac{1}{2}$), and $\mathbb{1}_{[a,b]}$ is the indicator function valued at 1 on the segment $[a,b]$.

NCF model	$R(r)$	$S(k)$
Gaussian	$\exp\left(-\pi\frac{r^2}{4l_c^2}\right)$	$\frac{l_c}{\pi}\exp\left(-\frac{l_c^2k^2}{\pi}\right)$
Markov	$\exp\left(-\frac{\lvert r\rvert}{l_c}\right)$	$\frac{l_c}{\pi}\left(1+l_c^2k^2\right)^{-1}$
von Karman	$\frac{2^{1-\nu}}{\sqrt{\pi}\Gamma\left(\nu+\frac{1}{2}\right)}\left(\frac{\lvert r\rvert}{l_c}\right)^\nu K_\nu\left(\frac{\lvert r\rvert}{l_c}\right)$	$\frac{l_c}{\pi}\left(1+l_c^2k^2\right)^{-(\nu+\frac{1}{2})}$
Triangular	$2\left(1-\frac{\lvert r\rvert}{l_c}\right)\mathbb{1}_{[-l_c,l_c]}(r)$	$\frac{l_c}{\pi}\mathrm{sinc}^2\left(\frac{kl_c}{2}\right)$
Rayleigh	$\delta\left(\frac{\lvert r\rvert}{2l_c}\right)$	$\frac{l_c}{\pi}$

Thus it has been seen that the energy densities do not couple in an isolated beam in the HF range, even in the random case. The last point to investigate in order to study an entire truss is the behavior of HF waves at junctions. It is shown in the subsequent section that it mixes the different wave modes by conversion rules. This is the subject of the next part of this chapter.

3.3 High-frequency power flow reflection/transmission operators in a beam junction

The HF energy density propagation in a beam is described by the transport equations (3.40). In order to use this model for complex three-dimensional beam trusses, the reflection/transmission processes at the junctions have to be described. They contribute to couple the energy mdoes α. This section deals with the description of the energy density propagation in a junction of two beams, and then an arbitrary number $\mathcal{N}$ of beams. Power flow reflection/transmission operators are derived along the same lines as in Savin [86] for two-dimensional junctions. The subsequent analysis considers the basic case where incident waves are travelling in a single beam and are reflected/transmitted in the other beams connected to the junction. Incidences in several or all members of the junction may be treated by superposition of this simple situation.

3.3.1 Energy transport in coupled structures

3.3.1.1 A junction of two beams

Let us consider two beams occupying the domains Ω_1 and Ω_2 of $\mathbb{R}^3$. They are parameterized by their curvilinear coordinates $\boldsymbol{s} = (s, s_2, s_3)^T \in \mathbb{R}^3$ such that $s \in \mathcal{S}_1 \subset \mathbb{R}$ for beam #1 and $s \in \mathcal{S}_2 \subset \mathbb{R}$ for beam #2. Here $\mathcal{S}_p$, $p = 1, 2$, is an interval of $\mathbb{R}$ such that $\mathcal{C}_p = \Psi_p(\mathcal{S}_p)$ is the curved line in $\mathbb{R}^3$ constituting the neutral fiber of beam #p. Their junction $\Gamma := \partial\Omega_1 \cap \partial\Omega_2$ reduces to a single point $\boldsymbol{x}_0 = \Psi_p(\boldsymbol{s}_0^p)$ in this parametrization. Let $\hat{\boldsymbol{t}}^p$ be the tangent vector to $\mathcal{C}_p$, $p = 1, 2$, pointing outward from beam #p at the junction. Then it is assumed for convenience that $\boldsymbol{s}_0^p$ may be written $\boldsymbol{s}_0^p = s_0\hat{\boldsymbol{t}}^p$ in the local Frenet frame of each beam #p. The Liouville equations (3.40) hold within each beam. However their Hamiltonians $\lambda_\alpha^p(s, \boldsymbol{k}) := c_\alpha^p(s)|\boldsymbol{k}|$ shall be preserved across the interface as in phase space description of geometrical optics [25, 48] where they remain constant along the (energy) rays. This applies even if they are reflected or transmitted by that interface. Here c_α^p stands for the different group velocities of longitudinal ($\alpha = \mathrm{P}_j$, $1 \le j \le 3$) and transverse ($\alpha = \mathrm{T}_j$, $1 \le j \le 3$) waves in beam #p. Thus one has:

$$\lambda_\alpha^p(s_0, \boldsymbol{k}) = \lambda_\beta^q(s_0, \boldsymbol{k}) := \omega\,, \quad \forall p, q = 1, 2\,, \quad \forall \alpha, \beta \in \mathsf{E}\,, \tag{3.57}$$

where E is given by Eq. (3.39). The condition (3.57) holds for either transmitted ($p \neq q$) or reflected ($p = q$) waves. It can be used to determine the reflected and transmitted wavenumbers $|k_\alpha^p|$ from either side of the interface given an incident wavenumber $|k|$. Moreover, the power flow (3.38) is conserved across the junction owing to the Rankine-Hugoniot condition written for the transport equations (3.40) [88]. For example, the energy density travelling in beam #1 and impinging the junction at $\boldsymbol{s}_0$ with an incident wave vector $\boldsymbol{k}$ such that $\boldsymbol{k} \cdot \hat{\boldsymbol{t}}^1 > 0$ is partially reflected and partially transmitted while the overall power flow remains constant. This property reads:

$$\boldsymbol{\pi}_\alpha^1(s_0, \boldsymbol{k}, t) \cdot \hat{\boldsymbol{t}}^1 = \sum_{\beta \in \mathsf{E}} \left(|\boldsymbol{\pi}_\beta^1(s_0, \boldsymbol{k}_\beta^1, t) \cdot \hat{\boldsymbol{t}}^1| + |\boldsymbol{\pi}_\beta^2(s_0, \boldsymbol{k}_\beta^2, t) \cdot \hat{\boldsymbol{t}}^2| \right)\,, \tag{3.58}$$

where the left traces of $\boldsymbol{\pi}_\alpha$ in beam #p at the junction are denoted by:

$$\boldsymbol{\pi}_\alpha^p(s_0, \boldsymbol{k}, t) := \lim_{h \downarrow 0} \boldsymbol{\pi}_\alpha(\boldsymbol{s}_0 \cdot \hat{\boldsymbol{t}}^p - h, \boldsymbol{k}, t)\,. \tag{3.59}$$

Here $c_\alpha^1|\boldsymbol{k}| = c_\beta^p|\boldsymbol{k}_\beta^p|\ \forall \alpha,\beta \in \mathsf{E}$ by Eq. (3.57), and $\boldsymbol{k}_\beta^1 = -|\boldsymbol{k}_\beta^1|\hat{\boldsymbol{t}}^1$, $\boldsymbol{k}_\beta^2 = -|\boldsymbol{k}_\beta^2|\hat{\boldsymbol{t}}^2$. The first and second terms on the right-hand-side in Eq. (3.58) correspond to the fluxes flowing away from the junction in beams #1 and #2, respectively, after reflection and transmission. They read:

$$|\boldsymbol{\pi}_\alpha^p(s_0,\boldsymbol{k},t)\cdot\hat{\boldsymbol{t}}^p| = \sum_{\beta\in\mathsf{E}}\left(\rho_{\alpha\beta}^{pp}(s_0)\boldsymbol{\pi}_\beta^p(s_0,\boldsymbol{k}_\beta^p,t)\cdot\hat{\boldsymbol{t}}^p + \tau_{\alpha\beta}^{pq}(s_0)\boldsymbol{\pi}_\beta^q(s_0,\boldsymbol{k}_\beta^q,t)\cdot\hat{\boldsymbol{t}}^q\right), \tag{3.60}$$

for $p \neq q \in (1,2)$ and $\hat{\boldsymbol{k}}\cdot\hat{\boldsymbol{t}}^p < 0$, with $\boldsymbol{k}_\beta^1 = |\boldsymbol{k}_\beta^1|\hat{\boldsymbol{t}}^1$ and $\boldsymbol{k}_\beta^2 = |\boldsymbol{k}_\beta^2|\hat{\boldsymbol{t}}^2$. $\rho_{\alpha\beta}^{pp}(s_0)$ and $\tau_{\alpha\beta}^{pq}(s_0)$ are power flow reflection/transmission operators of the junction, respectively. The above relations constitute the boundary/interface conditions to be used to solve the transport equations (3.40). It should be noted that they remain valid everywhere within the beams if the convention $\rho_{\alpha\beta}^{pp} = 0$ and $\tau_{\alpha\beta}^{pp} = \delta_{\alpha\beta}$ is adopted for all $s \neq s_0$.

3.3.1.2 A junction of $\mathcal{N}$ beams

Now this analysis can be generalized straightforwardly to a junction of $\mathcal{N} \geq 2$ beams. Eq. (3.60) for the fluxes flowing away from that junction in beam $\#p$ after reflection and transmission reads:

$$|\boldsymbol{\pi}_\alpha^p(s_0,\boldsymbol{k},t)\cdot\hat{\boldsymbol{t}}^p| \;=\; \sum_{\beta\in\mathsf{E}}\left(\rho_{\alpha\beta}^{pp}(s_0)\boldsymbol{\pi}_\beta^p(s_0,\boldsymbol{k}_\beta^p,t)\cdot\hat{\boldsymbol{t}}^p + \sum_{\substack{q=1\\q\neq p}}^{\mathcal{N}}\tau_{\alpha\beta}^{pq}(s_0)\boldsymbol{\pi}_\beta^q(s_0,\boldsymbol{k}_\beta^q,t)\cdot\hat{\boldsymbol{t}}^q\right) \tag{3.61}$$

for $\hat{\boldsymbol{k}}\cdot\hat{\boldsymbol{t}}^p < 0$, where $\boldsymbol{k}_\beta^q = |\boldsymbol{k}_\beta^q|\hat{\boldsymbol{t}}^q$ such that $c_\alpha^p(s_0)|\boldsymbol{k}_\alpha^p| = c_\beta^q(s_0)|\boldsymbol{k}_\beta^q| := \omega$ for $1 \leq p,q \leq \mathcal{N}$, $\alpha,\beta \in \mathsf{E}$ by Eq. (3.57). One may also define linear reflection operators $\mathcal{R}_{\alpha\beta}^{pp} : w_\beta \mapsto w_\alpha$ and transmission operators $\mathcal{T}_{\alpha\beta}^{pq} : w_\beta \mapsto w_\alpha$ provided that Eq. (3.61) is written in terms of the energy densities w_α rather than the flow densities $\boldsymbol{\pi}_\alpha$:

$$|\boldsymbol{\pi}_\alpha^p(s_0,\boldsymbol{k},t)\cdot\hat{\boldsymbol{t}}^p| = \sum_{\beta\in\mathsf{E}}\left(\mathcal{R}_{\alpha\beta}^{pp}(c_\beta w_\beta)^p(s_0,\boldsymbol{k}_\beta^p\cdot\hat{\boldsymbol{t}}^p,t) + \sum_{\substack{q=1\\q\neq p}}^{\mathcal{N}}\mathcal{T}_{\alpha\beta}^{pq}(c_\beta w_\beta)^q(s_0,\boldsymbol{k}_\beta^q\cdot\hat{\boldsymbol{t}}^q,t)\right) \tag{3.62}$$

for $\hat{\boldsymbol{k}}\cdot\hat{\boldsymbol{t}}^p < 0$. Here the same definition as for the flow density, Eq. (3.59), is used for the traces of c_α and w_α.

3.3.2 Computation of reflection/transmission operators for a beam junction

This section outlines how the power flow reflection/transmission operators $\rho_{\alpha_i\beta_j}^{pp}(s_0)$ and $\tau_{\alpha_i\beta_j}^{pq}(s_0)$ may be computed. Some examples are also presented in order to illustrate these results.

3.3.2.1 Theoretical analysis

A junction of $\mathcal{N}$ beams is considered. It is geometrically described by the Euler angles between beam $\#p$ and beam $\#q$. They are denoted by ψ_{pq}, θ_{pq} and φ_{pq} with the usual convention $(\hat{\boldsymbol{n}},\hat{\boldsymbol{b}},\hat{\boldsymbol{t}})$ meaning that the composition of three intrinsic rotations about the

moving frame axes is used to rotate the local Frenet frame of beam $\#p$ to the local frame of beam $\#q$. This rotation is denoted by $\boldsymbol{R}^{qp}$. Hence:

$$\boldsymbol{R}^{qp} = \boldsymbol{R}^{\#}(\varphi_{pq}, \hat{\boldsymbol{t}})\boldsymbol{R}^{\#}(\theta_{pq}, \hat{\boldsymbol{b}})\boldsymbol{R}^{\#}(\psi_{pq}, \hat{\boldsymbol{n}})\,,$$

where $\boldsymbol{R}^{\#}(\alpha, \boldsymbol{e})$ is the matrix corresponding to a rotation of angle α around the axis $\boldsymbol{e}$. Moreover, the beams may be connected at a point which is not on the neutral fiber of the first beam. The offset between the beam $\#p$ and the beam $\#q$ is denoted by the vector $\boldsymbol{\delta}_q^p$ going from the former to the latter. The junction is at $s = s_0$, and it is assumed without loss of generality in the remaining that $s_0 = 0$. It is also considered that waves are incident in beam #1. Fig. 3.2 shows an example of a junction of three beams, and the existing waves in each beam.

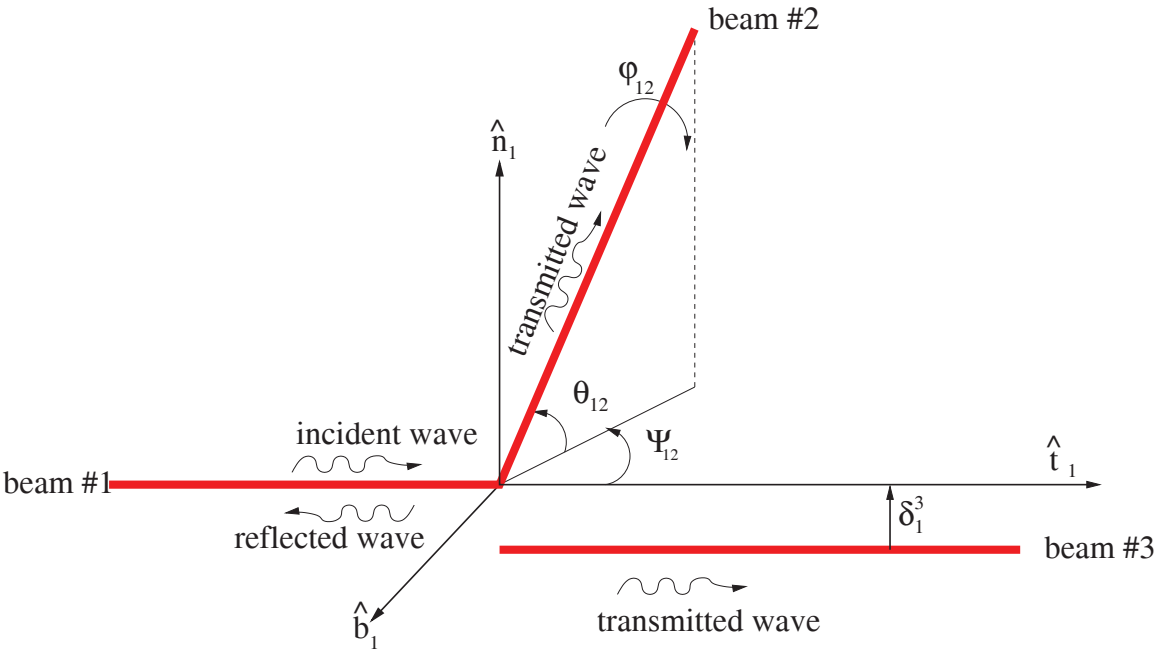

Figure 3.2: A junction of three coupled beams with travelling waves in each beam. The junction is defined by three Euler angles: the first one is ψ_{1q}, the second one is θ_{1q}, and the last one is φ_{1q} using the usual convention $(\hat{\boldsymbol{n}},\hat{\boldsymbol{b}},\hat{\boldsymbol{t}})$ for the junction between beam #1 and beam $\#q$, $q = 2, 3$. $\boldsymbol{\delta}_1^3$ represents the offset between the first and the third beams.

The energy reflection/transmission problem is studied considering first the reflection/transmission problem for planar waves, propagating in the direction $\hat{\boldsymbol{t}}$. The incident waves, travelling in beam #1 in the direction of increasing s may then be written as a linear superposition of the components:

$$\begin{aligned}
u_c^I &= \mathrm{e}^{-\mathrm{i}k_{\mathrm{P}}^1 s} && \text{for a longitudinal motion corresponding to } \hat{\boldsymbol{t}}_1\,,\\
v_c^I &= \mathrm{e}^{-\mathrm{i}k_{\mathrm{T}}^1 s} && \text{for a pure shear motion corresponding to } \hat{\boldsymbol{n}}_1\,,\\
w_c^I &= \mathrm{e}^{-\mathrm{i}k_{\mathrm{T}}^1 s} && \text{for a pure shear motion corresponding to } \hat{\boldsymbol{b}}_1\,,\\
\theta_1^I &= -\mathrm{i}k_{\mathrm{T}}^1 \mathrm{e}^{-\mathrm{i}k_{\mathrm{T}}^1 s} && \text{for a torsional motion corresponding to } \hat{\boldsymbol{t}}_1\,,\\
\theta_2^I &= -\mathrm{i}k_{\mathrm{P}}^1 \mathrm{e}^{-\mathrm{i}k_{\mathrm{P}}^1 s} && \text{for a bending motion corresponding to } \hat{\boldsymbol{n}}_1\,,\\
\theta_3^I &= -\mathrm{i}k_{\mathrm{P}}^1 \mathrm{e}^{-\mathrm{i}k_{\mathrm{P}}^1 s} && \text{for a bending motion corresponding to } \hat{\boldsymbol{b}}_1\,.
\end{aligned} \tag{3.63}$$

The coefficients $\mathrm{i}k_\alpha^1$ of the rotational component make them homogeneous to an angle. The corresponding reflected waves travelling in beam #1 in the direction of decreasing s read:

$$\begin{aligned}
u_c^R &= B_1^1 \mathrm{e}^{\mathrm{i}k_{\mathrm{P}}^1 s}\,,\\
v_c^R &= B_2^1 \mathrm{e}^{\mathrm{i}k_{\mathrm{T}}^1 s}\,,\\
w_c^R &= B_3^1 \mathrm{e}^{\mathrm{i}k_{\mathrm{T}}^1 s}\,,\\
\theta_1^R &= \mathrm{i}k_{\mathrm{T}}^1 C_1^1 \mathrm{e}^{\mathrm{i}k_{\mathrm{T}}^1 s}\,,\\
\theta_2^R &= \mathrm{i}k_{\mathrm{P}}^1 C_2^1 \mathrm{e}^{\mathrm{i}k_{\mathrm{P}}^1 s}\,,\\
\theta_3^R &= \mathrm{i}k_{\mathrm{P}}^1 C_3^1 \mathrm{e}^{\mathrm{i}k_{\mathrm{P}}^1 s}\,.
\end{aligned}$$

Accordingly, the transmitted waves travelling in beam #q in the direction of increasing s for that beam read:

$$\begin{aligned}
u_c^{Tq} &= B_1^q \mathrm{e}^{-\mathrm{i}k_{\mathrm{P}}^q s}\,,\\
v_c^{Tq} &= B_2^q \mathrm{e}^{-\mathrm{i}k_{\mathrm{T}}^q s}\,,\\
w_c^{Tq} &= B_3^q \mathrm{e}^{-\mathrm{i}k_{\mathrm{T}}^q s}\,,\\
\theta_1^{Tq} &= -\mathrm{i}k_{\mathrm{T}}^q C_1^q \mathrm{e}^{-\mathrm{i}k_{\mathrm{T}}^q s}\,,\\
\theta_2^{Tq} &= -\mathrm{i}k_{\mathrm{P}}^q C_2^q \mathrm{e}^{-\mathrm{i}k_{\mathrm{P}}^q s}\,,\\
\theta_3^{Tq} &= -\mathrm{i}k_{\mathrm{P}}^q C_3^q \mathrm{e}^{-\mathrm{i}k_{\mathrm{P}}^q s}\,.
\end{aligned}$$

This description of plane waves is chosen so as to be compatible with the eigenvectors Eq. (3.35) and eigenvalues Eq. (3.33) of the dispersion matrix $\boldsymbol{\Gamma}$. The coefficients B_i and C_i^q are obtained from the continuity of the displacements, rotations, forces, and moments at the junction:

$$\begin{aligned}
\boldsymbol{U}_c^I(0) + \boldsymbol{U}_c^R(0) &= \boldsymbol{R}^{1q}(\boldsymbol{U}_c^{Tq}(0) - \boldsymbol{\Theta}^{Tq}(0) \times \boldsymbol{\delta}_1^q)\,,\\
\boldsymbol{\Theta}^I(0) + \boldsymbol{\Theta}^R(0) &= \boldsymbol{R}^{1q}\boldsymbol{\Theta}^{Tq}(0)\,,\\
\boldsymbol{F}^1(0) &= \sum_{q=2}^{\mathcal{N}} \boldsymbol{R}^{1q}\boldsymbol{F}^q(0)\,,\\
\boldsymbol{M}^1(0) &= \sum_{q=2}^{\mathcal{N}} \boldsymbol{R}^{1q}(\boldsymbol{M}^q(0) - \boldsymbol{F}^q(0) \times \boldsymbol{\delta}_1^q)\,.
\end{aligned} \tag{3.64}$$

$\boldsymbol{F}^q$ and $\boldsymbol{M}^q$ correspond to the net force and net moment in beam #q, respectively, and $\boldsymbol{U}_n f^I$ and $\boldsymbol{\Theta}^I$ are the vectors of the amplitudes of the incident wave for the translational (u_c^I, v_c^I, w_c^I) and rotational $(\theta_1^I, \theta_2^I, \theta_3^I)$ motions respectively. Also $\boldsymbol{U}_c^R$ and $\boldsymbol{\Theta}^R$ are the vectors of amplitudes of the reflected waves for translational and rotational motions respectively, and $\boldsymbol{U}_c^T$ and $\boldsymbol{\Theta}^T$ are the vectors of transmitted waves for translational and rotational motions respectively. $\boldsymbol{R}^{1q}$ is the rotation matrix corresponding to the projection of the local frame of beam #q on the local frame of beam #1. Inserting the constitutive equations (3.12) and (3.13) into Eq. (3.64) yields a linear system in terms of displacement and rotation solely. An extended form of this system is given in the appendix A. It can be easily solved for each type of incident wave and allows to compute the coefficients B_i^q, C_i^q. To be consistent with the transport model (3.40) governing the phase space energy densities, the associated power flows are derived from the generic formula for the energy flux of a HF plane wave propagating in a beam [86]. The transient power flow in beam #q being:

$$\Pi^q = -\mathfrak{Re}\{\boldsymbol{F}^q \cdot \overline{\dot{\boldsymbol{U}}_c^q} + \boldsymbol{M}^q \cdot \overline{\dot{\boldsymbol{\Theta}}^q}\}\,,$$

where $\mathfrak{Re}\{\boldsymbol{z}\}$ denotes the real part of $\boldsymbol{z}$, the time average power flow associated to a plane wave is:

$$< \Pi^q >= \frac{1}{2}\mathfrak{Re}\{\mathrm{i}\omega(\boldsymbol{F}^q \cdot \overline{\boldsymbol{U}_c^q} + \boldsymbol{M}^q \cdot \overline{\boldsymbol{\Theta}^q})\}\,. \tag{3.65}$$

The HF power flow reflection/transmission operators for coupled Timoshenko beams are then defined by:

$$\rho_{\alpha\beta}^{11} = \frac{< \Pi_\alpha^R >}{< \Pi_\beta^I >}, \tag{3.66}$$

$$\tau_{\alpha\beta}^{q1} = \frac{< \Pi_\alpha^{Tq} >}{< \Pi_\beta^I >}, \tag{3.67}$$

respectively. Here $< \Pi_\alpha^R >$ is the time average power flow for the reflected waves corresponding to the mode $\alpha \in \mathsf{E}$, $< \Pi_\alpha^{Tq} >$ is the time average power flow for the transmitted waves corresponding to the mode α in beam $\#q$, and $< \Pi_\beta^I >$ is the time average power flow for an incident wave in the mode β. The linear reflection/transmission operators for the energy densities are given by:

$$\mathcal{R}_{\alpha\beta}^{pp}(c_\beta w_\beta)^p(s_0, \boldsymbol{k}_\beta^p \cdot \hat{\boldsymbol{t}}^p, t) = c_\beta^p \rho_{\alpha\beta}^{pp} w_\beta^p(s_0, k_\beta^p, t)\hat{\boldsymbol{k}}_\beta^p \cdot \hat{\boldsymbol{t}}^p\,,$$
$$\mathcal{T}_{\alpha\beta}^{pq}(c_\beta w_\beta)^q(s_0, \boldsymbol{k}_\beta^q \cdot \hat{\boldsymbol{t}}^q, t) = c_\beta^q \tau_{\alpha\beta}^{pq} w_\beta^q(s_0, k_\beta^q, t)\hat{\boldsymbol{k}}_\beta^q \cdot \hat{\boldsymbol{t}}^q\,.$$

3.3.2.2 Examples

It may be observed by computation that, in the case of a coincident junction (*i.e.* $\boldsymbol{\delta}_i^j = 0$) and in the HF limit, the reflection/transmission operators corresponding to translation incident motions u_c^I, v_c^I, or w_c^I, and rotational reflected/transmitted motions θ_i^R, θ_i^{Tq}, $i = 1, 2$ or 3, are null. This result can be understood as follows: Let us consider a translational incident motion given by Eq. (3.63). Then by Eq. (3.65) and Eq. (3.12), the corresponding power flow is of the order of $O(\omega^2)$. Now for a rotational motion, the power flow is by Eq. (3.13) and the expression of the rotation of an order $O(\omega^4)$. Thus reflection/transmission operators for this kind of displacements vanish in the HF limit. The operators related to rotational incident motions and translational reflected/transmitted motions vanish as well as shown by direct computation. All operators are independent of the circular frequency ω. Fig. 3.4 displays them for two rectangular (*i.e.* symmetric cross-sections) Timoshenko beams ($\mathcal{N} = 2$) with $E_2 = 2E_1$, all other parameters being identical ($\nu_1 = \nu_2$, $\rho_1 = \rho_2$, and $\boldsymbol{J}_1 = \boldsymbol{J}_2$). The Euler angles between the beams at the junction are $-\pi/2 \leq \psi_{12} \leq \pi/2$, $\theta_{12} = \pi/4$ and $\varphi_{12} = 0$. Obviously, the sum of the power flow reflection/transmission operators is equal to one for a given angle. This property expresses energy conservation. Fig. 3.5 displays the reflection/transmission operators for three Timoshenko beams ($\mathcal{N} = 3$) with the same geometrical and mechanical parameters ($E_2 = E_3 = 2E_1$, $\nu_1 = \nu_2 = \nu_3$, $\rho_1 = \rho_2 = \rho_3$, and $\boldsymbol{J}_1 = \boldsymbol{J}_2 = \boldsymbol{J}_3$). The Euler angles between the beams at the junction are $-\pi/2 \leq \psi_{12} \leq \pi/2$, $\theta_{12} = \pi/4$, $\varphi_{12} = 0$, $\psi_{13} = 0$, $\theta_{13} = 0$, and $\varphi_{13} = 0$. Again, the sum of the power flow reflection/transmission operators is equal to one for a given angle. For these situations, the property on the reflection/transmission operators related to the rotational/translational motions outlined above is retrieved. The last case in Fig. 3.6 represents a junction with a shift between the connecting points of the beams such that $\boldsymbol{\delta}_i^j \neq 0$. In this case, all the modes are likely be solicited at the junction.

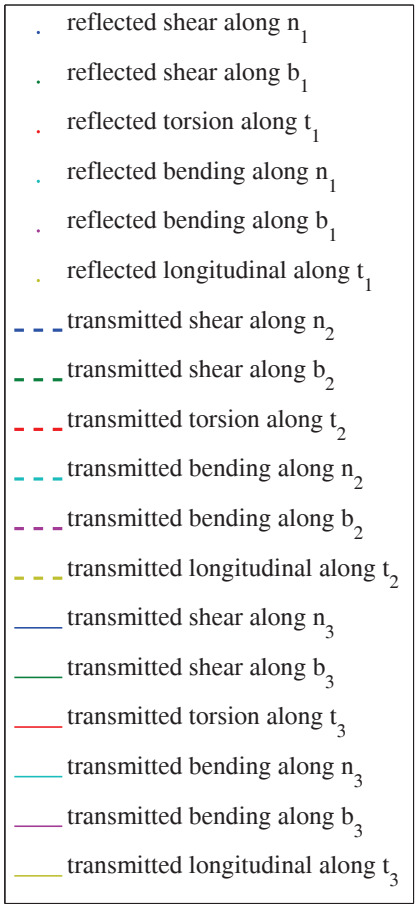

Figure 3.3: Legend corresponding to the reflection/transmission operators for the representation on Fig. 3.4, Fig. 3.5, and Fig. 3.6.

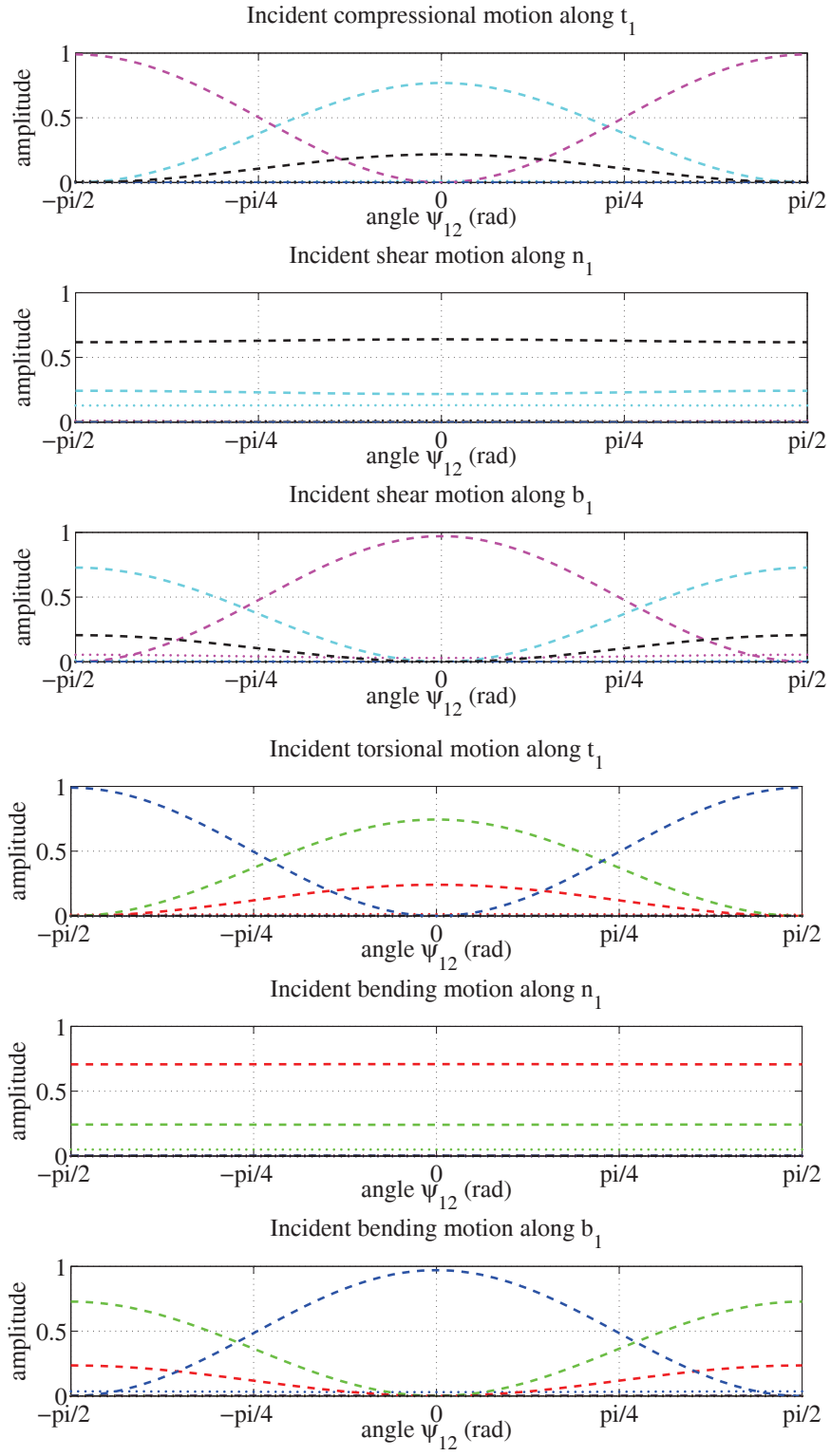

Figure 3.4: Evolution of the power flow reflection/transmission coefficients as functions of the angle ψ_{12} for a junction of two Timoshenko beams with $E_2 = 2E_1$, $\nu_1 = \nu_2$, $\rho_1 = \rho_2$, and $\boldsymbol{J}_1 = \boldsymbol{J}_2$. The Euler angles at the junction are $-\pi/2 \leq \psi_{12} \leq \pi/2$, $\theta_{12} = \pi/3$, and $\varphi_{12} = 0$.

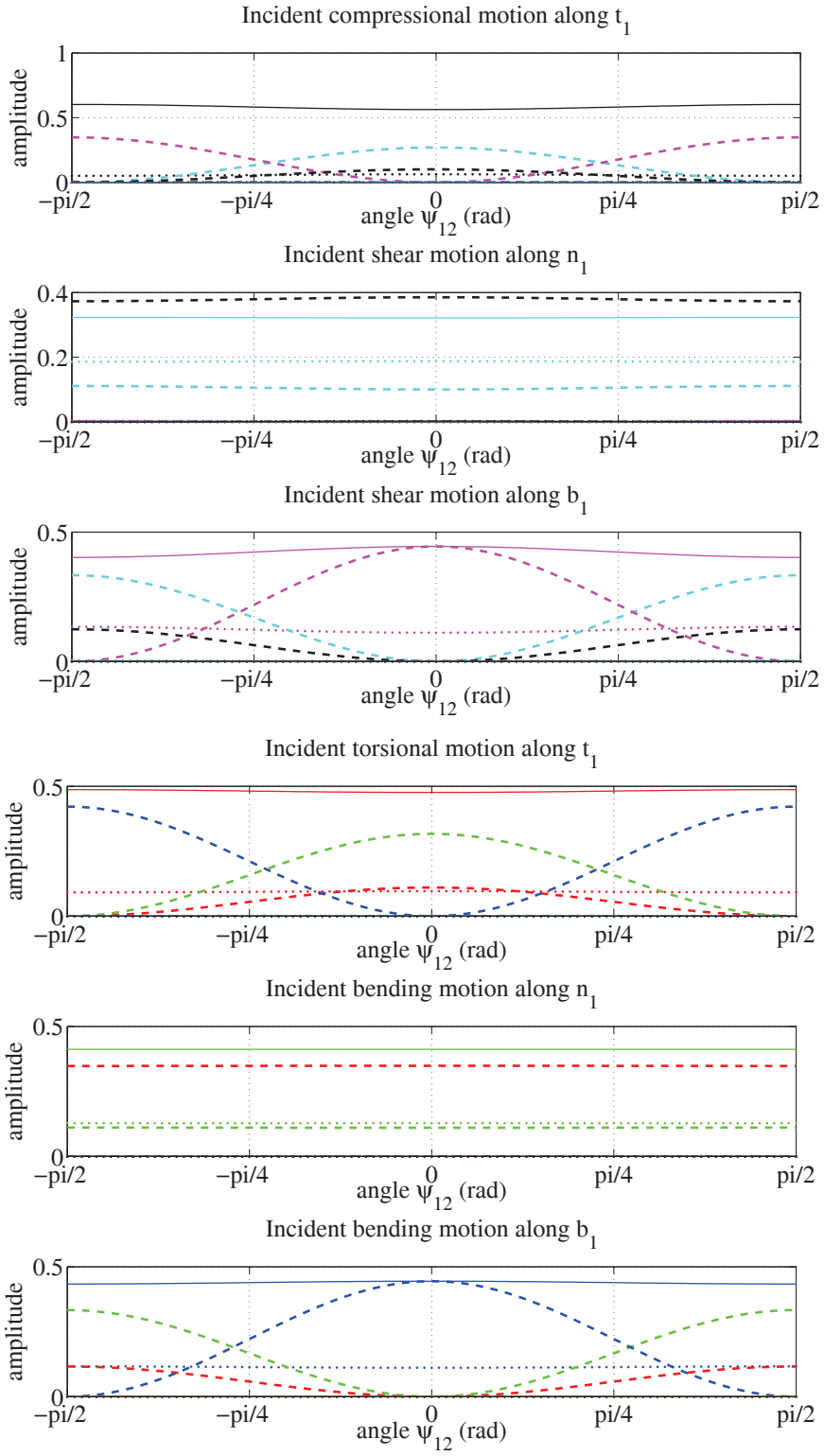

Figure 3.5: Evolution of the power flow reflection/transmission coefficients as functions of the angle ψ_{12} for a junction of three Timoshenko beams with $E_2 = 2E_1 = 2E_3$, $\nu_1 = \nu_2 = \nu_3$, $\rho_1 = \rho_2 = \rho_3$, and $\boldsymbol{J}_1 = \boldsymbol{J}_2 = \boldsymbol{J}_3$. The Euler angles between the beams at the junction are $-\pi/2 \leq \psi_{12} \leq \pi/2$, $\theta_{12} = \pi/3$, $\varphi_{12} = 0$, $\psi_{13} = 0$, $\theta_{13} = 0$, and $\varphi_{13} = 0$.

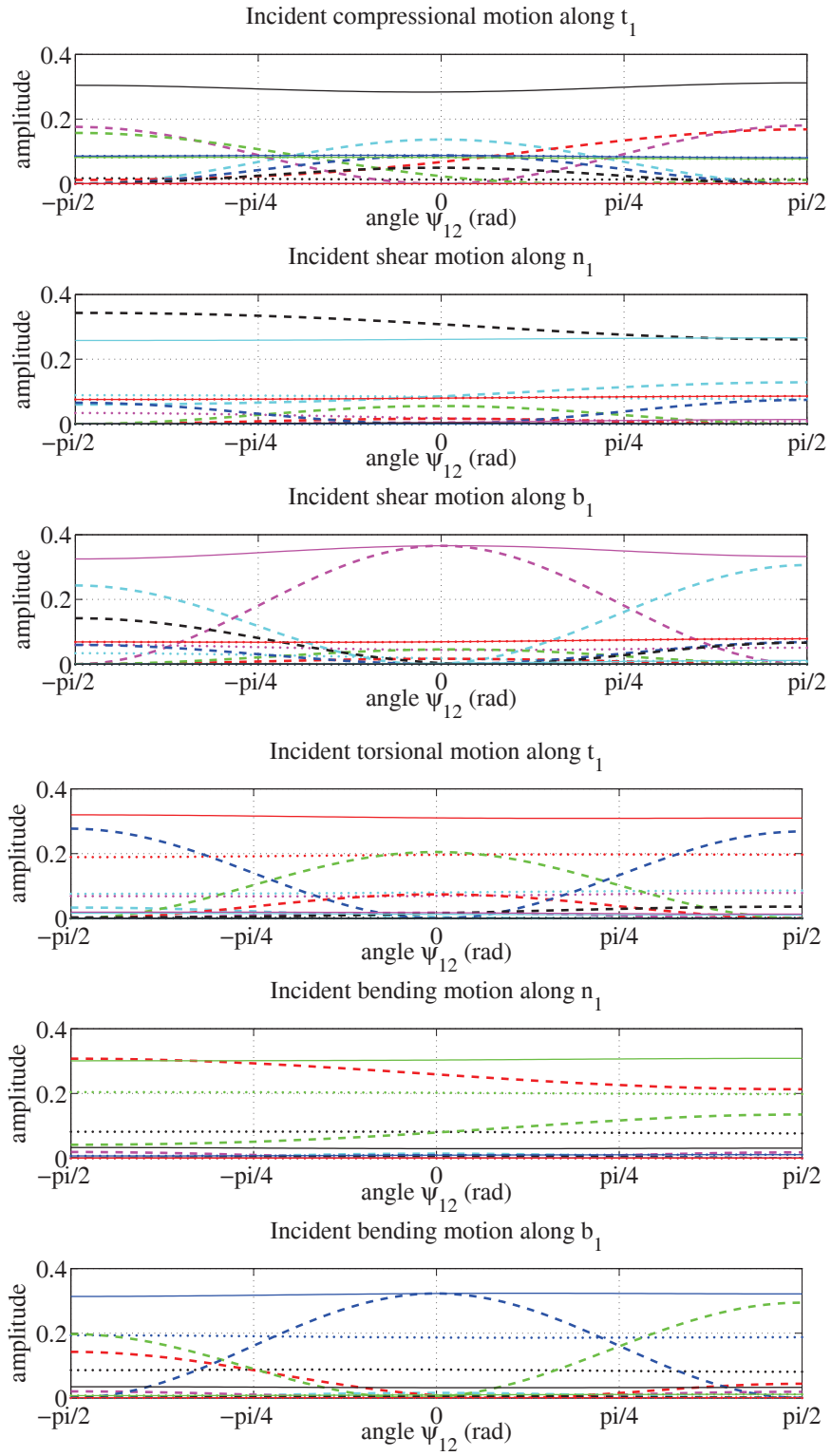

Figure 3.6: Evolution of the power flow reflection/transmission coefficients as functions of the angle ψ_{12} for a junction of three Timoshenko beams with an offset set to $\delta_1^2 = \hat{\boldsymbol{n}}_1 + \hat{\boldsymbol{b}}_1$ between the first and the second beam. The mechanical parameters are set to with $E_2 = 2E_1 = 2E_3$, $\nu_1 = \nu_2 = \nu_3$, $\rho_1 = \rho_2 = \rho_3$, and $\boldsymbol{J}_1 = \boldsymbol{J}_2 = \boldsymbol{J}_3$. The Euler angles between the beams at the junction are $-\pi/2 \leq \psi_{12} \leq \pi/2$, $\theta_{12} = \pi/3$, $\varphi_{12} = 0$, $\psi_{13} = 0$, $\theta_{13} = 0$, and $\varphi_{13} = 0$.

3.4 Conclusions

The HF behavior of an entire truss can be studied through the evolution of its energy density. First it has been shown that inside a beam the evolution of its vibrational energy density follows a transport equation (3.40) for a deterministic medium and a radiative transfer equation (3.54) for the case of random materials. The propagating energetic modes are longitudinal modes (gathering the compressional and the bending ones), and transverse modes (gathering the torsional and the shearing ones). There is no coupling between modes inside the beams and so all the coupling occurs at the junctions as described by Eq. (3.62). At a junction the energy densities of the different energetic modes are mixed thanks to reflection/transmission phenomena. They are quantified by reflection/transmission operators (Eq. (3.66) and Eq. (3.67)) computed from the transmission conditions of planar waves, Eq. (3.64). It has been remarked that if there is no offset between beams then the rotational (torsional and bending modes) and translational (compressional and shearing modes) energies are uncoupled. This means that no modes of the translational(respectively rotational) set can exist if the initial condition does not contain an other member of the translational (respectively rotational) set. The numerical computation of these operators has been validated by a requirement of energy conservation. In the next chapter the transport or radiative transfer equations will be discretized in order to be numerically integrated.

Chapter 4

The Runge-Kutta discontinuous finite element method for transport equations

Discontinuities in the velocity fields c_α at the junction do not allow to use classical finite element method to solve numerically the transport equation (3.40) and the radiative transfer equation (3.54) with the interface condition of Eq. (3.58) or Eq. (3.61). Indeed, although the overall power flow density is continuous across the junction owing to the Rankine-Hugoniot condition, the energy density itself does not necessarily have to be continuous across that junction. Therefore a discontinuous finite element method [14, 18, 41] is used to solve Eq. (3.40) or Eq. (3.54) together with the reflection/transmission conditions of Eq. (3.61). The theoretical background of the discontinuous method is recalled in Sect. 4.1 below, while the numerical implementation issues are addressed in Sect. 4.2. The last part of this chapter deals with the time integration by a strong stability-preserving Runge-Kutta scheme. The dissipation and dispersion errors of the numerical scheme will also be studied.

4.1 Discontinuous finite elements in one-dimensional wave guides

The discontinuous finite element method for the transport equations (3.40) or (3.54) is first written on a single beam $s \in \mathcal{S}$. Let us consider the subdivision $\mathcal{T}_h = \cup_{r=1}^{\mathsf{K}} \mathsf{D}_r$ of $\mathcal{S}$ (which is now assumed to be bounded) into K non-overlapping subdomains, or finite elements D_r. These elements are defined by $\mathsf{D}_r = [s_{r-\frac{1}{2}}, s_{r+\frac{1}{2}}]$, and its length is denoted by $\Delta s_r = s_{r+1/2} - s_{r-1/2}$. The largest element size of this mesh is $h = \max_{1\leq r\leq \mathsf{K}} |\Delta s_r|$. The group velocities of the energetic mode α over the element r are denoted by c_α^r. They are not necessarily continuous but constant over the element. Here $|k|$ is a fixed parameter, and the w_α's are considered as functions of $\hat{k}$, the direction of propagation, rather than k. A variational formulation of the equations (3.54) in an *ad hoc* functional space W_h defined

on $\mathcal{T}_h$ is: Find $w_\alpha \in \mathsf{W}_h$, $\alpha \in \mathsf{E}$, such that

$$\begin{aligned}\int_{\mathsf{D}_r} \Big(\Big(\partial_t w_\alpha(s,\hat{k},t) - \Sigma_\alpha\big(k\big)(\ w_\alpha(s,-\hat{k},t) - w_\alpha(s,\hat{k},t)\big)\Big)v - c_\alpha \hat{k} w_\alpha(s,\hat{k},t)\partial_s v\Big)\, ds \\ = -\Big[c_\alpha^r \hat{k} w_\alpha v\Big]_{s_{r-\frac{1}{2}}}^{s_{r+\frac{1}{2}}} \\ = -\big[\boldsymbol{\pi}_\alpha \cdot \hat{\boldsymbol{t}}^r\, v\big]_{s_{r-\frac{1}{2}}}^{s_{r+\frac{1}{2}}}\ , \quad \forall v(s,\hat{k}) \in \mathsf{V}_h\,, \end{aligned} \tag{4.1}$$

where V_h is a test space of piecewise continuous functions on $\mathcal{T}_h$. The power flow densities $\boldsymbol{\pi}_\alpha(s,\hat{\boldsymbol{k}},t)$ in the above formulation are defined by Eq. (3.41), and $\hat{\boldsymbol{t}}^r$ is the unit tangent vector to the mean fiber of D_r pointing from $s_{r-\frac{1}{2}}$ to $s_{r+\frac{1}{2}}$. Then the unit outward normal $\hat{\boldsymbol{t}}^r_{\text{out}}$ of this element is defined so as to point outward D_r at $\partial\mathsf{D}_r = \{s_{r-\frac{1}{2}}, s_{r+\frac{1}{2}}\}$. As the sought solutions w_α of Eq. (4.1) may be discontinuous at a junction of beams, or at the interfaces between elements, the *a priori* global space W_h is defined as $\mathsf{W}_h = \bigoplus_{r=1}^{\mathsf{K}} \mathsf{W}_h^r$, where the locally defined trial spaces $\mathsf{W}_h^r \subseteq H^1(\mathsf{D}_r)$ do not enforce any particular boundary conditions on $\partial\mathsf{D}_r$. As a consequence of the lack of such conditions for the local solution and the test functions, the former is *a priori* multiply defined at the interfaces between elements (a junction being only one of them). Thus the boundary flux $\boldsymbol{\pi}_\alpha \cdot \hat{\boldsymbol{t}}^r$ in Eq. (4.1) is not uniquely defined. That is why it is replaced by a numerical flux $\boldsymbol{\pi}^*_\alpha$, which depends on the traces of w_α from both sides of an interface between elements. Thus the discontinuous version of Eq. (4.1) reads:

$$\begin{aligned}\int_{\mathsf{D}_r} \Big(\Big(\partial_t w_\alpha(s,\hat{k},t) - \Sigma_\alpha\big(k\big)(w_\alpha(s,-\hat{k},t) - w_\alpha(s,\hat{k},t))\Big)v - w_\alpha(s,\hat{k},t) c_\alpha^r \hat{k}\partial_s v)\Big)\, ds \\ = -\big[\boldsymbol{\pi}^*_\alpha \cdot \hat{\boldsymbol{t}}^r\, v\big]_{s_{r-\frac{1}{2}}}^{s_{r+\frac{1}{2}}}\ , \quad \forall v(s,\hat{k}) \in \mathsf{V}_h^r\,, \end{aligned} \tag{4.2}$$

where V_h^r is the local test space defined by $\mathsf{V}_h = \bigoplus_{r=1}^{\mathsf{K}} \mathsf{V}_h^r$. The numerical flux $\boldsymbol{\pi}^*_\alpha$ at the interface $s = s_{r+\frac{1}{2}}$, say, is constructed from the computed values of $w_\alpha(s_{r+\frac{1}{2}},\hat{k},t)$ in W_h^r (the trace of w_α at $s_{r+\frac{1}{2}}$ in D_r) and $w_\alpha(s_{r+1-\frac{1}{2}},\hat{k},t)$ in W_h^{r+1} (the trace of w_α at $s_{r+\frac{1}{2}}$ in D_{r+1}) so as to be consistent and conservative. Let:

$$\boldsymbol{\pi}^*_\alpha(s_{r+\frac{1}{2}}) := \boldsymbol{\pi}^*(s_{r+\frac{1}{2}}; (c_\alpha w_\alpha)^r, (c_\alpha w_\alpha)^{r+1}) \tag{4.3}$$

for $w_\alpha(s_{r+\frac{1}{2}},\hat{k},t)$ in W_h^r and $w_\alpha(s_{r+1-\frac{1}{2}},\hat{k},t)$ in W_h^{r+1}, recalling the definition (3.59). Then consistency reads:

$$\boldsymbol{\pi}^*\left(s_{r+\frac{1}{2}}; c_\alpha w_\alpha, c_\alpha w_\alpha\right) = c_\alpha w_\alpha \hat{\boldsymbol{k}}\big|_{s=s_{r+\frac{1}{2}}}\,,$$

meaning that the true energy flux (3.41) is recovered when $\boldsymbol{\pi}^*$ is considered with a continuous function. As for conservation it reads:

$$\boldsymbol{\pi}^*(s_{r+\frac{1}{2}}; w_\alpha^r, w_\alpha^{r+1}) \cdot \hat{\boldsymbol{t}}^r + \boldsymbol{\pi}^*(s_{r+1-\frac{1}{2}}; w_\alpha^r, w_\alpha^{r+1}) \cdot \hat{\boldsymbol{t}}^{r+1} = 0$$

at $\{s_{r+\frac{1}{2}}\} = \partial\mathsf{D}_r \cap \partial\mathsf{D}_{r+1}$.

4.2 Numerical implementation

Four main ingredients are needed to complete the numerical implementation of the discontinuous method of Eq. (4.2) once the subdivision $\mathcal{T}_h$ has been performed: the definition of the numerical flux function $\boldsymbol{\pi}^*$ on all elements, the choice of the trial spaces W_h^r, the choice of the test spaces V_h^r, and the choice of a time-integration scheme.

4.2.1 Numerical fluxes

The numerical fluxes ensuring the stability and consistency of the discontinuous method for transport equations have the form [14, 18]:

$$\boldsymbol{\pi}^*(s_{r+\frac{1}{2}}; w_\alpha^r, w_\alpha^{r+1}) = \frac{1}{2}(w_\alpha^r + w_\alpha^{r+1})\hat{\boldsymbol{k}} + A_r(w_\alpha^r - w_\alpha^{r+1})\hat{\boldsymbol{t}}^r\,, \tag{4.4}$$

where A_r is a positive scalar. For example, the upwind flux corresponds to $A_r = \frac{1}{2}|\hat{\boldsymbol{k}}\cdot\hat{\boldsymbol{t}}^r|$ and the Lax-Friedrichs flux corresponds to $A_r = \frac{1}{2}$. Let $\mathcal{I}_r$ be the set of indices of the beam elements which are connected to the beam element $\#r$. Invoking Eq. (3.62), the expression (4.4) is generalized as follows for an interface (a junction) $\{s_{r+\frac{1}{2}}\} = \{s_{r'-\frac{1}{2}}\} = \partial\mathsf{D}_r \cap \partial\mathsf{D}_{r'}$, $r \neq r' \in \mathcal{I}_r$, where the group velocities c_α are discontinuous. For $\hat{k} = \hat{\boldsymbol{k}}\cdot\hat{\boldsymbol{t}}^r < 0$:

$$\boldsymbol{\pi}_\alpha^*(s_{r+\frac{1}{2}}, t)\cdot\hat{\boldsymbol{t}}^r = \sum_{\beta\in\mathsf{E}}\Big(\mathcal{R}_{\alpha\beta}^{rr}(c_\beta w_\beta)^r(s_{r+\frac{1}{2}}, \hat{\boldsymbol{k}}_\beta^r\cdot\hat{\boldsymbol{t}}^r, t) + \sum_{r'\in\mathcal{I}_r}\mathcal{T}_{\alpha\beta}^{rr'}(c_\beta w_\beta)^{r'}(s_{r'-\frac{1}{2}}, \hat{\boldsymbol{k}}_\beta^{r'}\cdot\hat{\boldsymbol{t}}^{r'}, t)\Big)\,, \tag{4.5}$$

where $\hat{k}_\beta^r = \frac{\hat{k}_\beta^r}{|k|}$and for $\hat{k} = \hat{\boldsymbol{k}}\cdot\hat{\boldsymbol{t}}^r > 0$:

$$\boldsymbol{\pi}_\alpha^*(s_{r+\frac{1}{2}}, t)\cdot\hat{\boldsymbol{t}}^r = \boldsymbol{\pi}_\alpha^r(s, \hat{\boldsymbol{k}}, t)\cdot\hat{\boldsymbol{t}}^r\,. \tag{4.6}$$

This choice corresponds to an upwind numerical flux whenever $\mathcal{R}_{\alpha\beta}^{rr} \equiv 0$ and $\mathcal{T}_{\alpha\beta}^{rr'} \equiv \delta_{\alpha\beta}$ at any point s which is not a beam junction, in which case $\mathcal{I}_r = \{r+1\}$. Eq. (4.5) corresponds to a junction where the elements are connected at $s_{r+1/2}$ and $s_{r'-1/2}$. The expression Eq. (4.5) may be generalized easily to junctions for which $\hat{\boldsymbol{k}}\cdot\hat{\boldsymbol{t}}^r \neq \hat{\boldsymbol{k}}\cdot\hat{\boldsymbol{t}}^{r'}$ and to junctions located at $s_{r-\frac{1}{2}}$. All the possible eventuality of junctions are displayed in Fig. 4.1. The numerical fluxes are then given by:

$$\begin{aligned}\boldsymbol{\pi}_\alpha^*(s_{r-\frac{\hat{k}}{2}}, t)\cdot\hat{\boldsymbol{t}}^r = \sum_{\beta\in\mathsf{E}}\Big(&\mathcal{R}_{\alpha\beta}^{rr'}(c_\beta w_\beta)^r(s_{r-\frac{\hat{k}}{2}}, \hat{\boldsymbol{k}}_\beta^r\cdot\hat{\boldsymbol{t}}^r, t)\\ &+ \sum_{r'\in\mathcal{I}_{r-\frac{\hat{k}}{2}}}\mathcal{T}_{\alpha\beta}^{rr'}(c_\beta w_\beta)^{r'}(s_{r'+\hat{k}_\beta^{r'}/2}, \hat{\boldsymbol{k}}_\beta^{r'}\cdot\hat{\boldsymbol{t}}^{r'}, t)\Big)\,,\end{aligned} \tag{4.7}$$

and

$$\boldsymbol{\pi}_\alpha^*(s_{r+\frac{\hat{k}}{2}}, t)\cdot\hat{\boldsymbol{t}}^r = \boldsymbol{\pi}_\alpha^r(s, \hat{\boldsymbol{k}}, t)\cdot\hat{\boldsymbol{t}}^r\,, \tag{4.8}$$

recalling that, from Eq. (3.57), $\hat{\boldsymbol{k}}_\beta^r = -\frac{c_\alpha^r}{c_\beta^r}\hat{\boldsymbol{k}}$, $\hat{k}_\beta^r$ is the sign of $\hat{\boldsymbol{k}}_\beta^r\cdot\hat{\boldsymbol{t}}^r$, and $\hat{\boldsymbol{k}}_\beta^{r'} = \frac{c_\alpha^r}{c_\beta^{r'}}\hat{k}\hat{\boldsymbol{t}}_{\text{out}}^{r'}$. At last $\mathcal{I}_{r\pm\frac{1}{2}}$ denotes the left $(-)$ or right $(+)$ indices of the connected elements.

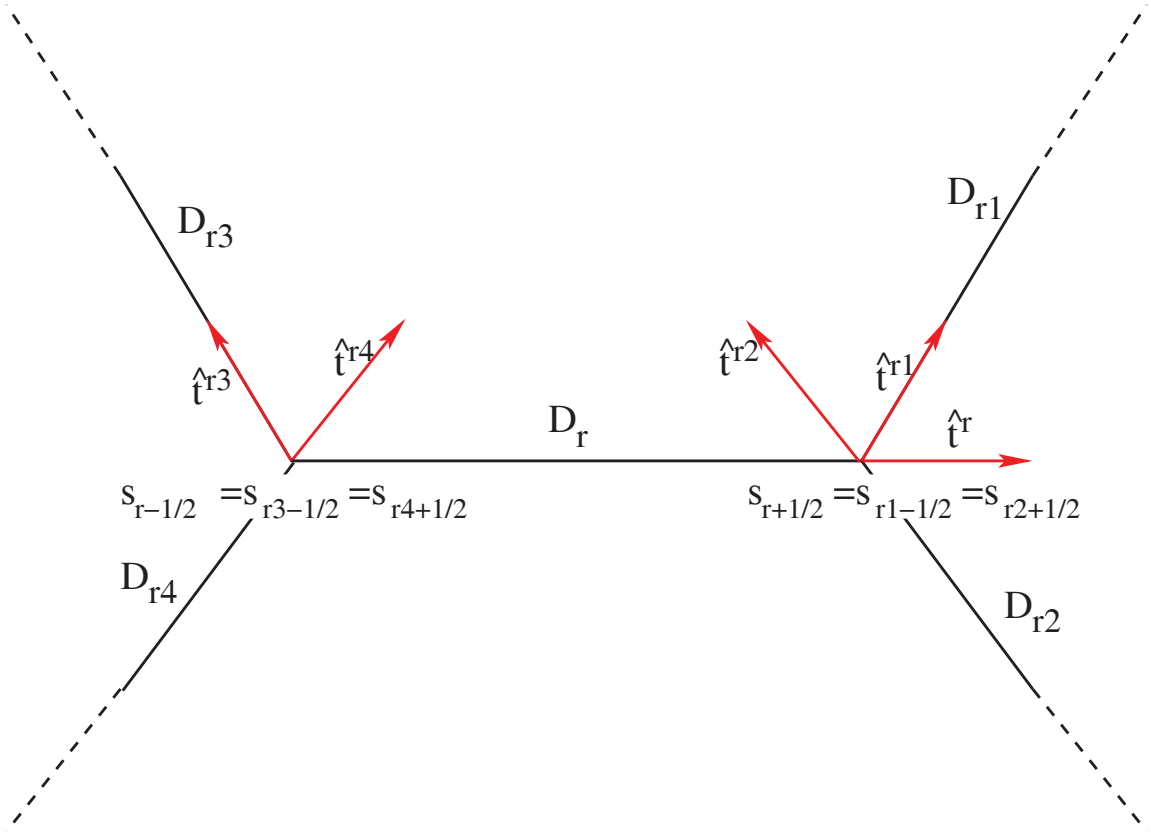

Figure 4.1: Sketch of all the situations of junction: the element D_r is connected on the right to the elements D_{r1} and D_{r2} and on the left to the elements D_{r3} and D_{r4}. The normals of each element are displayed in red. The latter are fixed to point from $s_{r-\frac{1}{2}}$ to $s_{r+\frac{1}{2}}$.

4.2.2 Approximation space

The local approximation spaces W_h^r used for the expansion of the solution of Eq. (4.2) are constructed as follows:

$$\mathsf{W}_h^r = \{w|_{\mathsf{D}_r} \in \mathbb{P}_P(\mathsf{D}_r), 1 \leq r \leq \mathsf{K}\}\,, \tag{4.9}$$

where $\mathbb{P}_P(\mathsf{D}_r) \subset H^1(\mathsf{D}_r)$ is typically a finite-dimensional set of univariate polynomials of maximum order P. Two approaches may be considered to define the trial functions in W_h^r: a nodal approximation by Lagrange interpolation, or a modal approximation by orthonormal polynomials.

4.2.2.1 Nodal approximation

In the nodal approximation, the approximate solution $\tilde{w}_\alpha$ of Eq. (4.2) on the actual element $\mathsf{D}_r = [s_{r-1/2}, s_{r+1/2}]$ is expanded with the Lagrange polynomials of order up to P defined on the reference element $\hat{\mathsf{D}} = [-1, 1]$ as:

$$\mathsf{G}_m(\xi) = \prod_{\substack{0\leq n\leq P\\ n\neq m}} \frac{\xi - \xi_n}{\xi_m - \xi_n}\,, \quad \xi \in \hat{\mathsf{D}}\,,$$

where $(\xi_m)_{0\leq m\leq P}$ are the interpolation nodes on the reference element. The linear mapping between the reference element and the actual element D_r is given by:

$$s^r(\xi) = s_{r-1/2} + \left(\frac{1+\xi}{2}\right)\Delta s_r\,.$$

The approximate solution $\tilde{w}_\alpha$ is then given as:

$$\tilde{w}_\alpha(s,\hat{k},t)|_{\mathsf{D}_r} = \mathcal{I}_P w_\alpha(s,\hat{k},t) = \sum_{m=0}^{P} w_\alpha(s_m^r,t,\hat{k})\mathsf{G}_m(\xi)\,, \tag{4.10}$$

where $\mathcal{I}_P u$ is the interpolation operator used for discrete approximations [40]. The nodes $(s_m^r = s^r(\xi_m))_{0\leq m\leq P}$ form the set of interpolation nodes on D_r. The unknowns are then the values of w_α at those interpolation nodes. Moreover the discrete approximation has the following property:

$$\mathcal{I}_P w_\alpha(s_m^r) = w_\alpha(s_m^r)\,. \tag{4.11}$$

It means that at the interpolation nodes, the interpolated values match the exact solution. The error between the exact solution w_α and the approximate solution $\tilde{w}_\alpha$ of Eq. (4.2) is called the truncation error.

4.2.2.2 Modal approximation

An other method of approximation is to use an expansion on a family of orthogonal polynomials. In that approach, the trial functions are orthonormal on the reference element $\hat{\mathsf{D}}$ for a given scalar product. One class of polynomials satisfying this property is the normalized Jacobi polynomials. It is convenient to focus on this class because it has been extensively studied and has nice convergence properties for non periodic functions [40]. The modal approximation using the Jacobi polynomials on the element D_r is given in this case by:

$$\tilde{w}_\alpha(s,\hat{k},t)|_{\mathsf{D}_r} = \mathcal{P}_P w_\alpha(s,\hat{k},t) = \sum_{m=0}^{P} \hat{w}_{\alpha m}^r(\hat{k},t)\mathsf{J}_m^{(a,b)}(\xi)\,, \tag{4.12}$$

where $\mathcal{P}_P u$ is the orthogonal projection operator used for the continuous expansion of u [40], and $\mathsf{J}_m^{(a,b)}$ denotes the normalized Jacobi polynomial of order m. It is defined from the usual Jacobi polynomial $\tilde{\mathsf{J}}_m^{(a,b)}$ by:

$$\mathsf{J}_m^{(a,b)}(\xi) = \frac{\tilde{\mathsf{J}}_m^{(a,b)}(\xi)}{\sqrt{\gamma_m}}\,,$$

where γ_m is the normalization constant such that:

$$< \tilde{\mathsf{J}}_m^{(a,b)}, \tilde{\mathsf{J}}_n^{(a,b)} >= \int_{\hat{\mathsf{D}}} \tilde{\mathsf{J}}_m^{(a,b)}(\xi)\tilde{\mathsf{J}}_n^{(a,b)}(\xi)p^{(a,b)}(\xi)d\xi = \gamma_m\delta_{mn}\,,$$

and $p^{(a,b)}(\xi) = (1-\xi)^a(1+\xi)^b$ is a weight function. It is given by:

$$\gamma_m = \frac{2^{a+b+1}(m+a)!(m+b)!}{(2m+a+b+1)(m+a+b)!m!}\,.$$

The normalized Jacobi polynomials are thus orthonormal:

$$< \mathsf{J}_m^{(a,b)}, \mathsf{J}_n^{(a,b)} >= \delta_{mn}\,. \tag{4.13}$$

More details about these polynomials are given in the appendix B.

By construction, the degrees of freedom $\hat{w}^r_{\alpha m}$ are the projections of the solution w_α on the normalized Jacobi polynomials $\mathsf{J}^{(a,b)}_m$ with the inner product of Eq. (4.13). They are given by:

$$\hat{w}^r_{\alpha m}(\hat{k},t) = \int_{\hat{\mathsf{D}}} w_\alpha(s^r(\xi),\hat{k},t)\mathsf{J}^{(a,b)}_m(\xi)p^{(a,b)}(\xi)d\xi\,. \tag{4.14}$$

The modal approach has a direct link with the nodal approach as shown in the next section.

4.2.2.3 Link between the modal and nodal approaches

The integral (4.14) may be evaluated using a Gauss-Jacobi quadratures. The latter are defined for an regular function $u(\xi)$ on $[-1,1]$ by:

$$\int_{-1}^{+1} u(\xi)p^{(a,b)}(\xi)d\xi \simeq \sum_{j=0}^{N_p} p_j u(\xi_j)\,, \tag{4.15}$$

where N_p+1 is the number of quadrature points, $(\xi_j)_{0\leq j\leq N_p}$, and $(p_j)_{0\leq j\leq N_p}$ are the associated weights. The above quadrature is then exact provided that u is a polynomial of degree $N \leq 2N_p+1$. It can be shown that a choice of the interpolation points ξ_j ensuring an uniform convergence for a smooth function u corresponds to the zeros of orthogonal polynomials of degree N_p+1 (typically the Jacobi polynomials $\tilde{\mathsf{J}}^{(a,b)}_{N_p+1}$ [77]). If the interpolation set is chosen differently, then Runge effects outbreak and become more important as N_p increases. The Runge effect corresponds to artificial oscillations arising when using polynomial interpolation of high degrees.

The set of interpolation points built as above does not include the extremities of the segment $[-1,+1]$. One can choose to add them, the set of interpolation points being then the zeros of $(\tilde{\mathsf{J}}^{(a,b)}_{N_p})'$, with $\tilde{\mathsf{J}}^{(a,b)}_{N_p}$ is the Jacobi polynomial of order N_p, and $\{-1,+1\}$. This quadrature is called a Gauss-Lobatto-Jacobi quadrature. The expansion is then exact for polynomials of orders up to $2N_p-1$. That quadrature presents the advantage to give the value of the function u on the edges of the element [70], leading to an exact interpolation of its trace on that edges owing to Eq. (4.11). This may be advantageous for a discontinuous finite element scheme since the trace of the approximate solution is necessary to define the numerical flux across an interfaces between elements, as given by Eq. (4.7). Applying this quadrature to the modal coefficient (4.14) leads to:

$$\hat{w}^r_{\alpha m}(\hat{k},t) \simeq \frac{1}{\hat{\gamma}_m}\sum_{j=0}^{N_p} p_j w_\alpha(s^r_j,\hat{k},t)\mathsf{J}^{(a,b)}_m(\xi_j)\,, \tag{4.16}$$

where $\hat{\gamma}_m$ is the "discrete" norm of $\mathsf{J}^{(a,b)}_m$ given by:

$$\hat{\gamma}_m = \sum_{j=0}^{N_p} p_j \left(\mathsf{J}^{(a,b)}_m(\xi_j)\right)^2\,.$$

Using a Gauss-Jacobi quadrature, one has $\hat{\gamma}_m = 1$. The Gauss-Lobatto-Jacobi quadrature rule introduces error by approximating the integral as a sum. This error is called aliasing error. It is given by [40, p.114]:

$$A_{N_p} w_\alpha = \sum_{k>N_p}^{\infty} (\mathcal{I}_{N_p} \mathsf{J}_k^{(a,b)}) \hat{w}_{\alpha k}^r \, .$$

It can be seen as a contamination of the discrete coefficients (4.16) by the high frequencies of the continuous approximation when performing a Gauss-Lobatto-Jacobi quadrature. Inserting the expression of the coefficients (4.16) into Eq. (4.12) gives:

$$\tilde{w}_\alpha(s, \hat{k}, t)|_{\mathsf{D}_r} \simeq \sum_{m=0}^{P} \mathsf{J}_m^{(a,b)}(\xi) \left(\sum_{j=0}^{N_p} p_j w_\alpha(s_j^r, \hat{k}, t) \mathsf{J}_m^{(a,b)}(\xi_j) \right) \, .$$

Setting $N_p = P$ yields:

$$\tilde{w}_\alpha(s, \hat{k}, t)|_{\mathsf{D}_r} \simeq \sum_{j=0}^{P} w_\alpha(s_j^r, \hat{k}, t) \left(p_j \sum_{m=0}^{P} \mathsf{J}_m^{(a,b)}(\xi) \mathsf{J}_m^{(a,b)}(\xi_j) \right) \, .$$

This last expression may be directly identified with Eq. (4.10), so that one has:

$$\mathsf{G}_j(\xi) = p_j \sum_{m=0}^{P} \mathsf{J}_m^{(a,b)}(\xi_j) \mathsf{J}_m^{(a,b)}(\xi) \, . \tag{4.17}$$

The identification of the discrete approximation of the solution w_α with the interpolation polynomials suggests a mathematically equivalent, but computationally different way of representing the discrete expansion of the solution w_α. Thus it is possible to compute the discrete expansion coefficients from the formula (4.16), or by using the Lagrange polynomial interpolation directly.

4.2.2.4 Test spaces V_h^r

Various spaces of test functions may be chosen. The most common methods are the Galerkin, the Petrov-Galerkin, and the collocation methods. In the Galerkin method, the test functions are the same as the trial functions. In the Petrov-Galerkin method, the trial and test functions may be different, hence the trail and test spaces are different. At last in the collocation method, the test functions are delta functions at given nodes. The variational formulation (4.2) is then solved exactly at these nodes.

In this work, a Galerkin method has been considered. In the specific case of Eq. (4.2), the test functions have been taken as:

$$v(\xi, \hat{k}) = \mathsf{J}_n^{(a,b)}(\xi) \delta(\hat{k} \pm 1) \, , \tag{4.18}$$

considering only the modal version. Indeed, when using Gauss-Lobatto-Jacobi quadrature rules, the modal and nodal expansion are mathematically equivalent as highlighted by Eq. (4.17).

4.2.2.5 Finite element projection

With the foregoing choices, it is now possible to spatially discretize Eq. (4.2). Inserting the modal expansion (4.12) and using the test functions given by Eq. (4.18) into Eq. (4.2), yields the discretized form of the variational formulation:

$$\mathbb{M}^r \dot{\mathbf{W}}^r + \mathbb{K}^r \mathbf{W}^r + \mathbb{F}^r \mathbf{W}^r + \sum_{r' \in \mathcal{I}_r} \mathbb{F}^{r'} \mathbf{W}^{r'} = \mathbf{0}\,, \tag{4.19}$$

with an energetic initial condition $\mathbf{W}^r(0) = \mathbf{W}_0^r$. The vector $\mathbf{W}^r(t)$ of the degrees of freedom for all the energetic modes $\alpha \in \mathsf{E}$, where E has been defined by Eq. (3.39) for beams, is:

$$\mathsf{W}^r_{\hat{k},\alpha,m}(t) = \hat{w}^r_{\alpha m}(\hat{k}, t)\,, \quad \hat{k} = \pm 1\,, \quad \alpha \in \mathsf{E}\,, \quad 0 \leq m \leq P\,.$$

Also the vector of the modal expansion coefficients for the initial conditions $w_\alpha(s, \hat{k}, 0)$ is:

$$(\mathsf{W}^r_0)_{\hat{k},\alpha,m} = \hat{w}^r_{\alpha m}(\hat{k}, 0)\,, \quad \hat{k} = \pm 1\,, \quad \alpha \in \mathsf{E}\,, \quad 0 \leq m \leq P\,,$$

where $\hat{w}^r_{\alpha m}(\hat{k}, 0)$ is computed by Eq. (4.14). The mass matrix is:

$$\mathbb{M}^r_{\epsilon\epsilon'} = \frac{\Delta s^r}{2} \delta(\epsilon - \epsilon') \boldsymbol{I}_M \otimes \boldsymbol{M}^{(a,b)}\,, \quad \epsilon, \epsilon' = \pm 1\,,$$

for the backward ($\epsilon = -1$) or the forward ($\epsilon = +1$) propagation direction, $M = \#\mathsf{E}$ is the number of propagating energetic modes in the beams, and the matrix $\boldsymbol{M}^{(a,b)}$, has entries given by:

$$M^{(a,b)}_{mn} = \int_{-1}^{+1} \mathsf{J}^{(a,b)}_m(\xi) \mathsf{J}^{(a,b)}_n(\xi) d\xi\,.$$

These integrals may be evaluated using Gauss-Jacobi quadratures. If normalized Legendre polynomials are used, then these integrals are equal to 1 because the normalized Legendre polynomials are orthonormal with respect to the weight function $p^{(0,0)}(\xi) = 1$.

The local stiffness matrix $\mathbb{K}^r$ is split into two parts as:

$$\mathbb{K}^r_{\epsilon\epsilon'} = \mathbb{B}^r_{\epsilon\epsilon'} + \mathbb{Q}^r_{\epsilon\epsilon'}\,. \tag{4.20}$$

The first one is related to the local stiffness given by:

$$\mathbb{B}^r_{\epsilon\epsilon'} = \frac{\Delta s^r}{2} \epsilon \delta(\epsilon - \epsilon') \boldsymbol{C}^r \otimes \boldsymbol{B}^{(a,b)}\,,$$

where $\boldsymbol{C}^r = \mathrm{diag}(c^r_\alpha)_{\alpha \in \mathsf{E}}$, assuming a piecewise homogeneous background medium (such that $(c^r_\alpha)' = 0$); the $(P+1) \times (P+1)$ matrix $\boldsymbol{B}^{(a,b)}$ has entries given by:

$$B^{(a,b)}_{mn} = \int_{-1}^{+1} (\mathsf{J}^{(a,b)}_m)'(\xi) \mathsf{J}^{(a,b)}_n(\xi) d\xi\,.$$

The derivatives of the Jacobi polynomials may be easily computed using Eq. (B.3) given in the appendix B, and the above integrals evaluated using Gauss-Jacobi quadratures. The second matrix of Eq. (4.20) is the local collision matrix $\mathbb{Q}^r$ given by:

$$\mathbb{Q}^r_{\epsilon\epsilon'} = \frac{\Delta s_r}{2} (\delta(\epsilon - \epsilon') - \delta(\epsilon + \epsilon')) \boldsymbol{\Sigma}^r(|k|) \otimes \boldsymbol{I}_{P+1}, \quad \boldsymbol{\Sigma}^r = \mathrm{diag}(\Sigma^r_\alpha)_{\alpha \in \mathsf{E}}\,. \tag{4.21}$$

Now let $\tilde{\mathbf{J}}^{(a,b)}(\epsilon) = [\mathsf{J}_0^{(a,b)}(\epsilon), \mathsf{J}_1^{(a,b)}(\epsilon), \dots \mathsf{J}_P^{(a,b)}(\epsilon)]^T$, and $\mathbb{J}^{(a,b)}(\epsilon,\epsilon') = \tilde{\mathbf{J}}^{(a,b)}(\epsilon) \otimes \tilde{\mathbf{J}}^{(a,b)}(\epsilon')$. Then the local flux matrix $\mathbb{F}^r$ is:

$$\mathbb{F}^r_{\epsilon\epsilon'} = \left[\delta(\epsilon-\epsilon')\boldsymbol{C}^r - \delta(\epsilon+\epsilon')\mathbb{R}^r(s_{r+\frac{\epsilon}{2}})\right] \otimes \mathbb{J}^{(a,b)}(\epsilon,\epsilon)\,, \quad \epsilon,\epsilon' = \pm 1\,,$$

where $\mathbb{R}^r$ is the reflection matrix having entries given by:

$$R^r_{\alpha\beta}(s_{r+\frac{\epsilon}{2}}) = c^r_\beta \rho^{rr}_{\alpha\beta}(s_{r+\frac{\epsilon}{2}})\,,$$

$\rho^{rr}_{\alpha\beta}$ being given by Eq. (3.66). The coupling flux matrices $\mathbb{F}^{r'}$ (coupling the element D_r with its neighbor $\mathsf{D}_{r'}$ at a junction $\partial\mathsf{D}_r \cap \partial\mathsf{D}_{r'}$) are:

$$\mathbb{F}^{r'}_{\epsilon\epsilon'} = -\delta(\epsilon - \epsilon'\hat{\boldsymbol{t}}^{r'}\cdot\hat{\boldsymbol{t}}^{r'}_{\text{out}})\mathbb{T}^{rr'}(s_{r'-\epsilon'/2}) \otimes \mathbb{J}^{(a,b)}(\epsilon,-\epsilon')\,, \quad \epsilon,\epsilon' = \pm 1\,,$$

where $\mathbb{T}^{rr'}$ is the transmission matrix having entries given by:

$$T^{rr'}_{\alpha\beta}(s_{r'-\frac{\epsilon'}{2}}) = c^{r'}_\beta \tau^{rr'}_{\alpha\beta}(s_{r'-\frac{\epsilon'}{2}})\,,$$

$\tau^{rr'}_{\alpha\beta}$ being given by Eq. (3.67).

4.2.3 Dissipation and dispersion errors of the semi-discretized scheme

The dispersion and dissipation errors of the semi-discretized transport equation are now studied by seeking solutions of Eq. (4.19) propagating freely in the positive direction on an uniform, periodic lattice $h\mathbb{Z}$ with $h > 0$ of the form:

$$\mathbf{W}^r_\alpha(t) = \tilde{\mathbf{W}}_\alpha \mathrm{e}^{\mathrm{i}(kh-\omega t)}\,, \tag{4.22}$$

where $\mathbf{W}^r_\alpha = (\mathsf{W}^r_{\alpha 1}, \mathsf{W}^r_{\alpha 2}, \dots \mathsf{W}^r_{\alpha P})$ is the vector gathering the coefficients of the approximate solution of order P on the r^{th}element in the $\hat{k}$ direction and for the energetic mode α. The $\tilde{\mathbf{W}}_\alpha$ are the solutions of an $2(P+1)\times 2(P+1)$ eigenvalue problem given by:

$$(-\mathrm{i}\omega\mathbb{M}^r + \mathbb{K}^r + \mathbb{F}^r + \mathrm{e}^{-\mathrm{i}kh}\mathbb{F}^{r-1} + \mathrm{e}^{\mathrm{i}kh}\mathbb{F}^{r+1})\tilde{\mathbf{W}}_\alpha = \mathbf{0}\,. \tag{4.23}$$

This equation is obtained by inserting Eq. (4.22) into Eq. (4.19). The one-dimensional medium is a uniform waveguide such that $\rho^{rr}_{\alpha\beta} = 0$ and $\tau^{rr\pm1}_{\alpha\beta} = 1$. From the non-dispersive property of the propagation of HF waves in a Timoshenko beam (see Sect. 3.2.2), the exact dispersion relation for the transport equation is:

$$\omega(k) = \pm c_\alpha |k|\,,$$

whereas the numerical dispersion relations is obtained from the non trivial solutions of Eq. (4.23). They are computed by finding the eigenvalues ω_n for a fixed value of kh as the solutions of:

$$\det(-\mathrm{i}\omega\mathbb{M}^r + \mathbb{K}^r + \mathbb{F}^r + \mathrm{e}^{-\mathrm{i}kh}\mathbb{F}^{r-1} + \mathrm{e}^{\mathrm{i}kh}\mathbb{F}^{r+1}) = 0\,.$$

According to the size of Eq. (4.23), $2(P+1)$ complex eigenvalues may be obtained. Two of them correspond to the propagating physical modes in the two directions, both denoted

by $m = m_0$ in the following, and the other $2P$ modes are spurious, or zero-energy modes (because they do not carry any energy [43]). The numerical eigenvalues being generally complex-valued, the numerical dispersion error is defined by:

$$e_{\text{disp}}(K) = \mathfrak{Re}(\Omega_{m_0}(K)) - K\,,$$

and the dissipation error by:

$$e_{\text{diss}}(K) = -\mathfrak{Im}(\Omega_{m_0}(K))\,,$$

where $K = h|k|$ and:

$$\Omega_m = \frac{h}{c_\alpha}\omega_m\,.$$

Fig. 4.2 shows the dispersion error of the semi-discretized scheme for different interpolation orders P, while Fig. 4.3 displays the dissipation error of these schemes. The shear velocity c_{T} of the waves has been normalized to 1. These plots show that the numerical dispersion and dissipation errors introduced by the spatial discretization are $\text{O}(K^{2P+3})$ and $\text{O}(K^{2P+2})$, respectively, retrieving the results of Ainsworth [3]. This property is called a "superconvergence" property when compared to the formal accuracy $O(h^{P+1})$ of the discontinuous Galerkin method [18]. It is very much desirable for long time simulations. At last, Fig. 4.4 displays the evolution of the numerical phase speed:

$$\frac{c_{\text{num}}}{c_\alpha} = \mathfrak{Re}\left(\frac{\Omega_{m_0}}{K}\right)$$

as a function of K for various orders P.

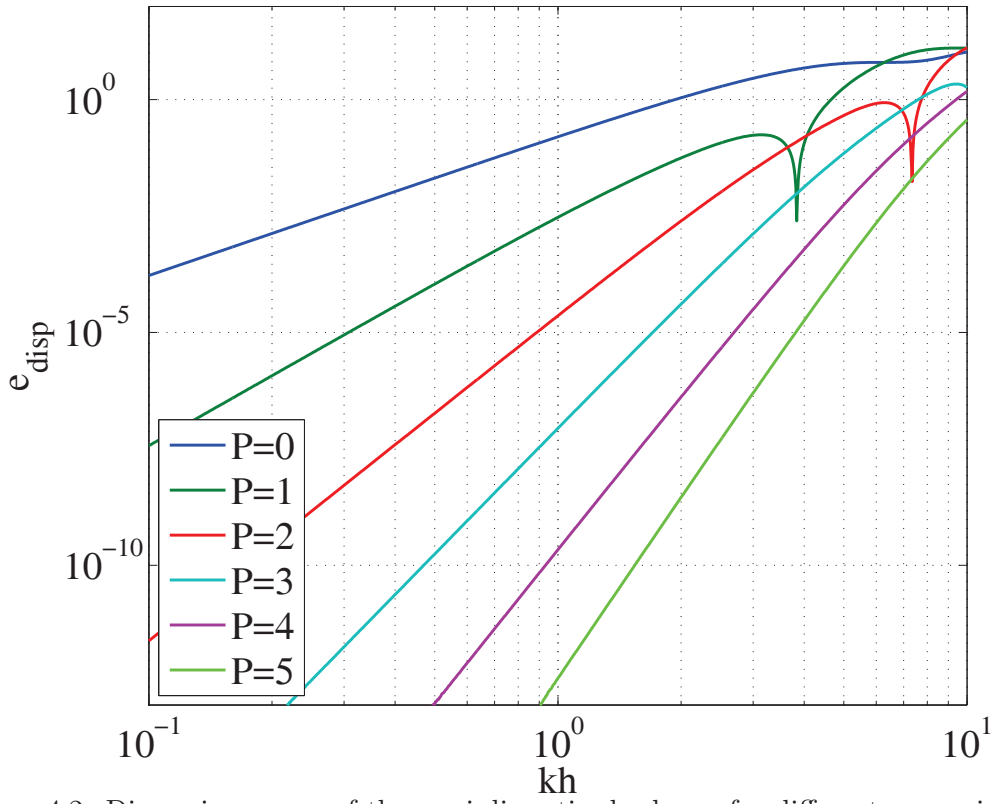

Figure 4.2: Dispersion errors of the semi-discretized scheme for different expansion orders P.

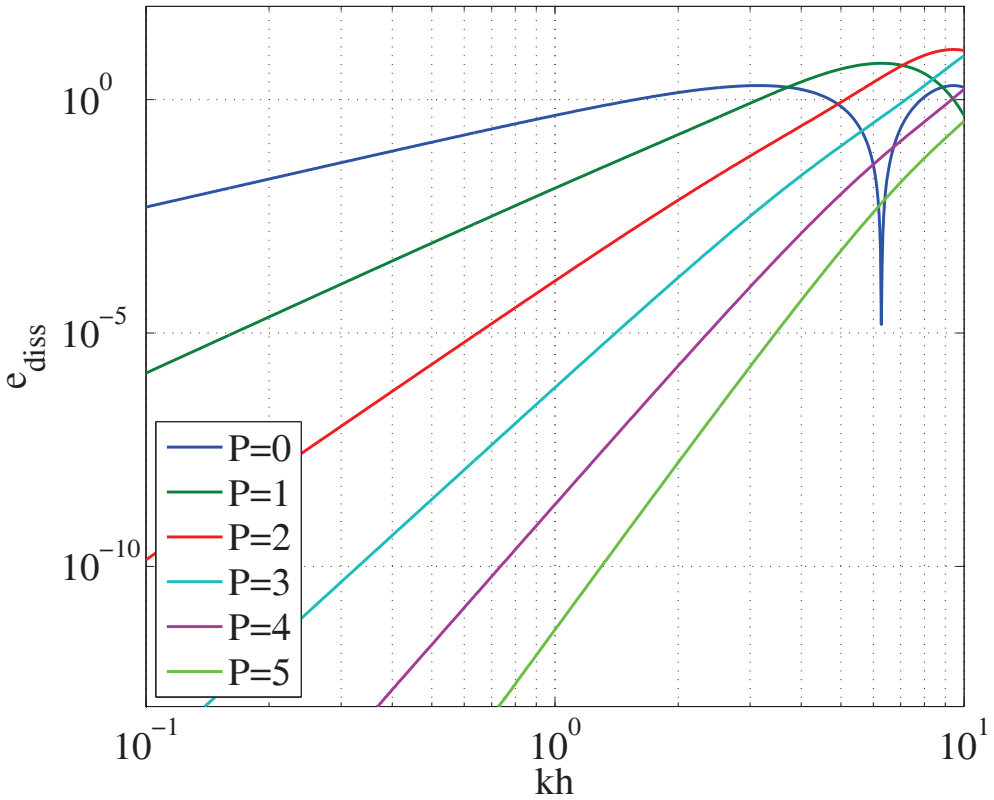

Figure 4.3: Dissipation errors of the semi-discretized scheme for different expansion orders P.

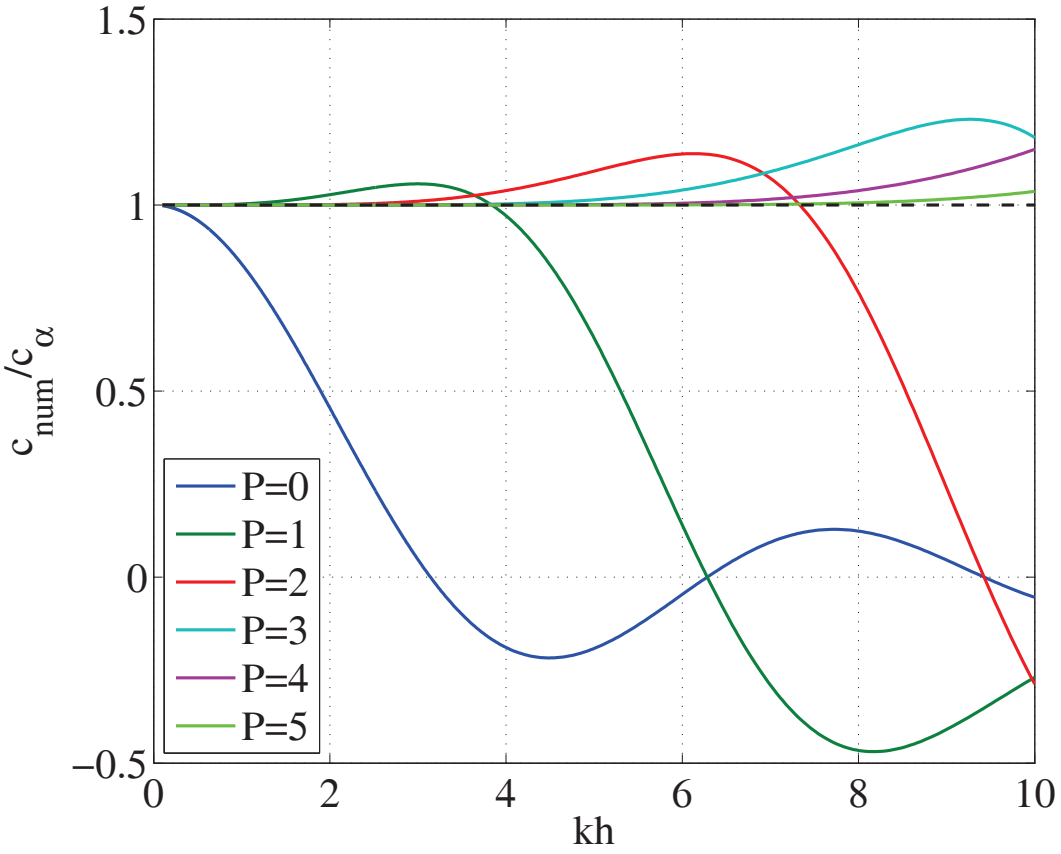

Figure 4.4: Normalized numerical phase velocity of the semi-discretized scheme for different expansion orders P.

4.2.4 Time integration

Finally, the time integration of the semi-discretized system (4.19) is performed by a strong stability-preserving (SSP) high-order Runge-Kutta scheme [33]. The aim of that scheme is to solve the ordinary differential equation:

$$\begin{cases} \dot{\mathbf{W}}(t) = \mathbb{A}\mathbf{W}(t)\,, \\ \mathbf{W}(0) = \mathbf{W}_0\,, \end{cases} \tag{4.24}$$

where $\mathbf{W}(t) = [\mathbf{W}^1(t), \mathbf{W}^2(t), \dots \mathbf{W}^{\mathsf{K}}(t)]^T$ is the vector of all degrees of freedom and $\mathbb{A}$ is the matrix operator coming out from the inversion of the mass matrix in Eq. (4.19) written for all elements $(\mathsf{D}^r)_{1\leq r\leq \mathsf{K}}$, where K is the number of finite elements. This inversion is straightforward because the mass matrix is block-diagonal, and even diagonal if Legendre polynomials are used. The time interval $[0, T]$ is first subdivided into N_t sub-intervals $[t_n, t_{n+1}]$, where $\Delta t = t_{n+1} - t_n$ denotes the time step. The class of linear, strong stability-preserving (SSP) Runge-Kutta schemes considered in this study are the ℓ-stages, ℓ-order accurate schemes built (recursively) as [33]:

$$\begin{aligned} \mathbf{W}_i &= \mathbf{W}_{i-1} + \Delta t \mathbb{A}\mathbf{W}_{i-1}\,, \quad i = 1, 2, \dots \ell - 1\,, \\ \mathbf{W}(t + \Delta t) \simeq \mathbf{W}_\ell &= \sum_{n=0}^{\ell-2} \alpha_{\ell,n}\mathbf{W}_n + \alpha_{\ell,\ell-1}\big(\mathbf{W}_{\ell-1} + \Delta t \mathbb{A}\mathbf{W}_{\ell-1}\big)\,, \end{aligned} \tag{4.25}$$

where the coefficients $\alpha_{\ell,n}$ are constructed with $\alpha_{1,0} = 1$ and:

$$\begin{aligned} \alpha_{\ell,n} &= \frac{1}{n}\alpha_{\ell-1,n-1}\,, \quad n = 1, 2, \dots \ell - 2\,, \\ \alpha_{\ell,\ell-1} &= \frac{1}{\ell!}\,, \quad \alpha_{\ell,0} = 1 - \sum_{n=1}^{\ell-1} \alpha_{\ell,n}\,. \end{aligned}$$

Tab 4.1 below gives them for various orders P. These schemes are SSP in the sense that $\|\mathbf{W}_{\ell+1}\| \leq \|\mathbf{W}_\ell\|$, and optimal in the sense that their Courant-Friedrichs-Lewy (CFL) number is not worse than the CFL number of the forward (explicit) Euler scheme applied to Eq. (4.24).

The stability of this time scheme is analyzed as follows. The ℓ^{th}-SSP Runge-Kutta scheme is applied to the scalar ordinary differential equation $\dot{u} + \lambda u = 0$. After discretization, this equation may be put in the form $u_{n+1} = P_\ell(z = \lambda\Delta t)u_n$. The function $P_\ell(z)$ is the stability function of the scheme because it is clearly apparent that the solution becomes unstable if $|P_\ell(z)| > 1$. The stability area is thus defined by $\mathcal{R}_\ell = \{z \in \mathbb{C}\,;\, |P_\ell(z)| \leq 1\}$. This area is displayed on Fig. 4.5 for various order ℓ. A necessary condition of stability for the ℓ^{th}-order SSP Runge-Kutta scheme is then $\lambda_i\Delta t \in \mathcal{R}_\ell$ for each eigenvalue λ_i of $\mathbb{A}$.

For a wave of wavenumber k, the matrix $\mathbb{A}^r$ corresponding to the r^{th}-element is given by:

$$\mathbb{A}^r = (\mathbb{M}^r)^{-1}(\mathbb{K}^r + \mathbb{F}^r + \mathrm{e}^{-\mathrm{i}\hat{k}K}\mathbb{F}^{r-1} + \mathrm{e}^{\mathrm{i}\hat{k}K}\mathbb{F}^{r+1})\,.$$

Its eigenvalues are displayed on Fig. 4.6 for the case $c_P = \sqrt{2}c_T$ for several values of interpolation order P and for K varying in the range $]0, 2\pi]$. Two curves are apparent because

Table 4.1: Coefficients $\alpha_{\ell,n}$ of the SSP method. After Gottlieb *et al.* [33].

order ℓ	$\alpha_{\ell,0}$	$\alpha_{\ell,1}$	$\alpha_{\ell,2}$	$\alpha_{\ell,3}$	$\alpha_{\ell,4}$	$\alpha_{\ell,5}$	$\alpha_{\ell,6}$	$\alpha_{\ell,7}$
1	1							
2	$\frac{1}{2}$	$\frac{1}{2}$						
3	$\frac{1}{3}$	$\frac{1}{2}$	$\frac{1}{6}$					
4	$\frac{3}{8}$	$\frac{1}{3}$	$\frac{1}{4}$	$\frac{1}{24}$				
5	$\frac{11}{30}$	$\frac{3}{8}$	$\frac{1}{6}$	$\frac{1}{12}$	$\frac{1}{120}$			
6	$\frac{53}{144}$	$\frac{11}{30}$	$\frac{3}{16}$	$\frac{1}{18}$	$\frac{1}{48}$	$\frac{1}{720}$		
7	$\frac{103}{280}$	$\frac{53}{144}$	$\frac{11}{60}$	$\frac{3}{48}$	$\frac{1}{72}$	$\frac{1}{240}$	$\frac{1}{5040}$	
8	$\frac{2119}{5760}$	$\frac{103}{280}$	$\frac{53}{288}$	$\frac{11}{180}$	$\frac{1}{64}$	$\frac{1}{360}$	$\frac{1}{1440}$	$\frac{1}{40320}$

there are two different velocities related to the propagating modes.

For our scheme to be stable in time, these eigenvalues have to lie in its stability area of the SSP Runge-Kutta scheme. Then the CFL coefficient is estimated as the constant $C_{P,\ell}$ of the homothety that brings all these eigenvalues back into the stability region. Tab. 4.2 gathers the coefficients $\hat{c}_{P,\ell} = C_{P,\ell}\frac{c_P}{c_T}$ evaluated for various interpolation orders P and ℓ. This table confirms the approximate CFL condition:

Table 4.2: CFL coefficients $\tilde{c}_{P,\ell}$ for different interpolation orders P and linear ℓ-stages, ℓ-order SSP time discretization schemes.

ℓ	P=0	P=1	P=2	P=3	P=4	P=5
2	1.0000	*0.3333*	0.1689	0.1044	0.0718	0.0529
3	1.2560	0.4187	*0.2121*	0.1311	0.0902	0.0664
4	1.3925	0.4642	0.2352	*0.1454*	0.1000	0.0736
5	1.6082	0.5361	0.2716	0.1679	*0.1155*	0.0850
6	1.7765	0.5922	0.3000	0.1855	0.1276	*0.0939*
7	1.9766	0.6589	0.3338	0.2064	0.1420	0.1045
8	2.1564	0.7188	0.3642	0.2251	0.1549	0.1140

$$c_\alpha \frac{\Delta t}{h} \leq \frac{1}{2N+1}$$

of Cockburn and Shu [19] for a ℓ-stages, ℓ-order scheme with $\ell = P+1$ (written in red and italic in the table 4.2). Moreover, it may be observed that increasing the order of

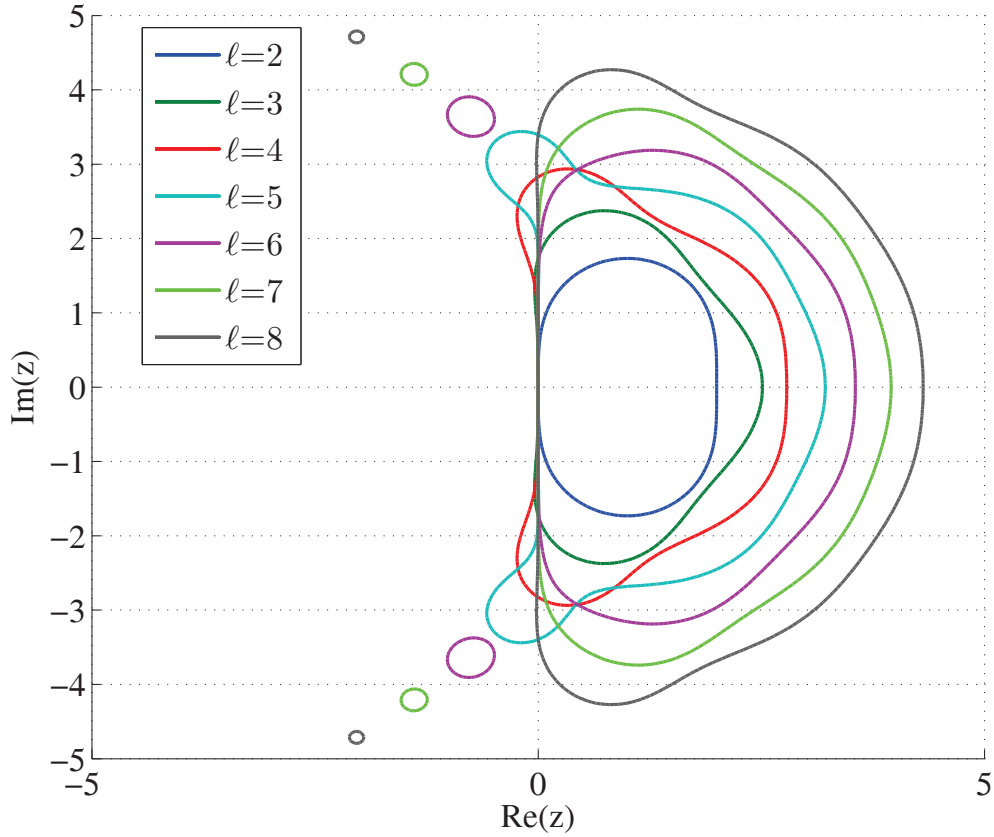

Figure 4.5: Regions of absolute stability of linear ℓ^{th}-order SSP Runge-Kutta schemes for $2 \leq \ell \leq 8$.

the scheme and the number of stages does not significantly improve its efficiency. The fully discretized scheme in space and time is referred to as the Runge-Kutta discontinuous Galerkin (RKDG) method in the dedicated literature; see [41] and references therein.

4.3 Comparison with an analytical solution

The error induced by the discretization of the scattering operator 4.21 is studied through the comparison with an exact analytical solution of Eq. (3.54) in an infinite beam. Such an exact solution is available in the case of an homogeneous background medium with uniform (Rayleigh) scattering and an initial condition of the form [107]:

$$w_\alpha^0(s, \hat{k}) = \delta(s - s_0) \otimes \delta(\hat{k} - \hat{k}_0)\,.$$

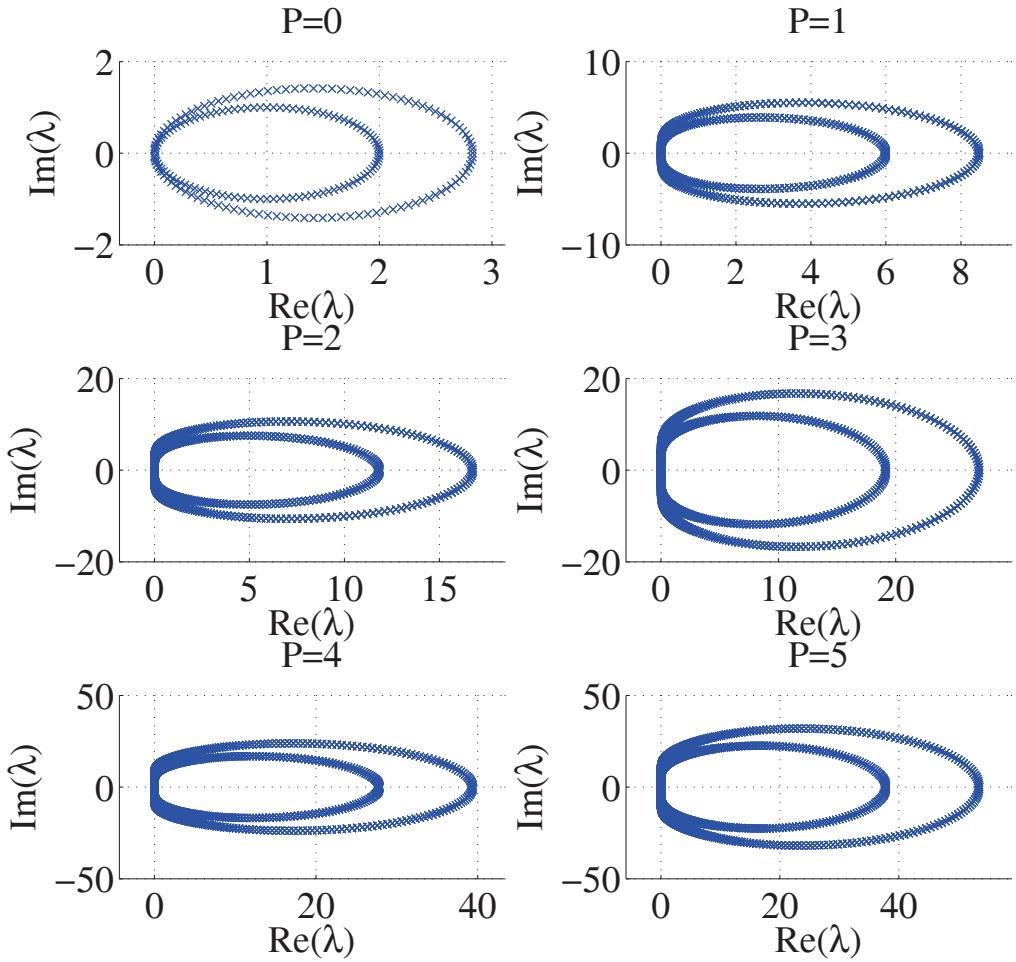

Figure 4.6: Location of the eigenvalues of $\mathbb{A}^r$ for various interpolation order P.

It is given for $L \to \infty$ by:

$$w_\alpha(s,t) = e^{-\Sigma_\alpha c_\alpha t}\Bigg[\delta(s-c_\alpha t) + \frac{\Sigma_\alpha}{2}\mathrm{H}(c_\alpha t-|s|)\times\left(I_0\left(\Sigma_\alpha\sqrt{c_\alpha^2t^2-s^2}\right)+\sqrt{\frac{c_\alpha t+s}{c_\alpha t-s}}I_1\left(\Sigma_\alpha\sqrt{c_\alpha^2t^2-s^2}\right)\right)\Bigg],$$

where $\mathrm{H}(z)$ is the Heaviside unit-step function, and $I_n(z)$ is the modified Bessel function of order n. The first term on the right-hand side is the coherent signal (the ballistic wave given by the Dirac function), and the second term is the incoherent signal produced by multiple scattering. This comparison allows to study the effect of the discretization of the scattering model on the accuracy of the scheme. The excited mode has a velocity c_α, and the simulation time is fixed to $T < \frac{L}{c_\alpha}$ in order to avoid reflection on the boundaries because the beam has finite length $2L$ in the numerical simulation. Fig. 4.7 compares the analytical and numerical solutions for $c = 1$, $\Sigma_\alpha = 0.5$, $\hat{k}_0 = 1$, $L = 5$ unit length, $\mathsf{K} = 200$ finite

elements, and local interpolations by Legendre polynomials up to the sixth order. The time scheme is a fifth-order SSP Runge Kutta scheme. The initial condition of the numerical simulation is a hat function of width $0.1L$ and it is normizalized such that its integral is 1. Hence it corresponds to an approximation of the Dirac distribution.

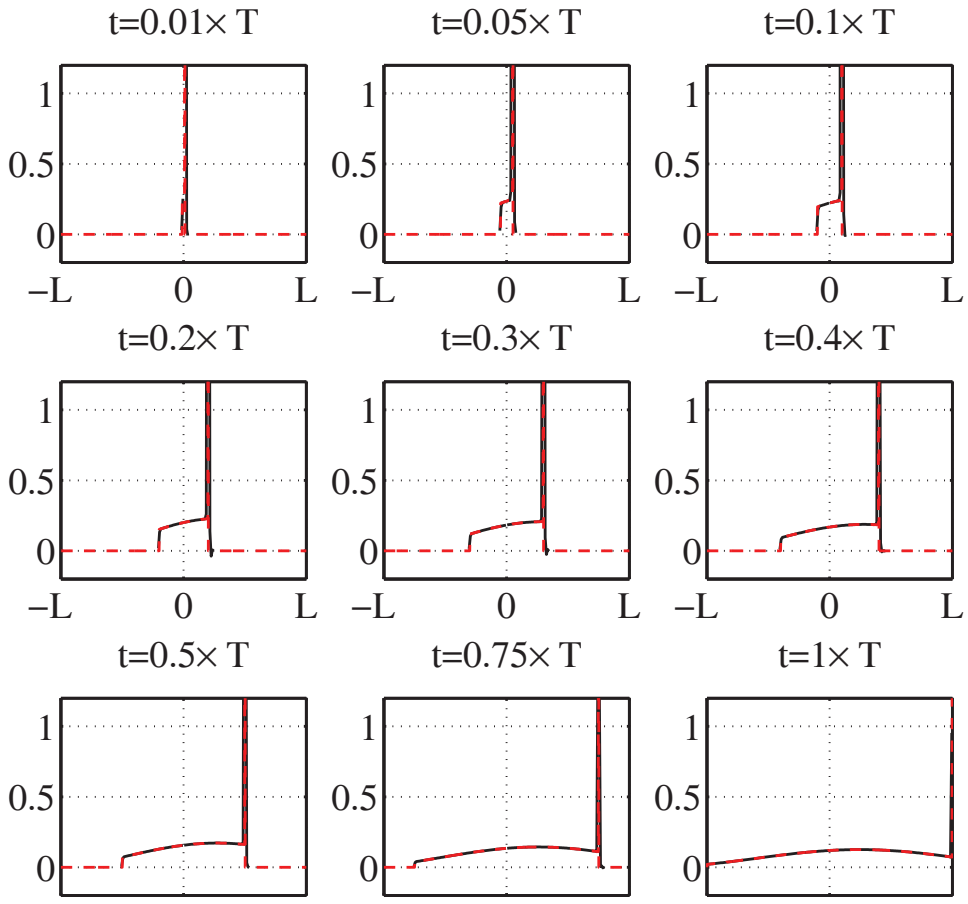

Figure 4.7: Comparison of numerical (full dark line) and analytical (dashed red line) solutions of the one-dimensional scalar radiative transfer equation with uniform scattering in an infinite beam.

Observation of Fig. 4.7 shows that the numerical and analytical simulations match very well. It exhibits the propagation of the coherent signal (the sharp peak on Fig. 4.7) and the effect of multiple scattering that spreads some energy backward. Both effects are recovered quantitatively and qualitatively by the numerical simulation. Moreover the total energy is conserved by the numerical scheme.

4.4 Conclusions

The transport equations (3.40) or the radiative transfer equations (3.51) have been fully discretized by a weakly dissipative and dispersive scheme. The physical fluxes (3.61)

and (3.62) at beam junctions are considered through the numerical fluxes chosen with this scheme. In the next chapter, some numerical examples are presented. They exhibit some equipartition phenomena, among others, such as the diffusion regime that arises at long times, or the effect of random materials. Moreover a time reversal process is developed, bringing an other evidence of the accuracy of the RKDG scheme.

Chapter 5

Numerical simulation of vibrational diffusion in beam trusses and time-reversal experiments

The equations describing the evolution of the energy density in a beam truss under impulse loads, Eq. (3.40) and Eq. (3.54) together with the boundary conditions (3.61), have been fully discretized in the foregoing chapter. Some numerical examples are now considered in this chapter. They focus on the emergence of the diffusion regime and equipartition of the vibrational energy in beam trusses on one hand, and on the possibility to perform time-reversed simulations on the other hand. Here energy equipartition is understood in two ways:

- *the first one is the observation of a rather spatially uniform energy level within a single or a group of beams;*
- *the second one is the observation of a rather uniform ratio of the transverse to longitudinal energies in a single beam or in a group of beams.*

The time reversal process is useful to test the efficiency of the numerical scheme and for possible future industrial applications such as non destructive testing and structural health monitoring.

5.1 The onset of diffusive waves in beam trusses

5.1.1 A single-bay truss

A beam truss constituted by $\mathcal{N} = 9$ three-dimensional beams is considered. Its base is a rectangle of 5×4 unit lengths, see Fig. 5.1. All beams have the same square cross-sections of area $S = 1$ and are made from homogeneous, isotropic elastic materials of unit density and Poisson's ratio equal to 0.3. The Table 5.1 sums up the normalized material and geometrical properties of the beams. The shear reduction factor is computed with the classical formula $\kappa = 5(1+\nu)/(6+5\nu)$, see Eq. (2.35). The transport equations (3.40) hold in each beam and the reflection/transmission coefficients at the junctions are directly computed from the approach outlined in Sect. 3.3.2. The forward and backward fluxes are

Table 5.1: Normalized mechanical and geometrical parameters of the beams.

beam $\#p$	length L_p	Young's modulus
1	5	1
2	4	0.75
3	5	1.2
4	5	1
5	2.5217	1.25
6	4	1
7	3.6988	1.25
8	5.6853	0.5
9	6.4031	1.5

given as the superposition of reflected and transmitted fluxes including all existing energy modes, $\alpha = \mathrm{P}_j, \mathrm{T}_j$, $j = 1, 2, 3$, as described in Sect. 3.3.1. The energetic initial pulse has a Gaussian shape and loads the mode P_1 (load case #1, a pure compressional wave) or the mode T_3 (load case #2, a pure torsional wave). It is applied to, say, beam labeled #1 with a fixed initial direction $\hat{k} = +1$; see again Fig. 5.1.

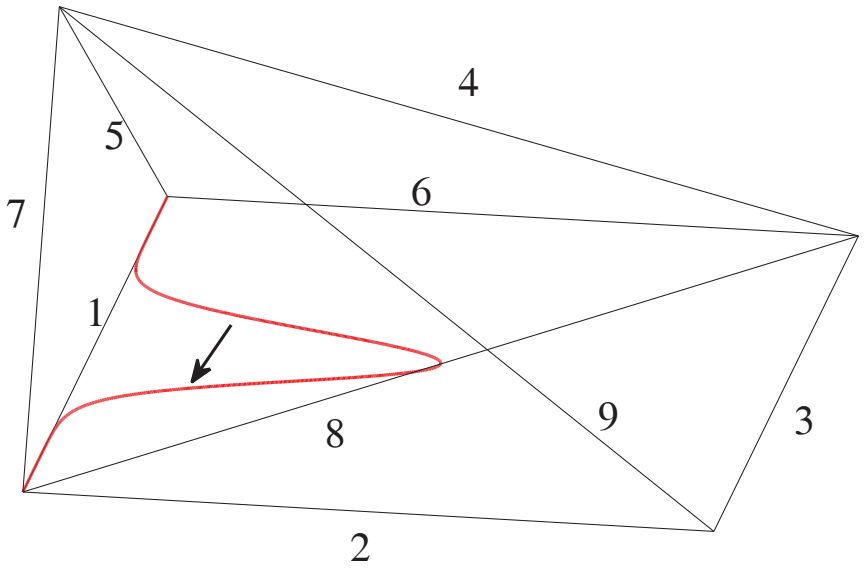

Figure 5.1: View of the single-bay beam truss with the Gaussian initial load in beam #1 (red line).

The nodal density is fixed at $h^{-1} = 20/L$ uniform spatial elements per unit length for all beams, where L is the length of beam #1. Legendre polynomials up to the fifth order ($P = 5$) are used as local basis functions. The integration in time is performed by a seventh-order Runge-Kutta SSP scheme. The time scale $T = L/c_{\mathrm{T}}$ is introduced: it is the time needed by a transverse wave to travel across the first beam. This parameter has been set to $T = 10$ in our simulations. The Courant number $\mathrm{CFL} := c_{\mathrm{T}}\Delta t/h$ has been fixed to $\mathrm{CFL} = 0.01$, Δt being the time step of the time integration scheme. The simulation lasts

about 2 minutes on a single 2GHz processor with 24Go RAM.

5.1.1.1 An homogeneous beam truss with point junctions

We first consider the beam truss of Fig. 5.1 without any offset at the junctions between the beams. Fig. 5.2 and Fig. 5.3 show the evolution of the overall energy density (3.37) computed in that beam truss for the compressional and the torsional load cases, respectively, on beam #1. Only the non-vanishing energy density is displayed on these plots. It can be seen in both cases that the energy is spread over the entire structure at late times. Discontinuities of the energy density are also noticeable at the junctions. At last, the observed numerical wave velocities agree with those of the theory, see Eq. (3.34), as exhibited by the difference of the travelling times for the initial compressional (load case 1) and torsional (load case 2) waves in the first beam. Thus the numerical scheme is practically non dispersive: the theoretical dispersion error is about $2.5\,10^{-16}$ for our choice $P = 5$ [3], which is below machine precision.

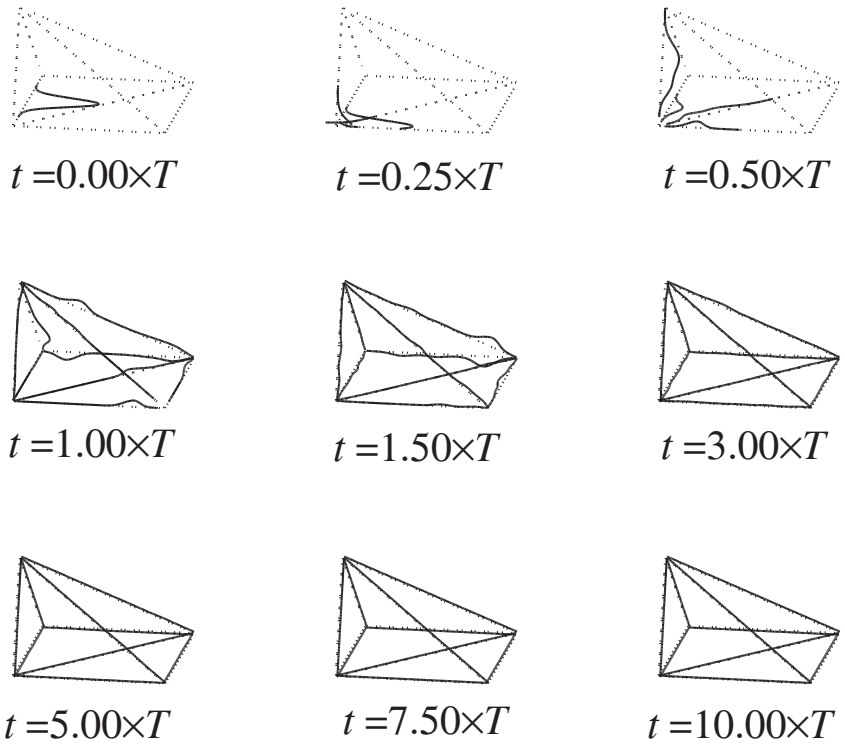

Figure 5.2: Evolution of the energy density within the truss of Fig. 5.1 at selected instants for a compressional initial pulse. Only the non-vanishing energy density is displayed on this plot. No offset at the junctions is considered.

Fig. 5.4 and Fig. 5.5 show the evolution of the total energy $\mathcal{E}^p(t) := \int_0^{L_p} \mathcal{E}(s,t)ds$ for each beam, $1 \leq p \leq 9$ where L_p is the length of beam p. It should be first observed that the total energy for the entire truss is numerically conserved. This is a required property of the numerical scheme retained: the theoretical numerical dissipation error being about

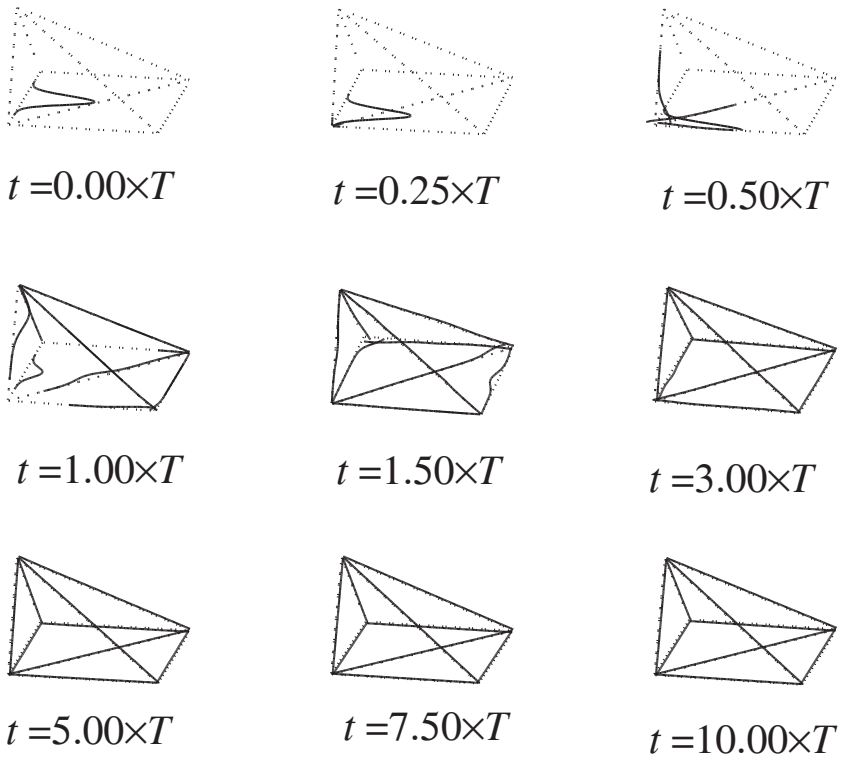

Figure 5.3: Evolution of the energy density within the truss of Fig. 5.1 at selected instants for a torsional initial pulse. Only the non-vanishing energy density is displayed on this plot. No offset at the junctions is considered.

$2.5\,10^{-15}$ for $P = 5$ [3]. Moreover, the total energy in each beam tends to a limit as $t \to \infty$ which apparently depends on its mechanical parameters. This phenomenon characterizes the diffusive regime holding at late times.

Finally, Fig. 5.6 and Fig. 5.7 show the ratio

$$\mathcal{E}_\alpha^p(t) = \sum_{j=1}^{3} \sum_{\hat{k}=\pm 1} \int_0^{L_p} w_{\alpha_j}(s, \hat{k}, t) ds\,, \quad 1 \le p \le 9\,, \quad \alpha = \mathrm{P}, \mathrm{T}\,,$$

between the overall transverse and longitudinal vibrational energy in each beam $\mathcal{E}_\mathrm{T}^p(t)/\mathcal{E}_\mathrm{P}^p(t)$. This ratio converges to a constant value of the form:

$$\frac{\mathcal{E}_\mathrm{T}^p(t)}{\mathcal{E}_\mathrm{P}^p(t)} \underset{t\to+\infty}{\longrightarrow} \frac{n_\mathrm{T} c_\mathrm{P}}{n_\mathrm{P} c_\mathrm{T}}\,, \quad 1 \le p \le 9\,,$$

where n_P and n_T are the number of longitudinal and transverse modes generated in each beam by the reflection/transmission processes at the junctions. Those numbers depend on the initial condition and the shape of the truss. However the limit should be analyzed theoretically more in details; this issue is out of the scope of this thesis but it is the subject of ongoing researches. For example, the initial motion in Fig. 5.4 and Fig. 5.6 is a compressional mode $\alpha = \mathrm{P}_1$ in beam #1. According to the reflection/transmission operators, it

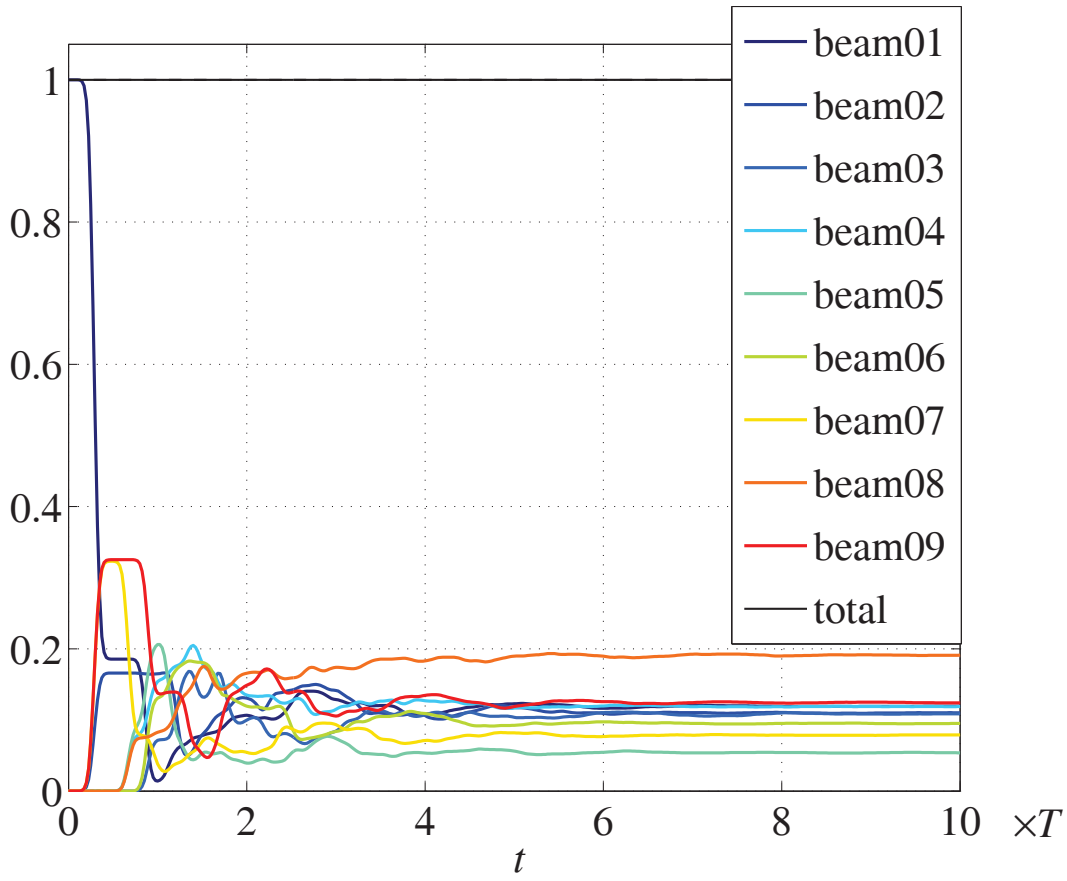

Figure 5.4: Evolution of the total energies $\mathcal{E}^p(t)$, $1 \leq p \leq 9$, in each beam of the truss of Fig. 5.1 for an initial compressional pulse. No offset at the junctions is considered.

is transmitted as transverse shear modes ($\alpha = \mathrm{T}_1$ or T_2) or the same compressional mode ($\alpha = \mathrm{P}_1$) in the beams connected to it (beams #2, #7). However no conversion to bending ($\alpha = \mathrm{P}_2$ or P_3) or torsional ($\alpha = \mathrm{T}_3$) modes occurs at any time. Thus $n_\mathrm{P} = 1$ and $n_\mathrm{T} = 2$ in this case. For Fig. 5.5 and Fig. 5.7 the initial mode is a pure torsional wave $\alpha = \mathrm{T}_3$ hit on beam #1 as well. According to the reflection/transmission coefficients for such a rotational incident wave, $n_\mathrm{P} = 2$ and $n_\mathrm{T} = 1$ (the transverse mode is the torsional mode $\alpha = \mathrm{T}_3$ and the longitudinal modes are the pure bending modes $\alpha = \mathrm{P}_2$ or P_3). That is why it is observed that the above energy ratios apparently converge to the aforementioned diffusion limit. It should be noted that the high variations observed at the beginning of the simulation occur because some beams are not yet loaded or loaded with compressional or transverse waves solely.

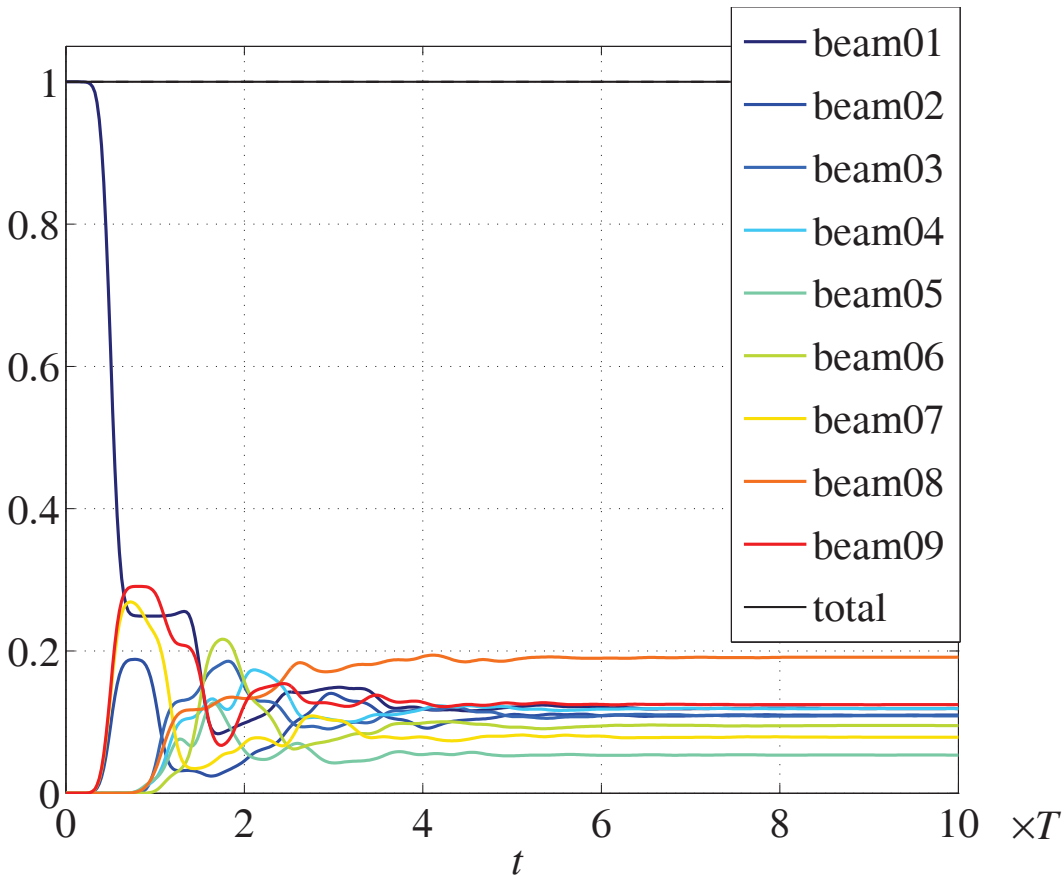

Figure 5.5: Evolution of the total energies $\mathcal{E}^p(t)$, $1 \leq p \leq 9$, in each beam of the truss of Fig. 5.1 for an initial torsional pulse. No offset at the junctions is considered.

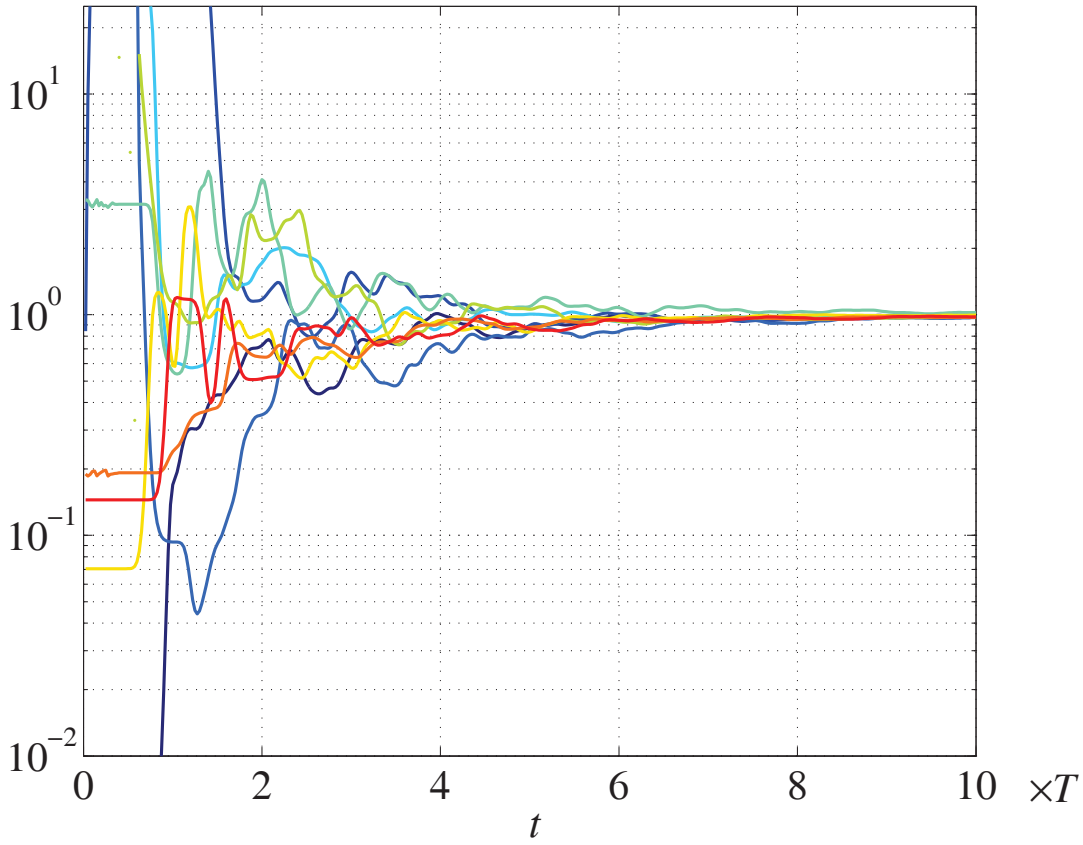

Figure 5.6: Evolution of the energy ratios $\dfrac{c_{\mathrm{T}}\mathcal{E}^p_{\mathrm{T}}(t)}{2c_{\mathrm{P}}\mathcal{E}^p_{\mathrm{P}}(t)}$, $1 \leq p \leq 9$, in each beam of the truss of Fig. 5.1 for an initial compressional pulse. No offset at the junctions is considered.

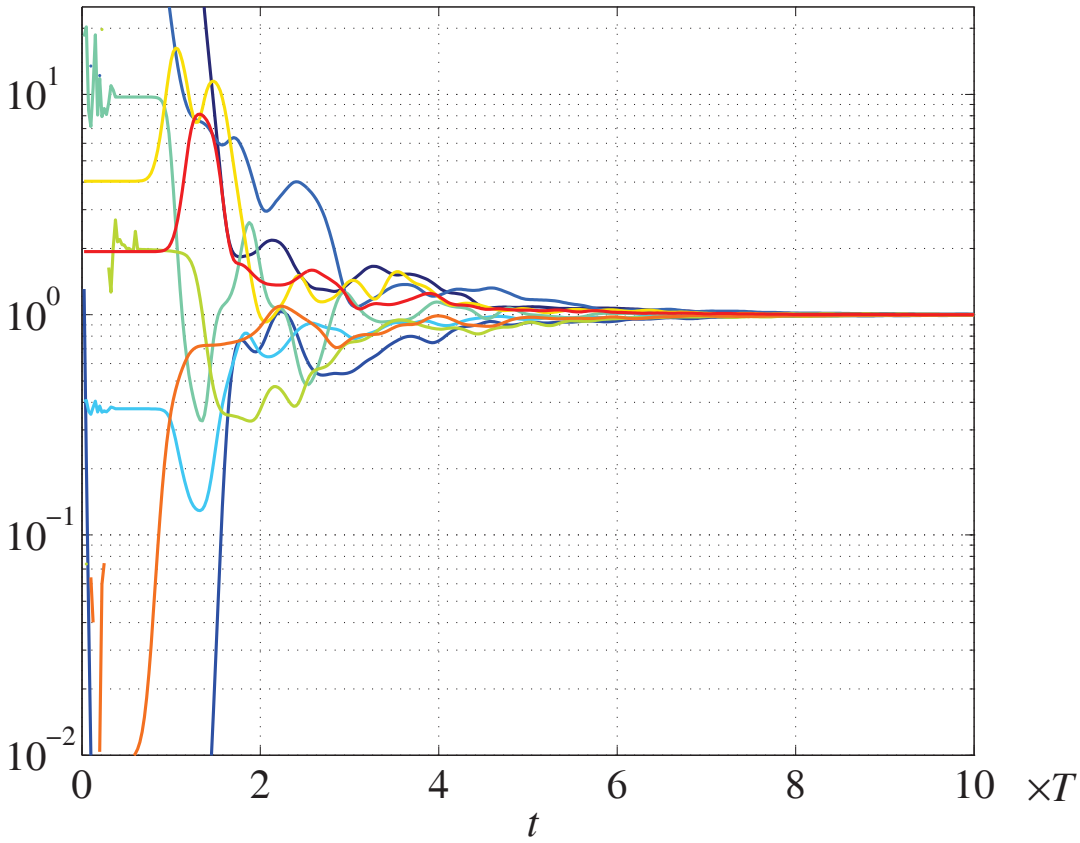

Figure 5.7: Evolution of the energy ratios $\dfrac{2c_{\mathrm{T}}\mathcal{E}_{\mathrm{T}}^{p}(t)}{c_{\mathrm{P}}\mathcal{E}_{\mathrm{P}}^{p}(t)}$, $1 \leq p \leq 9$, in each beam of the truss of Fig. 5.1 for an initial torsional pulse. No offset at the junctions is considered.

5.1.1.2 An homogeneous beam truss containing junctions with offsets

We now consider the beam truss of Fig. 5.1 with several offsets at the junctions. The latter are gathered in the Table 5.2 below. Fig. 5.8 and Fig. 5.9 display the evolution of the total energy density for each substructure, and the ratio between the transverse and the longitudinal energy densities, respectively.

Table 5.2: Offsets $\boldsymbol{\delta}_p^{p+1}$ between the beam $\#p$ and the beam $\#(p+1)$. The offsets between the beam $\#p$ and the other connected beams are deduced from $\boldsymbol{\delta}_p^{p+1}$.

beam p	$\boldsymbol{\delta}_p^{p+1}$
2	$\hat{\boldsymbol{n}}_2 + 0.8\hat{\boldsymbol{b}}_2$
4	$0.5\hat{\boldsymbol{n}}_4 - 0.2\hat{\boldsymbol{b}}_4$
6	$\hat{\boldsymbol{n}}_6 + 0.8\hat{\boldsymbol{b}}_6$
8	$-\hat{\boldsymbol{n}}_8 + 0.2\hat{\boldsymbol{b}}_8$

The expected diffusion limit has changed because the number of transverse and longitudinal modes generated at the junctions are different from the previous situation, see Sect. 5.1.1.1. Indeed, all the modes are now likely to be excited at the junctions (see Sect. 3.3). This means that one expects that all modes in each beam will take part to the equipartition rule of the diffusion regime at late times. Hence the diffusion limit is now:

$$\frac{\mathcal{E}_{\mathrm{T}}^p(t)}{\mathcal{E}_{\mathrm{P}}^p(t)} \underset{t\to+\infty}{\longrightarrow} \frac{c_{\mathrm{P}}}{c_{\mathrm{T}}}\,. \tag{5.1}$$

As compared to the previous case of a beam truss without offset at the junctions, the equipartition rule above is reached at slightly later times. This can be explained by the modifications of the reflection/transmission operators induced by the offsets. Although the offsets are large, their influence on the reflection/transmission coefficients is not very important. The conversion rates of a translational (respectively rotational) motion to rotational (respectively translational) motions are low and thus this translational (respectively rotational) motion is not significantly modified by the scattering processes at a junction with offsets. Then the time needed to reach the equipartition rule (1.1) is increased because the mixing of all modes is achieved at a slower pace.

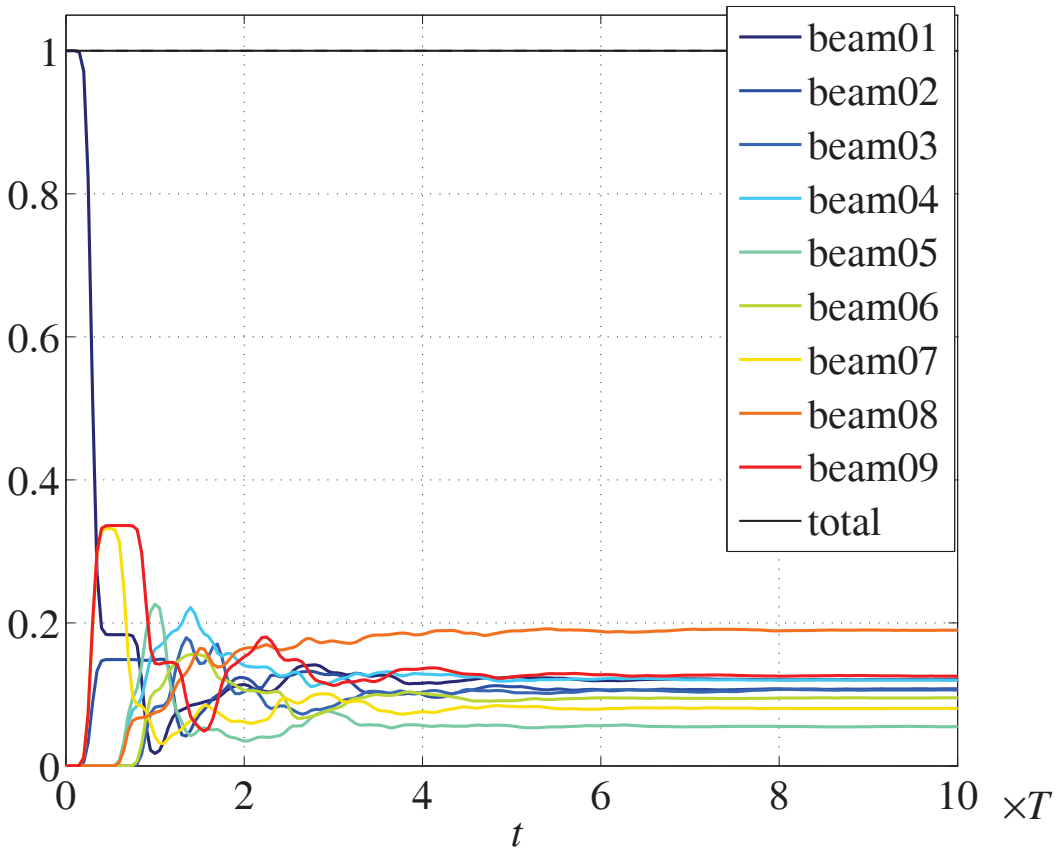

Figure 5.8: Evolution of the total energies $\mathcal{E}^p(t)$, $1 \leq p \leq 9$, in each beam of the truss of Fig. 5.1 for an initial compressional pulse. The offsets summarized in the Tab. 5.2 are considered for the junctions.

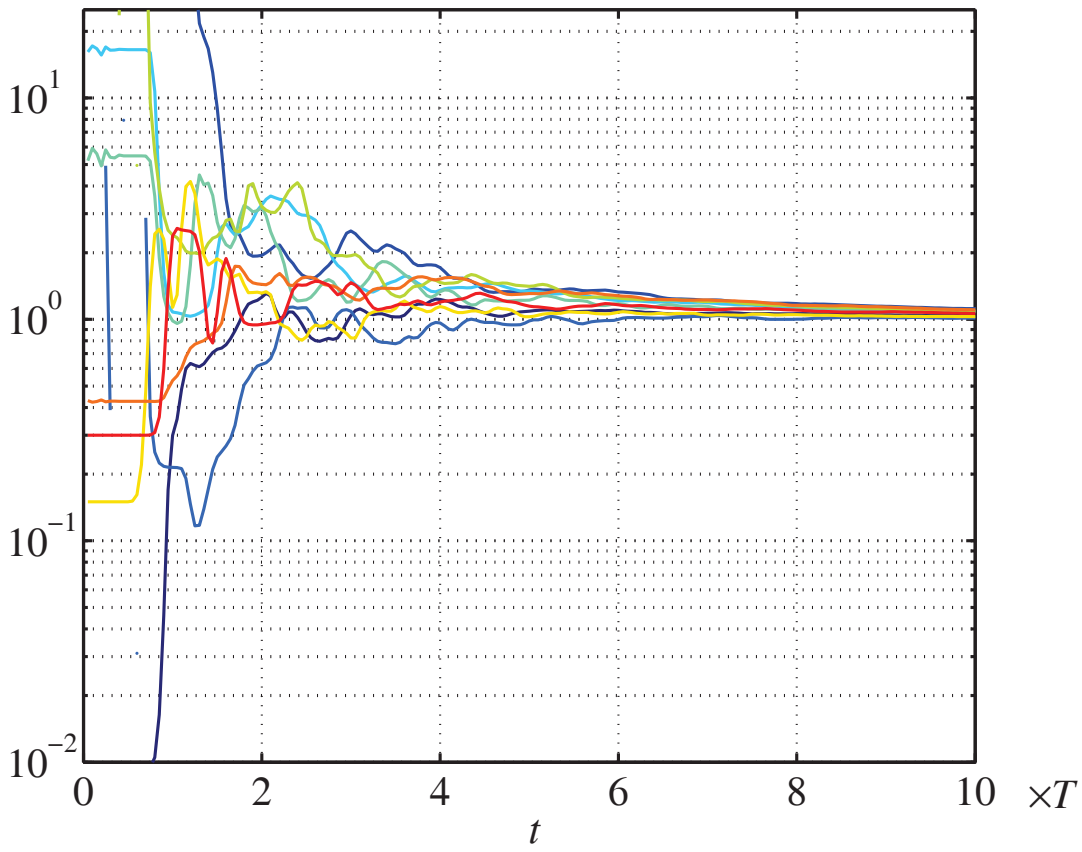

Figure 5.9: Evolution of the ratios $\dfrac{c_{\mathrm{T}}\mathcal{E}^p_{\mathrm{T}}(t)}{c_{\mathrm{P}}\mathcal{E}^p_{\mathrm{P}}(t)}$, $1 \leq p \leq 9$, in each beam of the truss of Fig. 5.1 for an initial compressional pulse. The offsets summarized in the Tab. 5.2 are considered for the junctions.

5.1.1.3 The single-bay beam truss with random materials

The radiative transfer model of Sect. 3.2.4 is now considered for the single-bay beam truss of Fig. 5.1 having random material characteristics, according to Eq. (3.52). The perturbations of these parameters are assumed to have Gaussian correlation, see Table 3.1, with $l_c k = 2$ and strength factors $\zeta_\alpha = 2$, see Eq. (3.55). Fig. 5.10, Fig. 5.11, and Fig. 5.12 show the same quantities as before in the present case of material randomness. Fig. 5.10, Fig. 5.11, and Fig. 5.12 display the evolution of the energy density (3.37) computed in that beam truss, the evolution of the total energy for each beam, and the ratio between the transverse and the longitudinal total energies, respectively.

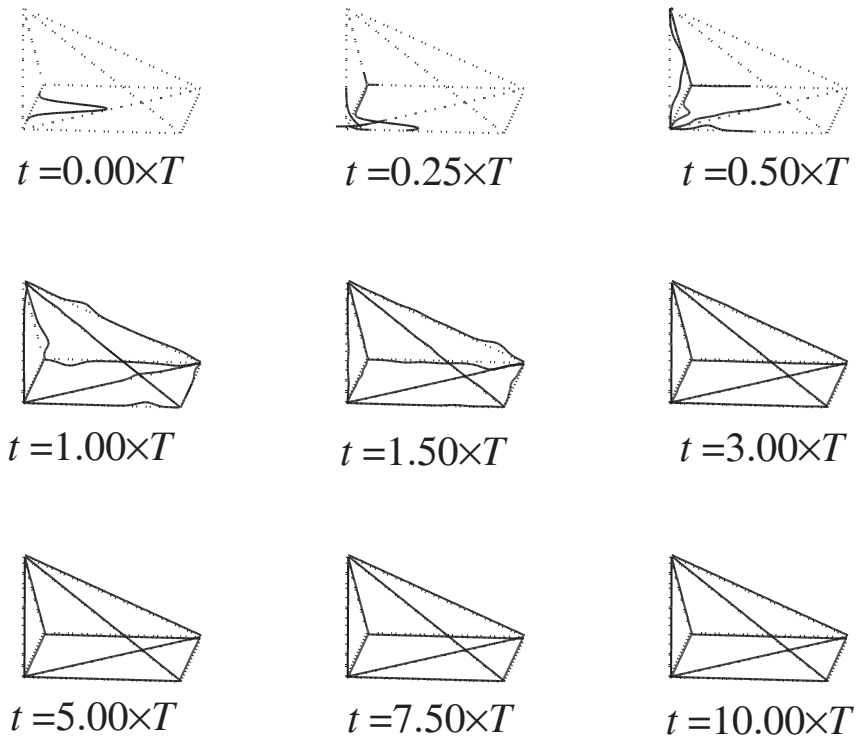

Figure 5.10: Evolution of the energy density within the truss of Fig. 5.1 at selected instants for a compressional initial pulse, accounting for some material randomness. Only the non-vanishing energy density is displayed on this plot. No offset at the junctions is considered.

Fig. 5.10 shows that a part of the energy flow is reflected in the opposite direction on account of the back-scattering effect induced by material randomness. But despite this spread of energy, comparison between the corresponding homogeneous case, Fig. 5.4 and Fig. 5.6, and the heterogeneous case, Fig. 5.11 and Fig. 5.12, shows that the diffusion limit is not reached faster in the latter case. These heterogeneities just contribute to erase the oscillations about a mean value at early times. Indeed, the scattering process induced by material randomness does not involve any modal conversion, thus it does not influence the evolution of the ratio between the transverse and the compressional energy modes. This explains why the time at which the diffusion limit is reached is not modified by the material randomness. The oscillations observed in each plot are thus due to the reflection/transmission

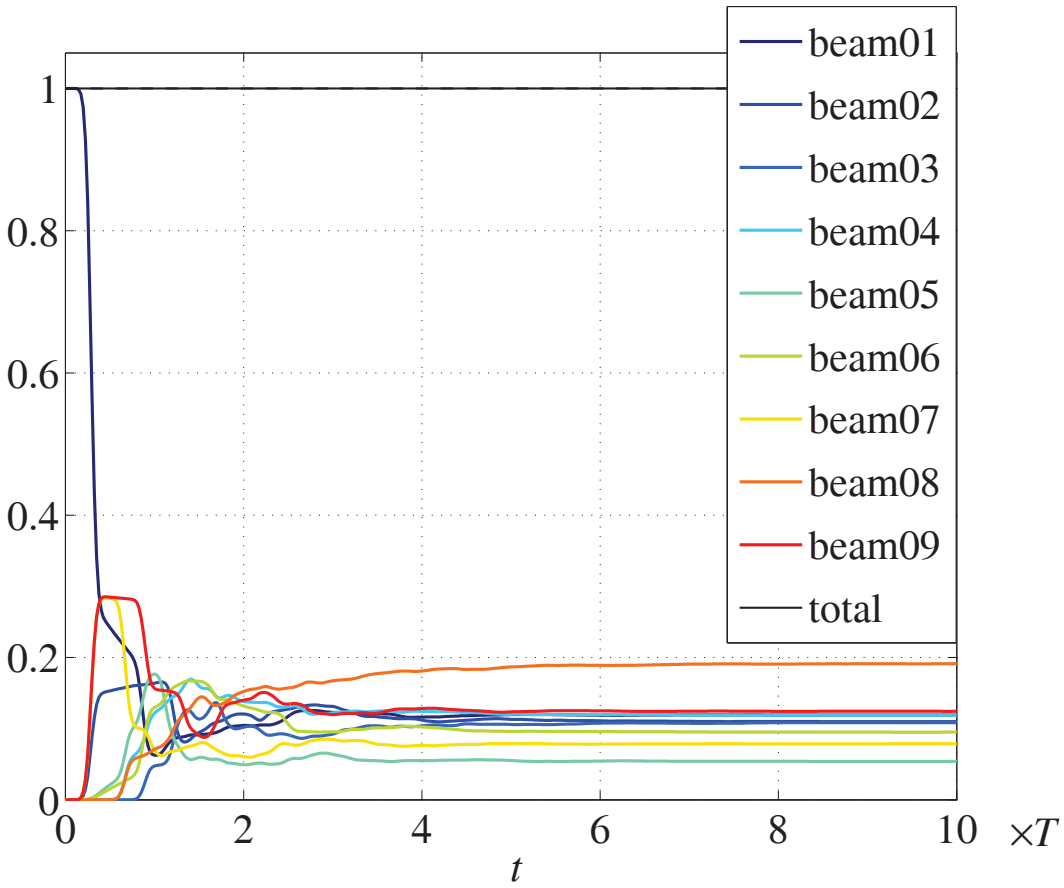

Figure 5.11: Evolution of the total energies $\mathcal{E}^p(t)$, $1 \leq p \leq 9$, in each beam of the truss of Fig. 5.1 for an initial compressional pulse, accounting for some material randomness. No offset at the junctions is considered.

phenomena at the junctions between beams. The material randomness only smooths out the energy densities by spreading them over the beams separately for each mode.

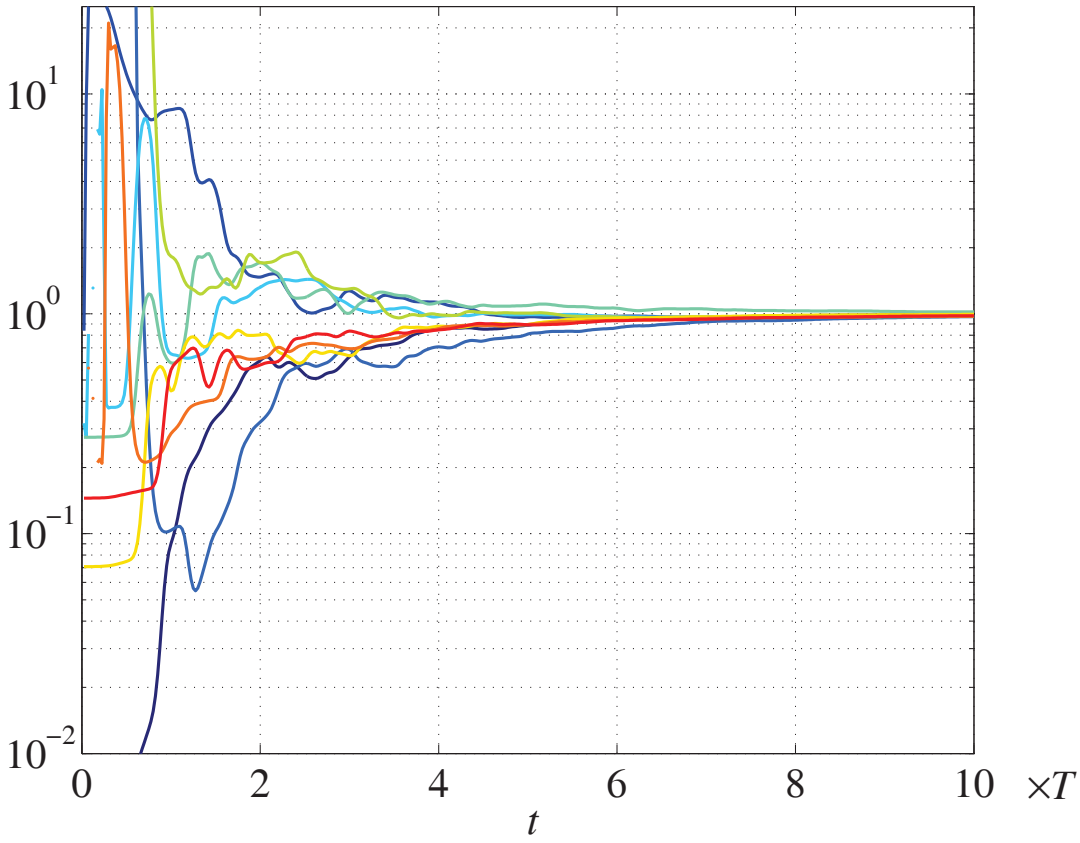

Figure 5.12: Evolution of the ratios $\dfrac{c_{\mathrm{T}}\mathcal{E}_{\mathrm{T}}^p(t)}{2c_{\mathrm{P}}\mathcal{E}_{\mathrm{P}}^p(t)}$, $1 \leq p \leq 9$, in each beam of the truss of Fig. 5.1 for an initial compressional pulse, accounting for some material randomness. No offset at the junctions is considered.

5.1.2 A multiple-bay truss

The evaluation of the performances of the numerical scheme is continued with the consideration of a larger structure, in order to test the efficiency of the method at larger scales. The truss is now composed of four plane-parallel cells, or bays. The height of the cells is 4 unit length and their width is 5 unit length. The length of the first cell is 7.5 unit length, the length of the second cell is 7 unit length, the length of the third cell is 8 unit length, and the length of the fourth cell is 6 unit length. Transverse beams are added in order to ensure the mixing of the energy modes by the reflection/transmission processes at the junctions. All the beams have the same mechanical parameters and have a square cross-section. Fig. 5.13 displays the beam truss and the triangular initial pulse impinging beam #1 with a compressional content. The simulation is continued up to $10 \times T$, where T is defined similarly as in the single-bay case. 4 elements per unit length are used for spatial discretization, so that there are 1212 elements for the entire truss. Legendre polynomials up to the order $P = 8$ are used for the approximation on each element, and a 7-th order Runge-Kutta SSP scheme is used for time integration with a CFL number fixed at $\mathrm{CFL} = 0.01$. The computation lasts 4115s (about 1 hour) on a single 2GHz processor with

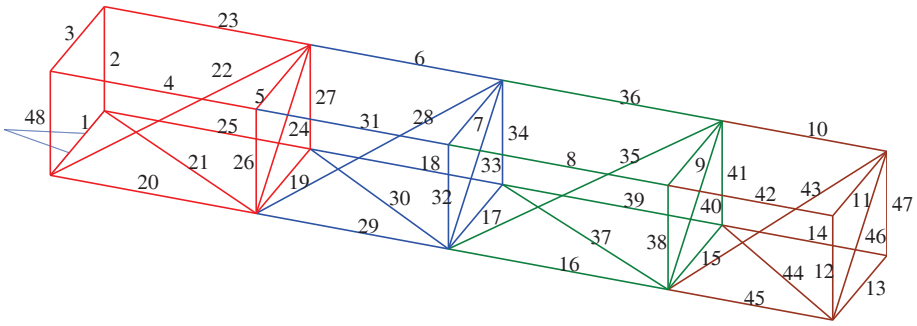

Figure 5.13: View of the multiple-bay beam truss with the triangular initial load in beam #1 (blue line). The colors represent the beam's group.

24Go RAM. Beyond these computational considerations, some interesting features can be highlighted by the simulation. Fig. 5.14 displays the evolution of the energy density at different times. It is spread over the entire truss as it reaches the opposite side of the truss at about $T = 10$. Fig. 5.15 displays the evolution of the total energy in each beam with respect to time. The beams have been gathered by substructures (colored on Fig. 5.13) for a sake of clarity, and the sum of the total energy for each substructure is plotted on Fig. 5.16. That total energies tend to decrease in the first substructure and increase in the others. At the end of the computation, only the second substructure has reached an uniform spatial distribution, and the total energy in the third and fourth substructure is very low. Fig. 5.17 and Fig. 5.18 show the evolution of the ratio between the total energies for the transverse and longitudinal modes in each beam, and its mean for each substructure, respectively. On account of the type of the initial condition and to the numbers of transverse and longitudinal modes generated at the junctions, the expected limit for the ratio between the transverse total energies on the longitudinal total energies is:

$$\frac{\mathcal{E}^p_{\mathrm{T}}(t)}{\mathcal{E}^p_{\mathrm{P}}(t)} \underset{t\to+\infty}{\longrightarrow} \frac{2c_{\mathrm{P}}}{c_{\mathrm{T}}}\,.$$

On Fig. 5.18, one can see that the mean values of the ratios tends toward this limit. For the farthest substructures (the third and the fourth ones), the ratio between the transverse and compressional energies stabilize faster than the total energy themselves. This may be explained by the fact that the farther the substructures are from the initial pulse, the more they benefit from the mixing of the energy modes that has taken place in the substructures closer to initial pulse. Contrarily, the total energy of the second substructure gets stabilized faster than the mean of the ratios the longitudinal and the transverse energies of its components, because this substructure benefits of the mixing that has taken place in the first substructure only. That second substructure is the first one to reach spatial equipartition because it is both close to the source, and can exchange energy with two substructures. These observations and the knowledge of the transient response to some pulse could be helpful for the design of spatial structures, or the placing of equipments at locations of low energy levels or specific energy ratios.

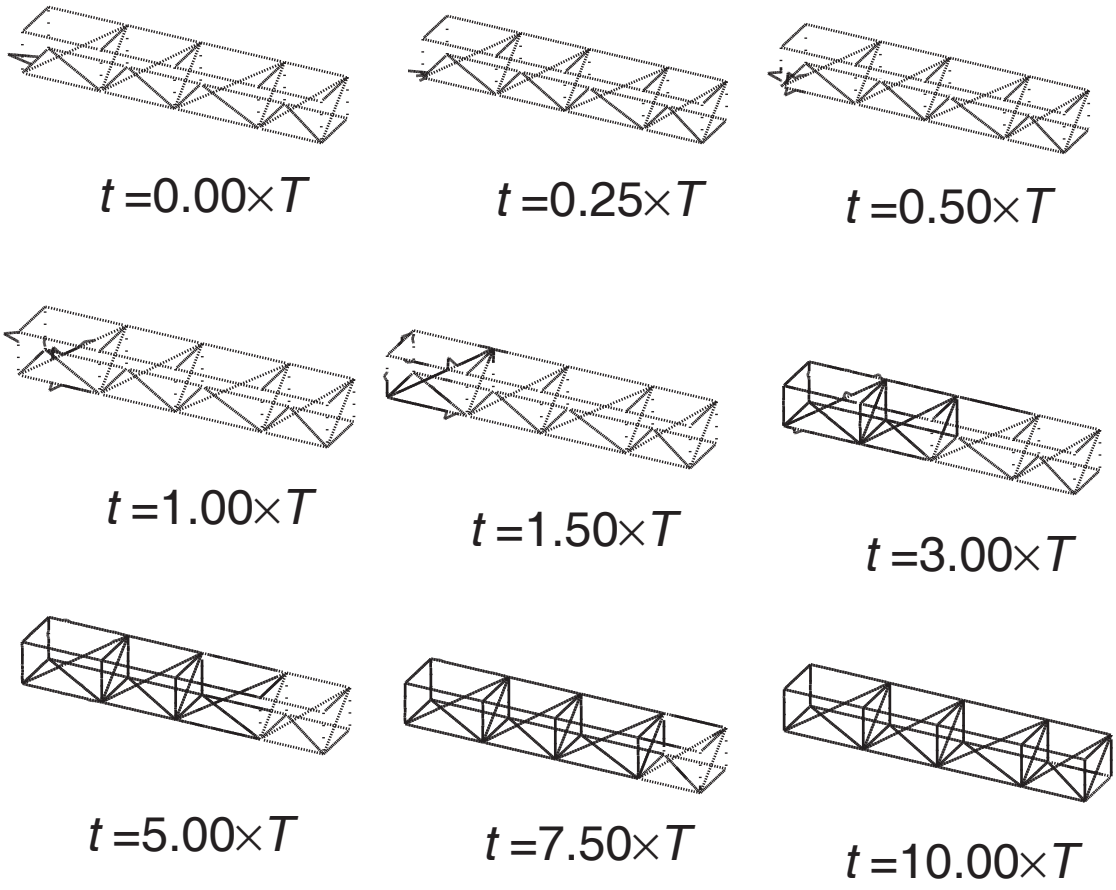

Figure 5.14: Evolution of the energy density within the truss of Fig. 5.13 at selected instants for a compressional initial pulse. Only the non-vanishing energy density is displayed on this plot. No offset at the junctions is considered.

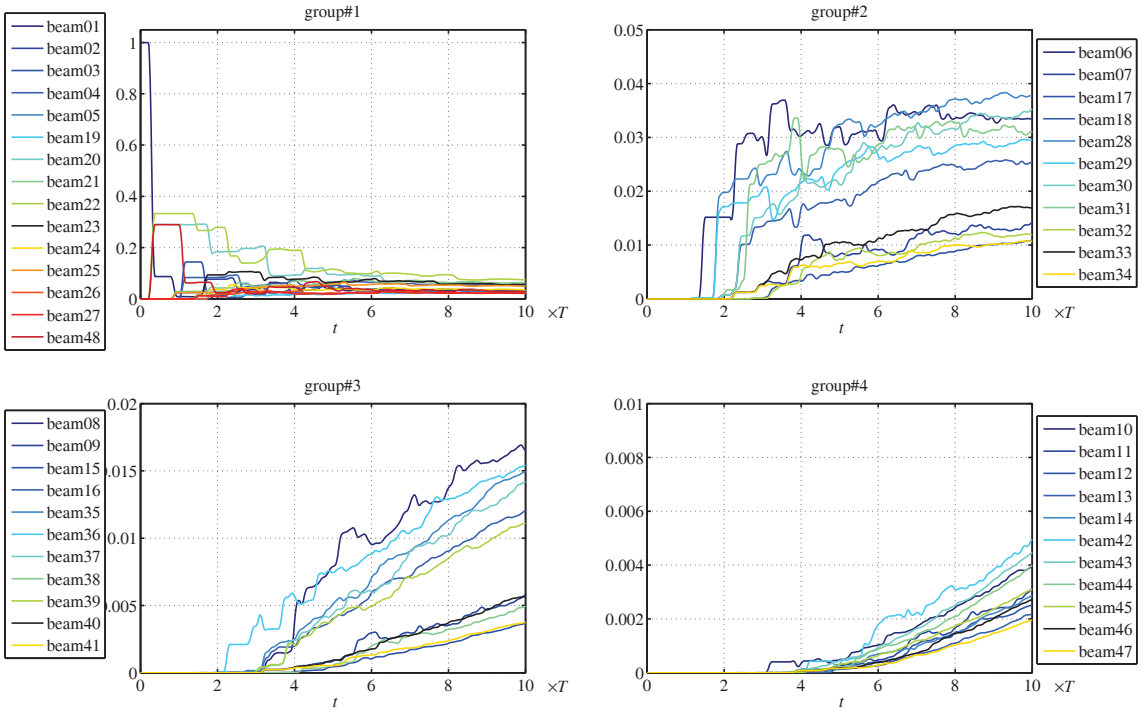

Figure 5.15: Evolution of the total energies $\mathcal{E}^p(t)$, $1 \leq p \leq 48$, in each beam of the truss of Fig. 5.13 gathered by beam group for an initial compressional pulse. No offset at the junctions is considered.

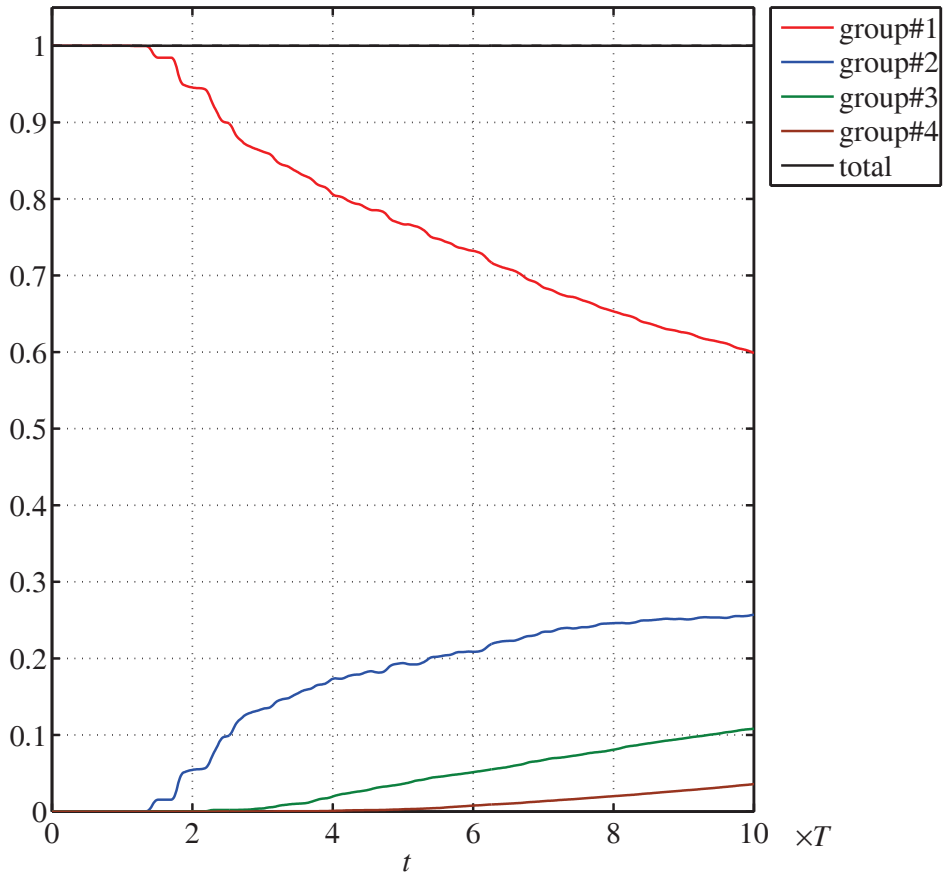

Figure 5.16: Evolution of the sum of the total energies in each beam group of the truss of Fig. 5.13 for an initial compressional wave. No offset at the junctions is considered.

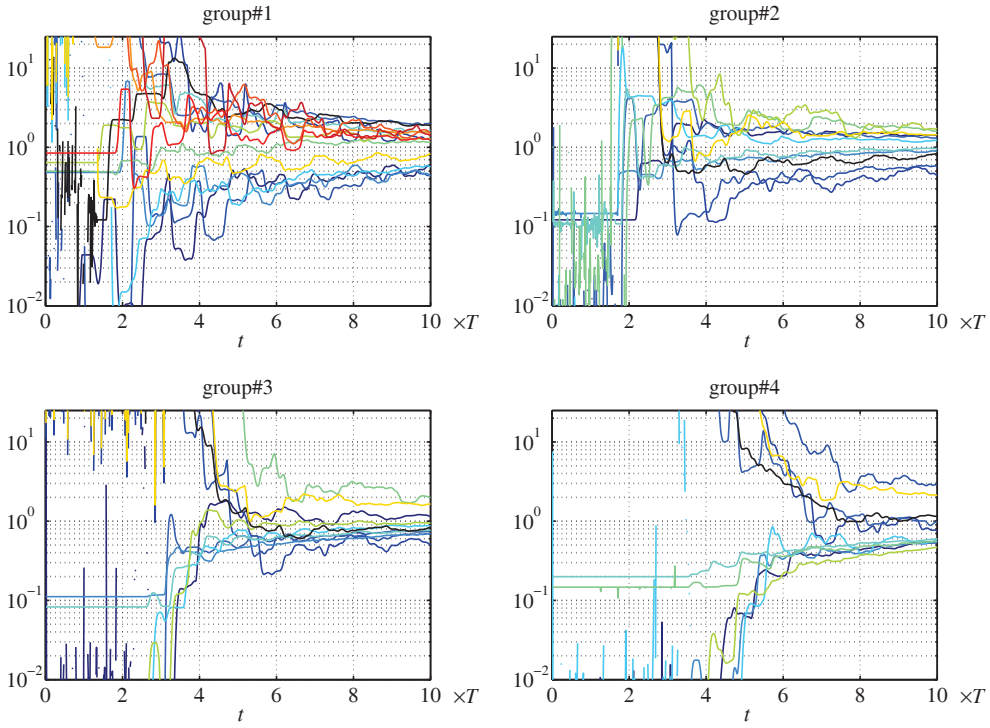

Figure 5.17: Evolution of the ratios $\dfrac{c_{\mathrm{T}}\mathcal{E}^p_{\mathrm{T}}(t)}{2c_{\mathrm{P}}\mathcal{E}^p_{\mathrm{P}}(t)}$, $1 \leq p \leq 48$, in each beam of the truss of Fig. 5.13 gathered by beam group for an initial compressional pulse. No offset at the junctions is considered.

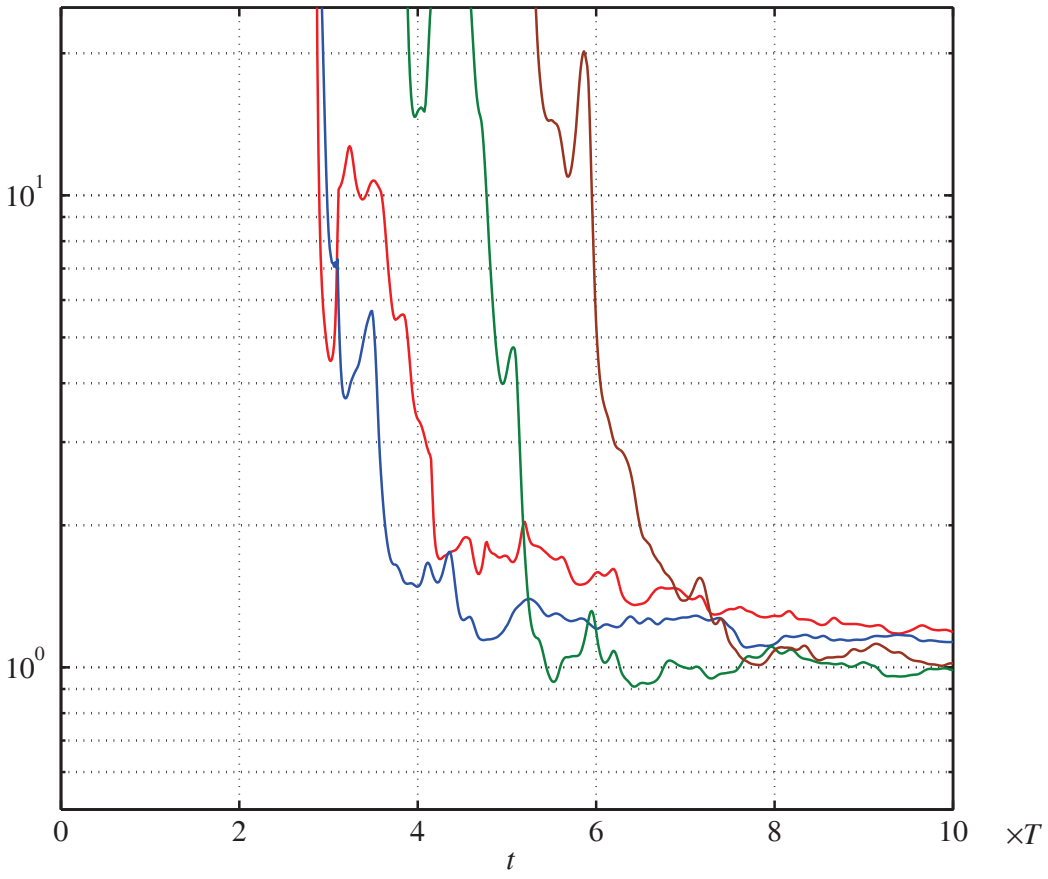

Figure 5.18: Evolution of the mean of the ratios $\dfrac{c_{\mathrm{T}}\mathcal{E}^p_{\mathrm{T}}(t)}{2c_{\mathrm{P}}\mathcal{E}^p_{\mathrm{P}}(t)}$, in each beam group of the truss of Fig. 5.13 for an initial compressional pulse. No offset at the junctions is considered.

5.2 Numerical experiments of time reversal

The aim of a time-reversal experiment is to possibly reconstruct an initial pulse from time-reversed signals. In the original setting of Fink [29], the time-reversed signals were amplified beforehand in order to reconstruct an amplified pulse able to break up kidney stones, for example. In the present case, time reversal is used to test the accuracy of the proposed RKDG scheme in terms of numerical dispersion and dissipation. A similar procedure has been performed in [96], for example, for a spectral finite element code solving the elastic wave equation in an unbounded, three-dimensional anisotropic random medium. This computation takes advantage of the reversibility of the wave equation (1.4). Here the time-reversal procedure is considered for the transport equation (3.40). The time-reversed signals are thus the energy density fields simulated by the RKDG scheme within the whole structure up to a final time t_{end}. The time-reversed energy density field $w_\alpha^{\text{TR}}(s,k,t)$ should have the property:

$$w_\alpha^{\text{TR}}(s,k,t) = w_\alpha(s,-k,t_{\text{end}}-t)\,, \tag{5.2}$$

meaning that the energy density travelling in a direction $\hat{k}$ at time t and position s in the direct simulation travels in a direction $-\hat{k}$ at time $t_{\text{end}}-t$ and position s in the reversed simulation. Considering first an isolated beam, the time-reversed energy density field within that beam is obtained straightforwardly. As the evolution law (3.36) is the same for both directions $\hat{k}=\pm 1$, the time-reversed evolution equation is the direct evolution equation with an opposite direction $\hat{k}=\mp 1$. Then the signal to be time-reversed is the energy density field at the end of the direct computation. The time-reversed computation is performed using the direct energy density field at t_{end} as the initial condition, considering however an opposite direction of propagation. Time-reversed numerical simulations require a proper definition of the reversed-time collision operator of Eq. (3.56), and the reversed-time reflection/transmission operators of Eq. (3.66-Eq. (3.67)).

5.2.1 Reversed-time collision operator

For a randomly heterogeneous medium, the reversed-time collision operator is derived as follows. Considering the right-hand side of Eq. (3.51) with the opposite direction as an entry, gives the new collision operator:

$$\begin{aligned}\mathcal{Q}_\alpha^{\text{TR}}(k) &= \Sigma_\alpha(-k)(w_\alpha(k)-w_\alpha(-k))\\ &= -\Sigma_\alpha(k)(w_\alpha(-k)-w_\alpha(k))\\ &= -\mathcal{Q}_\alpha(k)\,.\end{aligned} \tag{5.3}$$

Thus the reversed-time collision operator is the opposite of the collision operator of the direct simulation.

5.2.2 Reversed-time reflection/transmission operators

The reversed-time reflection/transmission operators at the junctions have also to be derived. Indeed, if the reflection/transmission operators of the direct simulation are used, the spread of the energy density over the truss will continue. Consider for example Fig. 5.19, which displays some energy waves in a direct and in a time-reversed simulation. In the

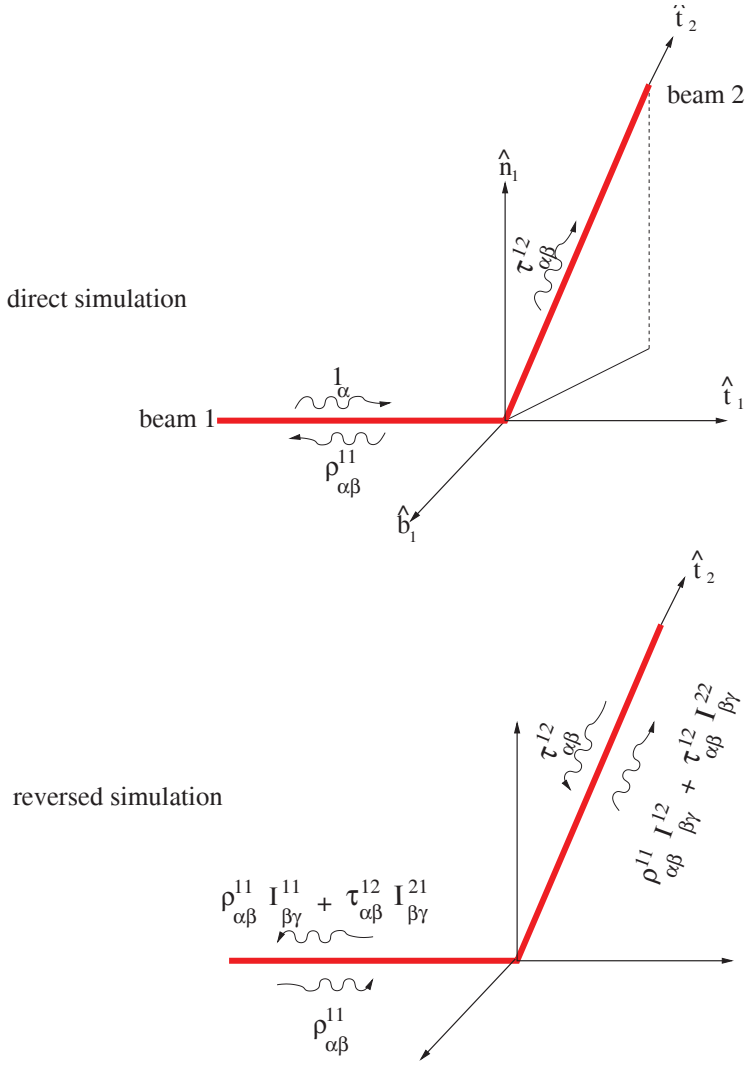

Figure 5.19: Energy waves in the direct simulation and their compatibility conditions for a time-reversed simulation. $\tau^{pq}_{\alpha\beta}$ is the transmission operator, $\rho^{pp}_{\alpha\beta}$ is the reflection operator, and $I^{pq}_{\alpha\beta}$ is the reversed-time reflection/transmission operator. The wavy arrows indicate propagation directions.

direct simulation, an incident wave normalized to 1 in the mode α generates reflected and transmitted waves of amplitudes given by the reflection/transmission coefficients Eqs.(3.66-3.67) when it impinges the junction. In the time-reversed simulation the wavenumber, and so the propagation direction, are the opposite from the direct simulation. Thus the impinging waves are now the reflected and transmitted waves once they have been time reversed. When impinging the junction, these waves generate reflected and transmitted waves themselves, according to the reversed-time reflection/transmission operators. So the latter should be constructed such that one recovers the initial energy wave in mode α from the reflected/transmitted waves. This yields to the following compatibility equations for an

incident wave in the first beam of a junction of two beams:

$$\begin{aligned} \sum_{\beta\in\mathsf{E}} \rho^{11}_{\alpha\beta} I^{11}_{\beta\gamma} + \tau^{12}_{\alpha\beta} I^{21}_{\beta\gamma} &= \delta_{\alpha\gamma}\,, \\ \sum_{\beta\in\mathsf{E}} \rho^{11}_{\alpha\beta} I^{12}_{\beta\gamma} + \tau^{12}_{\alpha\beta} I^{22}_{\beta\gamma} &= 0\,, \end{aligned} \tag{5.4}$$

where $I^{pq}_{\alpha\beta}$ is the reversed-time reflection/transmission operator for a wave in mode α in beam $\#p$ to a wave in mode β in the beam $\#q$. These operators are the unknowns of the system (5.4), while $\rho^{pq}_{\alpha\beta}$ and $\tau^{pq}_{\alpha\beta}$ are the reflection and transmission operators for the direct propagation defined in Sect. 3.3.2. The first equation describes how the incident wave is recovered in beam #1, and the second one is a statement of the absence of impinging wave in beam #2 for the direct simulation. There are four unknowns for two equations in this system. However applying the same analysis for an incident wave in beam #2 adds two equations, namely:

$$\begin{aligned} \sum_{\beta\in\mathsf{E}} \rho^{22}_{\alpha\beta} I^{22}_{\beta\gamma} + \tau^{21}_{\alpha\beta} I^{12}_{\beta\gamma} &= \delta_{\alpha\gamma}\,, \\ \sum_{\beta\in\mathsf{E}} \rho^{22}_{\alpha\beta} I^{21}_{\beta\gamma} + \tau^{21}_{\alpha\beta} I^{11}_{\beta\gamma} &= 0\,. \end{aligned} \tag{5.5}$$

The system (5.4)-(5.5) in a matrix form reads as follows. Let $\boldsymbol{\rho}^{pp}$ and $\boldsymbol{\tau}^{pq}$ be the matrices gathering the reflection and transmission operators for waves from beam p to beam q respectively, and let $\boldsymbol{I}^{pq}$ be the matrix gathering the reversed-time reflection and transmission operators for waves from beam p to beam q respectively; then the system (5.4)-(5.5) becomes:

$$\begin{pmatrix} \boldsymbol{\rho}^{11} & \boldsymbol{\tau}^{12} \\ \boldsymbol{\tau}^{21} & \boldsymbol{\rho}^{22} \end{pmatrix} \begin{pmatrix} \boldsymbol{I}^{11} & \boldsymbol{I}^{12} \\ \boldsymbol{I}^{21} & \boldsymbol{I}^{22} \end{pmatrix} = \boldsymbol{I}_{12}\,. \tag{5.6}$$

Thus it appears that the reversed-time reflection/transmission matrix for the junction is the inverse of the direct reflection/transmission matrix. If the number of connected beams exceeds two, the same analysis can be followed by adding the relations taking into account the waves in the additional beams. If for example three beams are connected, one has:

$$\begin{pmatrix} \boldsymbol{I}^{11} & \boldsymbol{I}^{12} & \boldsymbol{I}^{13} \\ \boldsymbol{I}^{21} & \boldsymbol{I}^{22} & \boldsymbol{I}^{23} \\ \boldsymbol{I}^{31} & \boldsymbol{I}^{32} & \boldsymbol{I}^{33} \end{pmatrix} = \begin{pmatrix} \boldsymbol{\rho}^{11} & \boldsymbol{\tau}^{12} & \boldsymbol{\tau}^{13} \\ \boldsymbol{\tau}^{21} & \boldsymbol{\rho}^{22} & \boldsymbol{\tau}^{23} \\ \boldsymbol{\tau}^{31} & \boldsymbol{\tau}^{32} & \boldsymbol{\rho}^{33} \end{pmatrix}^{-1} . \tag{5.7}$$

5.2.3 Numerical examples

The numerical time-reversal procedure has been applied to the truss of Fig. 5.1, considering some material randomness. The numerical and mechanical parameters are the same as for the case of Sect.5.1.1.3. The direct simulation is performed until $t_{\text{end}} = 2 \times T$, where T is as defined in Sect.5.1.1. Fig. 5.20, Fig. 5.21, and Fig. 5.22 show the evolution of the energy density in the truss at selected instants, the evolution of the total energies in each beam, and the evolution of the ratio between the transverse on the longitudinal energies,

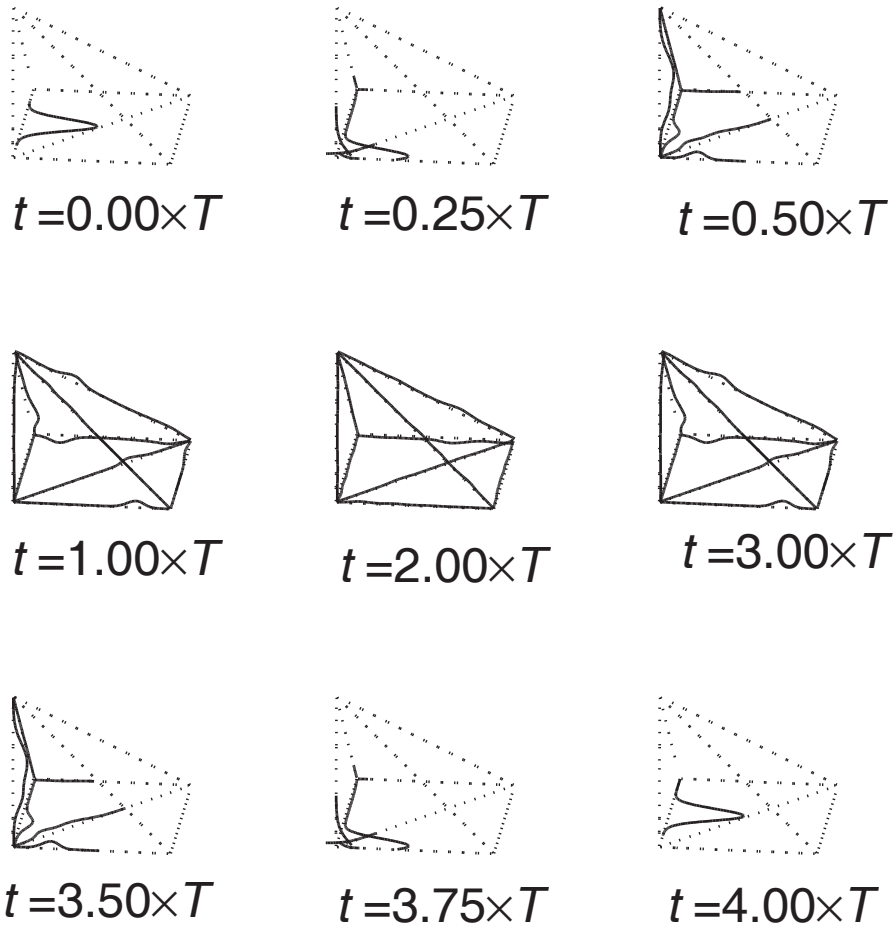

Figure 5.20: Direct and reversed evolution of the energy density within the truss of Fig. 5.1 at selected instants for a compressional initial pulse, accounting for some material randomness. Only the non-vanishing energy density is displayed on this plot. No offset at the junctions is considered. The time reversal is performed at $T = 2$.

respectively.

Fig. 5.21 shows that the energy is rather uniformly spread over the entire truss at $t = t_{\text{end}}$. All these plots are symmetric about t_{end}. This feature underlines the low dissipation and low dispersion of the numerical scheme because the evolution of the energy is the same for the direct and reversed simulations. If the scheme lacks these properties, then it is impossible to have this symmetry because the numerical dispersion and dissipation would have modified the signal too much to be able to retrieve the initial pulse. Moreover that initial pulse is well retrieved.

On Fig. 5.23 and Fig. 5.24 the energy density is plotted for $t_{\text{end}} = 3 \times T$. The time-reversed computation fails because t_{end} is too long, leading to a too much diffusive state. The latter is supposedly described by a diffusion equation, which is not reversible in time. All the information brought by the initial pulse is spread over the truss. Despite the failure of retrieving that initial condition (see the spurious oscillations at $t = 6 \times T$ on Fig. 5.23),

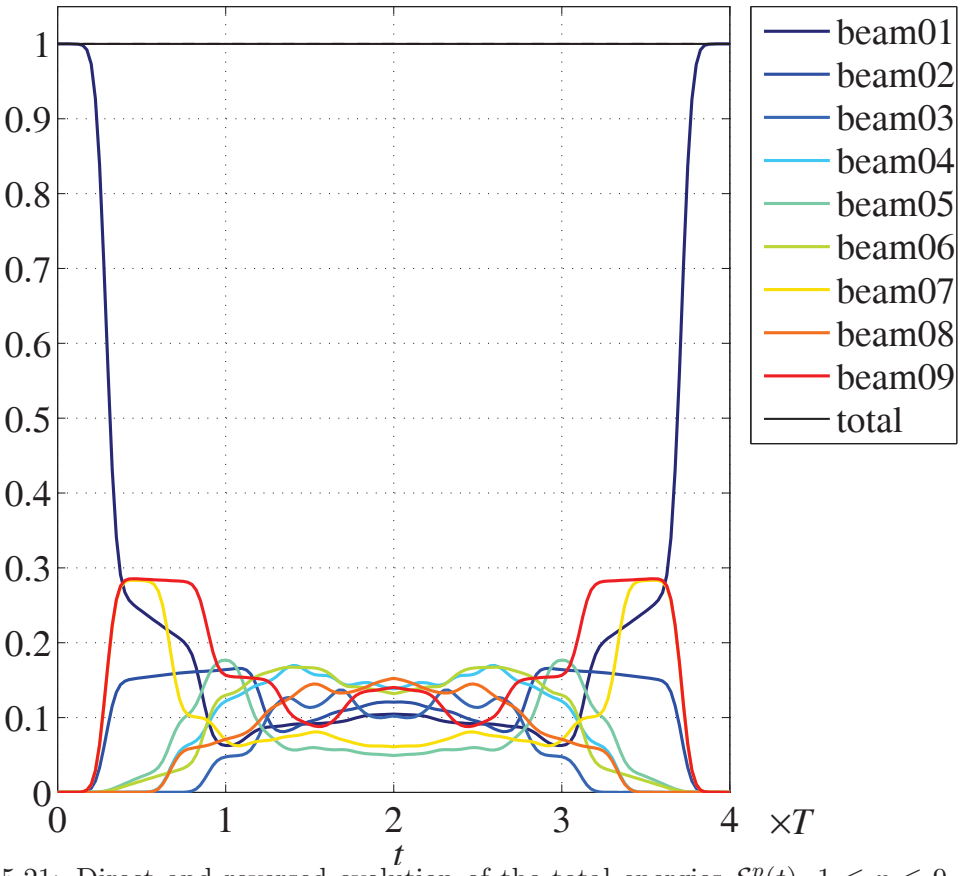

Figure 5.21: Direct and reversed evolution of the total energies $\mathcal{E}^p(t)$, $1 \leq p \leq 9$, in each beam of the truss of Fig. 5.1 for an initial compressional pulse, accounting for some material randomness. No offset at the junctions is considered. The time reversal is performed at $T = 2$.

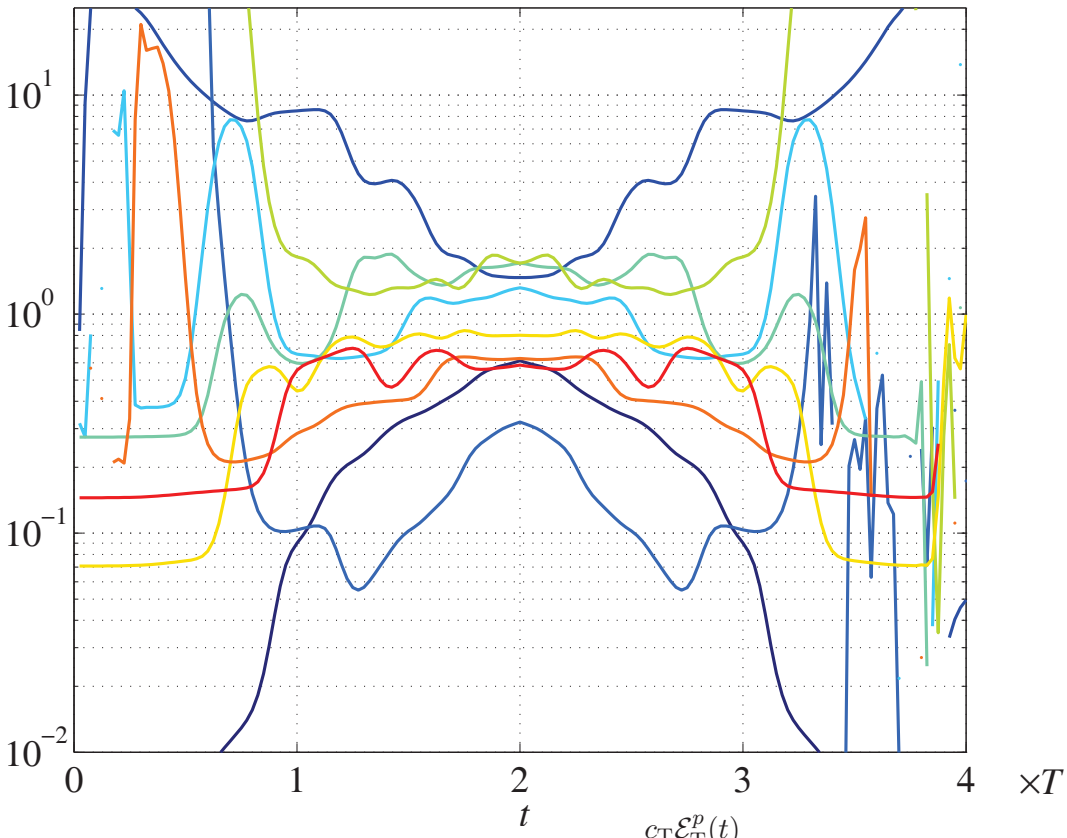

Figure 5.22: Direct and reversed evolution of the ratios $\dfrac{c_{\mathrm{T}}\mathcal{E}^p_{\mathrm{T}}(t)}{2c_{\mathrm{P}}\mathcal{E}^p_{\mathrm{P}}(t)}$, $1 \leq p \leq 9$, in each beam of the truss of Fig. 5.1 for an initial compressional pulse, accounting for some material randomness. No offset at the junctions is considered. The time reversal is performed at $T = 2$.

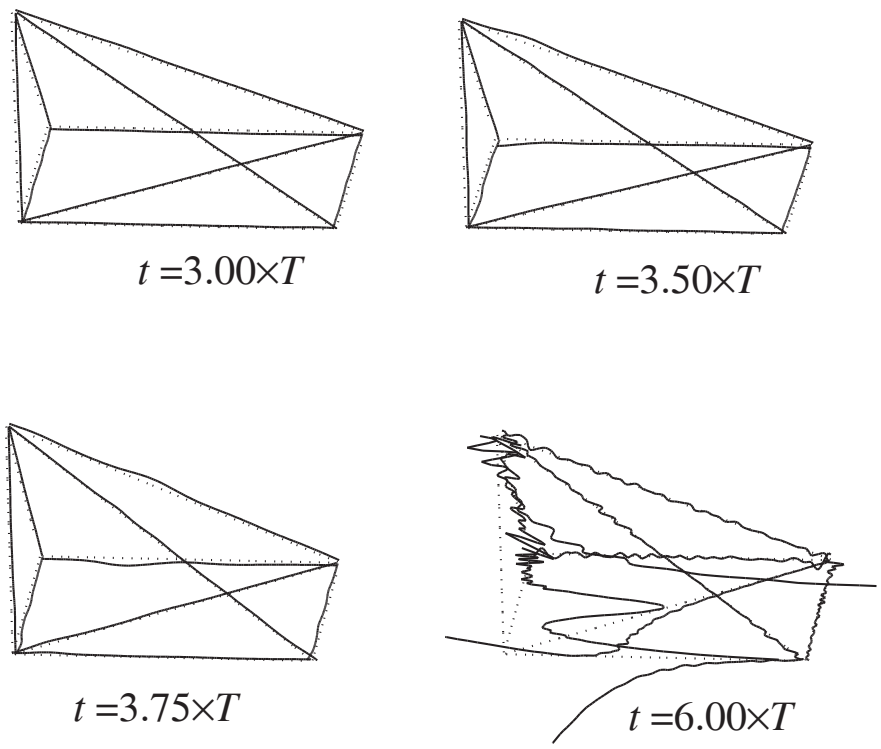

Figure 5.23: Direct and reversed evolution of the energy density within the truss of Fig. 5.1 at selected instants for a compressional initial pulse, accounting for some material randomness. Only the non-vanishing energy density is displayed on this plot. No offset at the junctions is considered. The time reversal is performed at $T = 3$.

the total energy on the entire truss is conserved all along the simulation (black line on Fig. 5.24). The divergence could be due to the spurious modes (see Sect.4.2.3) that are greatly amplified by the reversed-time reflection/transmission coefficients having a norm possibly greater than 1, together with the dispersion and the dissipation brought by the numerical scheme and the numerical accuracy of the computer. These so-called zero-energy modes are unavoidable in numerical simulations because they arise from the discretization of continuous problems.

Nevertheless this numerical time-reversal processing remains useful in view of the development of a real time-reversal processing, in order to perform non destructive monitoring for example. The difference with the technique of time-reversal mirrors used by Fink [29] concerns the data to be recorded and time reversed. In the first case the field over the entire domain at the end of the direct simulation is needed, whereas in the second case the history of the evolution during the entire direct process is required on a closed surface surrounding the target source.

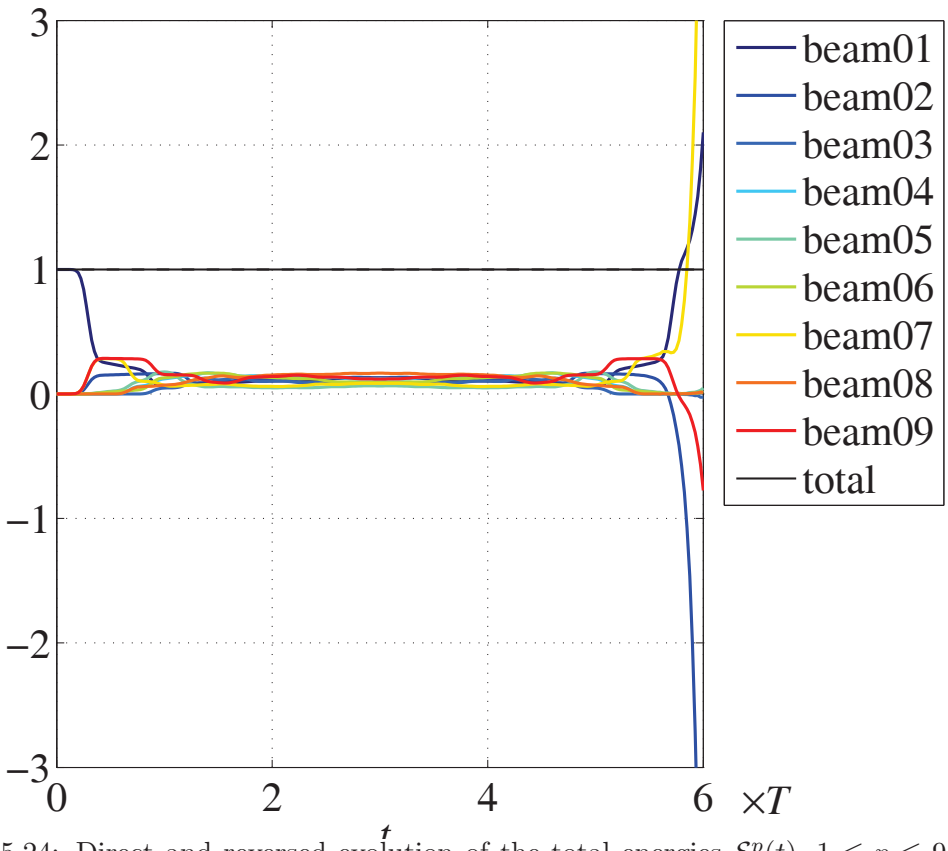

Figure 5.24: Direct and reversed evolution of the total energies $\mathcal{E}^p(t)$, $1 \leq p \leq 9$, in each beam of the truss of Fig. 5.1 for an initial compressional pulse, accounting for some material randomness. No offset at the junctions is considered. The time reversal is performed at $T = 3$.

5.3 Conclusions

The proposed RKDG numerical scheme has been tested on examples showing the behavior of the solutions of transport or radiative transfer equations at late times. The simulations detailed in this chapter describe the evolution of the energy density within beam trusses submitted to impulse loads. The computations performed for a single-bay truss constituted from homogeneous materials show that a diffusive behavior emerges at late times. It is characterized by a spatial spread of the energy density over the entire structure, as well as modal equipartition of the total energy. It agrees with the observations drawn in the general introduction of this thesis about the HF behavior of built-up structures. It also corresponds to the hypothesis of modal equipartition holding in SEA (see Sect.1.4.1). The diffusive behavior is prompted by the multiple reflections/transmissions of the energy density taking place at the junctions. Consequently, it has been highlighted that the ratio of the transverse energy to the longitudinal energy converges toward a limit depending on the number of modes generated at the junctions by the reflection/transmission phenomena. Taking into account some randomness of materials shows that the diffusive state is not modified. It only scatters the energy density of a given mode over the beams without modal conversion, making the transient smoother. But the diffusion state does not arise earlier.

The numerical method has also been tested on a larger structure, namely a four-bay beam truss, showing its potentiality to be applied for industrial purposes. At last a time-reversal processing has been implemented in order to test the low dispersive and low dissipative properties of the numerical scheme by demonstrating that it is possible to retrieve the initial pulse from the spread of the energy density at a late time. This time-reversal processing could be useful for the structural health monitoring of complex, multi-bay trusses.

Conclusions and perspectives

An analytical model of wave propagation in a waveguide has been derived and studied in the scope of the HF range. It allows to examine the accuracy of several beam models. Then a transient transport model for the propagation of the HF vibrational energy density in three-dimensional Timoshenko beam trusses has been derived. Particular attention has been paid to the generality of the formulation of the mechanical behavior of the beams. Hence the cross-section may have arbitrary shapes and the beams may be curved. It has been shown that the curvature and the shape of the beam do not influence the velocity of the energetic waves. Two family of waves have been highlighted. The longitudinal one that gathers the compressional and the two bending modes, and the transverse one that gathers the torsional and the two shearing modes. Within the beam, energetic modes do not couple, so all the conversion phenomena occur at the junctions between beams. Moreover the formulations of a prestressed beam and a beam constituted with random material have been investigated. These extensions do not modify basically the HF behavior of beams. The prestressing only modify the stiffness of the material and the random heterogeneities scatter the energy backward but with modal conversion.

The proposed model also accounts for the power flow reflection and transmission phenomena at the junctions in the HF range. They are characterized by reflection/transmission operator for the energy flux in order to be compatible with the energetic formulation of the beam vibrations. Here again, the derivation of these operators account for the generality of the junctions. Also the beams may be not connected at the same point on their cross-sections. If they are, then the shearing and bending modes are totally uncoupled, contrary to the low frequency case. It leads to two different kinds of reflection/transmission phenomena. The one concerning the translational motions (the longitudinal mode and the shearing modes), and the one concerning the rotational motions (the torsional mode and the bending modes). Both are totally uncoupled, thus if the initial condition contains only translational (respectively rotational) modes, then no rotational (respectively translational) modes are generated at the junctions. For the case of a junction with an offset between the connected beams, then all the modes are likely to arise at the junction.

The proposed analytical model is numerically solved by a Runge-Kutta discontinuous Galerkin (RKDG) finite element scheme. The dissipation and the dispersion of this scheme have been studied. It appears that both are very low and the scheme is thus suitable for long time simulations. Moreover, comparison to an analytical solution in the case of a beam made of random materials submitted to a impulse load shows that the numerical solution gives similar results.

Numerical results obtained for several examples of beam trusses illustrate the transient regime and the onset of a diffusive regime at late times. The latter is prompted by the multiple reflections and transmissions of the energy modes at the beam junctions, with possible mode conversions. This scattering process is different from the multiple scattering of waves on random heterogeneities or inclusions considered elsewhere see *e.g.* [58, 75, 87, 105], though it gives rise to the same qualitative behavior at late times. Diffusion is characterized by an equilibration of the total energy in each subsystem (the beam components of the truss), it is the spatial equipartition, and for each propagation mode, it is the modal equipartition. The outbreak of diffusion does not seem to arise more quickly in presence of random heterogeneities. Quantitatively, randomness would not however contribute to mix all wave modes because no conversion occurs on account of them. It only spreads the energy in the structure but not between the modes. This situation is comparable to the assumption of modal equipartition invoked in the Statistical Energy Analysis (SEA) of structural-acoustic systems. This model establishes hence the link between the microscopic model of wave propagation and a macroscopic model given by diffusion equations. However a rigorous mathematical model of the diffusive behavior induced by multiple scattering at the junctions and interfaces lacks at present, even if some conclusions about the expected equilibration rules have been drawn. An other interesting study concerning the diffusion behavior could consist in a characterization of the diffusion by a criteria depending on the value of the total energy density or/and the ratio of longitudinal on transverse energy densities. A parametrical study could also allow to study the effect of the truss geometry on the outbreak of the diffusion.

Beyond this investigation on the diffusion limit, the analysis for more complex junctions should also be considered in future works, including for example elastic constraints or dissipation phenomena [11]. It could also be interesting to consider the reflection/transmission operators directly by an energetic approach, avoiding to get back to a formulation of the boundary conditions in terms of displacements and resultant netforces and moments. For example, the interface condition can be taken into account directly in the transport equations by considering diffusion operators with small viscosity, as done in [30].

The time-reversal technique provides an other evidence of the stability and the accuracy of the proposed numerical scheme. But it could be used as a tool for non destructive evaluation in order to detect defaults in beam trusses for instance. The time-reversal process exposed here constitutes the first step of a complete time-reversal method with time reversal mirrors. This issue is the subject of an ongoing work and has given satisfactory results already.

Another topic could be the micro-local analysis of the Navier equation in a waveguide. Its purpose is to derive an exact model of HF wave propagation in beams, in order to further study the relevance of the Timoshenko model in the HF range. An other possibility of investigation of the link between the "exact" model and the Timoshenko model, concerns the study of the projection of the Timoshenko modes on the Lamb spectrum. Indeed, it may be useful to understand how the energy associated the Timoshenko modes spread over the propagating Lamb modes. A last point of concern is the analysis of the evolution of the mode's shapes resulting from the Lamb model with respect to the frequency range.

In short, many theoretical investigations could be carried out, but the numerical scheme and the modelling frame are robust and easily adaptable to modifications induced by the invoked studies.

Appendix A

Computation of the reflection/Transmission operators

The displacement and effort continuities are given by Eq. 3.64. The constitutive equations (3.12) and (3.13) provide the relation between the forces and displacements. In term of amplitude of reflected and transmitted waves, it is:

$$\begin{aligned}
\mathbb{1}_u + \boldsymbol{B}^1 &= \boldsymbol{R}^{1q}\Big(\boldsymbol{B}^q + i\boldsymbol{K}^q\boldsymbol{\Lambda}_1^q\boldsymbol{C}^q\Big)\\
-i\boldsymbol{K}^1\mathbb{1}_\theta + i\boldsymbol{K}^1\boldsymbol{C}^1 &= \boldsymbol{R}^{1q}\Big(-i\boldsymbol{K}^q\boldsymbol{C}^q\Big)\\
\boldsymbol{C}_1^1\boldsymbol{J}_0^1(\boldsymbol{D}_u^1\mathbb{1}_u + \boldsymbol{D}_{ur}^1\boldsymbol{B}^1 + i\boldsymbol{\Omega}\boldsymbol{K}^1(-\mathbb{1}_\theta + \boldsymbol{C}^1)) &= \sum_q \boldsymbol{R}^{1q}\Big(\boldsymbol{C}_1^q\boldsymbol{J}_0^q(\boldsymbol{D}_u^q\boldsymbol{B}^q - i\boldsymbol{\Omega}\boldsymbol{K}^q\boldsymbol{C}^q)\Big)\\
-i\boldsymbol{C}_2^1\boldsymbol{J}_2^1\boldsymbol{K}^1(-\boldsymbol{D}_\theta^1\mathbb{1}_\theta + \boldsymbol{D}_{\theta r}^1\boldsymbol{B}^1) &= \sum_q \boldsymbol{R}^{1q}\Big(i\boldsymbol{C}_2^q\boldsymbol{J}_2^q\boldsymbol{D}_\theta^q\boldsymbol{K}^q\boldsymbol{C}^q - \boldsymbol{\Lambda}_1^q\boldsymbol{C}_1^q\boldsymbol{J}_0^q(\boldsymbol{D}_u^q\boldsymbol{B}^q - i\boldsymbol{\Omega}\boldsymbol{K}^q\boldsymbol{C}^q)\Big)
\end{aligned}$$

where

$$\boldsymbol{D}_u^p = \begin{pmatrix} -ik_{\mathrm{P}}^p & \kappa_g^p & \kappa_n^p \\ -\kappa_g^p & -ik_{\mathrm{T}}^p & \tau^p \\ -\kappa_g^p & -\tau^p & -ik_{\mathrm{T}}^p \end{pmatrix},$$

$$\boldsymbol{D}_{ur}^p = \begin{pmatrix} ik_{\mathrm{P}}^p & \kappa_g^p & \kappa_n^p \\ -\kappa_g^p & ik_{\mathrm{T}}^p & \tau^p \\ -\kappa_g^p & -\tau^p & ik_{\mathrm{T}}^p \end{pmatrix},$$

$$\boldsymbol{D}_\theta^p = \begin{pmatrix} -ik_{\mathrm{T}}^p & \kappa_g^p & \kappa_n^p \\ -\kappa_g^p & -ik_{\mathrm{P}}^p & \tau^p \\ -\kappa_g^p & -\tau^p & -ik_{\mathrm{P}}^p \end{pmatrix},$$

$$\boldsymbol{D}_{\theta r}^p = \begin{pmatrix} ik_{\mathrm{T}}^p & \kappa_g^p & \kappa_n^p \\ -\kappa_g^p & ik_{\mathrm{P}}^p & \tau^p \\ -\kappa_g^p & -\tau^p & ik_{\mathrm{P}}^p \end{pmatrix},$$

$$\boldsymbol{K}^p = \mathrm{diag}(k_{\mathrm{T}}^p, k_{\mathrm{P}}^p, k_{\mathrm{P}}^p),$$

$$\boldsymbol{\Lambda}_1^q = \begin{pmatrix} 0 & -z_1^q & y_1^q \\ z_1^q & 0 & 0 \\ -y_1^q & 0 & 0 \end{pmatrix},$$

and $\mathbb{1}_{u,\theta}$ is the indicator function of the incident mode. $\boldsymbol{\Omega}$ is the matrix related to the operator $\hat{\boldsymbol{t}}\times$. Thus the local system for the beam 1 to be solved is:

$$\boldsymbol{I}_1 = \boldsymbol{\Psi}_1 \boldsymbol{X}_1 \,,$$

where

$$\boldsymbol{I}_1 = \begin{pmatrix} \boldsymbol{I}_3 & \boldsymbol{0} \\ \boldsymbol{0} & -i\boldsymbol{K}^1 \\ \vdots & \\ \boldsymbol{C}_1^1 \boldsymbol{J}_0^1 \boldsymbol{D}_u^1 & -i\boldsymbol{C}_1^1 \boldsymbol{J}_0^1 \boldsymbol{\Omega} \boldsymbol{K}^1 \\ \boldsymbol{0} & i\boldsymbol{C}_2^1 \boldsymbol{J}_2^1 \boldsymbol{K}^1 \boldsymbol{D}_\theta^1 \end{pmatrix},$$

$$\boldsymbol{X}_1 = (\boldsymbol{B}^1, \boldsymbol{C}^1, \boldsymbol{B}^q, \boldsymbol{C}^q, ...)^T \,,$$

$$\boldsymbol{\Psi}_1 = \begin{pmatrix} -\boldsymbol{I}_3 & \boldsymbol{0} & \boldsymbol{R}^{1q} & i\boldsymbol{R}^{1q}\boldsymbol{K}^q\boldsymbol{\Lambda}_1^q & \cdots \\ \boldsymbol{0} & -i\boldsymbol{K}^1 & \boldsymbol{0} & -i\boldsymbol{R}^{1q}\boldsymbol{K}^q & \cdots \\ \vdots & & & & \\ -\boldsymbol{C}_1^1\boldsymbol{J}_0^1\boldsymbol{D}_{ur}^1 & i\boldsymbol{C}_1^1\boldsymbol{J}_0^1\boldsymbol{\Omega}\boldsymbol{K}^1 & \boldsymbol{R}^{1q}\boldsymbol{C}_1^q\boldsymbol{J}_0^q\boldsymbol{D}_u^q & -i\boldsymbol{R}^{1q}\boldsymbol{C}_1^q\boldsymbol{J}_0^q\boldsymbol{\Omega}\boldsymbol{K}^q & \cdots \\ \boldsymbol{0} & i\boldsymbol{C}_2^1\boldsymbol{J}_2^1\boldsymbol{K}^1\boldsymbol{D}_{\theta r}^1 & -\boldsymbol{R}^{1q}\boldsymbol{C}_1^q\boldsymbol{J}_0^q\boldsymbol{\Lambda}_1^q\boldsymbol{D}_u^q & i\boldsymbol{R}^{1q}\boldsymbol{C}_2^q\boldsymbol{J}_2^q\boldsymbol{D}_\theta^q\boldsymbol{K}^q + i\boldsymbol{R}^{1q}\boldsymbol{\Lambda}_1^q\boldsymbol{C}_1^q\boldsymbol{J}_0^q\boldsymbol{\Omega}\boldsymbol{K}^q & \cdots \end{pmatrix}.$$

Appendix B

Jacobi polynomials

The normalized Jacobi polynomials are the solutions of the Sturm-Liouville eigenvalue problem:

$$-\frac{d}{d\xi}(1-\xi^2)p^{(a,b)}(\xi)\frac{d}{d\xi}\mathsf{J}_m^{(a,b)}(\xi) = m(m+a+b+1)p^{(a,b)}(\xi)\mathsf{J}_m^{(a,b)}(\xi)\,, \tag{B.1}$$

where $p^{(a,b)}(\xi) = (1-\xi)^a(1+\xi)^b$ is the weight function, with $a, b > -1$. The Jacobi polynomials $\tilde{\mathsf{J}}_m^{(a,b)}$ are given by:

$$\tilde{\mathsf{J}}_m^{(a,b)} = \sqrt{\gamma_m}\mathsf{J}_m^{(a,b)}$$

where the normalization constant γ_m is:

$$\gamma_m = \frac{2^{a+b+1}(m+a)!(m+b)!}{(2m+a+b+1)(m+a+b)!m!}\,.$$

The Jacobi polynomials are explicitly expressed by the Rodrigues' formula:

$$\begin{aligned}\tilde{\mathsf{J}}_m^{(a,b)}(\xi) &= \frac{(-1)^m}{2^m m!}p^{(-a,-b)}(\xi)\frac{d}{d\xi^m}p^{(m+a,m+b)}(\xi)\\ &= \frac{1}{2^m}\sum_{k=0}^{m} C_k^{m+a}C_{m-k}^{m+b}(\xi-1)^{m-k}(\xi+1)^k\,,\end{aligned}$$

with the generalized binomial coefficients [1] $C_p^z = \frac{z!}{(z-p)!p!}$. They have the property to be orthogonal with respect to the inner product:

$$< \tilde{\mathsf{J}}_m^{(a,b)}, \tilde{\mathsf{J}}_n^{(a,b)} >_{(a,b)} = \int_{\hat{\mathsf{D}}} \tilde{\mathsf{J}}_m^{(a,b)}(\xi)\tilde{\mathsf{J}}_n^{(a,b)}(\xi)p^{(a,b)}(\xi)d\xi = \gamma_m\delta_{mn}\,. \tag{B.2}$$

An other useful property of these polynomials concerns the computation of their derivatives:

$$\frac{d}{d\xi}\mathsf{J}_m^{(a,b)}(\xi) = \sqrt{m(m+a+b+1)}\mathsf{J}_{m-1}^{(a+1,b+1)}(\xi)\,, \tag{B.3}$$

Finally, the Jacobi polynomials have the symmetry relation:

$$\mathsf{J}_m^{(a,b)}(-\xi) = (-1)^m\mathsf{J}_m^{(b,a)}(\xi)\,.$$

1. It is reminded that $z! := \Gamma(z+1) = \int_0^{+\infty} t^z \mathrm{e}^{-t}dt$ and $\Gamma(p+1) = p!$, the usual factorial, if p is an integer. Indeed as $\Gamma(z+1) = z\Gamma(z)$, one has $z! = z(z-1)!$ *etc.*

Practically to compute the normalized Jacobi polynomials, one uses an induction relation:

$$\xi \mathsf{J}_n^{(a,b)}(\xi) = a_n \mathsf{J}_{n-1}^{(a,b)}(\xi) + b_n \mathsf{J}_n^{(a,b)}(\xi) + a_{n+1} \mathsf{J}_{n+1}^{(a,b)}(\xi)\,,$$

with:

$$a_n = \frac{2}{2n+a+b}\sqrt{\frac{n(n+a+b)(n+a)(n+b)}{(2n+a+b-1)(2n+a+b+1)}}\,,$$
$$b_n = -\frac{a^2-b^2}{(2n+a+b)(2n+a+b+2)}\,.$$

To get started, the initial values are given by:

$$\mathsf{J}_0^{(a,b)}(\xi) = \sqrt{2^{-a-b-1}\frac{\Gamma(a+b+2)}{\Gamma(a+1)\Gamma(b+1)}}\,,$$
$$\mathsf{J}_1^{(a,b)}(\xi) = \frac{1}{2}\mathsf{J}_0^{(a,b)}(\xi)\sqrt{\frac{a+b+3}{(a+1)(b+1)}}((a+b+2)\xi + (a-b))\,.$$

Some classical examples are:

- $a = b$: this choice yields to the family of ultraspherical or Gegenbauer polynomials $\mathsf{C}_m^{(\lambda)}(\xi)$ defined by:
$$\mathsf{C}_m^{(\lambda)}(\xi) := \frac{(2\lambda)_m}{(\lambda+\frac{1}{2})_m}\tilde{\mathsf{J}}_m^{(\lambda-1/2,\lambda-1/2)}(\xi)\,,$$
where $(z)_m := (z-1+m)!/(z-1)!$. The weight function is $p^{(\lambda-1/2,\lambda-1/2)} = (1-\xi^2)^{\lambda-1/2}$;
- $a = b = 0$: this choice yields to the family of Legendre polynomials $\mathsf{L}_m(\xi) = \mathsf{C}_m^{(1/2)}(\xi)$ such that the weight function is $p^{(0,0)} = 1$. The first six Legendre polynomials are displayed in Fig. B.1;
- $a = b = -1/2$: this choice yields to the family of Tchebychev polynomials $\mathsf{T}_m(\xi)$ defined by:
$$\mathsf{T}_m(\xi) = m \lim_{\lambda\to 0} \Gamma(2\lambda)\mathsf{C}_m^{(\lambda)}(\xi)\,.$$
The weight function is $p^{(-1/2,-1/2)} = (1-\xi^2)^{-1/2}$. They have an explicit analytical expression as:
$$\mathsf{T}_m(\xi) = \cos(m \arccos(\xi))\,.$$
The first six Tchebychev polynomials are displayed in Fig. B.2.

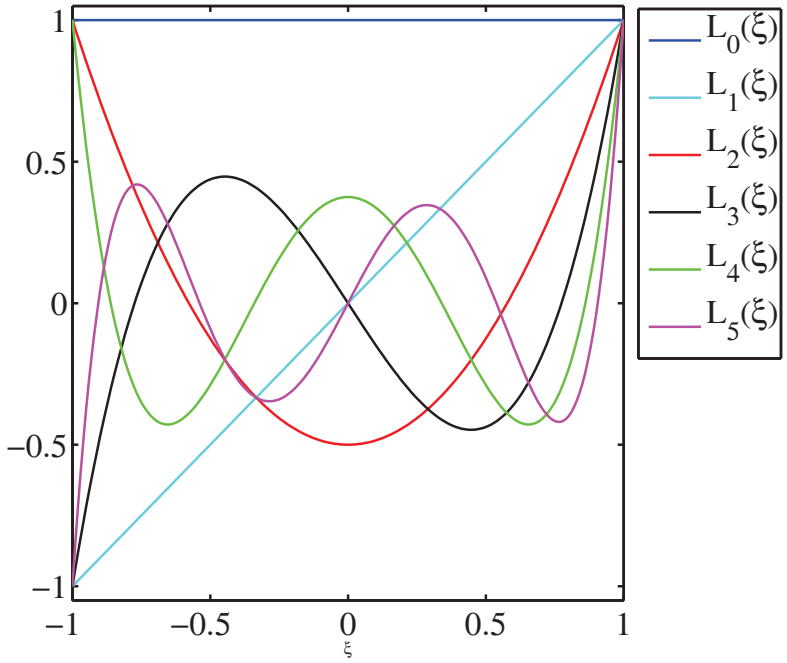

Figure B.1: First six Legendre polynomials.

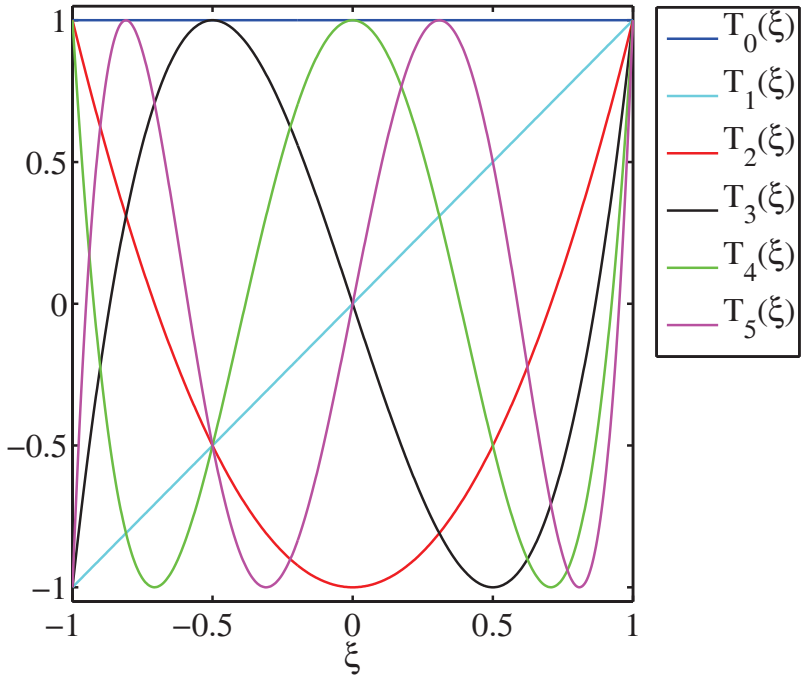

Figure B.2: First six Chebyschev polynomials.

Bibliography

[1] M. Abramowitz and I. A. Stegun. *Handbook of Mathematical Functions with Formulas, Graphs, and Mathematical Tables*. Dover, New York, NY, USA, ninth Dover printing, tenth GPO printing edition, 1964.

[2] J. D. Achenbach. *Wave Propagation in Elastic Solids*. North-Holland Pub. Co., American Elsevier Pub. Co., 1973.

[3] M. Ainsworth. Dispersive and dissipative behaviour of high order discontinuous Galerkin finite element methods. *Journal of Computational Physics*, 198(1):106–130, 2004.

[4] G. Bal. Kinetics of scalar wave fields in random media. *Wave Motion*, 43(2):132 – 157, 2005.

[5] G. Bal, T. Komorowski, and L. Ryzhik. Kinetic limits for waves in a random medium. *Kinetic and Related Models*, 3(4):529–644, 2010.

[6] D. Bancroft. The velocity of longitudinal waves in cylindrical bars. *Phys. Rev.*, 59 (7):588–593, 1941.

[7] V. Baronian. *Couplage des Méthodes Modales et Éléments Finis pour la Diffraction des Ondes Élastiques Guidées*. PhD thesis, École Polytechnique, France, 2009.

[8] K. Bathe. *Finite Element Procedures in Engineering Analysis*. Prentice-Hall Inc, Englewood Cliffs, NJ, USA, 1982.

[9] V. D. Belov, S. A. Rybak, and B. D. Tartakovskii. Propagation of vibrational energy in absorbing structures. *Journal of Soviet Physics Acoustics*, 23(2):115–119, 1977.

[10] T. Belytschko and R. Mullen. On Dispersive Properties of Finite Element Solutions. In J. Achenbach and J. Miklowitz, editors, *Modern Problems in Elastic Wave Propagation*, pages 67–82. Wiley, New York, NY, USA, 1978.

[11] S. Bograd, P. Reuss, A. Schmidt, L. Gaul, and M. Mayer. Modeling the dynamics of mechanical joints. *Mechanical Systems and Signal Processing*, 25(8):2801 – 2826, 2011.

[12] J. Bonini. *Contribution à la Prédiction Numérique de l'Endommagement de Stratifiés Composites sous Impact Basse Vitesse*. PhD thesis, École Nationale Supérieure des Arts et Métiers, 1995.

[13] S. Bougacha, J.-L. Akian, and R. Alexandre. Gaussian beams summation for the wave equation in a convex domain. *Communications in Mathematical Sciences*, 7(4): 973–1008, 2009.

[14] F. Brezzi, L. D. Marini, and E. Suli. Discontinuous Galerkin methods for first-order hyperbolic problems. *Mathematical Models and Methods in Applied Sciences*, 14: 106–130, 2004.

[15] E. Carrera, G. Giunta, P. Nali, and M. Petrolo. Refined beam elements with arbitrary cross-section geometries. *Computers and Structures*, 88(5-6):283 – 293, 2010.

[16] K. Chan, K. Lai, N. Stephen, and K. Young. A new method to determine the shear coefficient of Timoshenko beam theory. *Journal of Sound and Vibration*, 330(14):3488 – 3497, 2011.

[17] R. Clough and J. Penzien. *Dynamics of Structures*. McGraw-Hill, New York, NY, USA, 1975.

[18] B. Cockburn. Discontinuous Galerkin methods. *Journal of Applied Mathematics and Mechanics / Zeitschrift fr Angewandte Mathematik und Mechanik*, 83(11):731–754, 2003.

[19] B. Cockburn and C.-W. Shu. Runge-Kutta discontinuous Galerkin methods for convection-dominated problems. *Journal of Scientific Computing*, 16(3):173–261, 2001.

[20] G. R. Cowper. The shear coefficient in Timoshenko's beam theory. *Journal of Applied Mechanics*, 33(2):335–340, 1966.

[21] V. Damljanovic and R. L. Weaver. Propagating and evanescent elastic waves in cylindrical waveguides of arbitrary cross section. *The Journal of the Acoustical Society of America*, 115(4):1572–1581, 2004.

[22] C. Devaux. *Modélisation du Comportement Vibratoire des Structures par des Méthodes Énergétiques: Formulation Moyennée Spatialement pour des Systèmes Unidimensionnels*. PhD thesis, Université du Maine, France, 2006.

[23] J. F. Doyle. *Wave Propagation in Structures - Spectral Analysis Using Fast Discrete Fourier Transforms*. Mechanical Engineering. Springer-Verlag, 2nd edition, 1997.

[24] M. Eisenberger. Dynamic stiffness vibration analysis using a high-order beam model. *International Journal for Numerical Methods in Engineering*, 57(11):1603–1614, 2003.

[25] B. Engquist and O. Runborg. Computational high-frequency wave propagation. *Acta Numerica*, 12:181–266, 2003.

[26] B. Engquist, O. Runborg, and A.-K. Tornberg. High-frequency wave propagation by the segment projection method. *Journal of Computational Physics*, 178(2):373–390, 2002.

[27] B. Érin. *Modèles de Diffusion d'Énergie Vibratoire en Dynamique des Structures = Vibratory Energy Diffusion Models in Structural Dynamics*. PhD thesis, Université Paris 6, France; ONERA, France, 1995.

[28] E. Fatemi, B. Engquist, and S. Osher. Numerical solution of the high frequency asymptotic expansion for the scalar wave equation. *Journal of Computational Physics*, 120(1):145–155, 1995.

[29] M. Fink. Time reversed acoustics. *Physics Today*, 50(3):34–40, 1997.

[30] B. Fornet. *Problèmes Hyperboliques à Coefficients Discontinus et Pénalisation de Problèmes Hyperboliques*. PhD thesis, Université de Provence, 2007.

[31] P. Gérard, P. A. Markowich, N. J. Mauser, and F. Poupaud. Homogenization limits and Wigner transforms. *Communications on Pure and Applied Mathematics*, L:323–379, 1997.

[32] Y. M. Ghugal and R. P. Shimpi. A review of refined shear deformation theories for isotropic and anisotropic laminated beams. *Journal of Reinforced Plastics and Composites*, 20(3):255–272, 2001.

[33] S. Gottlieb, C.-W. Shu, and E. Tadmor. Strong stability-preserving high-order time discretization methods. *SIAM Review*, 43(1):89–112, 2001.

[34] K. F. Graff. *Wave Motion in Elastic Solids*. Ohio State University Press, 1975.

[35] F. Gruttmann and W. Wagner. Shear correction factors in Timoshenko's beam theory for arbitrary shaped cross-sections. *Computational Mechanics*, 27(3):199–207, 2001.

[36] M. Guo and X. Wang. Transport equations for a general class of evolution equations with random perturbations. *Journal of Mathematical Physics*, 40:4828–4858, 1999.

[37] S. M. Han, H. Benaroya, and T. Wei. Dynamics of transversely vibrating beams using four engineering theories. *Journal of Sound and Vibration*, 225(5):935–988, 1999.

[38] P. Hardy, M. Ichchou, L. Jzquel, and D. Trentin. A hybrid local energy formulation for plates mid-frequency flexural vibrations. *European Journal of Mechanics - A/Solids*, 28(1):121 – 130, 2009.

[39] P. C. Herdic, B. H. Houston, M. H. Marcus, E. G. Williams, and A. M.Baz. The vibro-acoustic response and analysis of a full-scale aircraft fuselage section for interior noise reduction. *The Journal of the Acoustical Society of America*, 117(6):3667–3678, 2005.

[40] J. Hesthaven, S. Gottlieb, and D. Gottlieb. *Spectral Methods for Time-Dependent Problems*. Applied and computational mathematics. Cambridge University Press, 2007.

[41] J. S. Hesthaven and T. Warburton. *Nodal Discontinuous Galerkin Methods: Algorithms, Analysis, and Applications*. Springer, 1st edition, 2007.

[42] F. Honarvar, E. Enjilela, and A. N. Sinclair. An alternative method for plotting dispersion curves. *Ultrasonics*, 49(1):15–18, 2009.

[43] F. Q. Hu, H. L. Atkins, and D. M. Bushnell. Eigensolution Analysis of the Discontinuous Galerkin Method with Non-uniform Grids–Part 1; One Space Dimension. Technical Report 20020025359, NASA, Langley Research Center, USA, December 2001.

[44] N.-C. Huang. Theories of elastic slender curved rods. *Zeitschrift fr Angewandte Mathematik und Physik*, 24(1):1–19, 1973.

[45] G. E. Hudson. Dispersion of elastic waves in solid circular cylinders. *Phys. Rev.*, 63 (1-2):46–51, 1943.

[46] J. R. Hutchinson. Shear coefficients for Timoshenko beam theory. *Journal of Applied Mechanics*, 68(1):87–92, 2001.

[47] G. Inquiété. *Simulation Numérique de la Propagation des Ondes dans les Structures Composites Stratifiées*. PhD thesis, École Centrale de Lyon, France, 2010.

[48] S. Jin and D. Yin. Computational high frequency waves through curved interfaces via the Liouville equation and geometric theory of diffraction. *Journal of Computational Physics*, 227(12):6106–6139, 2008.

[49] R. K. Kapania and J. Li. On a geometrically exact curved/twisted beam theory under rigid cross-section assumption. *Computational Mechanics*, 30(5):428–443, 2003.

[50] H. Kuttruff. *Room Acoustics*. Spon Press, 4th edition, 1999.

[51] A. Labuschagne, N. van Rensburg, and A. van der Merwe. Comparison of linear beam theories. *Mathematical and Computer Modelling*, 49(1-2):20 – 30, 2009.

[52] R. S. Langley. A wave intensity technique for the analysis of high frequency vibrations. *Journal of Sound Vibration*, 159:483–502, 1992.

[53] R. S. Langley and F. J. Fahy. High frequency structural vibration. In F. Fahy and J. Walker, editors, *Advanced Applications in Acoustics, Noise and Vibration*, pages 490–530. Spon Press, London, UK, 2004.

[54] A. Le Bot, M. N. Ichchou, and L. Jezequel. Energy flow analysis for curved beams. *The Journal of the Acoustical Society of America*, 102(2):943–954, 1997.

[55] Y. Le Guennec and E. Savin. A transport model and numerical simulation of the high-frequency dynamics of three-dimensional beam trusses. *The Journal of the Acoustical Society of America*, 130(6):3706–3722, 2011.

[56] M. Levinson. Further results of a new beam theory. *Journal of Sound Vibration*, 77: 440–444, 1981.

[57] P.-L. Lions and T. Paul. Sur les mesures de Wigner (On Wigner measures). *Revista Matemática Iberoamericana*, 9:553–618, 1993.

[58] O. I. Lobkis and R. L. Weaver. Anderson localization of ultrasound in plates: Further experimental results. *The Journal of the Acoustical Society of America*, 124(6):3528–3533, 2008.

[59] A. Love. *A Treatise on the Mathematical Theory of Elasticity*. Cambridge University Press, 4th edition, 1927.

[60] R. H. Lyon. *Statistical Energy Analysis of Dynamical Systems : Theory and Applications*. MIT Press, 1975.

[61] R. H. Lyon and R. G. DeJong. *Theory and Application of Statistical Energy Analysis*. Butterworth-Heinemann, Boston, M, USA, 2nd edition, 1995.

[62] R. H. Lyon and G. Maidanik. Power flow between linearly coupled oscillators. *The Journal of the Acoustical Society of America*, 34(5):623–&, 1962.

[63] B. R. Mace and E. Manconi. Wave motion and dispersion phenomena: Veering, locking and strong coupling effects. *The Journal of the Acoustical Society of America*, 131(2):1015–1028, 2012.

[64] H. Mechkour. The exact expressions for the roots of Rayleigh wave equation. In *Proceedings of The 2-nd International Colloquium of Mathematics in Engineering and Numerical Physics (MENP-2), April 22-27, 2002, University Politehnica of Bucharest, Romania*, pages 96–104, 2003.

[65] T. R. Meeker and A. H. Meitzler. Guided wave propagation in elongated cylinders and plates. In W. P. Masson, editor, *Principles and methods*, volume 1A of *Physical acoustics*, pages 111–167. Academic press, New York, NY, USA, 1964.

[66] J. Miklowitz. *The Theory of Elastic Waves and Waveguides*. North-Holland Pub. Co., 1978.

[67] C. J. Moening. Views of the world of pyrotechnic shock. *Shock and Vibration Bulletin*, 56(3):3 28, 1986.

[68] D. J. Nefske and S. H. Sung. Power flow finite element analysis of dynamic systems: basic theory and application to beams. *Journal of Vibration, Acoustics, Stress, and Reliability in Design*, 111(1):94–100, 1989.

[69] N. M. Newmark. A method of computation for structural dynamics. *Journal of the Engineering Mechanics Division*, 85(3):67–94, 1959.

[70] R. Niclasen and H. Blackburn. Gauss and GaussLobatto element quadratures applied to the incompressible NavierStokes equations. In J. Noye, M. Teubner, and e. A. Gill, editors, *Computational techniques and applications*, Singapore, SG, 1998. Research Publishing Services.

[71] M. Onoe, H. D. McNiven, and R. D. Mindlin. Dispersion of axially symmetric waves in elastic rods. *Journal of Applied Mechanics*, 29(4):729–734, 1962.

[72] P. Pai and M. J. Schulz. Shear correction factors and an energy-consistent beam theory. *International Journal of Solids and Structures*, 36(10):1523 – 1540, 1999.

[73] Y.-H. Pao and R. D. Mindlin. Dispersion of flexural waves in an elastic, circular cylinder. *Journal of Applied Mechanics*, 27(3):513–520, 1960.

[74] P. Papadopoulos. Introduction to the Finite Element Method. Lecture notes, University of California at Berkeley.

[75] G. C. Papanicolaou and L. V. Ryzhik. Waves and Transport. In L. Caffarelli and W. E, editors, *Hyperbolic Equations and Frequency Interactions*, volume 5 of *IAS/Park City Mathematics Series*, pages 305–382. American Mathematical Society, Providence, RI, USA, 1999.

[76] R. Pinnington and D. Lednik. Transient energy flow between two coupled beams. *Journal of Sound and Vibration*, 189(2):265–287, 1996.

[77] W. Press, S. Teukolsky, W. Vetterling, and B. Flannery. *Numerical Recipes: The Art of Scientific Computing*. Cambridge University Press, 3rd edition, 2007.

[78] L. Rayleigh. *Theory of Sound*. Macmillan, London, UK, 2nd edition, 1894-1896.

[79] J. Reddy, C. Wang, G. Lim, and K. Ng. Bending solutions of Levinson beams and plates in terms of the classical theories. *International Journal of Solids and Structures*, 38(26):4701 – 4720, 2001.

[80] M. Redwood and J. Lamb. On the propagation of high frequency compressional waves in isotropic cylinders. *Proceedings of the Physical Society, Section B*, 70(1):136, 1957.

[81] J. Renton. Generalized beam theory applied to shear stiffness. *International Journal of Solids and Structures*, 27(15):1955 – 1967, 1991.

[82] O. Runborg. Mathematical models and numerical methods for high frequency waves. *Commun Comput Phys*, 2(5):827–880, 2007.

[83] S. Rybak. Waves in a plate containing random inhomogeneities. *Soviet PhysicsAcoustics*, 17(3):345349, 1972.

[84] Z. Rychter. A simple and accurate beam theory. *Acta Mechanica*, 75(1):57–62, 1988.

[85] E. Savin. Midfrequency vibrations of a complex structure: experiments and comparison with numerical simulations. *AIAA Journal*, 40:1876–1884, 2002.

[86] E. Savin. A transport model for high-frequency vibrational power flows in coupled heterogeneous structures. *Interaction and Multiscale Mechanics*, 1(1):53–81, 2007.

[87] E. Savin. Diffusion regime for high-frequency vibrations of randomly heterogeneous structures. *The Journal of the Acoustical Society of America*, 124(6):3507–3520, 2008.

[88] E. Savin. High-frequency dynamics of heterogeneous slender structures. *Journal of Sound and Vibration*, in press, 2013.

[89] P. Shorter and R. Langley. Vibro-acoustic analysis of complex systems. *Journal of Sound and Vibration*, 288(3):669 – 699, 2005.

[90] C. Soize. A nonparametric model of random uncertainties for reduced matrix models in structural dynamics. *Probabilistic Engineering Mechanics*, 15(3):277 – 294, 2000.

[91] C. R. Steele. Asymptotic analysis of stress waves in inhomogeneous elastic solids. *Journal of American Institute of Aeronautics and Astronautics*, 7:896–902, 1969.

[92] C. R. Steele. *Application of the WKB Method in Solid Mechanics*, volume 3 of *Mechanics Today*. Franklin Book Co., Elkins Park, PA, USA, 1976.

[93] N. Stephen. Considerations on second order beam theories. *International Journal of Solids and Structures*, 17(3):325 – 333, 1981.

[94] N. G. Stephen and S. Puchegger. On the valid frequency range of Timoshenko beam theory. *Journal of Sound and Vibration*, 297(3-5):1082–1087, 2006.

[95] F. Sui. *Theoretical Study on Time-Varying Vibroacoustic Energy at High Frequency*. PhD thesis, École Centrale de Lyon, France, 2004.

[96] Q. A. Ta. *Modélisation des Propriétés Mécaniques Anisotropes Aléatoires et Impact sur la Propagation des Ondes Élastiques*. PhD thesis, École Centrale Paris, 2011.

[97] G. Tanner. Dynamical energy analysis–Determining wave energy distributions in vibro-acoustical structures in the high-frequency regime. *Journal of Sound Vibration*, 320:1023–1038, 2009.

[98] S. P. Timoshenko. On the correction for shear of the differential equation for transverse vibrations of bars of uniform cross-section. *Philosophical Magazine*, 41:744–746, 1921.

[99] S. P. Timoshenko. On the transverse vibrations of bars of uniform cross-section. *Philosophical Magazine*, 43:125–131, 1922.

[100] A.-K. Tornberg. *Interface Tracking Methods with Application to Multiphase Flows*. PhD thesis, Royal Institute of Technology, Sweden, 2000.

[101] F. Treyssède. Elastic waves in helical waveguides. *Wave Motion*, 45(4):457–470, 2008.

[102] C. Truesdell. *The Rational Mechanics of Flexible or Elastic Bodies 1638 - 1788*, volume 2,11 of *Leonhard Euler, Opera Omnia / Opera mechanica et astronomica*. Birkhuser Basel, 1960.

[103] H.-S. Tsay and H. B. Kingsbury. Vibrations of rods with general space curvature. *Journal of Sound and Vibration*, 124(3):539–554, 1988.

[104] Y. Tso and C. Norwood. Vibratory power transmission through three-dimensional beam junctions. *Journal of Sound and Vibration*, 185(4):595 – 607, 1995.

[105] J. A. Turner and R. L. Weaver. Diffuse energy propagation on heterogeneous plates: Structural acoustics radiative transfer theory. *The Journal of the Acoustical Society of America*, 100(6):3686–3695, 1996.

[106] N. F. J. van Rensburg and A. J. van der Merwe. Natural frequencies and modes of a Timoshenko beam. *Wave Motion*, 44(1):58–69, 2006.

[107] K. van Wijk, M. Haney, and J. A. Scales. 1D energy transport in a strongly scattering laboratory model. *Phys. Rev. E*, 69(3):036611, 2004.

[108] V. Červený. *Seismic Ray Theory*. Cambridge University Press, 2001.

[109] J. Virieux. SH-wave propagation in heterogeneous media: Velocity-stress finite-difference method. *Geophysics*, 49(11):1933–1942, 1984.

[110] E. Wester and B. Mace. Wave component analysis of energy flow in complex structures - Part I: a deterministic model. *Journal of Sound and Vibration*, 285(1):209 – 227, 2005.

[111] E. Wester and B. Mace. Wave component analysis of energy flow in complex structures - Part II: ensemble statistics. *Journal of Sound and Vibration*, 285(1):229 – 250, 2005.

[112] E. Wester and B. Mace. Wave component analysis of energy flow in complex structures - Part III: two coupled plates. *Journal of Sound and Vibration*, 285(1):251 – 265, 2005.

[113] A. Yu, M. Fang, and X. Ma. Theoretical research on naturally curved and twisted beams under complicated loads. *Computers and Structures*, 80(32):2529–2536, 2002.

[114] J. J. Zemanek. An experimental and theoretical investigation of elastic wave propagation in a cylinder. *The Journal of the Acoustical Society of America*, 51(1B):265–283, 1972.

[115] O. Zienkiewicz and R. Taylor. *The Finite Element Method*, volume 1 and 2. McGraw-Hill, 4th edition, 1994.